université PARIS-SACLAY

ENS ÉCOLE NORMALE SUPÉRIEURE

ÉCOLE POLYTECHNIQUE UNIVERSITÉ PARIS-SACLAY

NNT : 2019SACLX005

Thèse de doctorat

Étude du devenir des tourbillons des Aiguilles et de leur transport dans l'océan Atlantique Sud à partir d'observations satellitaires et in situ

Thèse de doctorat de l'Université Paris-Saclay
préparée à l'École Polytechnique

Ecole doctorale n°129 Sciences de l'Environnement d'Ile-de-France (SEIF)
Spécialité de doctorat : Météorologie, océanographie, physique de l'environnement

Thèse présentée et soutenue à Paris, le 28/02/2019, par

RÉMI LAXENAIRE

Composition du Jury :

Matthieu Roy-Barman Professeur des Universités, Université Paris-Saclay (LSCE)	Président
Rosemary Morrow Physicienne CNAP, Observatoire Midi-Pyrénées (LEGOS)	Rapportrice
Andrea Doglioli Maître de Conférences, Université d'Aix - Marseille (MIO)	Rapporteur
Gilles Reverdin Directeur de Recherche, Sorbonne Université (LOCEAN)	Examinateur
Francesco Nencioli PhD, Plymouth Marine Laboratory (RSG)	Examinateur
Sabrina Speich Professeure des Universités, École Normale Supérieure (LMD)	Directrice de thèse
Alexandre Stegner Chargé de recherche, École Polytechnique (LMD)	Co-directeur de thèse

Sommaire

1 Préface **1**

2 Introduction **3**

2.1 La circulation à grande échelle 4

2.2 Les tourbillons océaniques 7

2.2.1 Généralités 9

2.2.2 L'observation des tourbillons 12

2.2.3 Histoire de la vie d'un tourbillon 20

2.2.4 Impact des tourbillons océaniques 24

2.3 Les échanges océaniques de l'océan Indien vers l'océan Atlantique . 27

2.3.1 Le système du courant des Aiguilles 28

2.3.2 Les tourbillons des Aiguilles 30

2.4 Questions principales et approche 32

3 Caractérisation de la signature en surface des Anneaux des Aiguilles **35**

3.1 Résumé de l'article 35

3.2 Anticyclonic eddies connecting the western boundaries of Indian and Atlantic oceans 36

3.2.1 Introduction 36

3.2.2 Data and Methods 38

3.2.3 Validation and Comparison of Eddies Datasets 47

3.2.4 Results of the TOEddies method applied to Agulhas Rings . 53

3.2.5 Summary and Conclusions 70

4 Évolution de la structure thermohaline d'un Anneau des Aiguilles **73**

4.1 Résumé de l'article 73

4.2 Evolution of the thermohaline structure of one Agulhas Ring reconstructed from satellite altimetry and Argo floats 74

4.2.1 Introduction 74

4.2.2 Data and Methods 78

4.2.3 Results 83

4.2.4 Comparison with Agulhas Rings identified in the literature . 103

4.2.5 Summary and conclusion 110

5 Contenu thermique et transport de chaleur des Anneaux des Aiguilles dans l'Atlantique Sud **117**
5.1 Résumé de l'article 117
5.2 Agulhas Rings heat content and transport in the South Atlantic estimated by combining satellite altimetry and Argo profiling floats data 118
5.2.1 Introduction 118
5.2.2 Data and Methods 121
5.2.3 Hydrological properties of Indian Water AREN 125
5.2.4 Discussion 146
5.2.5 Conclusion 149

6 Conclusions et perspectives **151**
6.1 Conclusions 151
6.2 Perspectives 155

Appendices

A Activités scientifiques pendant la thèse **161**

B Validation of the TOEddies method and parameters **165**

C Supporting Information for "Anticyclonic eddies connecting the western boundaries of Indian and Atlantic oceans" **173**

D Additional Figures for "Evolution of the thermohaline structure of one Agulhas Ring reconstructed from satellite altimetry and Argo floats" **181**

E Additional Figures for "Agulhas Rings heat content and transport in the South Atlantic estimated by combining satellite altimetry and Argo profiling floats data" **193**

Bibliographie **197**

Liste des Figures **219**

Liste des Tableaux **229**

1

Préface

La réalité de la crise climatique qui touche notre siècle est, ou du moins devrait être, de notoriété publique. D'ailleurs, les preuves de l'influence de l'activité humaine sur le climat terrestre s'accumulent au fil des années, notamment l'explosion post-industrielle des émissions de gaz à effet de serre dont la concentration a très fortement augmenté dans les océans et l'atmosphère. Cela a pour conséquences, bien connues, la fonte des glaces en Arctique, l'acidification des océans, l'augmentation de la température globale ainsi que le déséquilibre du bilan énergétique terrestre tel qu'observé par les satellites. Pour la température, chacune des trois dernières décennies ont été successivement les plus chaudes depuis 1850. Cette augmentation est visible sur les observations de l'évolution globale des anomalies de températures (Figure 1.1.a).

Or, le changement climatique augmente la fréquence et la magnitude des risques naturels déjà existants. Il en créera certainement de nouveaux pour le système naturel et pour la société humaine. Cela se traduit, entre autre, par une augmentation des inondations, des événements météorologiques sévères, des pénuries d'eau et de nourriture pour les populations les plus pauvres.

Il est donc de la responsabilité du monde scientifique d'étudier ce sujet avec les outils dont il dispose afin d'en révéler l'évolution probable. Ce rôle d'expert est primordial pour apporter des éléments nécessaires à la prise de décision par la société. Cette investigation s'applique sur toutes les branches impactées par ce changement qui s'étendent de l'étude des populations à la compréhension du système climatique. Ainsi, outre la motivation intrinsèque à la recherche scientifique d'appréhender le monde qui nous entoure, cette compréhension est d'intérêt publique. Par exemple, les projections climatiques sont des outils formidables pour entrapercevoir les changements du climat dans le futur. Or, cet exercice nécessite une bonne

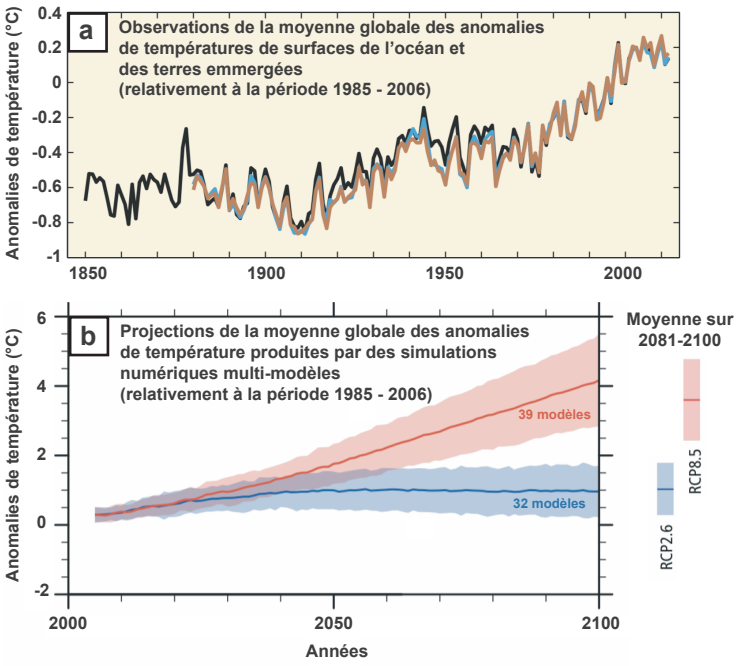


Figure 1.1: Évolution des anomalies de température historiques observées (a) et projetées par modélisation numérique (b) issus du 5^e rapport de GIEC [Pachauri et al. 2014]. Les couleurs du panneau a représentent différentes bases de données. Les deux couleurs dans le panneau b indiquent les résultats pour 2 scénarios d'émissions (RCP2.6 et RCP8.5) avec l'incertitude associée.

connaissance des différentes composantes agissant sur le système climatique. Ce système est extrêmement complexe suite aux multitudes de phénomènes physiques, chimiques, géologiques et biologiques qui entrent en jeux. On peut appréhender sa complexité en regardant l'incertitude qui apparait sur les projections climatiques du groupe d'experts intergouvernemental sur l'évolution du climat (GIEC) dans la figure 1.1.b. Il est donc nécessaire d'améliorer nos connaissances des processus agissant dans les différentes composantes du système climatique.

Avec plus de 90% des excès de chaleur accumulés dans les quarante dernières années, l'océan est le principal réservoir du surplus d'énergie emmagasiné par le système climatique au cours de cette période. Le milieu océanique étant caractérisé par des écoulements de grande envergure associés à des échelles de temps longues (i.e. jusqu'à plusieurs siècles), son adaptation à des changements relativement rapides (i.e. de l'ordre de la décennie) est difficile à appréhender. Ainsi, il est crucial de mieux décrire les processus dynamiques et les transferts de chaleur qui agissent dans ce milieu. C'est dans cette optique que se place ce travail de thèse en essayant d'améliorer notre description des transports d'eau de l'océan Indien vers l'océan Atlantique à partir d'observations modernes.

2

Introduction

Sommaire

2.1 La circulation à grande échelle 4
2.2 Les tourbillons océaniques 7
2.2.1 Généralités 9
2.2.2 L'observation des tourbillons 12
2.2.3 Histoire de la vie d'un tourbillon 20
2.2.4 Impact des tourbillons océaniques 24
2.3 Les échanges océaniques de l'océan Indien vers l'océan Atlantique 27
2.3.1 Le système du courant des Aiguilles 28
2.3.2 Les tourbillons des Aiguilles 30
2.4 Questions principales et approche 32

Cette thèse a pour but d'étudier le rôle des tourbillons océaniques dans les transports d'eau de l'océan Indien vers l'océan Atlantique. Ces échanges constituent une des branches de la circulation océanique globale et jouent donc un rôle majeur dans les transferts de chaleur entre ces deux océans.. Il est important d'avoir une vision large de cette circulation à grande échelle, des structures tourbillonnaires ainsi que de la zone d'étude afin de comprendre pleinement les motivations de ce travail et d'appréhender les résultats obtenus. Cette thèse étant structurée autour de trois articles scientifiques qui sont, par nature, composés d'une étude bibliographique thématique dans leur introduction, nous souhaitons offrir ici une vision qui se veut plus générale de ces sujets avant d'expliciter les questions ayant motivées ce travail.

2.1 La circulation à grande échelle

La Terre est forcée par le Soleil dont l'apport d'énergie n'est pas homogène à la surface du globe terrestre. Cela se traduit, en moyenne, par un gradient négatif de l'irradiation solaire qui est dirigé vers les pôles dans les deux hémisphères. En comparaison, la réémission de cette énergie par la Terre dépend peu de la latitude. Ainsi, la bande intertropicale reçoit un surplus d'énergie par rapport aux hautes latitudes qui doit être compensé par des transports méridiens dans les systèmes fluides que sont l'océan et l'atmosphère. De plus, les ondes électromagnétiques du soleil sont fortement absorbées par l'eau ce qui induit un réchauffement de la surface des océans. Ainsi, l'excès de chaleur accumulé par l'océan dans les quarante dernières années [Rhein et al. 2013] se concentre principalement à sa surface. En effet, les 500 premiers mètres de l'océan, qui représentent environ 10 à 15% du volume total, ont accumulé plus de 40% de cette énergie [Roemmich et al. 2015; Wijffels et al. 2016; Talley et al. 2016].

Nous voyons donc que des mouvements sont nécessaires pour répartir l'énergie sur la surface de la planète ainsi que dans les différentes couches de l'océan. A grande échelle, aussi bien spatiale que temporelle, la répartition méridienne de la chaleur dans l'océan et la ventilation des couches profondes se font par la circulation méridienne moyenne, ou encore circulation globale de retournement (GOC pour "Global Overturning Circulation"). Cette circulation est lente et séparée en plusieurs branches connectant les bassins océaniques entre eux ainsi que les eaux de surface avec les eaux profondes d'où son nom "de retournement" (Figure 2.1). Une vision 3D de cet écoulement est schématisée dans le panneau **b** de la Figure 2.1 où l'accent est mis sur l'océan Austral en tant que principale zone d'échange entre les 3 autres océans (Atlantique, Indien et Pacifique).

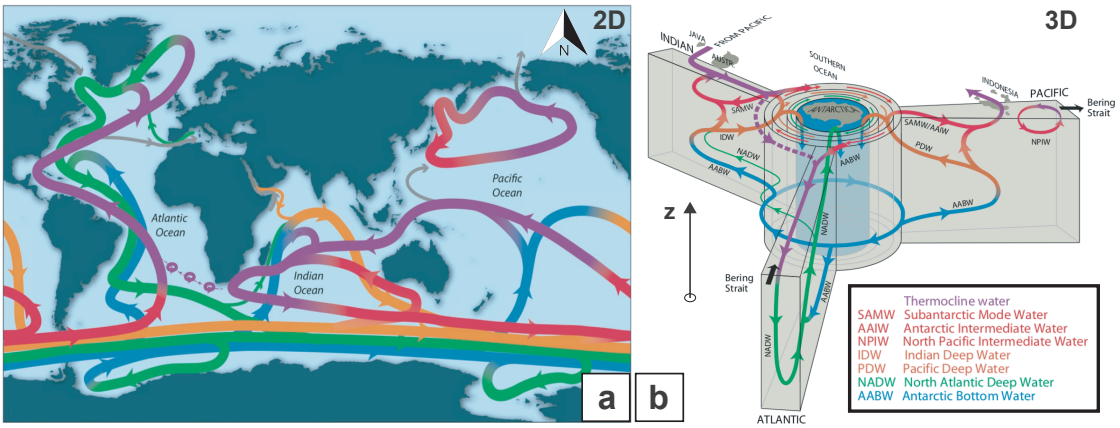


Figure 2.1: Schémas simplifiés 2D (panneau **a**) et 3D (panneau **b**) de la circulation globale de retournement. Les deux panneaux ont été reproduits depuis Talley [2013] d'aprés Talley [2011] à partir de Gordon [1986], Schmitz Jr [1995], Rahmstorf [2002] et Lumpkin and Pazos [2007].

La circulation de surface est caractérisée par de grands gyres subtropicaux forcés par le vent. Ils sont composés d'un transport vers l'équateur sous l'effet de l'équilibre de vorticité entre la tension de surface créée par le vent et le gradient latitudinal de vorticité planétaire tel que prédit par la relation de Sverdrup. Ce transport seul, qui se traduirait par une perte de masse aux fortes latitudes, ne peut pas expliquer la circulation dans chaque bassin. Il est donc compensé par un courant de retour, ou courant de bord ouest, fermant ces gyres et permettant ainsi de satisfaire la conservation de la masse. Ces courants, associés à une extension zonale faible en comparaison avec la largeur des bassins océaniques, peuvent être reproduits théoriquement en rajoutant à la relation de Sverdrup un terme de friction de fond dans le cas du modèle de Stommel [Stommel 1948] ou une fermeture turbulente pour le modèle de Munk [Munk 1950]. De tels courants avaient été observés depuis longtemps comme le prouve la première carte du Gulf Stream produite par Benjamin Franklin et Timothy Folger en 1769-1770 [Richardson 1980]. Les courants de bords ouest sont des vecteurs importants de transport méridien d'eau de surface vers les pôles. Cependant, l'océan Atlantique a la particularité d'avoir un transport net en surface vers le nord dans les deux hémisphères ce qui lui vaudra la dénomination de "mauvaise direction" lors de sa première observation par Wüst [1935].

La circulation des eaux de fond dans les trois océans qui ont une grande extension méridienne (i.e. Atlantique, Indien et Pacifique) a une structure générale similaire avec un déplacement vers le nord de l'eau de fond Antarctique (AABW pour "Antarctic Bottow Water") et un déplacement vers le sud des eaux profondes propres de ces bassins (NADW pour l'Atlantique Nord, IDW pour l'Indien et PDW pour le Pacifique avec DW pour "Deep Water"). La différence de circulation dans ces bassins vient principalement de la source de ces eaux profondes qui est une remontée de la AABW en PDW et IDW alors que, dans le nord de l'Atlantique, c'est de l'eau provenant de la thermocline qui plonge pour former la NADW. Cette formation est possible suite au transport net des eaux de la thermocline vers le nord dans l'hémisphère sud, comme décrit dans le paragraphe précédent, qui ferme le budget de masse. Ainsi, le nord de l'océan Atlantique est, avec l'océan Austral, une zone de transfert de chaleur vers les couches inférieures de l'océan. Les eaux de fond remontent dans l'océan Austral pour se transformer en eau de surface dans le cas de la IDW et PDW. La NADW, quand à elle, est plus lourde que ces dernières si bien qu'une partie reste sous la thermocline saisonnière et forme l'eau intermédiaire Antarctique (AAIW pour "Antarctic Intermediate Water").

L'existence d'un écoulement de fond vers l'équateur a tout d'abord été supposée par le Comte Rumford en 1798 à partir d'observations d'eaux profondes plus froides que les eaux locales dans les eaux subtropicales [Richardson 2008]. De nombreuses avancées sur la compréhension de ce phénomène ont été faites depuis grâce à des mesures directes mais aussi des simulations numériques. Cela s'est traduit par la proposition de trois hypothèses afin d'expliquer le forçage de cette circulation [Huang 2010] (Figure 2.2)

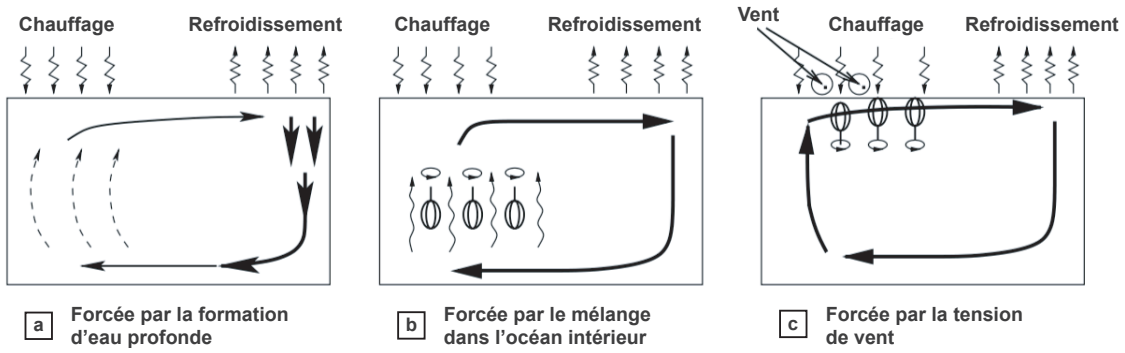


Figure 2.2: Représentation graphique des trois hypothèses sur le moteur de la GOC traduit depuis Huang [2010]

- **Hypothèse a**) Forçage par la formation des eaux profondes sur toute la colonne d'eau dans les hautes latitudes. En comparaison avec les eaux légères des zones de faibles latitudes, il existe un gradient de pression dans les profondeurs de l'océan qui pousse les courants profonds vers l'équateur et maintient donc la circulation thermohaline.

- **Hypothèse b**) Forçage par le mélange d'eaux profondes qui permet de les réchauffer et donc d'augmenter leur flottabilité. Il se produit donc une divergence en profondeur ce qui laisse de la place à une formation de nouvelles eaux profondes. Ce mélange diapycnal se fait sous l'effet de la marée, des ondes internes, de la friction sur le fond marin et, à plus faible niveau, des sources géothermales.

- **Hypothèse c**) Forçage par les remontées d'eaux profondes sous l'effet du pompage d'Ekman par les vents [Marshall and Speer 2012]. Selon cette hypothèse, l'eau profonde est renouvelée suite aux déplacements isopycnaux de la NADW avant d'être transformée en eau intermédiaire et en eau de surface dans le courant circumpolaire Antarctique (voir Figure 2.1). La tension du vent sur la surface de l'océan continue ce mélange.

De nombreuses études ont été entreprises pour identifier l'hypothèse la plus probable. La première hypothèse ne semble pas pouvoir apporter toutes les réponses car cela entrainerait le remplissage des fonds marins par de l'eau froide et seulement une GOC plus faible serait présente [Huang 2010]. Pour l'hypothèse **b** seule, cela nécessiterait un fort mélange dans la thermocline qui n'est pas observé [e.g. Ledwell et al. 1998; Kunze et al. 2006]. De nos jours, il semblerait que cette circulation soit la combinaison des mécanismes **b** et **c** [Kuhlbrodt et al. 2007]. Cela a été résumé par Talley [2013] qui indique que le retour des eaux profondes à la surface est, presque certainement, contrôlé par les remontées d'eaux profondes dans le courant circumpolaire Antarctique (ACC pour "Antarctic Circumpolar Current") mais que les propriétés de ces masses d'eaux dépendent des transformations diapycnales dans les couches profondes des océans Indien et Pacifique.

Finalement, les transports de la GOC participent activement aux échanges méridiens de chaleur à l'échelle de la planète en particulier aux tropiques [Trenberth and Caron 2001]. La circulation n'est pas identique dans tous les océans puisque le transport net s'effectue en surface de la bande équatoriale vers les pôles dans l'océan Indien et l'océan Pacifique alors que celui-ci est dirigé vers le nord tout au long de l'océan Atlantique. Cela se traduit par un transport vers le pôle dans l'Atlantique Nord qui est plus chaud d'environ 3°C à 40°N par rapport à la même latitude dans l'océan Pacifique. En particulier, un pic de 1,3 PW (1 PW = 10^{15} Watts) vers le Nord est présent à 26,5°N, un de 0,5 PW à travers la bande équatoriale [e.g. Trenberth and Caron 2001; Johns et al. 2011] et un de 0,5 PW à moyenne latitude dans l'Atlantique Sud [McDonagh and King 2005].

2.2 Les tourbillons océaniques

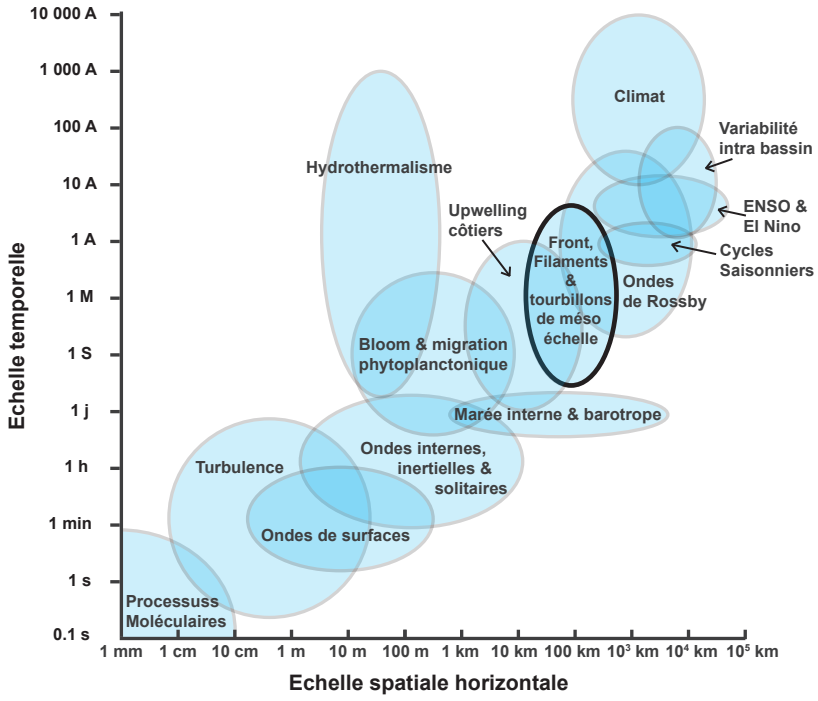


Figure 2.3: Représentation des principaux processus agissant sur l'océan en fonction de leur extension spatio-temporelle inspirés de Huang [2010], Lampitt et al. [2010] et Dickey [2003]. Pour l'échelle de temps, des symboles ne faisant pas partie du système international de mesures ont été ajoutés: S pour semaine, M pour mois et A pour années.

La circulation décrite précédemment n'est qu'une fraction de la dynamique présente dans l'océan puisque une multitude de processus agissent sur une large gamme d'échelles aussi bien spatiales que temporelles (cf. Figure 2.3). Ceux-ci s'étendent de la diffusion moléculaire, où agit le mélange irréversible, à la GOC qui couvre les bassins océaniques et évolue à l'échelle du climat. Il est aussi

possible d'appréhender la complexité dynamique de l'océan en identifiant les gammes d'échelles dans l'image satellite en fausse couleur du panneau **a** de la Figure 2.4.

La mésoéchelle, dont l'extension a été marquée par une limite noire dans la Figure 2.3, est particulièrement importante car associé à un pic d'énergie cinétique [Wunsch and Stammer 1995; Morrow and Le Traon 2012]. De plus, on peut remarquer dans le panneau **a** de la Figure 2.1 que le transport d'eau de la thermocline à l'est de l'Atlantique Sud se fait par des structures identifiées par leur circulation fermée : ce sont des tourbillons océaniques. De telles structures sont mises en évidence dans les images satellites des panneaux **b** et **c** de la Figure 2.4.

Par leur capacité à transporter des masses d'eau ainsi que par leur impact sur d'autres parties du réservoir climatique tel que l'atmosphère ou la biosphère, les tourbillons océaniques sont primordiaux dans la dynamique de l'océan. Ces tourbillons ont fait l'objet de nombreux articles de synthèse au cours des ces 40 dernières années aussi bien sur leurs observations en mer [e.g. Koshlyakov and Monin 1978; Olson 1991], leurs dynamiques [e.g. Carton 2010], leurs modélisations numériques [e.g. Carton 2001] et leurs impacts [e.g. Provenzale 1999; Martin 2003; McWilliams 2008; McGillicuddy Jr 2016].

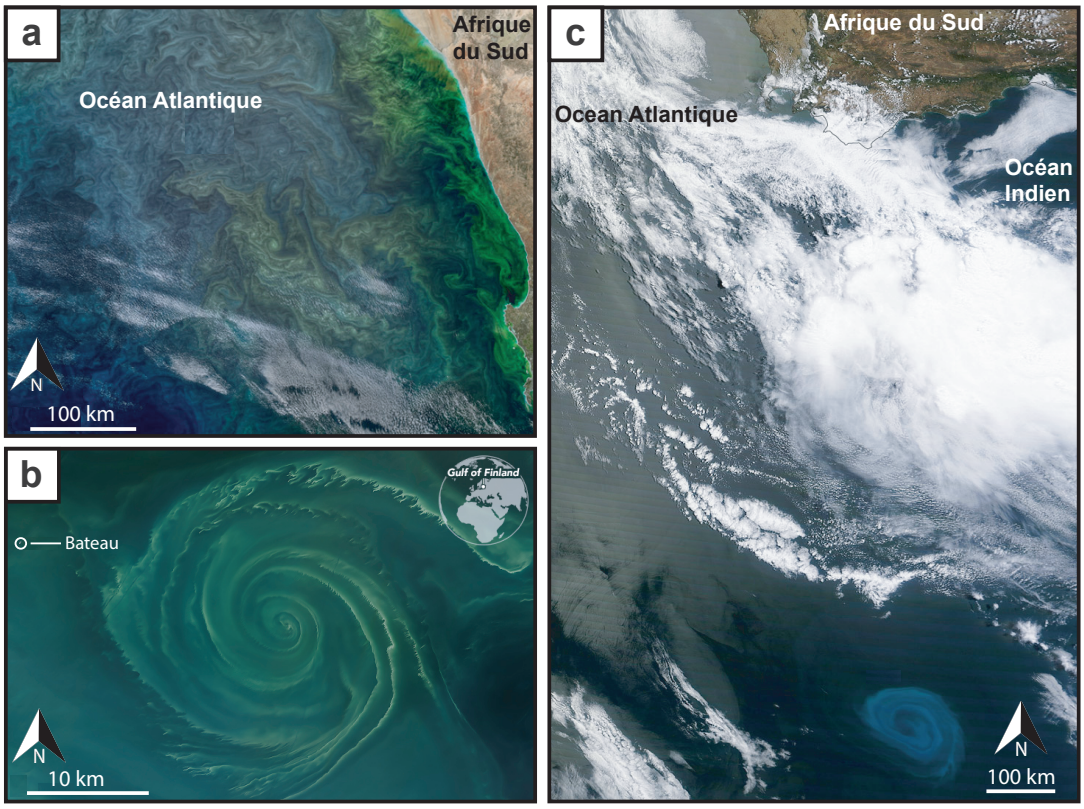


Figure 2.4: Sélection d'images satellites du site internet "Earth Observatory" de la NASA [`http://earthobservatory.nasa.gov/`]. **a**) Image en fausse couleur du MODIS sur le satellite Aqua le 2 septembre 2017, **b**) Image du OLI sur le satellite Landsat 8 le 18 juillet 2018 et **c**) Image du MODIS sur le satellite Terra le 26 décembre 2011.

Pour introduire quelques notions de base sur les tourbillons, nous commençons par donner un formalisme physique afin de mettre en évidence les grandeurs physiques importantes pour les appréhender. La variété des tourbillons océaniques est ensuite mise en avant à travers un historique de leurs observations. Nous évoquerons ensuite certaines de leurs propriétés dynamiques qui nous semblent importantes pour appréhender ce travail ainsi que des facettes de leurs influences sur l'environnement.

2.2.1 Généralités

De nombreux modèles physiques ont été utilisés pour étudier les tourbillons suivant le type de processus voulant être mis en exergue. Cela comprend aussi bien le set d'équations primitives que les modèles à couches dans de multiples régimes tels que la géostrophie et la quasi-géostrophie. Le but ici n'est pas de faire la liste de ces modèles que l'ont peut trouver dans des ouvrages de référence [e.g. Vallis 2006; Cushman-Roisin and Beckers 2011] mais d'identifier les variables et les nombres adimensionnels importants pour caractériser ces structures.

Les tourbillons océaniques présentent plusieurs caractéristiques communes propres à leur dynamique. En particulier, leur extension verticale est petite par rapport à celle horizontale ce qui implique qu'ils ont un faible rapport d'aspect. Cette propriété conduit à négliger les termes d'accélération verticale et donc d'utiliser l'équilibre hydrostatique. De plus, les variations de densité dans l'océan sont faibles par rapport à la valeur de densité moyenne (i.e. $|\rho'| << \rho_0$) ce qui permet d'appliquer l'approximation de Boussinesq. Finalement, écrire les équations gouvernant leur évolution en coordonnées cylindriques semble le plus approprié pour décrire ces structures associées à une circulation fermée autour de leur centre. En appliquant les approximations énoncées précédemment, le set d'équation gouvernant leur dynamique est :

$$\begin{aligned} \frac{Dv_r}{Dt} - \frac{v_\theta^2}{r} - fv_\theta &= \frac{-1}{\rho_0}\partial_r p + F_\theta + D_\theta, \\ \frac{Dv_\theta}{Dt} + \frac{v_r v_\theta}{r} + fv_r &= \frac{-1}{\rho_0 r}\partial_\theta p + F_r + D_r, \\ \partial_z p &= -\rho g \\ \frac{1}{r}\partial_r\left(rv_r\right) + \frac{1}{r}\partial_\theta v_\theta + \partial_z w &= 0 \end{aligned} \tag{2.1}$$

La dérivée particulaire, ou dérivée Lagrangienne, se décompose en $D/Dt = \partial_t + v_r\partial_r + \frac{v_\theta}{r}\partial_\theta + w\partial_z$ où v_r, v_θ et w sont, respectivement, les vitesses radiales dirigées vers l'extérieur, azimutales dans le sens trigonométrique et verticale. Le paramètre de Coriolis est $f = 2\Omega sin\left(\varphi\right)$, où Ω est le taux de rotation de la terre, φ la latitude,

ρ la masse volumique, ρ_0 la masse volumique de référence (i.e. $\rho_0 = 1000$ kg.m^{-3}), p la pression, F et D sont les termes de forçage et de dissipation sur l'horizontal.

Ce sont des structures cohérentes, ou du moins plus que leurs environnements, encapsulées dans des contours de circulation fermés. Ainsi, les tourbillons peuvent être dépeints comme des éléments composés de fluide en rotation se déplaçant telles des îles cohérentes au milieu d'un fluide désorganisé [Provenzale 1999]. Ils sont donc relativement persistants puisque leur temps de retournement au niveau du maximum de vitesse (i.e. temps nécessaire à une particule fluide pour effectuer un tour complet autour du centre) est typiquement de quelques jours ce qui est court comparé à la période de quelques semaines à plusieurs années où les tourbillons restent identifiables [Chelton et al. 2007; 2011].

Par exemple dans le cas d'un tourbillon parfaitement symétrique (i.e. $\partial_\theta = 0$) à l'équilibre (i.e. $\partial_t = 0$) qui n'est ni forcé (i.e. $F = 0$) ni dissipé (i.e. $D = 0$), la vitesse v_r s'annule. Ainsi, l'équilibre hydrostatique et l'approximation de Boussineq nous permettent d'écrire que $\partial_r p = \rho_0 g \partial_r h$ où h est la hauteur d'eau. Cette dernière peut être décomposée entre la somme de ses variations η et la hauteur au repos H_0. Ainsi, nous pouvons écrire l'équilibre cyclo-géostrophique, ou encore "gradient wind balance" [Cushman-Roisin and Beckers 2011] en fonction des gradients de pression ou de la déformation de la hauteur d'eau :

$$\frac{v_\theta^2}{r} + f v_\theta = \frac{-1}{\rho_0} \partial_r p = g \partial_r \eta \tag{2.2}$$

Nous voyons avec cet équilibre que, pour la même norme de vitesse, la direction de $f v_\theta$ est directement liée au signe du gradient de pression. Pour un gradient négatif, qui correspond à une anomalie de pression positive au cœur de la structure, $f v_\theta < 0$ et donc la vitesse azimutale est dans le sens inverse de la rotation de la terre. Cet état correspond à une structure anticyclonique. L'équilibre inverse existe avec un gradient positif pour les structures cycloniques.

Afin d'adimensionnaliser cette équation, nous introduisons le nombre de Rossby, qui est le ratio entre les termes d'advection et l'accélération de Coriolis, et le nombre de Burger, qui est le ratio entre les termes de flottabilité et l'accélération de Coriolis. Nous définissons les grandeurs suivantes :

-V_{max} la valeur maximale de la vitesse azimutale

-R_{Vmax} le rayon de la ligne de courant où la vitesse azimutale est maximum

- Δ_η la différence de hauteur d'eau entre le centre du tourbillon et la ligne de courant associée à R_{Vmax}

-$Ro = \frac{V_{max}}{f R_{Vmax}}$ le nombre de Rossby

-$Bu_{vortex} = \frac{g \Delta_\eta}{f^2 R_{Vmax}^2}$ le nombre de Burger pour les tourbillons qui caractérise les variations de l'interface tels que défini par [Chassignet et al. 1990].

Nous pouvons donc intégrer l'équation 2.2 entre 0 et R_{Vmax} afin d'obtenir :

$$Bu_{vortex} = -\frac{1}{f^2 R_{Vmax}^2} \int_0^{R_{Vmax}} \left(\frac{v_\theta^2}{r} + f v_\theta \right) dr \tag{2.3}$$

L'équilibre cyclo-géostrophique ainsi intégré peut être réécrit $\mu Ro^2 + \nu Ro = Bu_{vortex}$ où μ et ν sont des coefficients géométriques qui dépendent du profil de tourbillon choisi. Dans le cas d'un tourbillon Gaussien, dont le profil de vitesse est défini par $v_\theta = V_{max} \left(\frac{r}{R_{Vmax}} \right) e^{\frac{1}{2}\left(1 - \left(\frac{r}{R_{Vmax}}\right)^2\right)}$, les paramètres μ et ν deviennent, respectivement, $\frac{1}{2}(1-e)$ et $1-\sqrt{e}$ qui sont des constantes. Ainsi, en utilisant ces Ro et Bu_{vortex}, il est possible de mettre en évidence la relation entre les propriétés dynamiques (Ro) et celles de la structure thermohaline (Bu_{vortex}).

On peut ensuite définir 2 régimes particuliers de l'équilibre cyclo-geostrophique suivant la valeur du nombre de Rossby :

a) Faible nombre de Rossby ($Ro << 1$ tel que 0,05): la force centrifuge est faible (i.e. $Ro^2 << Ro$) et donc le tourbillon satisfait l'équilibre géostrophique où le gradient de pression radiale est équilibré par la force de Coriolis.

b) Fort nombre de Rossby ($Ro >> 1$ tel que 5 ou 10): la force centrifuge domine l'effet de la rotation planétaire (i.e. $Ro^2 >> Bu_{vortex}$) et donc le tourbillon satisfait l'équilibre cyclostrophique.

Il est habituel de séparer la dynamique des tourbillons en processus mésoéchelles et sous-mésoéchelles. Cette distinction correspond traditionnellement à leur échelle horizontale par rapport aux termes de stratification dans la zone. Ces termes de stratification sont définis par le rayon de déformation (R_d). Dans l'océan global, le Rd associé au premier mode baroclinique varie, à grande échelle, entre 10 et plus de 200 km [e.g. Chelton et al. 1998]. Les variations de Rd sont largement conditionnées par la latitude (Figure 6 de Chelton et al. [1998]). Cependant, il existe des variations régionales comme indiqué par des Rd de 8 à 15 km dans la mer Méditerranée [Escudier et al. 2016] alors qu'il sont de 20 à 40 km à la même latitude dans les océans Atlantique et Pacifique. Ainsi, les tourbillons mésoéchelles ont des rayons d'entre 20 et 200 km [Carton 2001] avec de faible Ro alors que la dynamique sous-mésoéchelle est caractérisée par de plus petites gammes d'échelles spatiales entre 0,1 et 10 km mais dont la dynamique reste toujours influencée par la rotation de la terre et la stratification (i.e. $Ro = O(1)$) [Mahadevan 2016; McWilliams 2016].

On peut ensuite dériver l'équation 2.2 sur la verticale en appliquant l'équilibre hydrostatique. On obtient l'équation du vent thermique non linéaire qui relie le cisaillement vertical des vitesses et les gradients horizontaux de densité :

$$\frac{1}{r}\partial_z v_\theta^2 + f\partial_z v_\theta = \frac{-g}{\rho_0}\partial_r \rho \tag{2.4}$$

La structure thermohaline (ou en densité) et le champ de vitesse des tourbillons sont donc étroitement liés. Ces deux aspects peuvent être simultanément caractérisés par la vorticité potentielle qui est une propriété conservative dans les fluides non visqueux lors de processus adiabatique. Cette variable (Q) combine la vorticité relative (ζ), celle planétaire (f) et la stratification. Il existe plusieurs notations suivant le modèle considéré mais, pour l'utilisation que nous en faisons ici, nous retiendrons à la composante verticale de la vorticité potentielle d'Ertel [Ertel 1942] qui s'écrit :

$$Q = -\frac{1}{\rho}\left(f + \zeta\right)\partial_z \rho \tag{2.5}$$

où ζ est la composante verticale de la vorticité relative (i.e. $\zeta = \frac{1}{r}\partial_r\left(rv_\theta\right) - \frac{1}{r}\partial_\theta u_r$), f est la vorticité planétaire et $\partial_z \rho$ représente la stratification.

2.2.2 L'observation des tourbillons

Après avoir présenté un formalisme théorique pour décrire ces structures, nous pouvons maintenant discuter de leurs observations.

Les prémices

Les premières descriptions de tourbillons océaniques ont été effectuées à partir de mesures hydrologiques mettant en évidence des anomalies de densité. Ainsi, à la fin des années trente, Iselin [1936] et son équipe ont échantillonné une anomalie de température froide au sud du Gulf Stream correspondant à ce que nous identifions de nos jours comme un tourbillon cyclonique. Il a fallu attendre plus de 10 ans avant que le même auteur décrive une anomalie chaude signant un tourbillon anticyclonique cette fois ci au nord de ce courant [Iselin and Fuglister 1948]. Les années quarante à quatre-vingt-dix ont été marquées par les premières observations de structures tourbillonnaires de surface au voisinage des courants de bord ouest tel que le courant du Korushio [Uda 1938], le courant des Aiguilles [Duncan 1968] et le courant d'Australie orientale [Hamon 1965]. Cependant, les observations de tourbillons océaniques ne se sont pas limitées aux régions proches d'un courant de bord ouest. Nous pouvons noter, entre autre, l'échantillonnage de tourbillons au nord de la Nouvelle Guinée [Burkov and Ovchinnikov 1960], au voisinage des

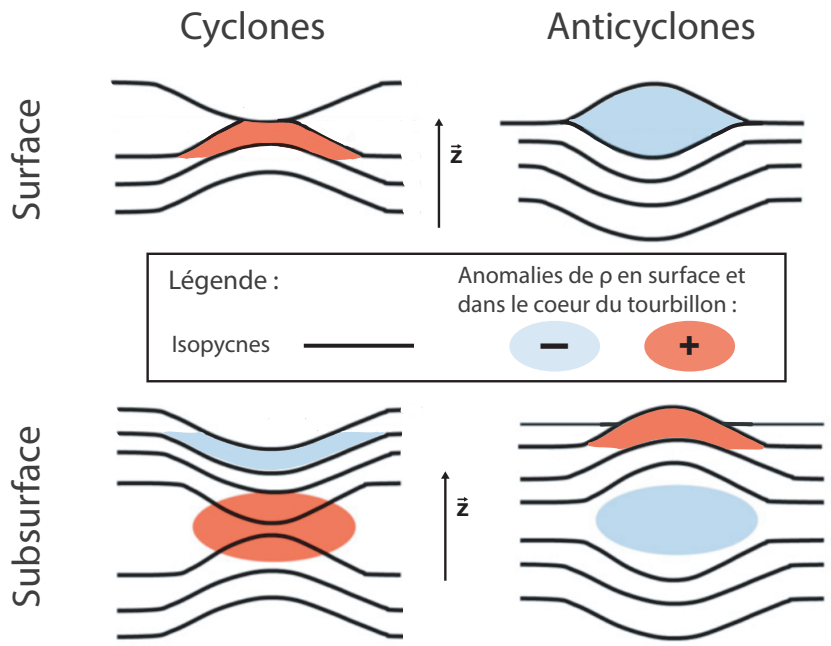


Figure 2.5: Types de tourbillons et anomalies de masses volumiques (ρ) en surface et dans le cœur hydrologique. Figure légèrement modifiée d'après Assassi et al. [2016].

îles hawaïennes [Wyrtki 1967], au niveau du courant Circumpolaire Antarctique [Savchenko et al. 1978] et au large de la mer d'Arabie [Koshlyakov et al. 1970].

Les tourbillons intensifiés en surface présentent des gradients de densité horizontaux forts qui peuvent être observés en mesurant les propriétés hydrologiques le long de la trace d'un bateau traversant une telle structure. Cela n'est pas le cas pour des tourbillons ne signant pas, ou peu, en densité à la surface tel que les tourbillons de subsurface. Une représentation schématique des différences entre ces deux types de structures est présentée dans le Figure 2.5. Contrairement aux tourbillons de surface, le cœur hydrologique d'un tourbillon de subsurface n'est pas en contact avec l'atmosphère. Par exemple, les Meddies sont des tourbillons anticycloniques contenant de l'eau méditerranéenne associée à des anomalies de salinité dans leur cœur vers 800-1200 m et qui se propagent dans l'océan Atlantique. Ils ont été identifiés dés 1969 par Swallow [1969] proche du Cap St Vincent puis dans différentes parties de l'Atlantique Nord telles que les îles Canaries [Armi and Zenk 1984]. Il existe aussi d'autres structures intensifiées en sub-surface telles que les Cuddies, formés dans le sous-courant Californien [e.g. Garfield et al. 1999; Collins et al. 2013], les Peddies et Reddies, formés respectivement par de l'eau de la mer Persique et de la mer Noire [e.g. Shapiro and Meschanov 1991], les Weddies formés par des eaux hivernales intermédiaires dans le mer Méditerranée [Pinot and Ganachaud 1999] ou d'autres de plus grande taille comme les tourbillons d'eaux modales [Brundage and Dugan 1986] dans la mer des Sargasses. Nous renvoyons tout lecteur intéressé par ce type de structure vers le travail de Ciani [2016] où un inventaire des tourbillons intensifiés en subsurface est proposé.

L'altimétrie satellitaire

L'identification des tourbillons océaniques étant dépendante des moyens en mer, la cartographie de ces structures par des mesures ponctuelles est une tâche ardue. Cependant, ces observations variées pouvaient permettre de penser que les tourbillons océaniques existaient dans de multiples régions du globe et sous différentes formes. La confirmation a été apportée grâce à l'avènement des observations satellitales. Celles-ci ont permis d'avoir une vision globale des variations des propriétés océaniques de surface. Pour l'océanographie, les prémices de ces observations ont eu lieu en 1978 avec la mise en orbite des missions Tiros-N et Seasat. Ces instruments dérivaient, respectivement, la température de surface via l'étude des rayonnements terrestres et la hauteur de l'eau à partir des mesures altimétriques. Après de nombreuses évolutions de ces technologies grâce au développement et à l'amélioration des appareils de mesures embarqués mais aussi des moyens de support terrestre, les variables fournies par les satellites sont, de nos jours, nombreuses : températures et salinités de surface, hauteur d'eau, tension de vent et production biologique primaire (Figure 2.4).

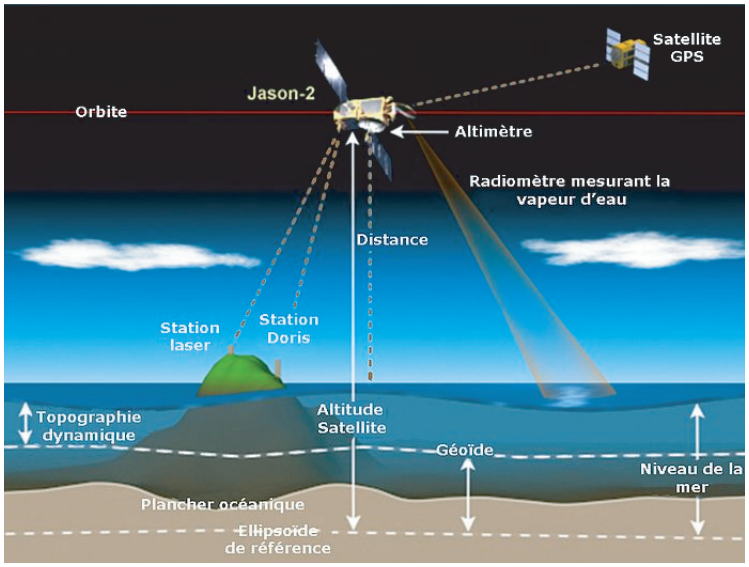


Figure 2.6: Principe de l'altimétrie par Cazenave and Massonnet [2004].

Pour l'étude dynamique des tourbillons, une révolution a été apportée par l'altimétrie satellitaire en relançant l'intérêt sur la dynamique de mésoéchelle [Le Traon 2013]. Un schéma du fonctionnement de cette technologie est présenté dans le Figure 2.6 . Un altimètre mesure la distance entre le satellite et la surface de l'eau ce qui, en connaissant l'altitude du satellite par rapport à un ellipsoïde de référence, peut être traduit en une mesure du niveau de la mer. Ainsi, en estimant l'écart entre le Géoïde et cet ellipsoïde, il est possible d'obtenir la mesure de topographie dynamique (ADT pour "Absolute Dynamical Topography") et donc de caractériser les variations de hauteur de l'eau en fonction d'une ligne équipotentielle du champ de pesanteur. Contrairement à l'imagerie dans le visible qui est affectée

par la couverture nuageuse ou par les flux de chaleurs engendrées par les vents forts, les données altimétriques permettent un suivi continu des variations de la surface océanique sous la trace des satellites ("along-track").

Un traitement est nécessaire afin de convertir ces observations en cartes où des structures peuvent être étudiées. Pour cela, les traces sont combinées afin de produire des cartes d'ADT (produit L4). Il existe plusieurs produits en fonction du nombre de satellites utilisés, de la zone d'intérêt mais aussi entre ceux opérationnels ("near-real-time") et ceux optimisés avec plusieurs mois de décalage ("delayed-time"). La procédure de création de ces cartes est décrite dans le Duacs/AVISO+ [2015] et nous présentons ici un résumé de la méthode de création des produits journaliers globaux en "delayed-time" regroupant toutes les mesures satellites disponibles ("all-sat") qui ont été utilisées au cours de ce travail. Aujourd'hui en Novembre 2018, plus de 24 ans (de 01/1993 à 06/2018) de ces cartes ont été produites par le Segment-Sol SSALTO et le système DUACS grâce au partenariat entre le Centre National d'Études Spatiales (CNES) et le "Copernicus Marine Environment and Monitoring Service" (CMEMS).

Dans un premier temps, les mesures "along-track" sont filtrées à basses fréquences par un filtre de Lanczos (fréquence de coupure de 65 km) puis sous-échantillonnées (14 km) afin de réduire le bruit instrumental. Une interpolation optimale [Le Traon et al. 2003] est ensuite appliquée à ces traces (enregistrées par 2 à 6 satellites suivant la date) afin d'obtenir un produit grillé à mailles régulières d'$1/4^{\circ}$ pour l'océan globale [Ducet et al. 2000]. Les échelles de covariance, aussi bien temporelle que spatiale, utilisées lors de cette interpolation sont définies à priori. De même, des modèles de propagation ont été ajoutés à ce processus afin de prendre en compte le déplacement des structures. Ces modèles ont été définis à partir de 5 années de cartes obtenues à partir des satellites Topex/Poseidon et european remote-sensing (ERS). Afin de donner un exemple du produit final, une extraction de la carte ADT du 1er janvier 2017 centrée sur l'Atlantique Sud est présentée en 3D sur la Figure 2.7.

Les écoulements visibles sur les cartes altimétriques dépendent grandement des différents paramètres de covariance et des modèles de propagations [e.g. Dibarboure et al. 2011; Dussurget et al. 2011]. Cependant, plusieurs versions des produits ont été développées où la fréquence de création de ces cartes ainsi que les paramètres de corrélation ont été modifiés. Ainsi, utiliser les estimations de résolution données dans la littérature pour caractériser la précision des produits utilisés dans cette thèse est compliqué. C'est d'autant plus vrai qu'une même procédure ne permet pas d'obtenir une résolution constante sur toutes les cartes. En effet, une augmentation du nombre de satellite disponible améliore les résultats [e.g. Le Traon and Dibarboure 1999]. Similairement, cette résolution n'est pas identique sur tout le globe à une date donnée car la précision en un point de grille va être dépendante de la distance et du temps qui le séparent de la trace la plus proche. Cependant, on peut indiquer que la précision verticale visée par le programme altimétrique est d'obtenir une erreur moyenne inférieure à 1 cm et maximale inférieure à 2 cm [Le Traon and Dibarboure

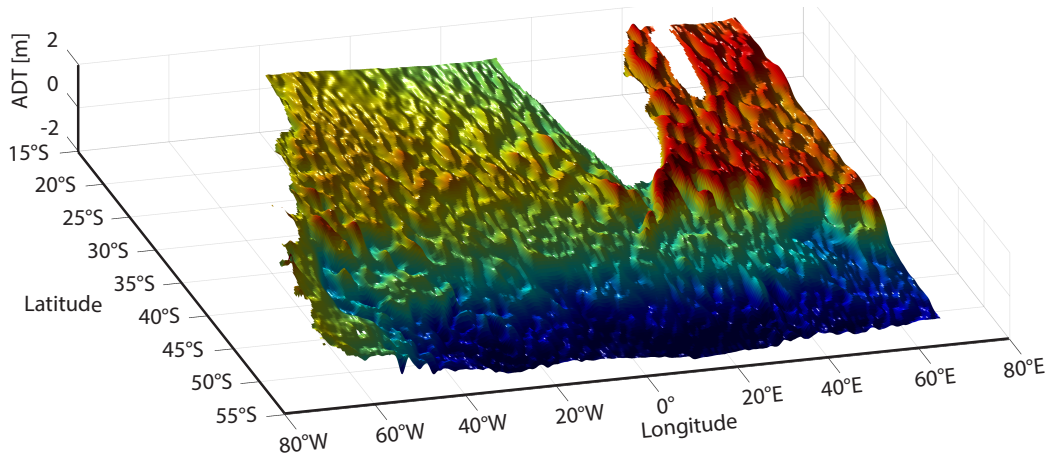


Figure 2.7: Visualisation 3D centrée sur l'Atlantique Sud de la carte ADT en "delayed-time" du 1er janvier 2017.

1999; Ducet et al. 2000; Lambin et al. 2010; Dibarboure et al. 2011]. La résolution spatio-temporelle des structures visibles est de l'ordre de 150 à 200 km pour des processus durant plus de 15 jours. Finalement, des phénomènes de plus petites échelles peuvent être visibles sur les champs altimétriques mais ils seront représentés par des structures plus larges et moins intenses [e.g. Dussurget et al. 2011].

L'équation de l'équilibre cyclo-géostrophique (équation 2.2) ainsi que la Figure 2.5 nous indiquent clairement que les cartes d'ADT, et donc de variations de la hauteur d'eau, sont particulièrement adaptées pour la caractérisation de la signature en surface des tourbillons océaniques. De plus, les mesures directes, telles que la température, sont limitées par la très faible pénétration des ondes électromagnétiques dans l'eau de mer et ne peuvent donc qu'identifier les structures associées à des anomalies de propriétés hydrologiques ou biologiques en surface. Au contraire, la hauteur d'eau obtenue par l'altimétrie apporte des informations sur la structure interne et donne accès aux vitesses géostrophiques de surface. Cette technologie permet de détecter des tourbillons de surface mais aussi, plus surprenant, des tourbillons intensifiés en subsurface comme cela a été prouvé pour la détection des Meddies par Stammer et al. [1991]. Cependant, l'altimétrie seule ne permet pas de différencier le type de structure puisque la signature de surface est similaire. Cette différenciation est possible en utilisant d'autres champs hydrologiques de surface, tels que la température de surface (SST pour "Sea Surface Temperature"), comme cela a été utilisé par Schütte et al. [2016] et rationalisé par Assassi et al. [2016] dont la figure de synthèse a été adaptée pour créer la Figure 2.5.

Cependant, comme cela a été indiqué par Chaigneau et al. [2008] et Chelton et al. [2011], la détection et le suivi des tourbillons océaniques sur les champs altimétriques nécessitent un algorithme approprié. Cela devient très frappant sur la détection lorsque l'on s'attarde sur les études ayant comparé les résultats de leurs détections de tourbillons avec ceux obtenus visuellement par des "groupes d'océanographes experts" sur les mêmes champs d'entrées [e.g. Chaigneau et al. 2008; Faghmous

et al. 2015]. Dans l'article de Chaigneau et al. [2008], 5 experts identifiant des tourbillons sur 10 cartes altimétriques n'étaient en accord que sur 70 % de leurs identifications en moyenne. Nous voyons donc que la définition des tourbillons sur des champs altimétriques est loin d'être triviale. Ainsi, de nombreux algorithmes ont été proposés afin de détecter ces structures à partir d'images altimétriques.

En schématisant, les algorithmes de détection peuvent être catégorisés en 4 grands groupes : les algorithmes eulériens basés sur les propriétés physiques de l'écoulement [e.g. Okubo 1970; Weiss 1991; Nencioli et al. 2010], ceux basés sur les propriétés géométriques [e.g. Chelton et al. 2011; Chaigneau et al. 2011], ceux combinant les deux approches [e.g. Halo et al. 2014; Le Vu et al. 2018] et les algorithmes lagrangiens [e.g. Haller and Beron-Vera 2013; Abernathey and Haller 2018]. La diversité existe aussi sur les champs d'entrées utilisés qui peuvent être la hauteur d'eau, les vitesses géostrophiques ou les anomalies de ces deux variables. De plus, de nombreuses méthodes dépendent de paramètres qui influent grandement sur les résultats obtenus. Cela a par exemple été démontré par Le Vu et al. [2018] qui ont mis en avant les différences de taille et d'intensité des tourbillons détectés en variant le seuil de détection de la méthode d'Okubo-Weiss [e.g. Okubo 1970; Weiss 1991]. Ainsi, nous pourrions faire une liste des différents algorithmes présents en essayant d'énumérer leurs avantages et inconvénients mais une difficulté majeure persiste : il n'existe pas, de nos jours, de méthode quantitative pour comparer les algorithmes entre eux. Par exemple, un travail de comparaison qualitatif a été effectué par Escudier et al. [2016] où trois algorithmes de détection [Chelton et al. 2011; Nencioli et al. 2010; Halo et al. 2014] ont été utilisés sur des champs de d'anomalies de ADT (SLA pour "Sea Level Anomaly") d'une simulation numérique. Escudier et al. [2016] conclurent qu'aucun de ces algorithmes, appartenant chacun à un type différent d'algorithme Eulérien, ne semble être significativement supérieurs aux autres. De plus, d'après les auteurs des méthodes Lagrangiennes [e.g. Haller and Beron-Vera 2013; Abernathey and Haller 2018], les tourbillons détectés par des méthodes eulériennes ne sont pas forcément des structures piégeant des masses d'eaux. Cependant, les reconstructions d'Anneaux des Aiguilles ayant capté des flotteurs dérivants entrepris par Souza et al. [2011a] et Nencioli et al. [2018] à partir d'algorithme eulérien semblent indiquer le contraire.

Ainsi, les validations de détection sont soit effectuées en comparant les résultats avec les connaissances des tourbillons dans la région d'étude [e.g. Souza et al. 2011b], soit faites via l'expertise de "groupes d'océanographes experts" [e.g. Chaigneau et al. 2008; Faghmous et al. 2015]. Par conséquent, ces validations ne semblent pas objectives. Or, lors d'une étude récente, Amores et al. [2018] ont mis en évidence les limites de l'altimétrie pour la détection des tourbillons. Pour se faire, ils ont développé une OSSE ("Observing System Simulation Experiment") où des champs synthétiques de produits grillés altimétriques ont été produits à partir de champs de sortie de simulations numériques. Ainsi, ces auteurs ont montré que, en moyenne, seulement 10% des tourbillons océaniques sont détectés sur des champs altimétriques et que 50% de ceux détectés correspondent à des agrégations de plusieurs tourbillons. Ce résultat s'explique par le grand nombre de tourbillons de trop petite taille pour

être résolus sur les champs altimétriques comme mis en avant par Capuano et al. [2018b] en comparant la distribution des rayons des tourbillons détectés sur des champs de simulations numériques de différentes résolutions à celle sur les champs d'altimétrie satellitaire.

Comme pour la détection des tourbillons, il existe différents algorithmes d'identification de leurs trajectoires. Pour les algorithmes lagrangiens, les surfaces successives occupées par les tourbillons sont obtenues en advectant par le champs de vitesse le centre ou la ligne de courant délimitant la limite du tourbillon considéré [e.g. Beron-Vera et al. 2013; Abernathey and Haller 2018]. Ceux eulériens sont basés sur le lent déplacement des tourbillons mésoéchelles par rapport à leur taille. Ainsi, la méthode la plus commune [e.g. Chelton et al. 2011; Le Vu et al. 2018] consiste à apparier deux tourbillons à des temps consécutifs en identifiant les couples minimisant des fonctions de coût basées sur des propriétés géographiques, géométriques et dynamiques. Une seconde méthode détecte la superposition de la surface occupée par un tourbillon entre 2 cartes consécutives [Pegliasco et al. 2015] et la présence du centre dans la surface du tourbillon suivi [Doglioli et al. 2007].

Ces algorithmes de suivi des tourbillons varient sur la prise en compte de la disparition de ces derniers avec l'extension de la recherche ou sur les paramètres utilisés dans la fonction de coût. Cependant, la diversité émerge principalement par la prise en compte des événements d'interactions entre tourbillons qui peuvent fusionner (merging) ou se fractionner en plusieurs plus petits (splitting). L'implémentation de tels algorithmes est récente comme indiqué par les premiers efforts qui ont eu lieu en 2014 [e.g. Du et al. 2014; Li et al. 2014; Yi et al. 2014]. L'identification de ces processus est directe avec la méthode de superposition en regardant plusieurs tourbillons dont les surfaces se superposent avec un seul. Ce n'est pas le cas pour les algorithmes utilisant uniquement des fonctions de coût car elles se limitent à l'appariement d'un couple de tourbillon. Certains algorithmes contournent cette difficulté en identifiant les tourbillons composés de plusieurs cœurs [e.g. Du et al. 2014; Le Vu et al. 2018] qui est une étape de transition avant un splitting ou un merging. Il est à noter que la prise en compte de ces événements complique la vision d'une trajectoire "classique" où une structure tourbillonnaire peut être décrite par une formation, une vie et une dissipation. En effet, après un merging, le segment de trajectoire créé est associé à deux zones de formations ou, dans le cas d'un splitting, deux zones de dissipation. Ainsi, lorsque de nombreux épisodes d'interactions entre structures se produisent, cette notion de trajectoire "simple" ne peut plus être appliquée.

Mesures in-situ

En plus de fournir des images, les satellites ont permis de communiquer avec des instruments de mesure autonomes qui sont disséminés dans l'océan. Avant, cela n'était possible au large que grâce à des systèmes acoustiques équipant des bateaux [Swallow 1955] ou des réseaux préalablement installés sur les fonds marins tel le

réseau SOFAR dans l'Atlantique Nord Ouest [Spain 1980] . Parmi les multiples technologies, les profileurs dérivants et les bouées de surface sont détaillés (Figure 2.8) car ils sont utilisés dans ce travail.

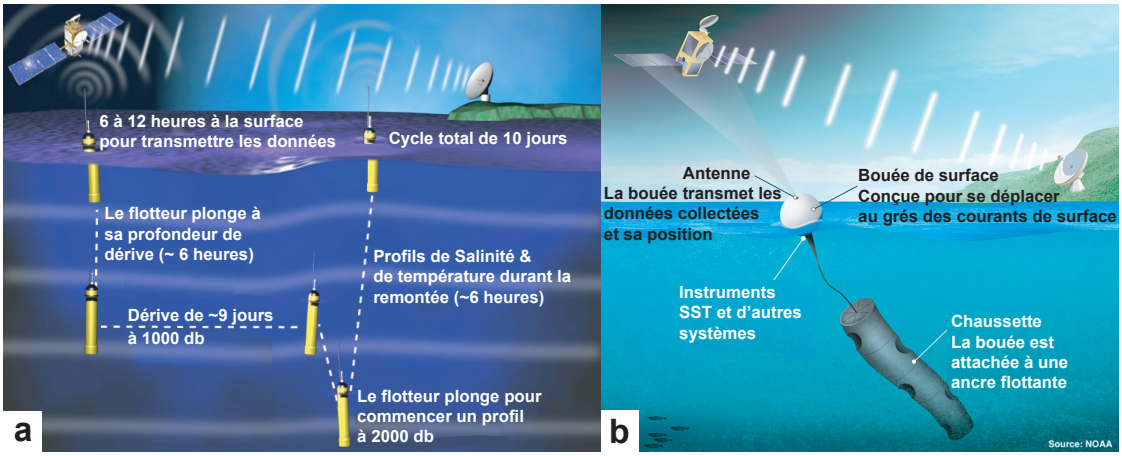


Figure 2.8: Schémas de fonctionnement des instruments de mesure dérivants. **a**) Cycle d'un flotteur Argo traduit d'après une figure produite par le International Argo Project Office. **b**) Fonctionnement d'une bouée de surface traduit d'aprés une figure produite par le National Oceanic and Atmospheric Administration.

Les profileurs dérivants sont des systèmes instrumentés qui effectuent des cycles décomposés en deux profils hydrologiques, une période longue de dérive à leur profondeur de parking puis une dérive à la surface où les données enregistrées ainsi que la position sont envoyées par satellite. Les paramètres de profondeur de parking, de longueur de cycle ainsi que les variables mesurées peuvent changer suivant le type d'instrument mis à l'eau. Ceux tels que définis lors de la création du programme Argo, détaillés dans le panneau **a** de la Figure 2.8, comprennent des mesures de la pression, de la conductivité et de la température qui permettent ensuite de dériver la densité. Cette convention a permis, depuis sa mise en place en 2000, de multiplier le nombre de profils hydrologiques disponibles. En effet, 8000 profils hydrologiques ont été effectués en 7 ans (1991-1997) lors du "World Ocean Circulation Experiment" alors que le cap d'un million de profils Argo a été dépassé au cours de la 8^e année du programme Argo. De nos jours, les flotteurs Bio-Argo peuvent aussi caractériser l'environnement biogéochimique en mesurant, par exemple, la fluorescence de la chlorophylle et la réflexion optique ("backscattering"). De plus, la technologie Iridium permet d'envoyer des ordres aux flotteurs lorsqu'ils sont à la surface afin de modifier les propriétés de leurs cycles pour les adapter à la région échantillonnée ou à un épisode d'intérêt tel qu'un bloom phytoplanctonique. Il est ainsi possible d'utiliser les tourbillons détectés à partir d'images satellites pour sélectionner les profileurs Argo qui les échantillonnent. Cela a permis d'aller plus loin dans la caractérisation des structures identifiées à partir de l'altimétrie en rendant possible la reconstruction et l'étude de l'évolution de leur structure verticale [e.g. Chaigneau et al. 2011; Zhang et al. 2014b; Pegliasco et al. 2015].

Les bouées dérivantes sont aussi des instruments lagrangiens qui restent à la

surface et peuvent donc envoyer leur position plusieurs fois par jour. Ces instruments, dont un schéma est présenté dans le panneau **b** de la Figure 2.8, sont généralement associés à une ancre flottante en subsurface afin que leur déplacement caractérise les courants des premières couches de l'océan. Les trajectoires ainsi obtenues ont permis de détecter les bouées piégées dans des tourbillons grâce à leur trajectoire effectuant des boucles. Comme pour les champs altimétriques, il existe des algorithmes de détection des tourbillons basés sur la géométrie de ces trajectoires [e.g. Dong et al. 2011a; Lankhorst 2006] ou sur les propriétés physiques de l'écoulement [e.g. Lilly et al. 2011; Lumpkin 2016]

Finalement, la détection de tourbillons sur les champs altimétriques a pu permettre d'identifier des épisodes d'échantillonnage de ces structures par d'autres types d'instruments tels que les mouillages [e.g. Kersalé et al. 2018] ou de cibler des structures lors de missions en mer [e.g. Villar et al. 2015]. Ainsi, après maintenant plus de quatre-vingt années d'études sur les tourbillons océaniques, il est clair que ces structures sont omniprésentes dans l'océan. Ceci a été confirmé suite à l'augmentation rapide des capacités de calculs permettant la mise en place de simulations numériques à haute résolution. Elles dépeignent un océan dominé par de nombreux tourbillons présentant une grande hétérogénéité de taille et d'intensité qui sont enveloppés dans une circulation moyenne de grande échelle.

2.2.3 Histoire de la vie d'un tourbillon

D'après Mason et al. [2014] et Pegliasco et al. [2015], on peut séparer la vie d'un tourbillon en 3 phases : sa phase de croissance, celle de maturité et celle de décroissance. Les études statistiques faites sur un nombre important de trajectoires détectées sur des champs altimétriques leur ont permis d'obtenir un taux de croissance pour ces trois étapes en étudiant les propriétés géométrique (i.e. taille et intensité) des tourbillons ainsi que leur âge (cf. Figure 2.9). Cependant, cette vision statistique est simplifiée car elle ne prend pas en compte les interactions entre les structures ou les épisodes d'intensification [e.g. Ioannou et al. 2017]. La prise en compte de ces événements semble plutôt indiquer que les tourbillons ont des vies très complexes qui peuvent être décomposées en plusieurs segments de trajectoires interagissant entre eux lors d'épisodes de fusion et de fractionnement de ces segments.

Nous nous proposons d'étudier séparément les mécanismes agissant sur la formation, sur la vie et enfin sur la dissipation des tourbillons. De nouveau, ce sont des sujets très variés et nous ne présenterons ici que les résultats qui nous semblent les plus pertinents pour ce travail de thèse.

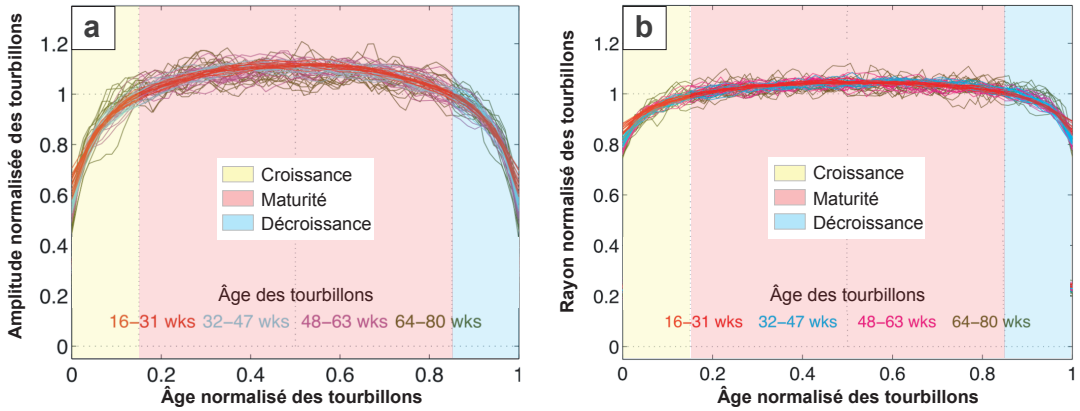


Figure 2.9: Visions statistiques de l'évolution de **a**) la taille (rayon) et de **b**) l'intensité (amplitude) normalisée des tourbillons en fonction de leur durée de vie normalisée en concaténant deux figures produites par Mason et al. [2014] et Pegliasco et al. [2015]. Ces deux auteurs ont utilisé des trajectoires obtenues à partir de suivis des tourbillons sur des cartes altimétriques afin d'obtenir ces statistiques.

Formation

Les tourbillons océaniques de mésoéchelle sont issus d'instabilité et peuvent avoir de nombreuses sources et régions de formation. Des tourbillons peuvent être générés suite au détachement d'une couche cisaillée ("sheddies" [Southwick et al. 2016]) au contact de variation topographique tel que dans le sillage d'une île [e.g Arístegui et al. 1994; Isoguchi et al. 2009] ou suite à des variations géométriques du trait de côte comme un cap [e.g Swallow 1969; Jiang et al. 2011]. Un ajustement (cyclo)géostropique après un mélange vertical important [McWilliams 1985] tel qu'un épisode de convection [Legg and Marshall 1993] peut aussi donner naissance à ce type de structure. Cependant la déstabilisation d'un jet est la plus courante source de formation de tourbillon [Flierl and McGillicuddy 2002]. On peut décomposer ces instabilités en fonction du réservoir d'où est extraite l'énergie des tourbillons océaniques. Ils peuvent puiser de l'énergie cinétique des courants moyens en présence d'un cisaillement horizontal important lors d'instabilités barotropes ou extraire l'énergie potentielle de grande échelle en présence de cisaillements verticaux (et donc de gradients horizontaux de densité comme indiqué par l'équation 2.4) dans des cas d'instabilités baroclines [Gill et al. 1974; Ferrari and Wunsch 2009]. Finalement, on peut noter le cas d'éjections de tourbillons dans les zones de changement rapide de direction d'un courant comme le courant des Aiguilles, le courant Australien oriental ou le courant Nord du Brésil. Ces éjections s'expliquent par la conservation de la quantité de mouvement [Pichevin et al. 1999; Nof 2005] puisque, lors du changement de direction, la quantité de mouvement du courant est déviée et la conservation de cette dernière nécessite l'éjection de masse d'eau dans une autre direction.

Vie

Les tourbillons sont des structures qui, généralement, se déplacent dans leur environnement. Il a été montré théoriquement [Nof 1981; Cushman-Roisin et al. 1990] mais aussi observé [Chelton et al. 2011] que, lorsqu'ils ne sont pas advectés par un courant, les tourbillons mésoéchelles se déplacent vers l'ouest. Ceci peut s'expliquer par une simple méthode graphique comme reproduit dans le panneau **a**) de la Figure 2.10. Les variations méridiennes de la force de Coriolis dans un anticyclone (cyclone) initient sa propagation vers l'ouest (est). Ce mouvement zonal entraine le déplacement mériodional des eaux environnantes qui vont gagner ou perdre de la vorticité relative pour compenser les changements de vorticité planétaire afin de satisfaire la conservation de la vorticité potentielle présentée dans l'équation 2.5. La vorticité relative ainsi créée dans l'environnement va rétroagir sur le tourbillon en entrainant une propagation vers l'ouest qui domine sur le déplacement zonal initial [Cushman-Roisin et al. 1990].

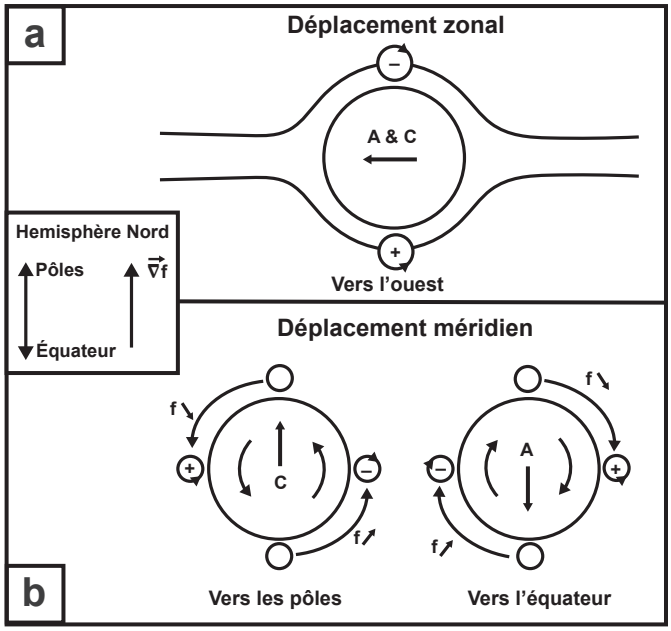


Figure 2.10: Explication graphique des déplacements zonaux (panneau **a**) et méridiens (panneau **b**) des tourbillons d'échelle moyenne sous l'effet de gradient de voriticité planétaire. Ces schémas ont été adaptés d'après Cushman-Roisin et al. [1990], Cushman-Roisin and Beckers [2011] et Morrow et al. [2004]

En parallèle à cette propagation, la vorticité relative d'un tourbillon va produire un déplacement méridien de l'eau environnante dont la direction dépend de son sens de rotation. La vorticité relative des eaux ainsi déplacées va retroagir sur le tourbillon (voir le panneau **b**) de la Figure 2.10). Il en résulte un transport méridien vers les pôles pour les tourbillons cycloniques et vers l'équateur pour ceux anticycloniques [Cushman-Roisin and Beckers 2011; Morrow et al. 2004].

Cependant, cette théorie de déplacement d'un tourbillon sous l'effet du gradient

de vorticité planétaire est seulement valide dans le cas d'une structure se trouvant dans un environnement relativement calme puisqu'ils peuvent être advectés par le courant environnant. Ceci est clairement visible dans le courant circumpolaire Antarctique (ACC) [e.g. Frenger et al. 2015] ou le courant Algérien [Millot et al. 1990] où les tourbillons se propagent vers l'est. Finalement, on peut noter que des tourbillons peuvent rester plusieurs mois dans la même région tel que le tourbillon Ierapetra au sud de la Crête [Mkhinini et al. 2014; Ioannou et al. 2017].

Au cours de leur vie, les tourbillons sont rarement isolés et peuvent interagir ensemble. Les tourbillons de même signe peuvent entrer en contact puis échanger des masses de fluides avant d'éventuellement fusionner (merging). Ces mergings peuvent résulter en la création d'un tourbillon de plus grande taille. Cette fusion totale ou partielle peut se produire si des tourbillons se trouvant à un même niveau dans la colonne d'eau sont à une distance inférieure à une distance critique dépendant de leur rayon, de leur intensité et du champ de courant environnant [Melander et al. 1988; Yasuda and Flierl 1997; Perrot and Carton 2010]. Cette fusion a pour effet de transférer de l'énergie des petites échelles (les tourbillons initiaux) vers des échelles plus grandes (le tourbillon final). Cependant, des tourbillons à plusieurs niveaux peuvent s'aligner tel que, par exemple, un tourbillon de surface et un autre intensifié en subsurface [Cresswell 1982; Garreau et al. 2018]. Il en résulte deux cœurs hydrologiques partageant le même axe de rotation. L'observation de merging de structures est une tâche ardue. De nombreuses mises en évidence de tels événements ont été effectuées sur des champs altimétriques [Ioannou et al. 2017; Le Vu et al. 2018; Nencioli et al. 2018] mais rares sont les observations de l'évolution de leur structure interne [e.g. Cresswell 1982; Schultz Tokos et al. 1994; Sangrà et al. 2005]. De plus, deux tourbillons de signes différents à deux profondeurs peuvent aussi s'apparier pour former un heton. Cependant, à notre connaissance, aucun algorithme de détection prend en compte l'appariement de tourbillon de polarité différente.

Le mécanisme inverse existe dans le cas de la séparation d'une structure en plusieurs plus petites structures. Ce phénomène a été prouvé théoriquement pour les cyclones [Nof 1991] et pour les anticyclones s'ils rencontrent des barrières bathymétriques [Simmons and Nof 2000]. De tels événements ont aussi été décrits à partir de données satellites [Arhan et al. 1999; Dencausse et al. 2010a].

Il a été mis en évidence que les mergings peuvent résulter en une structure plus intense que les deux d'origine mais des événements d'intensification peuvent aussi s'observer sans fusion. On peut ainsi noter plusieurs épisodes d'intensification pour l'anticyclone de Ierapetra [Ioannou et al. 2017]. Le fait que ce tourbillon soit forcé par le vent semble indiquer un impact de ces processus mais cela reste à être étudié.

Dissipation

Comme pour leur formation, la dissipation des tourbillons est un processus difficile à observer. C'est d'autant plus compliqué lors de leur détection sur des champs altimétriques car la perte de signal en surface se traduisant par la fin d'une trajectoire n'est pas forcément associée à une dissipation. Cependant, il a été montré que des phénomènes tels que des interactions avec de la bathymétrie [e.g. Herbette et al. 2003; Frenger et al. 2015; Nencioli et al. 2018], l'interaction avec un courant intense [e.g. Richardson 1993] ou la dissipation sous forme de tourbillons de sous-mésoéchelle [e.g. Müller et al. 2005; Zhang et al. 2016] peuvent altérer les tourbillons voire résulter en leur disparition. On peut aussi noter que, dans le cas de simulations numériques, Renault et al. [2016] a identifié que la rétroaction des courants initiés par les tourbillons sur la tension relative du vent va modifier le pompage d'Ekman qui agit comme un "Eddy Killer" car l'énergie des tourbillons est étroitement liée à leur structure thermohaline. De plus, un transfert de chaleur intense d'un tourbillon de surface vers l'atmosphère tel qu'observé par Arhan et al. [2011] peut résulter en une perte d'anomalie de densité. Finalement, les tourbillons se dissipent en échangeant de faible quantité de fluides avec leur environnement lors de leur déplacement ce qui se traduit par une érosion lente du tourbillon [e.g. Armi et al. 1989].

2.2.4 Impact des tourbillons océaniques

Nous avons vu en discutant de la vie des tourbillons qu'ils interagissent avec leur environnement. Ils peuvent, par exemple, extraire de l'énergie à un courant moyen lors de leur formation ou, à l'inverse, lui en transférer lors de leur dissipation. Les effets des tourbillons sur les autres parties de la dynamique océanique sont donc multiples. Nous explicitons ici les impacts en relation directe avec avec notre travail et nous orientons tout lecteur intéressé par une approche globale de ce sujet vers l'étude bibliographique de McWilliams [2008].

Lors de l'étude des transports de chaleur effectués par les tourbillons, le premier candidat à expliciter est leur advection. En effet, un tourbillon peut déplacer de l'eau ayant des caractéristiques de sa zone de formation. Cette advection se fait dans son cœur dynamique où la vitesse azimutale est supérieure à la vitesse de translation [Flierl 1981]. Ainsi, ils participent activement au transport à travers les fronts océaniques tel que dans le Courant Antarctique Circumpolaire [Bryden 1979; Speer et al. 2000]. Les tourbillons du Gulf Stream sont un bon exemple de ce phénomène puisque les tourbillons d'anomalies froides, comme ceux identifiés par Iselin [1936], résultent du transport d'eau de la partie nord dans celle sud à travers le courant. De même, ils peuvent advecter des masses d'eau dans un océan ouvert comme les meddies précédemment décrits qui participent à une advection de sel dans l'océan Atlantique [e.g. Carton 2001; Bashmachnikov et al. 2015]. Quantitativement, l'effet des tourbillons sur les transports s'est révélé d'un ordre de grandeur comparable

aux transports de grandes échelles [Zhang et al. 2014b; Dong et al. 2014].

De plus, les tourbillons se déplacent isopycnalement. Ainsi, l'affleurement d'un front océanique peut agir telle une barrière où des tourbillons vont se mouvoir en dessous et ainsi devenir des tourbillons de subsurface [e.g. Dugan et al. 1982]. Ce processus de ventilation des couches profondes a été analysé numériquement dans un article de Herbette et al. [2004] dont la Figure 2.11 a été reproduite. L'advection d'eau d'un tourbillon peut avoir une composante verticale importante lorsqu'un tourbillon de surface se détache de l'atmosphère en plongeant sous le front. Nous avons été confronté à des questions de sémantiques sur ce phénomène au cours de ce travail de thèse. Afin de le caractériser, nous suivons la définition de la subduction telle que donnée dans " l'Encyclopedia of Ocean Sciences" [Williams 2001]: "Ocean subduction involves the transfer of fluid from the mixed layer into the stratified thermocline". Nous désignerons donc la transformation d'un tourbillon de surface en tourbillon de subsurface sous la thermocline saisonnière comme une processus de subduction. À notre connaissance, ce type de processus n'a jamais été observé puisque cela nécessite la reconstruction lagrangienne de l'évolution thermohaline d'un tourbillon.

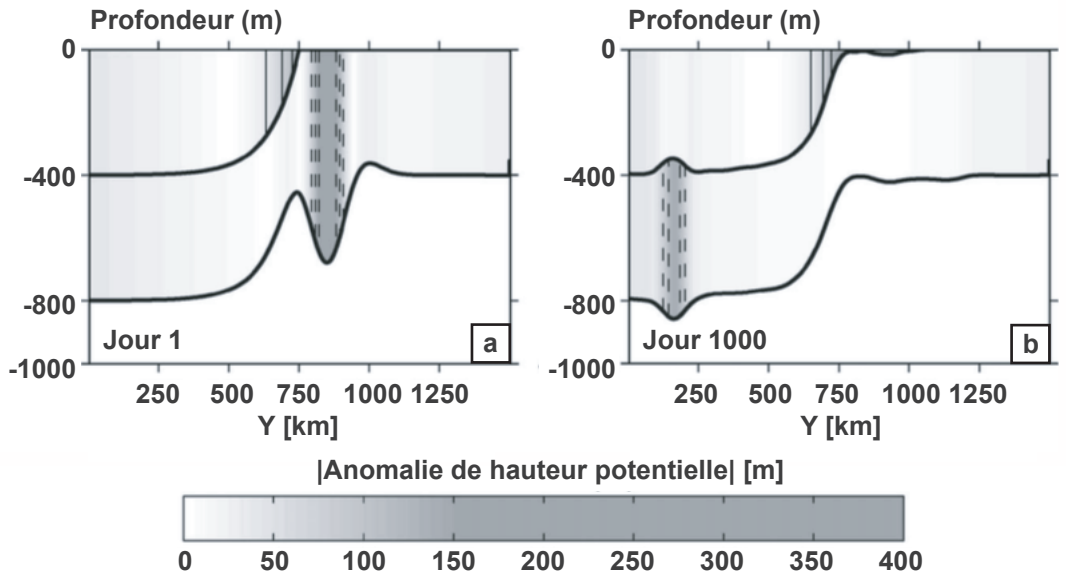


Figure 2.11: Subduction d'un tourbillon anticyclonique sous un front tel que simulé par Herbette et al. [2004]. La vorticité potentielle (Q) est indiquée par les anomalies de hauteur potentielle correspondant aux anomalies de Q normalisées par Q.

Les tourbillons peuvent aussi induire des transports en impactant les eaux environnantes, qui ne sont pas piégées dans leur cœur, en les déplaçant autours d'eux. Ce processus à été montré dans la Figure 2.10 pour expliquer le déplacement des tourbillons. On peut ainsi observer la subduction de masses d'eaux poussées par les tourbillons sous des fronts océaniques [e.g. Xu et al. 2016]. Ce processus diffère de la subduction précédemment énoncée puisque ce transfert se fait autours du tourbillons et non pas suite au déplacement de son cœur hydrologique.

Lorsqu'ils sont associés à de fortes anomalies de température de surface, les tourbillons peuvent modifier les propriétés de l'atmosphère proche de la surface. Ils peuvent, par exemple, engendrer une modification des vents de surface, de la turbulence dans la couche limite ou des précipitations comme schématisé sur la Figure 2.12 produite par Frenger et al. [2013]. Les structures de mésoéchelle peuvent aussi être une source d'intensification pour les cyclones tropicaux [Shay et al. 2000]. Les anomalies de température associées à ces structures peuvent donc impacter la position des trains de tempête [Foussard et al. 2018]. En plus de cette relation directe, les tourbillons anticycloniques (cycloniques) de surface présentent des couches de mélanges plus (moins) profondes que leur environnement (voir le Figure 2.5). Ainsi, la diminution des températures de surface, associées au pompage d'Ekman induit par les dépressions atmosphériques, est réduite par les tourbillons anticycloniques et augmentée par ceux cycloniques [Jullien et al. 2014]. De plus, la vorticité associée à ces structures modifie le pompage d'Ekman comme mise en évidence par Stern [1965] et discuté, par exemple, par Renault et al. [2016].

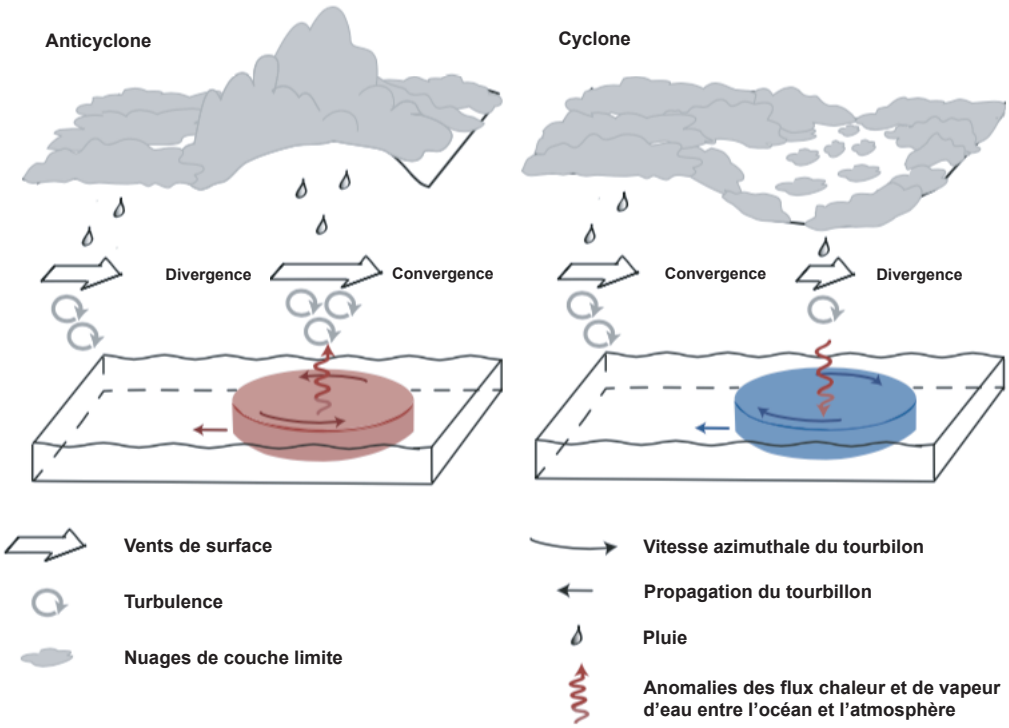


Figure 2.12: Synthèse de l'impact des tourbillons océaniques de surface sur l'atmosphère traduit depuis Frenger et al. [2013]. Il est à noter que ce schéma représente des tourbillons dans l'hémisphère sud.

Finalement, il semble important d'indiquer que les tourbillons agissent aussi sur d'autres parties de l'environnement océanique. Par exemple, les tourbillons peuvent participer aux transports de sédiments [O'Brien et al. 2011; Zhang et al. 2014a] ou à l'agrégation de phytoplanctons (voir Figure 2.4). De nouveau, l'impact des tourbillons mésoéchelles sur les communautés biologiques peut se décomposer en deux mécanismes : leur advection de masses d'eau en leur cœur et la modifi-

cation de l'environnement local tel que la favorisation de mouvements verticaux [McGillicuddy Jr 2016]. Cependant, quel que soit le mécanisme étudié, les tourbillons peuvent aussi bien favoriser que réduire la production biologique. Par exemple, la propagation ou la subduction des tourbillons d'upwelling a tendance à diminuer la production primaire en transportant les nutriments et la biomasse hors de la zone d'upwelling [Rossi et al. 2008] ou sous la surface [Gruber et al. 2011]. Finalement, les modifications de la production primaire peuvent se répercuter ensuite sur les parties supérieures des réseaux trophiques comme, par exemple, sur la distribution des tortues marines, des poissons pélagiques ainsi que des mammifères et oiseaux marins [e.g. Nel et al. 2001; Davis et al. 2002; Seki et al. 2002; Gaube et al. 2017; 2018].

2.3 Les échanges océaniques de l'océan Indien vers l'océan Atlantique

Nous avons vu précédemment la particularité de l'océan Atlantique Sud où le transport de chaleur s'effectue vers l'équateur et non vers les pôles. Or, la circulation de surface dans cet océan forme un gyre : le courant du Brésil est le courant de bord ouest [Stramma and Peterson 1989], le courant sud Atlantique est sa limite vers les pôles [Stramma and Peterson 1990], le courant du Benguela [Stramma and Peterson 1989] et le courant équatorial sud [Stramma 1991] ferment ce gyre. Ainsi, cette vision n'est pas complète puisque le transport net vers le nord des eaux de surface nécessite des entrées d'eau de surface.

Il y a deux voies possibles pour le retour des eaux de la thermocline dans l'Altantique Sud [e.g. Donners and Drijfhout 2004]: du Pacifique vers l'Atlantique par le Passage de Drake au sud de l'Amérique et de l'Indien vers l'Atlantique par le système des Aiguilles au sud de l'Afrique. La fuite d'eau au niveau du courant des Aiguilles (AL pour "Agulhas Leakage") est, d'après Gordon [1985], la seule source possible d'eau suffisamment chaude et salée pour maintenir l'équilibre observé dans la thermocline Atlantique et fermer le budget de la GOC dans ce bassin. De récents résultats par Rühs et al. [2018] mettent en évidence que l'AL domine en effet ces apports en contribuant entre 50 et 60% du transport total. De plus, il a été montré qu'un changement de cette source impacte les propriétés thermohalines de l'océan Atlantique ce qui, en changeant sa stratification, peut modifier sa formation d'eau profonde [De Ruijter et al. 1999a; Weijer et al. 2002]. Ainsi, ces échanges ont un impact direct sur la GOC en modulant l'intensité de son effet de retournement [Gordon 1985; 1986; Biastoch et al. 2008a; Speich et al. 2001].

La région au sud du continent Africain est au confluent des océans Atlantique, Austral et Indien. Ainsi, ce transport de masses d'eau de l'océan Indien vers l'océan Atlantique connecte les deux gyres subtropicaux de ces océans ce qui amène à la création du super-gyre de l'hémisphère Sud [Speich et al. 2007; Ridgway and Dunn 2007] reliant les océans Indien, Pacifique et Atlantique. Ce super-gyre est indiqué en

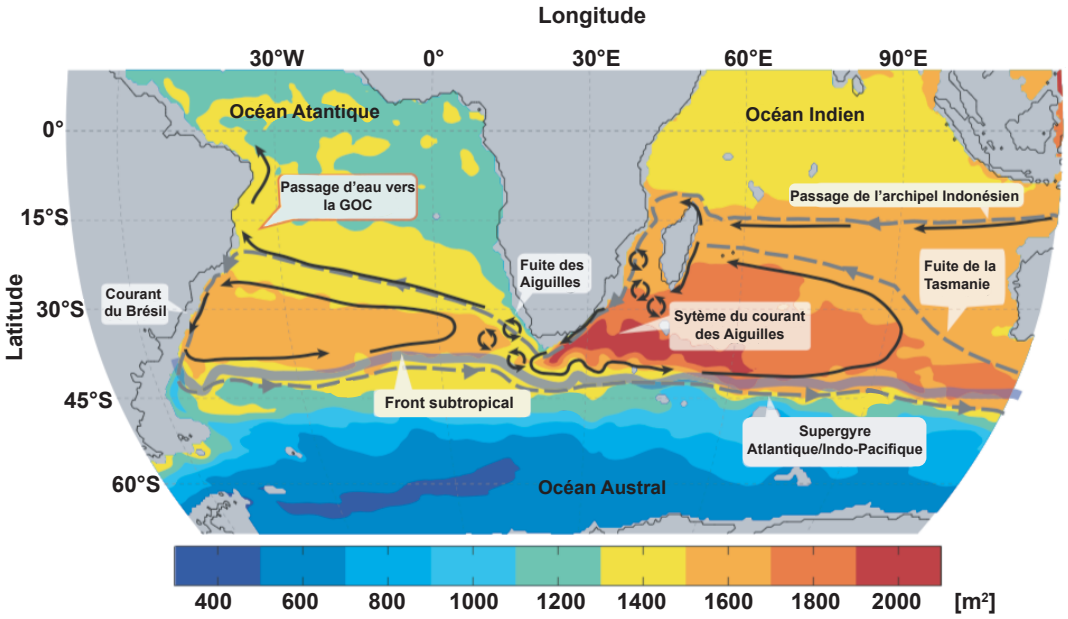


Figure 2.13: Représentation schématique du super-gyre de l'hémisphère Sud. Les couleurs indiquent la hauteur dynamique intégrée dans les 2000 premiers mètres de la base de données CARS [Ridgway and Dunn 2007]. Les flèches noires et les étiquettes indiquent des éléments importants de l'écoulement. Le super-gyre de l'hémisphère sud est marqué par des lignes pointillées grises. Figure traduite d'après Beal et al. [2011].

gris dans le Figure 2.13 et les différentes structures bathymétriques dans la région sont présentées dans le Figure 2.14.

2.3.1 Le système du courant des Aiguilles

Les échanges d'eau de l'océan Indien vers l'Atlantique sont intimement liés au comportement du courant des Aiguilles (AC pour "Agulahas Current") qui sépare ces deux océans. L'AC, qui est le courant bord ouest du gyre subtropical de l'océan Indien, est formé le long de l'Afrique du Sud entre 25° S et 30° S où il suit la pente continentale vers le sud-sud-est. Cette pente est raide et continue [Lutjeharms 2006] ce qui le stabilise en amont de ~35° S. Il est donc caractérisé par peu de méandres dans cette partie contrairement aux autres courants de bord ouest tel que le Kuroshio ou le Gulf Stream. Une exception existe au niveau de la ville de Durban (30 ° S) où un large méandre nommé "Natal Pulse" [Lutjeharms and Roberts 1988] peut se former et se propager vers le Sud avec le courant [De Ruijter et al. 1999b; Schouten et al. 2002].

En aval de 35° S, le plateau continental s'élargit au niveau du Talus des Aiguilles ("Agulhas Bank" voir Figure 2.14) où de larges méandres apparaissent dans ce courant alors qu'il s'écarte du continent et, finalement, se détache de la pente continentale. La circulation de cette région est caractérisée par une dynamique

fortement non-linéaire. Il a été démontré que la position géographique du rotationel du stress de vent est décisive sur la position de l'extrémité du courant des Aiguilles [De Ruijter 1982; Speich et al. 2007]. Ainsi, comme la ligne de changement de signe du rotationel du stress de vent (~45° S), au niveau du maximum des vents d'ouest, est plus sud que la pointe africaine, le courant devient un jet libre lorsqu'il n'est plus contraint par la bathymétrie. Sans inertie, la totalité du courant tournerait vers l'ouest en entrant dans l'océan Atlantique comme montré numériquement par De Ruijter [1982]. Ce n'est pas le cas car le courant des Aiguilles change de direction en virant vers l'est dans cette région. Le coude ainsi formé a été nommé retroflection par Bang [1970] par analogie avec l'anatomie des intestins des mammifères.

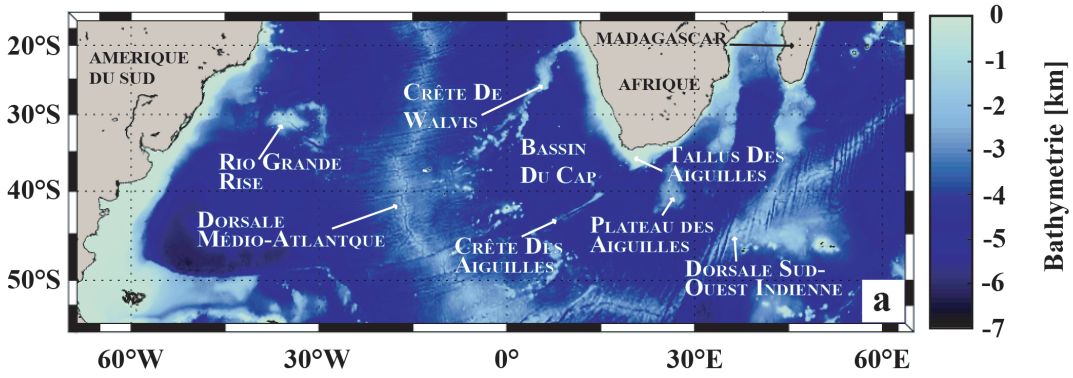


Figure 2.14: Domaine d'étude et bathymétrie extraite de la base de données ETOPO2 [Smith and Sandwell 1997]

Cette région très instable est marquée par des éjections de masses d'eau sous forme de tourbillons et de filaments advectés par l'AC qui s'échappent ensuite vers l'océan Atlantique ce qui correspond à la fuite d'eau appelée l'"Agulhas Leakage" [Lutjeharms and Gordon 1987; Lutjeharms 1981; Lutjeharms and Cooper 1996]. Pichevin et al. [1999] ont montré que, pour satisfaire la conservation de la quantité de mouvement, l'éjection de masse d'eau est nécessaire afin de maintenir la rétroflection. Il est à noter que, si le courant contenait une plus grande quantité d'inertie ou si le changement de signe du rotationnel du vent était plus au nord, le courant effectuerait un changeant de direction plus en amont ce qui ne permettrait pas ce type de transfert [Beal et al. 2011]. La position en longitude de cette rétroflexion n'est pas constante puisqu'elle varie entre 12 et 28° E [Dencausse et al. 2010b]. Ces variations s'expliquent par une progression vers l'ouest de la rétroflexion à une vitesse estimée entre 7 et 10 km/jour [Lutjeharms and Ballegooyen 1988; Feron et al. 1992] entre deux éjections de tourbillon. Au contraire, une éjection d'eau vers l'Atlantique se traduit par un déplacement rapide vers l'est de cette rétroflection.

En aval de la rétroflection, la plus grande fraction du courant se dirige vers l'est en formant le Courant de Retour des Aiguilles (ARC pour "Agulhas Return Current"). Sa position marque la limite entre l'océan Indien et l'océan Austral où d'importants cisaillements peuvent donner naissance à des tourbillons [Lutjeharms and Valentine 1988]. Ce courant de retour est aussi constitué de méandres stationnaires liés aux

nombreux obstacles bathymétriques. Une de ces déviations vers le nord au niveau du plateau des Aiguilles (vers ~25°E et 40°S) est visible dans la Figure 2.13.

Avant d'étudier la fuite d'eau vers l'océan Indien, il est important de discuter des sources de ce courant. L'AC est constitué d'eau de la thermocline (voir Figure 2.1)[Gordon et al. 1987] provenant de la partie ouest de l'océan Indien. Plus précisément, le Canal du Mozambique entre l'Afrique et Madagascar et le courant Est de Madagascar émettent des tourbillons (voir Figure 2.13) qui sont soit absorbés [Braby et al. 2016] par l'AC soit semblent être advectés au large de ce dernier [Schouten et al. 2002]. Ces tourbillons sont constitués d'eaux du super-gyre ayant traversé zonalement l'océan Indien depuis leur entrée au niveau de l'archipel indonésien ou de sud de la Tasmanie (voir Figure 2.13). Cependant, l'augmentation du transport vers l'aval de l'AC pourrait aussi indiquer la présence d'une recirculation entre l'ACR et l'AC [Harris 1972; Lutjeharms et al. 1997]. Cela a été confirmé par l'analyse de cartes altimétriques [Feron et al. 1998] ainsi que par des observations [Garzoli and Goni 2000; Lutjeharms and Ansorge 2001] et des simulations numériques [Lutjeharms et al. 2003].

2.3.2 Les tourbillons des Aiguilles

Les masses d'eau détachées du courant des Aiguilles à l'ouest de sa nouvelle position se stabilisent sous forme de filaments ou de tourbillons océaniques [Doglioli et al. 2006]. Les tourbillons anticycloniques ont été identifiés comme étant ceux permettant la plus grosse fraction de ces échanges car les filaments participent à 15 % du flux de masse au maximum [Lutjeharms and Cooper 1996]. Les tourbillons ainsi créés sont composés d'une bande de courant englobant de l'eau de l'océan Indien ce qui explique leur dénomination d'Anneaux des Aiguilles (AR pour "Agulhas Rings"). La fréquence d'éjection de ces AR a été estimée à 4 à 6 par an [Byrne et al. 1995; Duncombe Rae et al. 1996] ce qui correspond à la fréquence de déplacement rapide vers l'est de la rétroflection obtenue par Dencausse et al. [2010b].

Après leur éjection, les AR sont de larges structures ayant des rayons supérieurs à 100 km [Duncombe Rae 1991] et pouvant atteindre des profondeurs de 4,5 km [Van Aken et al. 2003]. Ils sont associés à une signature en température de surface distincte de l'environnement [Lutjeharms and Gordon 1987] mais celle-ci tend à disparaitre en quelques semaines suite aux échanges intenses avec l'atmosphère [Olson et al. 1992; Schouten et al. 2000].

Une fois détachés, les AR se propagent vers l'ouest en direction du bassin du Cap [Gründlingh 1995]. Cependant, ces structures peuvent se séparer avant leur entrée dans ce bassin. Il existe un ratio d'environs 0,65 à 1 entre le nombre de tourbillons issus de séparation d'AR et ceux initialement créés [Schouten et al. 2000; Dencausse et al. 2010a]. De plus, ils ont aussi des parcours très variés en traversant la chaîne de montagne sous marine des Aiguilles ("Agulhas Ridge" en Anglais). En effet, Dencausse et al. [2010a] a différentié trois routes en fonction de la latitude où les AR

traversent une ligne imaginaire passant par cette crête. Cela a un impact important sur les échanges avec l'atmosphère qu'ils subissent [McDonagh and Heywood 1999]. Par exemple, ceux au sud vont perdre plus d'énergie vers l'atmosphère ce qui va se traduire par la création d'importantes couches de mélanges comme celle de plus de 600 m dans l'anticyclone M décrit par Arhan et al. [2011].

Une fois rentrés dans ce bassin, les AR se déplacent principalement vers le nord-nord-ouest où ils rencontrent d'autres structures tourbillonnaires. Ces rencontres sont d'autant plus nombreuses dans la partie orientale du bassin appelée Chaudron du Cap [Boebel et al. 2003b] où ils peuvent subir des fusions et des séparations. De plus, le bassin du Cap est composé d'obstacles bathymétriques ce qui peut déstabiliser les AR et aussi se traduire par leur fragmentation en plusieurs tourbillons [Arhan et al. 1999]. Les AR dans cette région présentent donc une grande variété de propriétés cinématiques ainsi que hydrographiques. Un exemple de cette diversité est l'identification de certains AR comme étant originaires du courant du Brésil par Duncombe Rae et al. [1996]. Il a été montré que ce sont des AR ayant passé un temps long dans le sud qui ont perdu beaucoup d'énergie vers l'atmosphère modifiant leur structure thermohaline [McDonagh and Heywood 1999]. Finalement, des études statistiques de AR détectés sur les champs altimétriques ont mis en évidence que leur signature en surface (i.e. amplitude et vorticité) diminue exponentiellement lors de leur traversée de cette région [Byrne et al. 1995; Guerra et al. 2018].

La crête de Walvis ("Walvis Ridge" voir Figure 2.14) constitue un obstacle majeur à la sortie du bassin du Cap. Des simulations numériques ont mis en évidence que seuls les tourbillons barocliniques peuvent la traverser [Kamenkovich et al. 1996; Beismann et al. 1999; Matano and Beier 2003] et des observations indiquent qu'ils suivent principalement les zones les plus profondes [Olson and Evans 1986; Gordon and Haxby 1990; Byrne et al. 1995; Arhan et al. 1999]. Ainsi, seuls 2/3 des AR parviennent à fuir ce bassin [Gordon and Haxby 1990; Schouten et al. 2000]. Pour ceux y parvenant, l'étude récente de Nencioli et al. [2018] a mis en évidence qu'ils perdent une importante fraction de leur volume (~25 %) lors du passage de cette crête.

Une fois sortis, les tourbillons changent de direction en se déplaçant zonalement vers l'ouest. Leur signature en surface, telle que décrite par l'altimétrie, continue à réduire pendant leur traversée de l'Atlantique Sud [Byrne et al. 1995; Wang et al. 2016; Guerra et al. 2018]. De nouveau, la bathymétrie est leur principal obstacle puisqu'ils perdent une importante fraction de leur volume lorsqu'ils traversent la dorsale médio-atlantique [Nencioli et al. 2018]. Il est important de noter que les AR peuvent être intensifiés en surface ou en subsurface dans cet océan comme mis en évidence par deux d'entre eux observés par Arhan et al. [1999]. Or, la reconstruction de la vie de ces deux tourbillons sur les champs altimétriques indiquent qu'ils sont tous les deux issus d'un même anneau qui s'est subdivisé plusieurs mois auparavant. De nouveau, cela s'explique par une stagnation du tourbillon de subsurface pendant plusieurs mois d'hiver dans les latitudes élevées alors que l'autre s'est déplacé plus rapidement vers le nord-ouest [Arhan et al. 1999].

Il a été supposé depuis longtemps que certains tourbillons pouvaient traverser l'océan Atlantique [Byrne et al. 1995]. La confirmation est arrivée très récemment par une nouvelle étude de Guerra et al. [2018] où l'interaction d'un tourbillon des Aiguilles avec des structures le long du continent américain a été observée par des mesures hydrographiques.

Finalement, la grande diversité de processus subis par les AR rendent difficiles l'estimation des transports de chaleur engendrés par ces tourbillons [Lutjeharms and Ballegooyen 1988]. Cela a souvent été entrepris en étudiant quelques structures puis en extrapolant cette estimation au nombre de tourbillons présents [e.g. Souza et al. 2011a]. Pris dans leur ensemble, les estimations de flux varient entre $0,03 - 0,09$ PW [van Ballegooyen et al. 1994; Gründlingh 1995; Souza et al. 2011a]. Cependant, ces résultats sont difficilement comparables puisqu'ils dépendent de la définition du volume considéré et de la région utilisée pour calculer les propriétés hydrologiques de l'environnement.

2.4 Questions principales et approche

Nous avons vu que les Anneaux des Aiguilles ont largement été observés, aussi bien par des mesures en mer que par des images satellites. Cependant, de nombreuses questions subsistent sur le devenir de ces structures depuis leur formation jusqu'à leur dissipation. Cela s'explique principalement par les multiples effets non-linéaires qu'ils subissent tels que des séparations (splitting) et des fusions (merging). Des études ont été entreprises régionalement afin d'analyser l'impact de ces processus mais, suite au faible nombre d'algorithmes de détection les prenant en compte, aucune estimation des modifications engendrées par ces événements sur la reconstruction complète des tourbillons des AR n'a été entreprise. Cela semble d'autant plus important en vu des travaux ayant supposé des connections entre les AR et d'autres tourbillons de l'océan Indien ainsi que la capacité des AR à traverser l'océan Atlantique où ils interagissent avec d'autres structures tourbillonnaires aux abords du courant du Brésil.

En plus de la détermination de leur histoire d'après les champs de surface, peu de choses sont connues sur leur évolution dans la colonne d'eau. On peut noter, par exemple, que la dissipation de ces structures sur les champs de surface a été décrite lorsqu'ils se propagent dans l'océan Atlantique mais que la manière dont cela se traduit dans l'intérieur de l'océan reste un mystère. De plus, nous avons mis en avant l'importance de leur histoire sur les processus, dont les échanges avec l'atmosphère, qui modifient leur structure interne. Or, pour étudier les transferts de chaleur, c'est une détermination de cette structure thermohaline qui est nécessaire.

Ainsi, de multiples interrogations restent en suspens sur la vie des tourbillons des Aiguilles et, par conséquent, sur la quantité de chaleur transportée par eux dans l'océan Atlantique. Ce travail de thèse a pour but d'améliorer nos connaissances

dans ce domaine en tentant de répondre explicitement aux questions suivantes :

- Est-il possible de valider les algorithmes de détection tourbillonnaire à partir de données in-situ indépendantes ?
- De quelle manière la prise en compte des interactions entre tourbillon influence t-elle la vision traditionnelle du parcours des tourbillons des Aiguilles ?
- Comment caractériser l'extension verticale et la structure de subsurface des AR ?
- Comment les AR contrôlent-ils le transport de chaleur en subsurface dans l'Atlantique Sud ?

Nous proposons dans ce travail d'analyser des données satellites conjointement à des mesures in-situ pour essayer d'apporter des réponses à ces questions. La méthode utilisée est la reconstruction des trajectoires des AR et l'analyse de l'évolution de leur structure interne afin d'aboutir à une nouvelle estimation des transports de chaleur engendrés par les AR. Pour cela, nous avons modifié une méthode de détection et de suivi des tourbillons sur les champs altimétriques. Sa description ainsi que sa validation à partir de mesures indépendantes sont présentées dans le troisième chapitre. La caractérisation des tourbillons des Aiguilles obtenue grâce à cet outil y est ensuite décrite à travers le concept de réseau de trajectoire développé au cours de cette thèse qui a pour but de prendre en compte la complexité de leur trajectoire. La reconstruction de l'évolution hydrologique d'un tourbillon échantillonné par des profileurs dérivants Argo est effectuée dans le quatrième chapitre. La perte de contact entre le cœur hydrologique de cette structure et l'atmosphère ainsi que sa comparaison avec les tourbillons des Aiguilles échantillonnés dans la littérature y sont discutées. Une caractérisation de la régionalisation des types de tourbillons des Aiguilles ainsi qu'une estimation des transferts de chaleur effectués par ces structures par des approches Eulériennes et Lagrangienne sont proposées dans le cinquième chapitre. Finalement, les avancés sur la compréhension des AR résultants de ce travail thèse et les perspectives en découlant sont présentées dans un chapitre de conclusion.

3

Caractérisation de la signature en surface des Anneaux des Aiguilles

Sommaire

3.1 Résumé de l'article 35
3.2 Anticyclonic eddies connecting the western boundaries of Indian and Atlantic oceans 36
3.2.1 Introduction 36
3.2.2 Data and Methods 38
3.2.3 Validation and Comparison of Eddies Datasets 47
3.2.4 Results of the TOEddies method applied to Agulhas Rings 53
3.2.5 Summary and Conclusions 70

3.1 Résumé de l'article

Nous avons vu dans le chapitre 2 que les échanges interocéaniques indo-atlantiques réalisés par les tourbillons des Aiguilles (AR) sont étroitement liés à la circulation océanique mondiale et au climat. Pourtant, ils sont encore mal compris car difficiles à identifier et à suivre. En particulier, nous avons mis en évidence, à travers une étude bibliographique sur ces structures, qu'ils peuvent avoir des parcours extrêmement variés et que de nombreuses questions subsistent sur leur potentiel lien avec d'autres tourbillons en amont de la rétroflection du courant des Aiguilles et sur le devenir de ceux atteignant le courant du Brésil. De plus, de nombreux

épisodes de fusions et séparations de ces tourbillons ont été décrits régionalement mais aucune vision globale de ces phénomènes n'a été effectuée.

Nous proposons dans ce chapitre, publié dans le "Journal of Geophysical Research : Ocean" [Laxenaire et al. 2018], une évaluation originale des AR réalisée par TOEddies, un nouvel algorithme d'identification et de suivi des tourbillons, que nous avons appliqué à 24 années d'altimétrie satellitaire. Sa principale nouveauté réside dans la détection d'événements de division et de fusion des tourbillons. Ces évènements sont particulièrement abondants et ont un impact significatif sur le concept de trajectoire associée à un tourbillon simple, qui devient moins évident que les descriptions antérieures. Pour surmonter cette difficulté, nous avons défini un réseau de segments qui se regroupent dans des trajectoires relativement complexes. Un tel réseau fournit une évaluation originale des itinéraires et de l'histoire des AR. Il relie 730 481 tourbillons en 6 363 segments qui se regroupent en trajectoires d'AR de différents ordres. Un tel ordre dépend de l'affiliation des tourbillons et des segments, de la même manière qu'un arbre de vie. Parmi ces trajectoires, nous avons identifié 122 trajectoires d'ordre 0 pouvant être considérées comme les trajectoires principales associées à un tourbillon simple, bien que celui-ci ait subi lui-même des événements de division et de fusion. Malgré la disparition de nombreux tourbillons du signal altimétrique dans le bassin du Cap, une fraction significative peut être suivie de l'océan Indien au courant sud du Brésil en traversant, en moyenne, l'Atlantique Sud en 3,5 années.

3.2 Anticyclonic eddies connecting the western boundaries of Indian and Atlantic oceans

3.2.1 Introduction

Mesoscale eddies and meanders are ubiquitous structures in the ocean and are one of the major sources of ocean variability [Stammer 1997; Wunsch 1999]. They are thought to contribute significantly to the transfer of heat, salt, mass and biogeochemical properties across the World Ocean [McWilliams 1985]. South of Africa, large mesoscale eddies [Lutjeharms 2006], the so called Agulhas Rings, are shed from the Agulhas Current into the Cape Basin at the Agulhas Retroflection [Olson and Evans 1986; Lutjeharms and Gordon 1987; Lutjeharms and Ballegooyen 1988; Gordon and Haxby 1990; Duncombe Rae 1991] transporting Indian waters into the Southeast Atlantic [Ballegooyen et al. 1994; Garzoli et al. 1999; Arhan et al. 1999; 2011] affecting the heat, salt and biogeochemistry of the Atlantic Ocean [Gordon et al. 1992; Lehahn et al. 2011; Paul et al. 2015; Villar et al. 2015]. They participate in the Agulhas Leakage [De Ruijter et al. 1999a; Lutjeharms 2006], the Indo-Atlantic interocean exchange of water that has a strong impact on the Atlantic Meridional Overturning Circulation (AMOC), influencing its strength [Weijer et al. 1999; 2002; van Sebille and van Leeuwen 2007], stability [Weijer et al.

2001] and variability [Biastoch et al. 2008a; Biastoch and Böning 2013]. Therefore, the origins, number and fate of Agulhas Rings are key elements in assessing global ocean circulation and its variations in a changing climate.

Since 1992 several altimetry satellites have revealed the richness, complexity, and some surface properties of mesoscale ocean dynamics [Hernandez et al. 1995; Chelton et al. 2007; 2011]. Based on these data, a number of studies have estimated eddies and their trajectories, mainly from mid to high latitudes, using various automatic eddy detection algorithms [e.g., Isern-Fontanet et al. 2006; Doglioli et al. 2007; Chelton et al. 2007; Chaigneau et al. 2008; Nencioli et al. 2010; Chelton et al. 2011; Mason et al. 2014; Faghmous et al. 2015; Ashkezari et al. 2016; Matsuoka et al. 2016; Qiu-Yang et al. 2016; Le Vu et al. 2018]. All these detection methods are based either on physical criteria (such as the estimation of the Okubo-Weiss parameter [Okubo 1970; Weiss 1991]) or geometrical properties of the flow. Several of these methods and eddy atlases are proposed to the scientific community and are made public. However, to our knowledge, none of them were quantitatively qualified against independent data. Efforts have been made to evaluate one or more methods, but this evaluation has been undertaken at a very local scale or using subjective assessments. Souza et al. [2011b], for example, have attempted to compare and validate three different detection methods using current knowledge of South Atlantic eddies as independent criteria. Chaigneau et al. [2008] and Faghmous et al. [2015] compared their detection to structures identified by various experts. However, this procedure proved to be very sensitive, as experts often disagreed. Finally, Mkhinini et al. [2014] and Casanova-Masjoan et al. [2017] undertook a more objective, albeit still qualitative, assessment of the skill of their method by using respectively, 10 and 2 surface drifters trapped in specific anticyclonic eddies.

Using different eddy detection methods, several authors have attempted to reconstruct and analyze Agulhas Rings trajectories in and across the South Atlantic [e.g. Gordon and Haxby 1990; Byrne et al. 1995; Souza et al. 2011a; Wang et al. 2015]. In the published studies, most reconstructions of the trajectories of Agulhas Rings leaving the Cape Basin are identified initially well within the Cape Basin and not at the Agulhas Current Retroflection where they are believed to originate [e.g. Byrne et al. 1995; Souza et al. 2011a; Wang et al. 2015; 2016; Guerra et al. 2018]. Taking into account the separation of an eddy into smaller structures, to which, in what follows, we will refer to as an eddy splitting event, Dencausse et al. [2010a] tracked the Agulhas Rings formed in the Agulhas Retroflection area and entering the Cape Basin. They have shown that such events are very frequent. Indeed, the ratio obtained between the number of trajectories formed after a split and the number of trajectories tracked from the Agulhas Retroflection is close to 1. This process has an impact on the concept of Agulhas Ring trajectories and on the number of Agulhas Rings formed per year (traditionally estimated between 3 and 6) [e.g Gordon and Haxby 1990; Ballegooyen et al. 1994; Byrne et al. 1995; Goni et al. 1997]. In fact, Dencausse et al. [2010a] have shown that up to 14 Agulhas Rings per year enter the Cape Basin. However, these authors have only followed Agulhas Rings in a very limited region without addressing the question of the

impact of these eddy-eddy interactions on the recovery of the full extent of Agulhas Rings trajectories. For example, Schouten et al. [2002] showed that certain eddies formed in the Mozambique Channel or at the southern limit of Madagascar can, in addition to triggering Natal Pulses, be advected until the Retroflection region leading to shedding of an Agulhas Ring. Downstream from the Cape Basin, most of the Agulhas Rings described in the literature do not cross the South Atlantic entirely. To our knowledge, the only exceptions are a trajectory followed by Byrne et al. [1995] that reached 40°W near the American Margin and another by Guerra et al. [2018] that clearly drifted south along the Brazilian coast. All these individual regional pictures of Agulhas Ring trajectories must, in one way or another, be incorporated into a global vision taking into account the eddy-eddy interactions.

In this article, we present a new eddy detection and tracking algorithm applied to the 24-year satellite altimetry time series in a space domain covering the South Atlantic and Southwest Indian oceans. The eddy detection and tracking steps of this new algorithm are a development of the geometric method of Chaigneau et al. [2008], Chaigneau et al. [2009], and Pegliasco et al. [2015]. To obtain an objective measure of the capabilities of our method and the robustness of our eddy database, we have developed a systematic procedure that tests the presence and properties of eddies against a totally independent data set, so called the "loopers", which are upper-ocean eddies identified from surface drifters and provided by Lumpkin [2016].

While the method is developed and tested on all eddies detected in the domain of study, particular emphasis will be placed on the results concerning the Agulhas Rings. Indeed, the new eddy detection and tracking method gives access to an unprecedented assessment of the origin and fate of the Agulhas Rings and the Indo-Atlantic exchange of waters they carry out. Moreover, we will discuss their characteristics and variations along the trajectories in terms of various kinematic and dynamical properties that can be deduced from altimetry.

The paper is organized as follows. In Section 3.2.2, the data we have used are described and the methods we have developed are presented. Validation and comparisons of our eddy detection algorithm with a published databases are presented in Section 3.2.3. Section 3.2.4 focuses on the Agulhas Rings. We discuss their origins, their disappearance from the altimetry field, their trajectories, and statistics on the different properties of Agulhas Rings. In the last section, the results are discussed and we draw the main conclusions of this study.

3.2.2 Data and Methods

Satellite Altimetry Data

This study is based on more than 24 years (01/1993 to 05/2017) of daily maps of delayed time absolute dynamic topography (ADT) and derived geostrophic

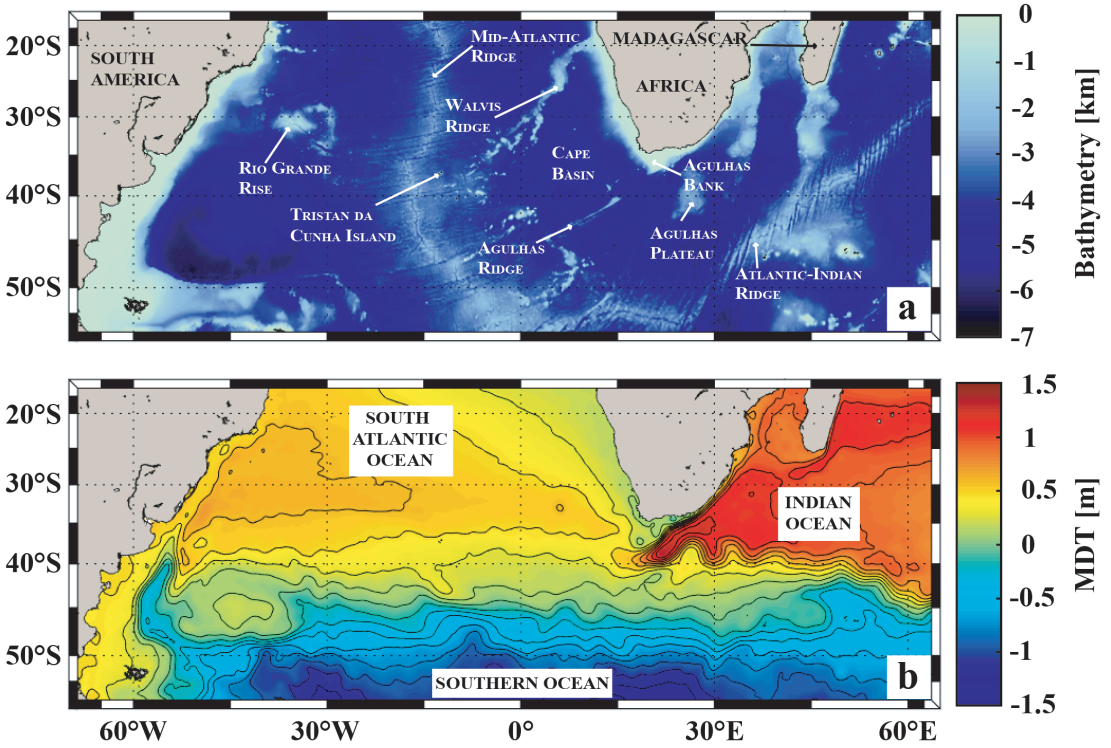


Figure 3.1: Study domain and a) bathymetry from the ETOPO2 data set [Smith and Sandwell 1997] and b) Mean Dynamic Topography (MDT, [Duacs/AVISO+ 2014]) with the main currents indicated.

velocity fields in the South Atlantic and Southeast Indian oceans [70°W-65°E; 55°S-15°S] (see Figure 3.1). These maps are produced by Ssalto/Duacs and distributed by the Copernicus Marine Environment Monitoring Service (`https://marine.copernicus.eu/`) in the version released in April 2014 (DT14) [Duacs/AVISO+ 2014; Pujol et al. 2016]. They correspond to the gridded Sea Surface Height (SSH) above the geoid calculated by combining all the data recorded by the satellites available among the 12 altimetric missions (Topex/Poseidon, ERS-1 and -2, Jason-1, OSTM/Jason-2, SARAL/Altika, Cryosat-2, Envisat, Geosat, Haiyang-2A, Jason-3 and Sentinel-3A). Objectively mapped ADT is the sum of Sea-Level Anomalies (SLA) and Mean Dynamic Topography (MDT) maps, both referenced over a 20-year period in the Ssalto/Duacs 2014 version [Duacs/AVISO+ 2015]. The improved data processing used in DT14 provides a better description of mesoscale activity than previously distributed products [Capet et al. 2014; Pujol et al. 2016].

Most published studies, which also include previous developments of the current method [Chaigneau et al. 2011; Pegliasco et al. 2015], have applied an eddy-detection algorithm applied to SLA. This was essentially to avoid errors due to the imprecision of the definition of the Earth geoid. Recently, the availability of the latest version of MDT (MDT CNES-CLS13, [Rio et al. 2014]), calculated from a 20-year average (1993-2012) of altimetry data and a geoid obtained by correcting the Gravity and

Ocean Circulation Experiment (GOCE) model with dynamic height and velocity estimates derived from in situ observations [Rio et al. 2011; 2014] provides a better estimate of the geopotential surface height of the ocean, which significantly improves ADT and associated ocean dynamics [Rio et al. 2014]. Like Halo et al. [2014], we choose to use ADT instead of SLA maps because the latter are strongly affected by the position and displacement of large SSH gradients associated with intense currents and quasi-stationary meanders and eddies, all included in MDT as shown in Figure 3.1b. This is particularly true for the Agulhas Current system. In fact, small shifts relative to average current positions can generate artificial dipoles of positive and negative SLA. These dipoles are identified as two eddies in SLA whereas they are not detected in ADT. In addition, ADT is directly associated with important physical variables such as ocean currents and the geostrophic stream function.

The Ocean Eddy Detection and Tracking Algorithms (TOEddies)

This eddy detection algorithm is an evolution of the method proposed and developed by Chaigneau et al. [2008; 2009]. It is based on the key assumption that for geostrophic eddies, the streamlines correspond to the closed contours of Sea Surface Height (SSH). The eddy detection algorithm is a two-step process: it identifies the occurrence of eddies before deriving their trajectories.

First and foremost, the method identifies the local extrema (maxima and minima) of ADT as possible eddy centers. Then, it looks for the outermost closed ADT contours around each extremum. The module of the ADT difference between the extremum and this contour defines the detected eddy amplitude which is considered as a proxy of the eddy (surface) signature. Cipollone et al. [2017] showed that two close extrema can be dependent and thus defined a minimum distance between extrema so that they are considered as possible eddy centers. In this study, we introduced as a parameter of the eddy detection method, a minimum threshold for the amplitude of the eddy extrema. This ensures that a detected extremum can be considered as an eddy center. Extrema associated with an amplitude below the threshold will not be a constraint for the detection of the outermost closed ADT contours associated with others extrema.

This parameter (the eddy amplitude threshold) can be interpreted as an eddy "persistence", a notion of topological simplification introduced by Edelsbrunner et al. [2002] and Edelsbrunner and Harer [2010] which has been widely used since [e.g. Tierny et al. 2018]. The persistence criterion by reducing the number of extrema aims to avoid the over-representation of dynamically insignificant structures because it should prevent the artificial separation of a large eddy into two or more smaller elements. Therefore, in the following, the amplitude threshold parameter will be called "persistence" to distinguish it from the minimum amplitude criterion that has been widely used in the literature [e.g. Chelton et al. 2011]. Faghmous et al. [2015] showed that the minimum amplitude criterion, with its typical value of 1 cm, could lead to the loss of significant structures. A sensitivity test on eddy persistence

is presented in Table B.1 of the Appendix B according to the method presented in Section 3.2.3. It shows that a non-zero value for the persistence parameter (set to 1 mm) increases the number of structures as well as the ability of our detection method to define eddies. However, a further increase in the persistence parameter value does not show significant improvements in the eddy detection capability. This is why we have set this parameter value to 1 mm. Note that this value, which acts somewhat like a low-pass filter, is considerably smaller than the resolution of 1 to 2 cm defined in the literature as the nominal resolution of satellite altimetry.

The detected ADT extrema that pass the persistence threshold are each identified as the center of an eddy if there is at least one closed ADT contour containing only one local extreme and including at least 4 connected grid points. The size of each eddy is then characterized by two distinct radii. The equivalent outermost radius, R_{out}, which corresponds to the radius of a disk having the same area (A_{out}) as that delimited by the outermost closed contour. Its value is given by the equation:

$$R_{out} = \sqrt{\frac{A_{out}}{\pi}} \tag{3.1}$$

However, the outermost closed contour is often strongly distorted by the surrounding flow and interactions with others mesoscale structures. For this reason, we also used, as a reference variable for the method, the contour corresponding to the ADT contour along which the mean azimuthal geostrophic velocity is maximum (V_{max}). This limit, called the "characteristic contour" in this study, tends to be more robust and coherent in time than the outermost contour. We then defined the maximum speed radius, R_{Vmax}, associated with the area delimited by the characteristic contour. R_{Vmax} is always smaller or equal to R_{out}. It characterizes the eddy core and allows easy comparisons with in situ measurements such as ADCP transects or drifter trajectories [Mkhinini et al. 2014; Ioannou et al. 2017]. The accuracy of each eddy center (associated with a local ADT extremum) is limited by that of the ADT field defined at a horizontal resolution of 1/4°. Because of this precision limit, we chose to use the centroid of the area associated with the eddy core as the center of each structure. Indeed, this variable is less affected by the ADT resolution. An example of the two boundaries of two cyclones and an anticyclone and their eddy centers is shown in Figure 3.2.

The vortex surface Rossby Number (Ro) is used to compare eddy characteristics in different regions [e.g. Chelton et al. 2011; Mkhinini et al. 2014; Le Vu et al. 2018], as it is a proxy of the surface intensity of the dynamic core (equation 3.2, where f is the Coriolis parameter).

$$Ro = \frac{V_{max}}{f R_{Vmax}} \tag{3.2}$$

In a second step of the eddy detection method, a complete and continuous set of

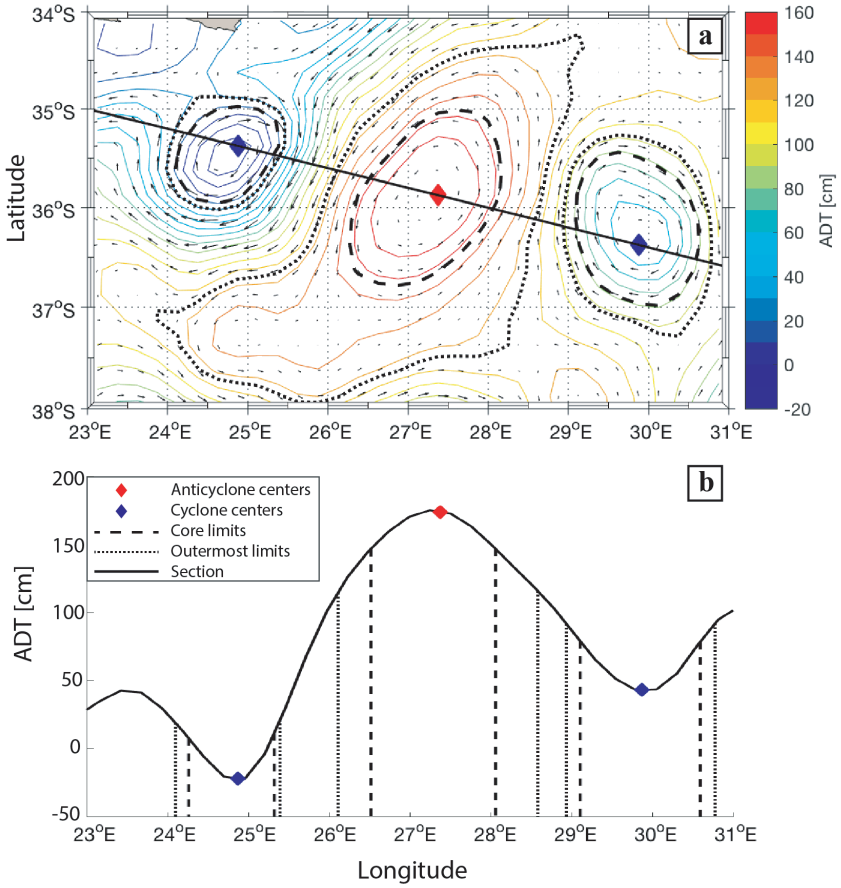


Figure 3.2: Example of eddies detected near the Agulhas Current on 23 March 2000. Two cyclones and one anticyclone are shown in a) an ADT map and b) in terms of ADT amplitude along a section crossing the extrema of the eddies detected in (a). For each eddy, the ADT contours where the azimuthal speed is maximum (eddy core limit definition - dashed lines) and the outermost closed contour (eddy outer limit definition - dotted line) are shown. ADT isolines with 10 cm intervals and the geostrophic velocity vectors distributed by AVISO are superimposed in (a).

eddy trajectories is recovered by following the paths of the eddies between successive ADT maps. Taking advantage of daily AVISO fields the method relies on the fact that mesoscale eddies move slowly (displacements of less than 10 km/day, see also Chelton et al. [2011]) relative to their radii that typically extend from 20 to 200 km [Carton 2001]. This ensures that the areas covered by the same eddy for two consecutive days overlap. This overlap can be used to track eddies [Pegliasco et al. 2015]. We use the characteristic contour (R_{Vmax}), less distorted than the outermost contour, to define the surface of the eddy core. However, in sporadic cases, the eddy surfaces defined by R_{Vmax} for two consecutive days do not overlap. Hence, we set the method to check in parallel the overlap of the eddy surface defined by the outermost contour. To avoid false eddy associations, a minimum percentage of overlap is required when considering this larger eddy surface. This overlap threshold, which is calculated as the ratio of the overlap area to the area of the smaller of

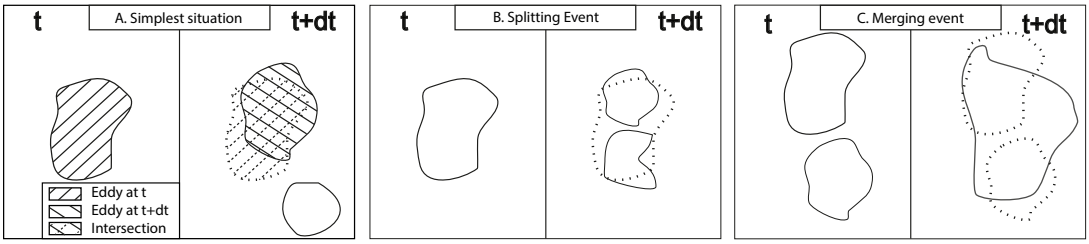


Figure 3.3: Schematic diagram of the eddy tracking step of the algorithm. a) Simplest situation where a single eddy is identified at the two different time intervals, t and $t + dt$. The area of the two eddy occurrences and their overlapping surface are shown, the latter in the form of a hatched surface. b) Splitting event. c) Merging event. Although the overlap threshold is applied in b) and c), these areas have not been represented to ensure readability of the figures.

the two eddies, provides robust eddy tracking (Figure 3.3a). Indeed, assuming a small circular eddy with a radius of 20 km moving at a speed of 10 km/day, 73% of its surface will overlap for two days. Therefore, the threshold should be less than 70%. Unfortunately, due to the small number of long life trajectories identified from drifting buoys (see Section 3.2.3), this parameter could not be tested quantitatively. Instead, qualitative trajectory inspections using different percentages of the overlap threshold (0, 25 and 50%) were undertaken. Due to the need for confidence in the method and the fact that comparisons between drifting buoys and eddy trajectories derived from altimetry showed suspicious trajectories using small overlap threshold values, the value of 50% was chosen. As some authors have already documented [e.g., Chaigneau et al. 2008; Chelton et al. 2011; Faghmous et al. 2015; Le Vu et al. 2018], eddies can disappear from altimetry maps for several days as a consequence of the heterogeneous distribution of the altimetry tracks. To take into account this possible lack of detection, an eddy, which has no parents in the previous time step or children in the following time step, is allowed to continue to exist if its disappearance does not last more than 5 consecutive days.

Nonlinear interactions between distinct eddies or between eddies and topography are some of the processes that can induce the splitting or merging of eddies. These processes have been theoretically supported [e.g., Melander et al. 1988; Simmons and Nof 2000; Drijfhout 2003] and observed [e.g., Cresswell 1982; Schultz Tokos et al. 1994; Isoda 1994; Sangrà et al. 2005]. The TOEddies algorithm belongs to the very few eddy detection and tracking algorithms [Yi et al. 2014; Matsuoka et al. 2016; Qiu-Yang et al. 2016; Le Vu et al. 2018] that consider both processes. It combines the separation of a large eddy with two or more smaller eddies in the case of splitting (see Figure 3.3b), and relates the coalescence of two or more small eddies into a larger eddy in the case of merging (see Figure 3.3c).

To take these processes into account, a relationship tree is created associating each eddy with its potential parents and children. Independent eddy trajectory segments are constructed by scanning this tree. These segments are trajectories

that link the eddy positions between the merging and splitting events. Therefore, each segment begins either after the detection of a new eddy, or after the merging of two eddies or the splitting of an eddy into two or more smaller eddies, and ends the time step before a new eddy-eddy interaction or when the eddy disappears from the altimetry maps.

The next step is to combine these segments to reconstruct the main eddy trajectories. To do this, the method first evaluates the overlap of the eddy surfaces associated with the characteristic contours (A_{Vmax}). In many cases, only two segments can be associated. From their assembling a main eddy trajectory is defined. In the next step, the method searches for overlapping eddy surfaces associated with R_{out}. This step is used to define trajectories that split from or merge with the eddy main trajectory. During eddy merging and splitting events, an eddy defined by the surfaces associated with R_{Vmax} can be associated with more than one segment. In these cases, we use a cost function to identify the main eddy trajectories. Using a cost function to define eddy trajectories is a relatively standard approach [e.g. Penven et al. 2005; Chaigneau et al. 2008; 2009; Frenger et al. 2015; Le Vu et al. 2018]. The cost function we defined (equation 3.3) takes into account the distance between the successive eddies and the change in eddy core surface properties (i.e., within the R_{Vmax} limit). Independent segments that minimize the cost function are linked together. The resulting long series of segments is identified as the main eddy trajectory. The remaining trajectories are classified as the result of an eddy splitting from the main trajectory or an eddy merging with the main trajectory.

$$CF = \sqrt{\left(\frac{\Delta Center - \overline{\Delta Center}}{\sigma_{\Delta Center}}\right)^2 + \left(\frac{\Delta Ro - \overline{\Delta Ro}}{\sigma_{\Delta Ro}}\right)^2 + \left(\frac{\Delta R_{Vmax} - \overline{\Delta R_{Vmax}}}{\sigma_{\Delta R_{Vmax}}}\right)^2} \tag{3.3}$$

The cost function we used (called CF in the following) is presented in equation 3.3 where, for a difference $\Delta\alpha$ of the generic variable α between two independent segments, $\overline{\Delta\alpha}$ and $\sigma_{\Delta\alpha}$ denote, respectively, the mean and the standard deviation of the differences. They are calculated between all pairs of a parent eddy associated with a single child eddy. The variables we used in defining the cost function are based on the work of Le Vu et al. [2018]. In addition, we prescribed the mean and the standard deviation estimates of the variables used in the cost function following Pegliasco et al. [2015] to ensure similar ranges of variation for every variable to assign them the same weight.

In order to reduce the effect of spurious variations in the gridded ADT product, the values used in CF are averaged over the last or the first seven days of each independent segment in the case of eddy merging and splitting, respectively. In this way, the CF can, for example, identify two trajectories that merge for only few time steps before splitting again. In this case, this event is identified as an interaction instead of a real merging followed by a splitting. This is close to the

neutral interactions presented in Le Vu et al. [2018] with an interaction period set at 5 days. To limit the number of short life segments that connect the trajectories or increase the number of eddy-eddy interactions, each independent segment must last more than 4 weeks to be taken into account. This ensures that the segments of a trajectory are consistent over a relatively long period of time.

Taking into account eddy merging and splitting, the meaning of an eddy trajectory radically changes the traditional view of mesoscale eddies moving as isolated and coherent structures from their formation zone to their dissipation zone. This is why we propose here to characterize the evolution of these structures not in terms of eddies, but by a network of trajectories. Such a network is composed of several branches identified as independent segments that begin either with a merging or splitting event or with the formation of a new structure, and end with another merging or splitting event or with the disappearance of the structure in the altimetry maps.

To match the in situ observation of isolated eddies with the associated trajectory network, we propose assigning an order to each segment of a main trajectory as shown in Figure 3.4. In this formalism, the "order 0" of the trajectory network is the main trajectory identified by applying the CF for each occurrence of merging and splitting. With "order 1", we assign segments that are linked to the main trajectory either by an eddy splitting or an eddy merging. Similarly, the "order 2" refers to segments that are associated with eddy merging or splitting with "order 1" trajectories, etc. This recursive classification in ordered trajectories continues until no new orders are detected. Each network is therefore associated with an order n of trajectories. The "order 0" of each network of trajectories is defined according to the target of the study as, for example, the assessment of the origin and fate of a mesoscale eddy identified by in situ observations or a global view of mesoscale eddies formed in a particular region of the ocean, such as the Agulhas Rings.

The AVISO+ Mesoscale Eddy Trajectory Atlas

Chelton et al. [2011] is the most publicly available atlas cited for mesoscale eddies automatically defined from satellite altimetry data. A new version of this algorithm has been implemented by Schlax and Chelton [2016] which is used by SSALTO/DUACS to produce the Mesoscale Eddy Trajectory Atlas (hereafter META2017) [Duacs/AVISO+ 2017] distributed by AVISO+ (`https://www.aviso.altimetry.fr/`) with support from CNES, in collaboration with Oregon State University with support from NASA.

The META2017 detection method is based on the geographical properties of the "two-sat-merged" SLA maps after application of a spatial high-pass filter. The META2017 algorithm identifies anticyclonic (cyclonic) eddies by locating the pixel at a local maximum (minimum) of SLA and successively finding all neighboring pixels with SLA values above (below) a sequence of decreasing (increasing) thresholds

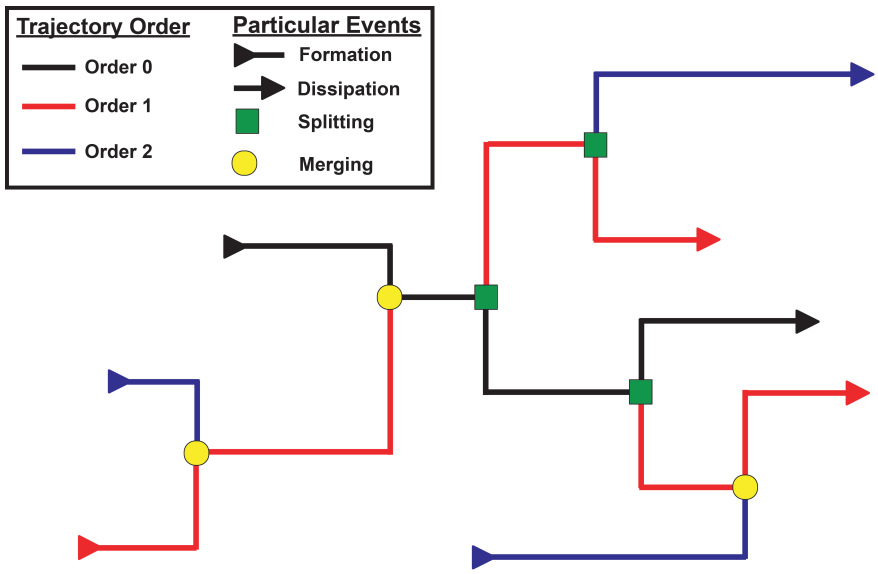


Figure 3.4: Schematic of a simple network of trajectories up to order 2. This network is characterized by 4 formations, 4 disappearances, and 3 merging and splitting events. With each merging and splitting, the cost function is applied to follow the main trajectory by associating a segment with a higher order.

following the "growing method" of Williams et al. [2011]. This "growth" of the eddy structure continues until one of the five criteria defining a compact and coherent structure is violated. The five criteria used are chosen to generate eddies statistically similar to those obtained by Chelton et al. [2011]. Eddies with an amplitude of less than 1 cm are not included in META2017. This algorithm is described in detail in Schlax and Chelton [2016] and the eddy atlas in Duacs/AVISO+ [2017].

One of the main differences between TOEddies and META2017 algorithms is the eddy tracking step. META2017 applies a cost function to the eddies in the successive maps in an elliptical search area whose size depends on latitude. TOEddies, instead, requires eddy areas to overlap. The META2017 cost function compares the amplitude and position of the identified eddies with those of the next time step. It then selects only one structure to define the trajectory of the eddy. It therefore does not take into account eddy merging nor eddy splitting processes. In META2017, only eddies of at least 4 weeks are documented.

"Loopers" recovered from Surface Drifters

The robustness of the method and the related parameter choices were evaluated by comparing our results with independent in situ data. To do this, we used the eddies identified by Lumpkin [2016] (hereafter LU16) from the Global Drifter Program quality-controlled surface drifters data [Lumpkin and Pazos 2007] over the world ocean from February 1979 to July 2017 (`https://www.aoml.noaa.gov/phod/loopers/index.php`). In LU16, the eddies are automatically identified as

"looping" trajectories of drifters buoys reconstructed from the 4 positions they send each day. To do this, the methodology initially introduced by Veneziani et al. [2004] and developed by Griffa et al. [2008] and LU16 is used. In this method, the spin Ω of each trajectory that can be related to the vorticity of the Eulerian fluid field for a particle following the rotation of a solid body [Veneziani et al. 2004] is computed at each position. Using the properties of circular motion, we can estimate both the period and radius of these loop trajectories. We refer to LU16 for a complete description of the method.

It should be noted here that LU16 underestimates the total number of eddies because it only accounts for eddies captured by the small number of drifting buoys deployed in the ocean. In addition, LU16 estimates only the radius of the loops of each drifter, which may be different (essentially smaller) than the actual radius of the eddy sampled. Indeed, it has been shown by Chaigneau and Pizarro [2005], by comparing the eddies detected from altimetry with drifting buoys, and by Pegliasco et al. [2015], with Lagrangian profiling floats that, on average, these instruments sample the eddy at 2/3 of the R_{out} which corresponds to a random sampling of a disk with a radius equal to R_{out}. Therefore, to avoid erroneous comparisons of eddy radii, only LU16 eddy center positions are used. We followed LU16 to evaluate such a center: it is defined as the mean center position of the buoy's looping trajectory during a rotation period. The instantaneous radius of each eddy detected by LU16 is computed as the distance between the estimated position of the eddy center and the position of the drifter along its loop.

3.2.3 Validation and Comparison of Eddies Datasets

The Validation Approach

For validation purposes, a daily collocation was performed between the five eddy datasets listed in Table 3.1 in the South Atlantic - Southeast Indian geographical domain [70°W-65°E; 55°S-15°S] during the period 1 January 1993 to 31 December 2016. Only LU16 eddies whose center is at least 5° away from the limits of the geographical domain are taken into account. Indeed, eddies close to the limits of the domain may not be detected by TOEddies. In what follows, LU16 will be the reference dataset. Within this framework, only the trajectories of drogued surface drifters for which a position of an eddy center could be estimated and whose radius is less than 300 km are chosen, which constitutes a reasonable upper limit for mesoscale ocean eddies [Carton 2001].

This selection results in 38503 anticyclonic and 40251 cyclonic eddy centers identified by LU16 in the study area. Only surface drifters trapped in a structure for more than a week are used here for the validation of eddy trajectories. Only 431 anticyclonic and 414 cyclonic LU16 trajectories last more than seven weeks in the region. This number is relatively small because we only took into account LU16

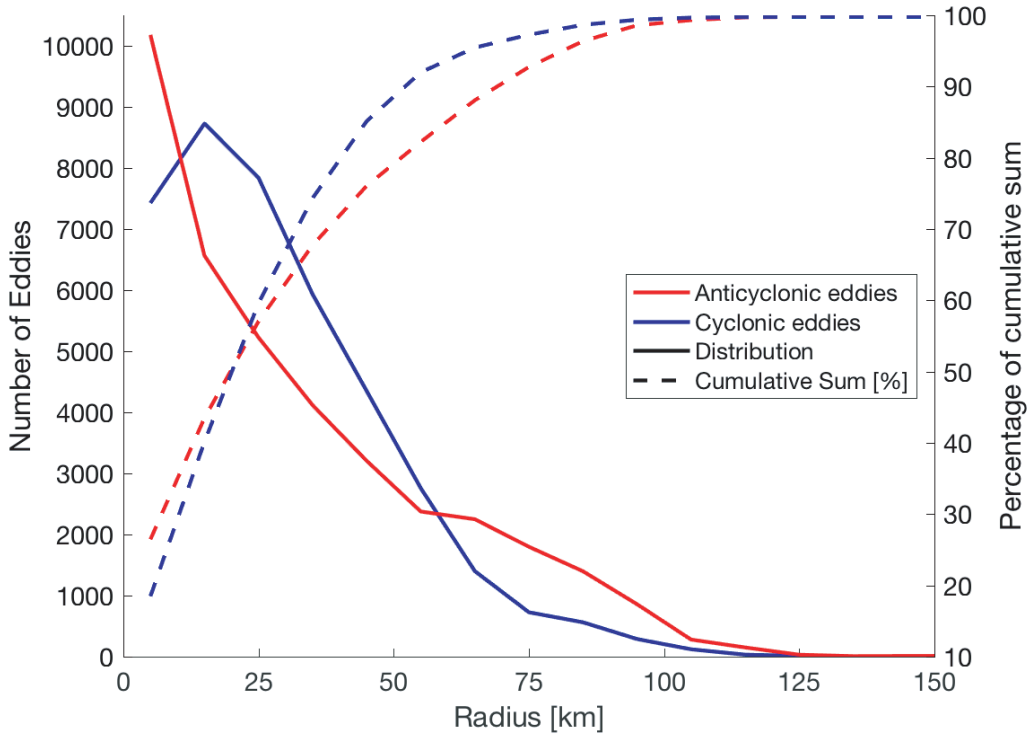


Figure 3.5: Number of eddies (on the ordinate) identified from surface drifting buoys by Lumpkin [2016] and used to validate the robustness of the eddies identified by the TOEddies algorithm shown as function of their radii (on the abscissa). The radii are sampled every 10 km. These numbers are computed separately for anticyclonic and cyclonic eddies.

loopers associated with radii less than 300 km. Therefore, the LU16 trajectories used in this study are shorter than originally estimated.

In Figure 3.5 the number of LU16 eddies available for cross detection are plotted according to their radii that we recalculated. The resulting LU16 mean radii are between 0 and 10 km for anticyclones and between 10 and 20 km for cyclones. The number of eddies in each size interval decreases as the size of the structure increases. The median is about 25 km for both types of eddies. 90% of cyclones have a radius less than 56 km and 90% of anticyclones have a radius less than 74 km. Fewer than 1% of cyclones and 2% of anticyclones have a radius greater than 100 km.

As mentioned earlier, the estimated radii of the LU16 loopers cannot be an estimate of the true size of mesoscale eddies, as surface drifters loop along circles that are smaller than the eddy cores. However, they can be used to define a minimal size for mesoscale eddies. Half of the LU16 distributions have radii greater than 25 km, which corresponds approximately to the pixel size of 1/4° horizontal resolution in altimetry gridded products. It is therefore reasonable to use LU16 loopers to validate the eddies detected in the altimetry fields. Since only a small fraction of the LU16 eddies have a radius greater than 100 km, we have set the maximum radius to be taken into account at this value.

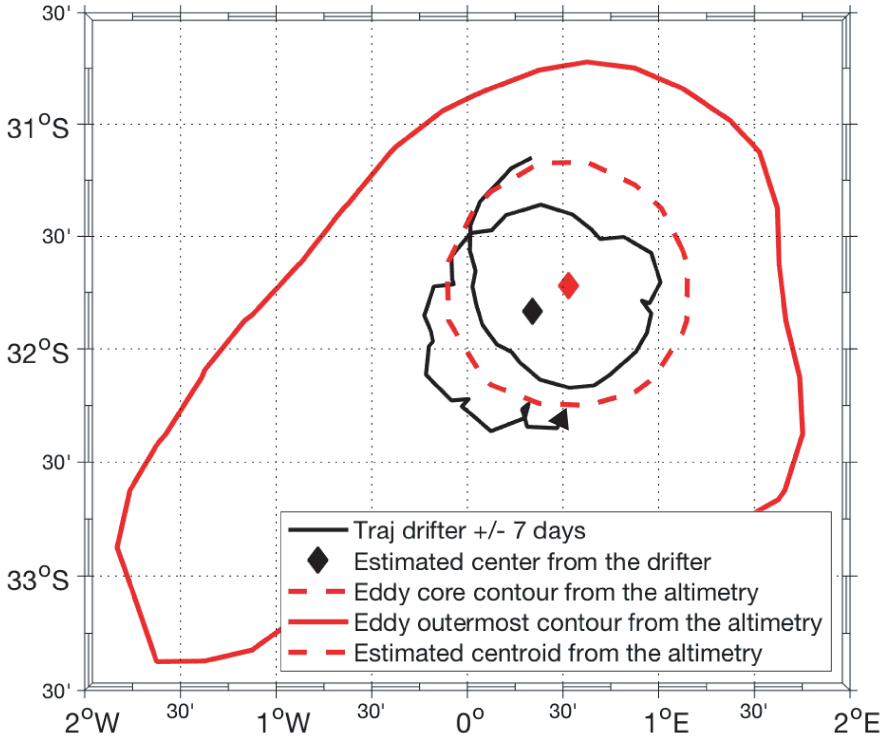


Figure 3.6: Example of cross-detection of eddies for 12 December 2012 where an eddy identified from a surface drifter trajectory by LU16 (in black with a diamond symbol locating its center) and an anticyclone detected in the TOEddies Atlas (red contours for its outer limit and its maximum speed core) overlap.

For validation, we consider that two eddies are co-located (i.e, a valid cross-detection) if the center of a LU16 eddy falls in the area occupied by an eddy of the same sign detected by one of the altimetry-based algorithms. An example of this matching is shown in Figure 3.6. For datasets that do not explicitly provide the eddy contour (e.g., META2017), a correspondence exists if the center of one LU16 eddy and the center of one eddy in the other dataset is within a distance smaller than the eddy radius defined in such dataset.

We implemented the collocation with LU16 loopers to the datasets listed in Table 3.1. The first four datasets correspond to the TOEddies detection algorithm applied to the two different altimetry maps (SLA and ADT) and parameter thresholds. The first three letters of these datasets indicate the type of map used as input. Moreover, while in TOEddies we apply a 4-week threshold on the life of eddy segments that filters out segments associated with short-lived eddies, the suffix "_raw" is added when this filtering is not applied. The suffix "_rad" refers to the results of LU16-TOEddies collocation performed in the same manner as LU16-META2017, i.e. using the eddy radius instead of the eddy area criterion.

Table 3.1: Parameters of the six data sets tested against the independent LU16 eddy atlas derived from surface drifter buoys. Each row corresponds to a different dataset for which the version and the type of satellite altimetry maps used for the detection is specified. The suffix "_raw" is added when the 4-week threshold on lifetime eddy segments is not applied. The suffix "_rad" refers to the results of the LU16-TOEddies collocation performed using the eddy radius instead of the eddy area criterion. N/A (not applicable) is added when a parameter is not relevant for a dataset.

Dataset Name	Persistence or Minimum Amplitude [mm]	Minimum surface [%]	Lifetime [week]
SLA_raw	1	N/A	N/A
ADT_raw	1	N/A	N/A
TOEddies	1	50	4
TOEddies_rad	1	50	4
META2017	10	N/A	4

Validation of the Eddy Detection and Tracking Algorithms

In the following we summarize the main results of the cross-validation between LU16 and the different eddy satellite altimetry databases listed in Table 3.1, as well as the different threshold parameters and a thorough comparison with the META2017 atlas. Details of validation and comparisons are discussed in the Appendix B.

All datasets tested (Table 3.1) show both, a decrease in error and an increase in detection efficiency for LU16 eddies with large radii (see Table 3.2. This is most likely due both to the limited spatial resolution of satellite altimetry and its limited ability to capture small structures [e.g. Chelton et al. 2011] but also to the lower probability that drifting buoys are captured in small eddies rather than in large eddies. However, it should also be noted that LU16 eddy radii may provide an underestimate of the actual size of structures. Indeed, drifting buoys are drawn by the movement of the upper ocean at different distances from the center of the eddy and they do not necessarily move along the outer eddy edge of the eddy or along its maximum velocity. Indeed, it has been shown that drifters sample randomly eddy structures Chaigneau and Pizarro [2005].

Test results show that the TOEddies algorithm detects significantly fewer structures when applied to ADT maps than SLA maps. Consequently, the total area occupied by the eddies identified on ADT maps is 30 to 50% less than on SLA maps. Compared to LU16, the TOEddies identification of anticyclones on the ADT maps shows better skill, especially when eddies are identified by the maximum velocity contour. Conversely, cyclones are better identified from SLA maps. However, the fact that the number of eddies detected in ADT maps is significantly lower than that in SLA maps convinced us to use the former. We also noted that detection efficiency increases significantly when eddies are defined by their actual contours instead of assuming circular eddies with assigned equivalent

Table 3.2: Detection and collocation matching statistics with LU16 eddies. "max" refers to the eddy contours associated with their maximum speed while "out" refers to their outer contours. The percentages indicate the proportions of eddies by polarity as defined in LU16. Anti and Cyclo mean, respectively, anticyclones and cyclones. N/A (not applicable) is added when a parameter is not relevant for a dataset.

Dataset	Number Eddies anti / cyclo [10^6]	Sum A_{max} anti / cyclo [10^{10} km^2]	Sum A_{out} anti / cyclo [10^{10} km^2]	Match Anti max / out [%]	Mismatch Anti max / out [%]	Match Cyclo max / out [%]	Mismatch Cyclo max / out [%]
SLA_raw	4.3 / 4.5	4.3 / 4.2	7.7 / 7.6	62 / 69	2 / 4	72 / 78	1 / 2
ADT_raw	3.2 / 3.3	3.2 / 2.8	5.2 / 4.6	66 / 71	2 / 3	71 / 75	1 / 2
TOEddies	2.4 / 2.5	2.8 / 2.5	4.7 / 4.2	63 / 67	2 / 3	65 / 69	1 / 2
TOEddies_rad	2.4 / 2.5	2.8 / 2.5	4.7 / 4.2	60 / 63	1 / 3	64 / 65	1 / 4
META2017	1.8 / 1.8	4.1 / 4.1	N/A / N/A	50 / N/A	3 / N/A	53 / N/A	3 / N/A

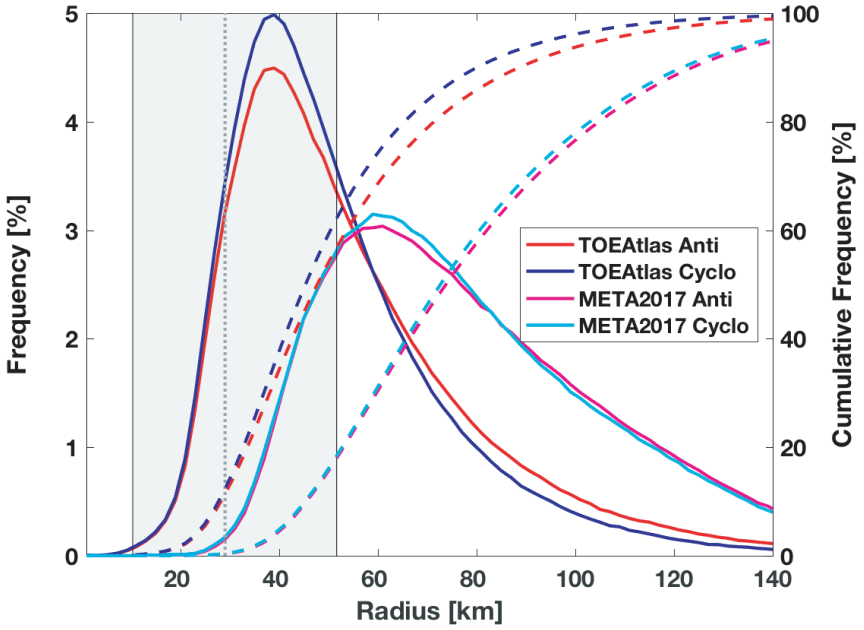


Figure 3.7: Histograms (solid lines) and cumulative frequency (dashed lines) of the eddy R_{max} for TOEddies (red and blue lines) and META2017 (pink and light blue lines) computed over 2-km intervals. The vertical dotted line is the mean first baroclonic Rossby radius (L_R) of deformation in the area and the grey dashed area limits the 10 and 90 percentiles. The baroclonic Rossby radius of deformation is computed by applying the Chelton et al. [1998] method on the World Ocean Database [Boyer et al. 2013] averaged over seven years (i.e. 2005 to 2012).

radii.

The comparison of TOEddies with META2017 shows that the former has better skill in both stages, eddy detection and eddy tracking. TOEddies detects more eddies, and their size is smaller than those detected by META2017 (Figure 3.7). It also shows particularly good performance in identifying large structures (with a radius greater than 40 km). Figure 3.8 shows that for a 25 km radius (which represents the average radius of the LU16 loopers, Figure 3.5, and the average grid size of the altimetry maps) more than 65% of the eddies are identified by TOEddies whereas they represent only 48% (52%) for the anticyclones (cyclones) in META2017. Finally, 50% of the TOEddies trajectories correspond to those of LU16. Therefore, the results of the validation and skill assessment of TOEddies against another eddy detection method or independent data give us confidence in our algorithm in the study area. To be noted that TOEddies eddies are close in size to the regional first baroclinic Rossby Radius of deformation (Figure 3.7).

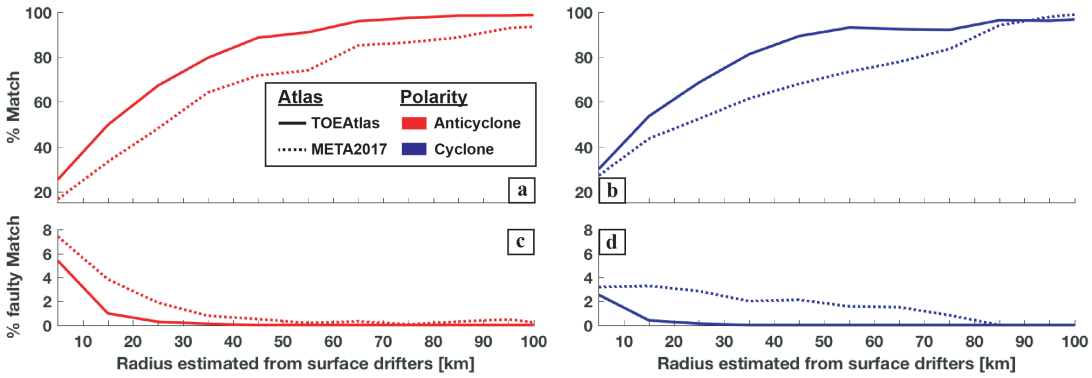


Figure 3.8: Percentage of matching of LU16 eddies with TOEddies (solid lines) and META2017 (dashed lines) eddies as a function of LU16 eddy size. Values are expressed as a percentage of LU16 eddies collocated at 10 km intervals. We consider that eddies match if their polarity in LU16 and in the atlases based on altimetry is the same. When the polarities of the collocalised eddies differ, this is counted as a mismatch. Anticyclones are in red, cyclones are in blue.

3.2.4 Results of the TOEddies method applied to Agulhas Rings

Identification of Agulhas Rings and distribution of the associated trajectories

TOEddies has identified, overall, more than 3 million eddies in the daily ADT maps in the selected Indo-Atlantic domain and for the given time period (>24 years). This corresponds to 120 000 anticyclonic trajectory segments identified from the full tree of segments, using the cost function. These figures are reduced to 2.5 million eddies and 30 000 segments after application of the minimum 4-week lifetime threshold. Among these eddies and segments, the Agulhas Rings (hereafter referred to as AR) are defined as anticyclonic eddies initially detected in the Indian Ocean sector of the domain, and entering the Atlantic Ocean by crossing an imaginary line connecting specific topographic structures (the Protea, Simpson, Wyandot, Schmit-Ott seamounts and the Agulhas Ridge) that define the southeastern limit of the Cape Basin, southwest of Africa. This line (marked with the letter "C" in Figure 3.10a) extends from the southern tip of Africa (Cape Agulhas, 35°S and 20°E) to 45°S and 5°E at the southern limit of the Agulhas Ridge in the Southern Ocean. This definition of AR assumes that it is possible to track these eddies and their origin and fate in order to identify them carefully. This identification is carried out for the entire ADT time series. However, in this work, we focus only on AR properties during the period January 1, 2000 to December 31, 2016 to ensure that all AR detected during this period can be tracked back to their origins. Indeed, as we will see later in this section, AR have a particular long life span and can take years to cross the Indo-Atlantic domain.

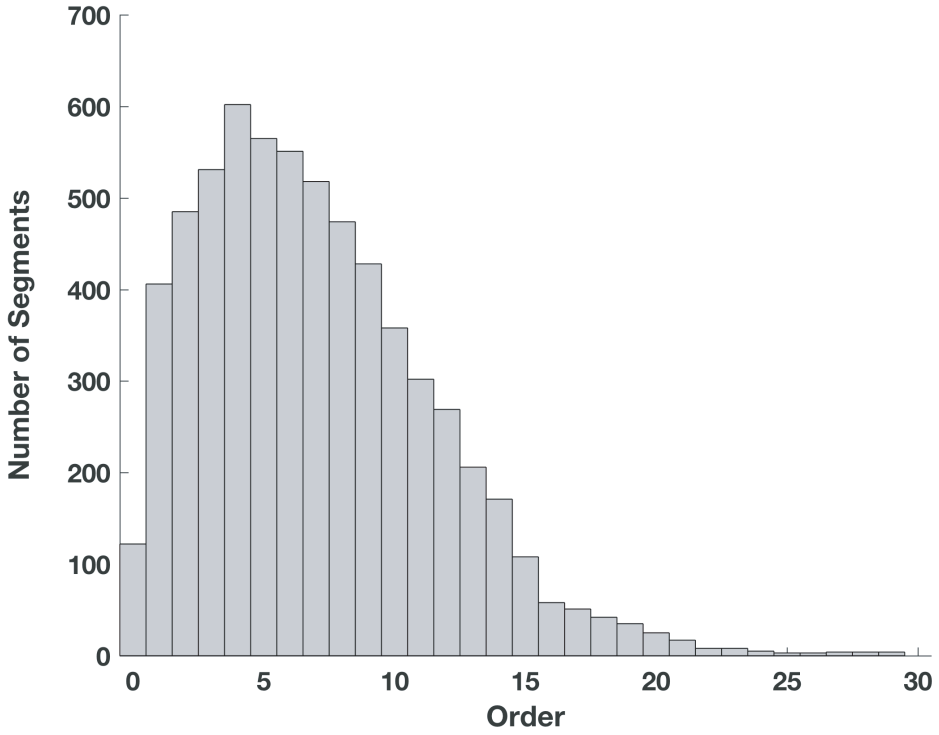


Figure 3.9: Number of trajectories according to their order associated with Agulhas Rings.

In what follows, to describe eddy trajectories that include eddy merging and splitting, the concept of "segment network" and "main trajectories" introduced in Section 3.2.2 are used. 32 080 anticyclonic eddies that cluster in 122 "main trajectories" (i.e., "order 0" trajectories) are identified as AR entering the South Atlantic from the Indian Ocean. It is then possible to recover the entire network of segments associated with these "main trajectories" by identifying higher order trajectories that are linked to the main trajectories by additional merging and splitting events. The total AR network consists of secondary trajectories up to order 29, combining a total of 730 481 anticyclonic eddies and 6 363 segments.

The distribution of AR trajectories according to their order is shown in Figure 3.9. The distribution is characterized by an increase in the number of segments as a function of trajectory order, from order 0 to the peak corresponding to order 4. Then, the number of new higher order trajectories associated with AR reduces gradually. The median order of the AR trajectories is 6.

The whole set of AR trajectories (from order 0 to order 29) is presented in Figure 3.10a while Figure 3.10b shows the percentage of time during which each 2°x2° grid cell is inside an anticyclonic eddy connected to the AR trajectory network. The corresponding Figures for order 0, 1 to 4, 5 to 10, 11 to 20 and 21 to 29 are provided in Figures C.1 to C.5 in the appendices C as well as that of the 19 302 trajectories (1 397 533 eddies) that do not interact with the AR network in the

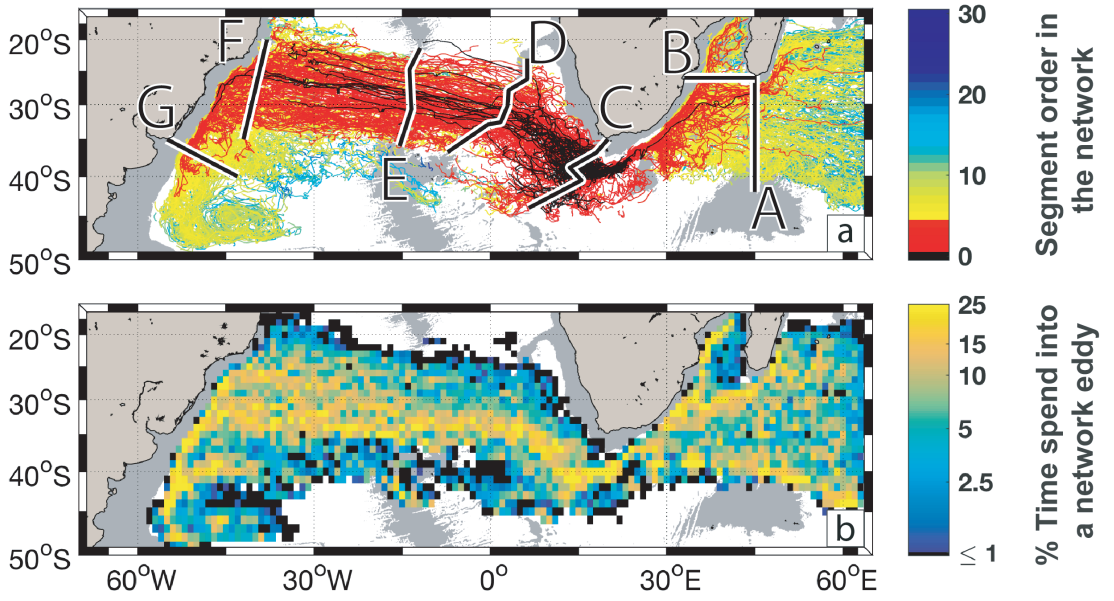


Figure 3.10: a) Whole set of Agulhas Ring Eddy Network (AREN) trajectories (from order 0 to maximum order 27). The color of the trajectories is related to their order. The black color is for order 0, which we defined as the main trajectories for the Agulhas Rings. 7 sections [A-G] were used to derive the AR properties across the basins. b) percentage of time each 2°x2° grid cell is within an AREN trajectory. The gray shading in each figure represents water depths less than 3500 m in the ETOPO2 data set [Smith and Sandwell 1997].

Figure C.6. In the following, we will refer to the eddies of the AR network as the AR Eddy Network (AREN), which clusters the main AR trajectories (i.e., order 0) and all the additional eddies associated with them via eddy merging and splitting until the maximum order found (29).

Figure 3.10a shows how TOEddies provides a very different overview of the origins, pathways and fate of AR. Indeed, although the "main" AR trajectories (in black in Figure 3.10a and in the appendices Figure C.1) are relatively similar to the results of the published studies [e.g., Dencausse et al. 2010a; Chelton et al. 2011; Souza et al. 2011b], most of them are lost in the Cape Basin or associated with other higher order trajectories. However, those crossing the South Atlantic basin may be directly related to AR and their region of formation, whereas in previous studies [e.g., Byrne et al. 1995; Arhan et al. 1999; Souza et al. 2011a] this connection could not be made via an objective tracking algorithm because the first detections were found mostly in the Cape Basin, far downstream from the Agulhas Retroflection. This is due to the strength of the TOEddies algorithm, which allows eddies to merge and split and to soundly connect a more complex eddy structure into a "main" trajectory instead of dealing only with single and well-separated eddies. In addition, the complete set of AREN trajectories (Figure 3.10a) shows a much richer diversity in terms of origins and fate of AR, and this for AREN

trajectories of order 4 or even less (red trajectories in the Figure). The resulting AREN trajectories suggest that the eddies contributing to the formation of AR may originate from the southwestern tropical Indian Ocean, further upstream than the Agulhas Retroflection. Figure 3.10a shows that one AR main trajectory connects directly to the area south of Madagascar. Moreover, AREN trajectories reach regions further downstream than the Cape Basin or the Mid-Atlantic Ridge in the South Atlantic. Indeed, AREN trajectories of orders 1-4 reach the southern end of the South Brazil Current. In particular two AREN trajectories of order 0 veer south along the South American slope. Furthermore, AREN trajectories of higher order penetrate the Zapiola gyre. The AR trajectories estimated by TOEddies show a clear eddy pathway linking the western boundaries currents of the Indian and Atlantic oceans.

The main routes undertaken by AREN trajectories are clearly shown in Figure 3.10b. Three main routes associate Indian Ocean anticyclones to AR: one follows the western boundary slope in the Mozambique Channel, another the slope at the southeastern tip of Madagascar, and the third follows the Agulhas Return Current. The first two seem to merge north of the Agulhas Plateau, around 32°S and 25°E, where the Agulhas Current and the Agulhas Return Current flow in a very narrow corridor between the African slope and this plateau. West of the Agulhas Retroflection (i.e., west of line C in Figure 3.10a), the AREN trajectories follow, in the Cape Basin, a broad northwesterly route toward a more zonal direction (along the 35°S parallel) once the eddies leave this basin and enter the South Atlantic. At the Mid-Atlantic Ridge, the AREN main path widens until reaching the South American slope between 25°S and 35°S. This wide route in the western part of the South Atlantic seems to consist essentially of trajectories from order 0 to order 4 (Figures 3.10a, C.1 and C.2). Once they reach the South American boundary, most eddies head south with the South Brazil Current. However, some trajectories turn north along the western boundary and cross the Cruzeiro do Sul and Vitoria Trinidade seamounts.

Characteristics of the Agulhas Rings network of trajectories

Although satellite altimetry gives access to ADT 2D time series, it does not directly infer the 3D properties of eddies. However, altimetry provides sufficient information to characterize the kinematic and dynamical behavior of eddies, at least in their surface expression and as long as the eddies are detectable from the satellite field. In particular, the TOEddies method gives access to information on horizontal eddy extent (R_{out} and R_{Vmax}), amplitude, azimuthal velocity and propagation speed. The geographical distribution of the median of these properties is presented in Figures 3.11 and 3.12. More precise estimates of these variables are provided in Table 3.3 at fixed locations. Eddy merging and splitting lead to complex trajectories that can be independent for short periods of time. This highly complicates the description of eddies and their fate in terms of classical eddy trajectories. Indeed, an AR can be associated with many different trajectories because, during its lifetime,

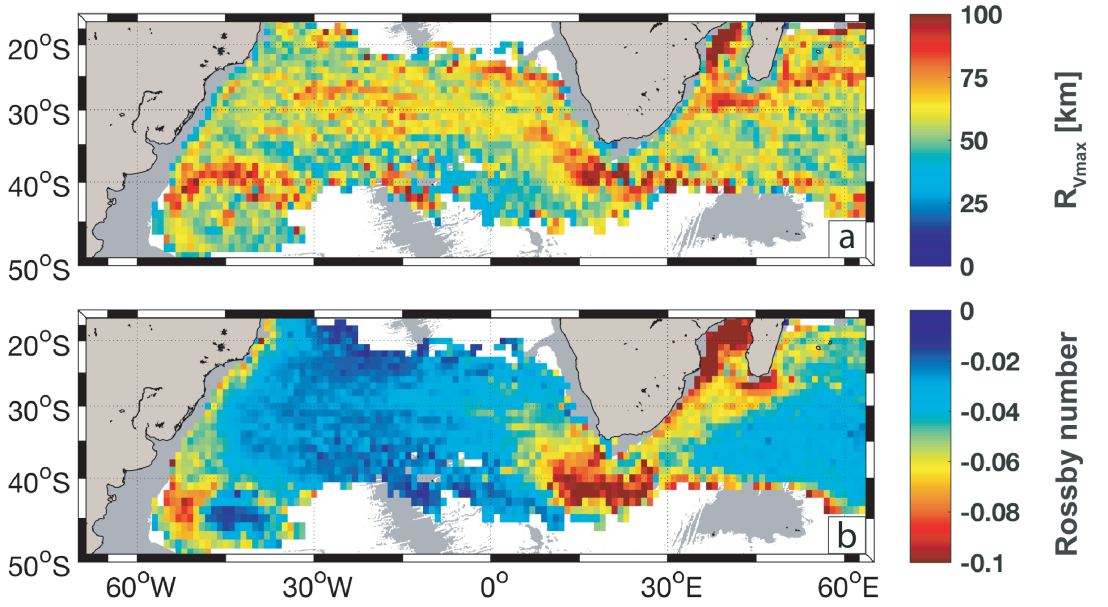


Figure 3.11: a) Median of Rossby number (Ro) and of the b) Equivalent radius of the characteristic contour (R_{Vmax}) of the Agulhas Ring Eddies Network. These properties are computed on a 2°x2° grid. The gray shading in each figure represents water depth shallower than 3500 m in the ETOPO2 data set [Smith and Sandwell 1997].

it splits in small eddies and eventually merges with other eddies (which can be either AR or anticyclones of different origins). Therefore, we decided to describe the fate of AR by counting the AREN trajectories only when they cross particular sections (lines [A-G] in Figure 3.10a). In Table 3.3 the characteristics of the AREN trajectories across the basin are summarized (in terms of the median and standard deviation of various properties calculated for the geographical lines A to G in Figure 3.10a). The contributions of the five groups of different AREN trajectory orders (0, 1-4, 5-11, 12-20, and 21-29) to the total number of AREN trajectories crossing the control sections are presented as a percentage in Table 3.4.

The number of segments entering the Cape Basin since 2000 is 119. This number of segments varies across the domain due to the numerous eddy-eddy interactions and the disappearance of eddies from altimetry maps. The AREN median radii, R_{out} and R_{Vmax}, are relatively constant throughout the domain (see Table 3.3 and Figure 3.11a). The median (± one standard deviation) R_{out} and R_{Vmax} are 79 km (± 38 km) and 59 km (± 29 km), respectively. The estimate of R_{Vmax} in the Cape Basin, where most AR are documented in the literature, ranges from 58 to 65 km which are values close to the lower limit of the 65-100 km range derived from in situ observations in the Cape Basin by Garzoli et al. [1999] and Arhan et al. [1999]. The median amplitude and the azimuthal speed of the AREN are maximum (21 cm and 47 cm/s respectively) when entering the Cape Basin. Since R_{Vmax} does not vary significantly across the entire domain (Figure 3.11a), the median of the eddy vortex Rossby Radius, Ro, (Figure 3.11b) provides an indirect measure of changes in eddy

azimuthal velocity. This velocity is highest in the Agulhas Current System and in the southern half of the Cape Basin and from there it decreases rapidly and remains constant across the South Atlantic Ocean. It is only when the AREN trajectories reach the South American boundary that Ro increases again, most likely due to the interactions of eddies with the South Brazil Current and local anticyclones.

In addition to the inherent properties of the AREN eddies it is interesting to evaluate their median propagation speed (Figure 3.12), as it can be used to estimate their transit time through the different zones. The regions where AREN eddies move faster correspond to the western boundary currents (WBCs) of the Indian Ocean but also of the South Atlantic (reaching speeds higher than 0.1 m/s). The AREN propagation speed remains high in the Cape Basin (although it is higher in the Southern than in the Northern Cape Basin) and in the South Atlantic, especially for the northern sector of the route, west of the Mid-Atlantic Ridge. The AREN direction of propagation (Figure 3.12b) clearly shows different regimes of fast southwestward flow in the WBCs, northwestward flow in the Cape Basin and westward flow in the South Atlantic. It also shows that the AREN path along the Agulhas Return Current involves eddies moving eastward. These eddies are most likely related to AR as a product of AR splitting in the Agulhas Retroflection area which are successively advected eastward in the intense Agulhas Return Current.

To better characterize the kinematics and dynamics of the AREN eddies, their median propagation velocity can be compared with the mean surface geostrophic velocity estimated from AVISO satellite altimetry (Figure 3.13). The AREN and AVISO estimates of velocity intensities compare relatively well in terms of propagation direction with the mean surface velocity in the WBCs and the Agulhas Return Current with, in general and, as expected, the AREN propagation speed being an order of magnitude less than the surface geostrophic velocity. Here, the eddies are advected with the mean current. However, differences between AVISO and AREN mean velocities occur in the northern subtropical South Atlantic where eddies appear to move westward at a higher velocity (about 6 cm/s) than the mean surface geostrophic velocity (about 2 to 4 cm/s), and in the southern subtropical Atlantic (south of 30°S) where they move westward against the mean surface current (which flows eastward as expected for the poleward branch of the South Atlantic gyre: see Figure 3.12, Figure 3.13, and Figure 3.1b). The ratio of the AREN translation speed and the mean geostrophic current are computed in each 2°x2° grid cell (Figure C.8 in the Appendices Information). It shows that AREN move faster than the mean surface gesotrophic current in 60% of these cells.

McDonagh et al. [1999] studied the mechanisms responsible for the translation of Agulhas Rings in the Cape Basin. They showed from two specific AR that the self-advection mechanism [Rhines 1975; Cushman-Roisin et al. 1990] is not sufficient and conclude that the main factor appears to be the advection by the main flow. These results are consistent with our findings that high AREN translation values are found where geostrophic surface velocities are also important. This is verified in the WBCs and in the Cape Basin. However, in the South Atlantic, AREN eddies

Table 3.3: Properties of the Agulhas Ring Eddy Network throughout the geographical domain. The values are computed at the lines [A-G] plotted in Figure 3.10a. For each variable, estimates of the median and standard deviation (STD) are provided.

Segment of control	Number of Segments	R_{out} [km] Median ± STD	Amplitude [m] Median ± STD	R_{Vmax} [km] Median ± STD	V_{max} [m/s] Median ± STD
A: SW Indian Ocean	191	78 ± 43	0.08 ± 0.11	60 ± 35	0.22 ± 0.16
B: Mozambique Channel	30	94 ± 38	0.13 ± 0.14	66 ± 29	0.40 ± 0.17
C: SE Cape Basin	119	81 ± 38	0.21 ± 0.21	65 ± 30	0.47 ± 0.23
D: Walvis Ridge	160	91 ± 39	0.08 ± 0.09	58 ± 22	0.18 ± 0.11
E: Mid-Atlantic Ridge	167	87 ± 42	0.05 ± 0.06	64 ± 27	0.12 ± 0.07
F: S. American Slope	217	74 ± 33	0.04 ± 0.03	57 ± 27	0.12 ± 0.04
G: S. Brazil Current	71	88 ± 41	0.13 ± 0.11	74 ± 37	0.29 ± 0.12

Table 3.4: Distribution of the orders of the Agulhas Ring Eddy Network expressed as percentage when they cross the lines [A-G] plotted in Figure 3.10a.

Segments of control	Order 0 [%]	Orders 1 to 4 [%]	Orders 5 to 10 [%]	Orders 11 to 20 [%]	Orders 21 to 29 [%]
A: South-west Indian Ocean	1	9	66	22	2
B: Mozambique Channel	0	27	60	13	0
C: Southeastern Cape Basin	100	0	0	0	0
D: Walvis Ridge	12	80	8	0	0
E: Mid-Atlantic Ridge	7	75	16	2	0
F: South American Slope	2	44	52	2	0
G: Southern Brazil Current	0	13	80	7	0

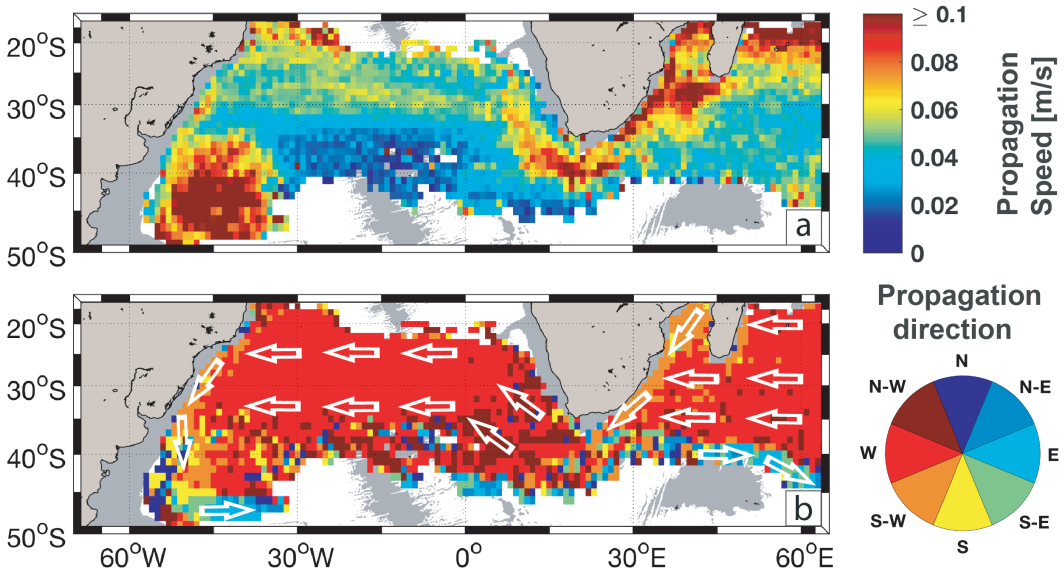


Figure 3.12: a) Median of the propagation velocity of the Agulhas Ring Eddy Network (in m/s) and b) associated main propagation direction. These properties are calculated on a 2°x2° grid and the propagation direction is computed from the eddy positions one week apart. Schematic white arrows have been added in the bottom panel to highlight the main propagation direction. The gray shading in each figure represents water depth shallower than 3500 m in the ETOPO2 data set [Smith and Sandwell 1997].

move faster, if not against the surface geostrophic flow. Here, most likely, the main mechanism of translation is the self-advection of eddies.

Agulhas Rings origins, disappearance, splitting and merging

To better describe the AREN, we discuss here the statistics in the regions where they are initially identified, where they disappear as well as the distribution of eddy merging and splitting events. The description of AR as anticyclonic eddies participating in the AREN may not be appropriate because they are associated with a large number of eddy merging and splitting events (i.e. high order trajectories). For this reason, we put a particular emphasis on estimates of AREN trajectories up to order 4, which correspond to the peak of the number of trajectories as a function of the trajectory order (Figure 3.9). In the following, we will call this subgroup of AREN, AREN4.

The distribution of eddy formation, disappearance, and merging and splitting within AREN4 is presented in Figure 3.14 and that of the total AREN in Figure 3.15. To better assess the regionalization of these processes, only the 2°x2° cells showing more than 5 (10) or 10 (10) first/last detections (merging/splitting) events for AREN4 and AREN, respectively, are presented. The difference in threshold used

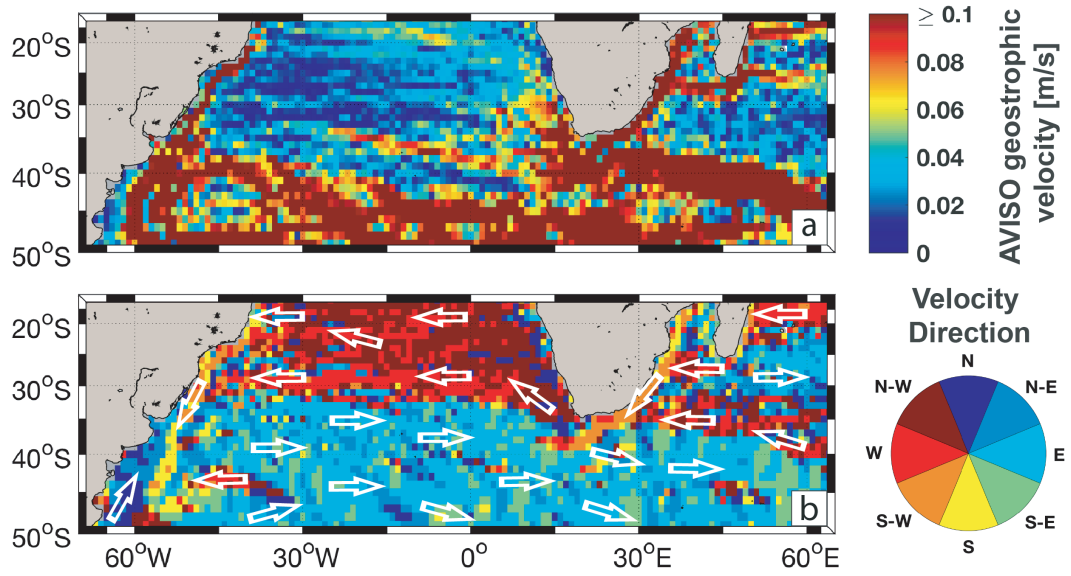


Figure 3.13: a) Mean surface geostrophic velocity estimated from AVISO satellite altimetry (in m/s) and b) associated main direction. These properties are computed on a 2°x2° grid. Schematic white arrows have been added in the bottom panel to highlight the main velocity direction. The gray shading in each figure represents water depth less than 3500 m in the ETOPO2 data set [Smith and Sandwell 1997].

for the two different types of events is explained by the fact that TOEddies records ~twice as many trajectory interactions as eddy formation or disappearance events. 119 AREN cross, flowing west, line C in Figure 3.10 (Table 3.3). This line defines the AR trajectories, which explains why only 0-order eddies enter the Cape Basin (Table 3.4). Most AR are initially identified at the Agulhas Retroflection as shown by the large red patches near the Cape Basin in Figure 3.14a and the starting points of the black and red trajectories in Figure 3.10a. This region extends over a large area, between the Agulhas Bank, the Agulhas Plateau and the Agulhas Ridge, and agrees with the entire Agulhas Retroflection position, from 8°E to 25°E-28°E [e.g., Lutjeharms and Ballegooyen 1988; Dencausse et al. 2010b].

In addition to this traditional view of AR shedding from the Agulhas Current at the Agulhas Retroflection, our method identifies anticyclonic eddies formed at the southern edge of the Agulhas Return Current as previously observed by Lutjeharms and Ballegooyen [1988] and Boebel et al. [2003b]. Indeed, some eddies can merge with or split from a newly shed AR, which is why we classify them as AREN. Many new AREN4 are located near the African continent in the northeastern part of the Cape Basin. Other locations of AREN4 origins appear near the Walvis Ridge and further west the South Atlantic. These areas of eddy formation may be related to splitting of AREN4 eddies or to the merging of eddies of distinct origins with AREN4 trajectories.

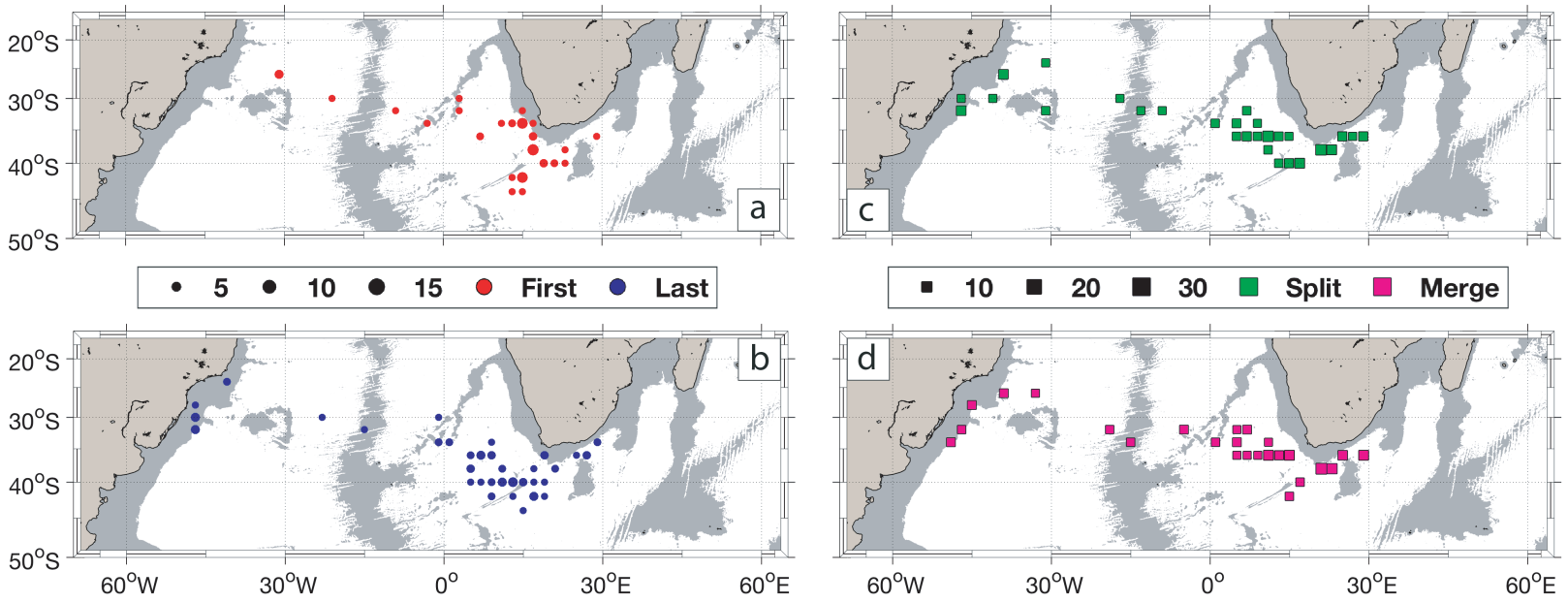


Figure 3.14: 2°x2° gridded positions and number of first detections (a), last detections (b) , merging events (c) and splitting events (d) of the AREN4 (i.e. AREN with orders less than 4). Each dot size represents the number of events for each grid cell associated with more than 10 occurrences. The gray shading in each figure represents water depth shallower than 3500 m in the ETOPO2 data set [Smith and Sandwell 1997].

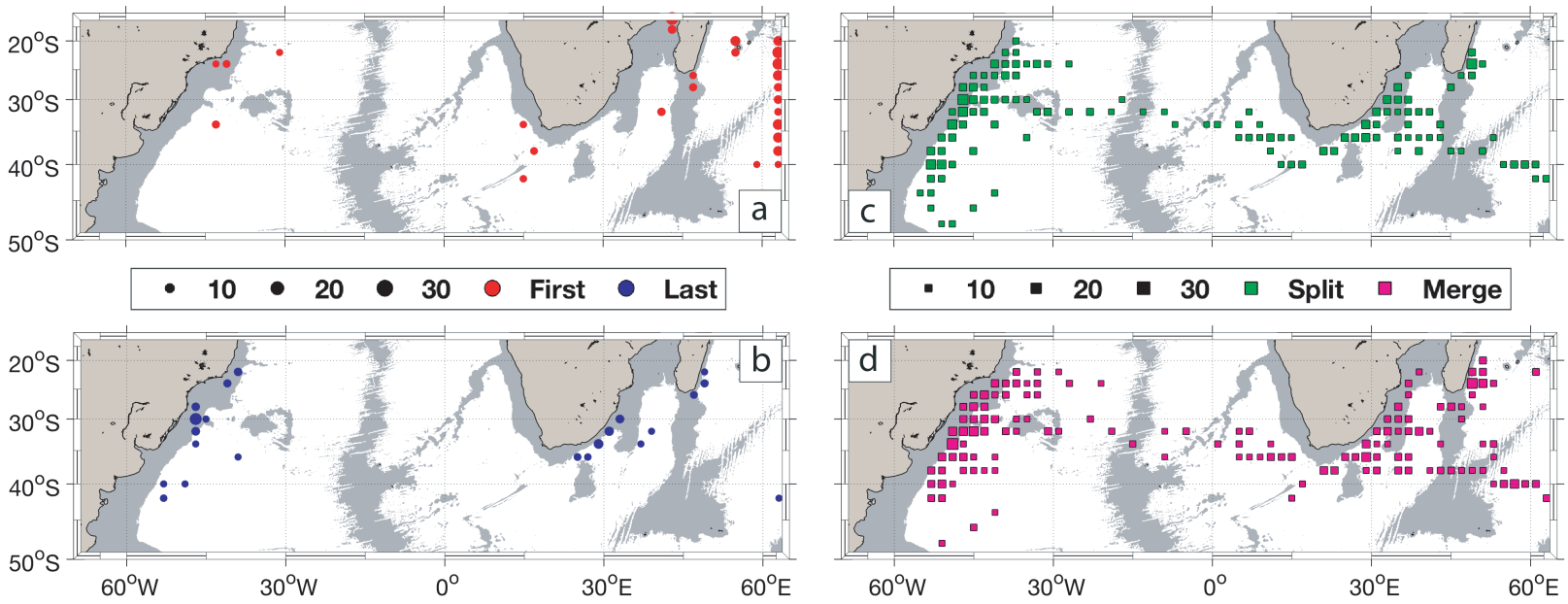


Figure 3.15: 2°x2° gridded positions and number of first detections (a), last detections (b) , merging events (c) and splitting events (d) of the AREN. Each dot size represents the number of events for each grid cell associated with more than 10 occurrences. The gray shading in each figure represents water depth shallower than 3500 m in the ETOPO2 data set [Smith and Sandwell 1997].

Moreover,113 of the 888 anticyclonic eddies that start an AREN4 trajectory are east of 30°E. Taking into account the AREN as a whole (Figure 3.15), the results suggest that a relatively small number of AREN4 originate as far north as the Mozambique Channel or east of the Madagascar Ridge while many higher-order AREN trajectories are as it appears from Table 3.4. Only one third of the AREN trajectories formed in the Mozambique Channel are reconstructed taking into account trajectories of order 4 or less, whereas 90% of the trajectories originating in the Southwest Indian Ocean are obtained by taking into account trajectories at orders greater than 4. Figure 3.10b, which highlights the area where many AREN eddies are present over the period of interest, shows a clear link between these northeast formation regions and the Agulhas Retroflection. This pattern is very similar to the many large eddies detected from surface drifters documented by Zheng et al. [2015] .

The existence of these anticyclones and their possible role in the destabilization of the Agulhas Current, leading to meanders, have already been documented [e.g., Schouten et al. 2002; Penven et al. 2006; Biastoch et al. 2008a;b; Halo et al. 2014; Elipot and Beal 2015]. Schouten et al. [2002] also found that some of these eddies do not create meanders and are advected downstream to the Retroflection. Detections of these eddies could be associated with an artificial interruption of the Agulhas Current due to the interpolation used to estimate the gridded altimetry field from the altimeters along-track data. However, the amplitude of these eddies is greater than 10 cm near the Agulhas Current. Therefore, they appear to be well-defined structures and not an artifact of data interpolation. A composite view of the 0-order trajectory that originates from the southern tip of Madagascar is shown in Figure 3.16a. This eddy forms near Madagascar and remains very coherent until it reaches the Cape Basin. Furthermore, this type of eddies is also well captured by looping drifters [Zheng et al. 2015; Lumpkin 2016] and the in-situ data recorded by current meter moorings [Donohue et al. 2000]. Many new detections of AREN eddies are also occurring in the open Indian ocean, which corresponds to the eastern part of our domain of study. In particular, Reunion Island, southeast of Madagascar, seems to be an active region for the identification of new AREN eddies. In summary, our results suggest that AR can form upstream of the Agulhas Retroflection, move relatively rapidly southward with the Agulhas Current (Figure 3.10d) until they are blocked between the Agulhas Current and its Return Current in the Retroflection area where they may merge with another eddy or be shed.

While AR origins have often been discussed in the literature, although not in the more complex context of the AREN, their disappearance has not yet been examined thoroughly. The TOEddies method and the AREN approach make it possible to quantitatively infer the vanishing of AR from satellite altimetry maps. Figure 3.14b documents a very well-structured pattern for the main regions where TOEddies lose the AREN4 ADT signature. This occurs mainly in the Cape Basin, not far from the main source regions of AREN4. This suggests that most AREN4 trajectories are lost within the Cape Basin, relatively soon after entering the region. The general pattern of disappearance of AREN4 is not evenly distributed: Most eddies disappear

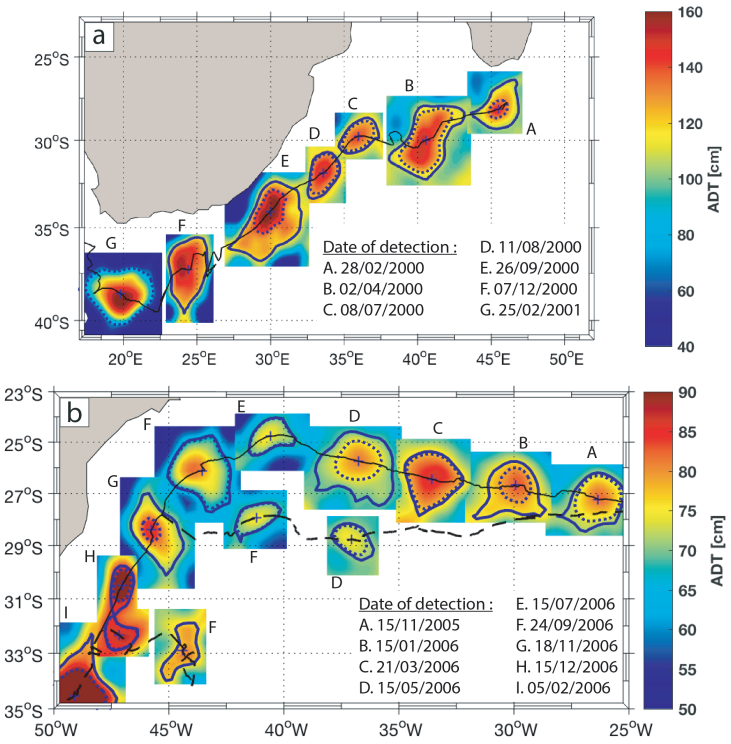


Figure 3.16: Composite figure of the order-0 AREN starting the most to the east (a) and ending the most to the west (b). Snapshots on selected dates are given, with in blue the eddy centroid (cross symbol), the ADT contour associated with the maximum speed (dotted) and the outermost ADT (solid line) contours. The trajectory of panel b interacts with two order-1 trajectories whose paths are drawn in dashed lines.

in the southern half of the basin as well as near the Walvis Ridge. Other regions where AREN4 vanish from ADT maps are found north of the Agulhas Plateau, south of Africa, and near the South American slope. There is no appearance or disappearance of AR, within AREN4, in the open ocean in the South Atlantic except occasionally.

According to the TOEddies method, there are more merging and splitting events than appearance and disappearance. The recurrence of such eddy-eddy interactions in the Retroflection area and in the Cape Basin has been demonstrated by various authors from in situ and remote sensing data [Byrne et al. 1995; Arhan et al. 1999; Boebel et al. 2003a; Dencausse et al. 2010a; Baker-Yeboah et al. 2010]. Our study shows that these regions correspond to areas where these processes are particularly active (Figures 3.14b and c). Topographic features are also regions where many merging and splitting events occur.

To complete the description of AR behavior in the South Atlantic, we discuss in the following sections the AREN regional behavior and statistics in more detail.

Agulhas Rings in the Cape Basin

Taking into account our definition of AR (anticyclones leaving the Indian Ocean and entering the Cape Basin, Figure 3.10a) we have identified 119 AREN4 (see Table 3.3). This is equivalent to a rate of 7 AR entering the Cape Basin per year. This represents a higher ratio than previous estimates that typically suggested one event every two to three months [e.g., Gordon and Haxby 1990; Goni et al. 1997; Schouten et al. 2002]. However, some authors [Schouten et al. 2000; Baker-Yeboah et al. 2010; Dencausse et al. 2010a] suggested that AR often split shortly after their shedding from the Agulhas Retroflection, before entering the Cape Basin. This may explain why our estimate is higher than those provided in previous studies that did account for splitting events. Indeed, eddy splitting and merging are particularly abundant near the Retroflection area (Figure 3.14c).

Looking separately at newly formed AR and those resulting from a splitting, we find a mean value of 4.3/year for newly formed AR entering the Cape Basin (i.e. a total of 73) while 2.8/year result from a splitting. Thus, about two thirds of the AR entering the Cape Basin are newly formed and the remainder result from a splitting. These results are very similar to those of Dencausse et al. [2010a] although their estimate is twice as high. To conclude, on average, every 2.8 months, a newly formed AR enters the Cape Basin. This rate is very similar to those found in the literature in terms of AR shedding [e.g., Gordon and Haxby 1990; Goni et al. 1997; Schouten et al. 2002].

At the Agulhas Retroflection and in the southern Cape Basin, the AREN trajectories are essentially made by AREN4 (i.e., rows C and D in Table 3.4 and Figures C.1 to C.5 in the Appendices). Here, AREN are characterized by large Ro (Figure 3.11a) in the area where they are mainly spawned (Figure 3.14a and line C in Table 3.3). A sudden transition in Ro appears when AR enter the Cape Basin (Figure 3.10b and 3.11a). This transition is due to a decrease in AR surface V_{max} and amplitude (and thus surface vorticity), whereas the radii remain relatively constant (Table 3.3). A decrease in vorticity in the Cape Basin has already been observed although not quantitatively documented [e.g., van Sebille et al. 2010].

Eddies in the Cape Basin have a particularly complex behavior that has been suggested by previous studies [e.g., Arhan et al. 1999; Schouten et al. 2000; Boebel et al. 2003a; Dencausse et al. 2010a]. Here, we can try to characterize this type of behavior more extensively. As already mentioned, TOEddies takes into account numerous AR separations and coalescences throughout the Cape Basin (Figure 3.14c and d). Although Figure 3.14b shows a main path of AR to the northwest suggesting straight trajectories, their individual behavior is truly complex due to eddy-eddy interactions, and induces relatively long residence times. The real impossibility of associating a trajectory with a single eddy but rather the need to consider the full set of AREN trajectories complicates the definition of a mean residence time associated with AR for each specific region of the domain considered. We propose here to overcome this difficulty by considering all the AREN trajectories reconstructed from

each segment crossing each line in Figure 3.10a. In this way, we can estimate the residence time of the AREN eddies in the Cape Basin by considering the segments that cross the Walvis Ridge (i.e. Line D in Figure 3.10a) and that are associated (backward in time) with segments that cross the southeast limit of the Cape Basin (i.e. Line C in the Figure 3.10a). We limit the reconstruction of the network to trajectories of order 15.

100 of the 119 AREN4 trajectories crossing line C are associated with a median order of 2 (i.e. 2 eddy-eddy interactions that include eddy splitting and merging). Based on these trajectories, we find that the mean residence time of AR in the Cape Basin is about one year (median of 1.0 ± 0.5 years), which corresponds to the estimate of Schouten et al. [2000]. During their journey in the Cape Basin, AR undergo important changes affecting their surface signature, as shown in Figures 3.11, 3.12 and Table 3.3 in terms of several dynamical and kinematic properties. In particular, although their sizes remain relatively stable, their initial surface signatures in amplitude, Ro and V_{max} decrease by ~50% on average.

While 119 AREN4 enter the Cape Basin, 160 cross the Walvis Ridge and enter the South Atlantic (Table 3.4). Again, because TOEddies does not associate a trajectory with a single eddy, these two values cannot be linked directly. Indeed, the number of eddy splitting and merging events in the Cape Basin is very high (Figure 3.14c) as is the number of eddy disappearances. In particular, Figure 3.14b shows that many of the initial 119 AR are lost on satellite altimetry maps in the southern Cape Basin.

Agulhas Rings across the South Atlantic

The fate of the 119 AREN4 that cross the Walvis Ridge and enter the South Atlantic Basin appears more linear and less turbulent than in the Cape Basin. They flow in a very zonal direction (centered around 35 ° S and about 5° wide). Here, their disappearance from the altimetry maps is almost nil (Figure 3.14b for AREN4 and Figure 3.15b for the whole AREN). The number of merging and splitting events is also significantly reduced. The main area where eddy-eddy interactions become important again corresponds to the Rio Grand Rise in the western part of the South Atlantic while the Mid-Atlantic ridge is not associated with such events but has an impact on the AREN zonal route by increasing its width (which becomes 10° wide).

A large portion of the AREN4 crossing the Walvis Ridge reaches the Mid-Atlantic Ridge (line E in Figure 3.10a) which represent 82% of the AREN passing this ridge. The very coherent behavior of the AREN crossing the South Atlantic is well captured by reconstructing the network and crossing times between lines E and D. On average, AREN eddies cross the eastern South Atlantic in about 1 year (a median time of 1.0 ± 0.3 years) with a median of only 1 eddy-eddy interaction. However, the AREN behavior changes on the other side of the Mid-Atlantic Ridge.

Here, the contribution of AREN4 to AREN reaching the South American slope is only 46%. This may be the result of the numerous eddy-eddy interactions at the Rio Grand Rise that has an impact on the overall behavior of the trajectories. The western part of the South Atlantic is crossed in 1.5 years (a median value of 1.5 ± 0.6 years computed between lines E and F) with a median of 3 eddy-eddy interactions.

Finally, Figure 3.10c shows a clear decrease in the surface intensity (Ro) of AREN eddies across the South Atlantic, associated with a 43% decrease in their surface azimuthal velocity V_{max} and 60% in their amplitude, while their size remains relatively stable (from lines D to F in Table 3.3).

Many authors [e.g., Gordon and Haxby 1990; Byrne et al. 1995; Schouten et al. 2000] have demonstrated the ability of AR to penetrate the South Atlantic Ocean, claiming that they gradually dissipate and vanish in this basin. Our study suggests a different fate for these eddies since nearly half of the AREN4 reaches the South American continent. Among these trajectories, 4 are order-0 AREN.

Agulhas Rings along the South American margin

Despite their relatively low surface signature, the few AREN eddies that are still detectable by satellite altimetry and that reach the American slope maintain their coherence. Near the South-American coast, they propagate southward in the South Brazil Current (Figure 3.10) for about half of a year (0.9 ± 0.5), as suggested by Byrne et al. [1995]. Along this path, AREN eddies undergo numerous eddy-eddy interactions as indicated by the large number of merging and splitting events (Figure 3.15b). These interactions are characterized by a sudden increase in surface signature and propagation speed (Figures 3.11 and 3.12). Moreover, some newly formed anticyclonic eddies are identified as AREN when they merge with older structures. A composite view of the trajectory at 0-order that ends further west is shown in Figure 3.16a. This AR veers south when it reaches the South-American coast. There, another anticyclonic eddy merges with it in October 2006. Two months later, the trajectory of order 0 merges with a newly formed anticyclone which results in the formation of an intense and large anticyclone.

At the southern limit of the Brazil Current and in the Zapiola Gyre, AREN eddies show an intense surface signature, as high as in the Cape Basin, before their trace is gradually lost. However, assessing the effective contribution of the original AR to these long trajectories remains a challenge due to the numerous merging and splitting events that occurred during their lifetime, and, in particular, along the Brazilian continental slope.

3.2.5 Summary and Conclusions

In this study, we present TOEddies, a new eddy identification and tracking algorithm that takes into account the detection of eddy splitting and merging events which has been applied to gridded multi-satellite ADT maps. Because of the many eddy-eddy interactions and the resulting eddy subdivisions and coalescences, the concept of a trajectory associated with a single eddy becomes less obvious than previously admitted. However, to be able to track the origins, fate and changes of these eddies we have reconstructed a network of segments and trajectories that allow us to reconstruct the history of the eddies.

We also developed a method to objectively assess the robustness and skill of TOEddies against "loopers", an eddy atlas derived from the completely independent set of drifting buoy data [Lumpkin 2016]. This allowed us to quantitatively compare and test TOEddies against the eddy atlas distributed by SSALTO/DUACS [Duacs/AVISO+ 2017]. TOEddies proved to be more robust because the eddies it detects correspond better (by 10 % and with a smaller error) to those identified from surface drifter data.

After validation, this algorithm was applied to daily AVISO ADT maps from 1993 to mid-2017 to uncover and characterize quantitatively the dynamics of Agulhas Rings entering the South Atlantic Ocean. After the complete recovery of the trajectories, the eddy statistics from January 2000 to December 2016 were explored. To differentiate with the stricto-sensu definition of Agulhas Rings formed in the Indian Ocean and disappearing in the South Atlantic, we used the concept of trajectory networks to define the Agulhas Rings Eddy Network (AREN).

The characteristics of the AREN, such as their surface signature and propagation speed near the Agulhas Retroflection, compare particularly well with previous estimates produced for a limited number of structures [e.g., Gordon and Haxby 1990; Garzoli et al. 1999; Arhan et al. 1999; Schouten et al. 2002; Dencausse et al. 2010a]. However, our study contradicts the traditional view of large coherent Agulhas Rings shed at the Agulhas Retroflection that are propagating and dissipating rapidly in the South Atlantic Ocean. For example, our results suggest that Agulhas Rings, and other anticyclonic eddies connected via merging and splitting, may originate as far upstream from the Agulhas Retroflection as in the Mozambique Channel or South of Madagascar. From there, they are advected southward by the Agulhas Current as distinct coherent structures without being absorbed or dissipated by the current.

Throughout their existence, Agulhas Rings interact intensely with neighboring eddies, giving rise to very complex trajectories. These interactions are particularly vigorous in the Cape Basin and influence the time these eddies spend in the region which is, on average, relatively long (about 1 year). Here, they undergo major changes in their surface properties (dynamic height, azimuthal velocity) while their lateral size remains relatively constant. These changes are likely due to local air-sea,

eddy-eddy and eddy-topography interactions [Arhan et al. 1999; Dencausse et al. 2010a; Arhan et al. 2011].

Numerous Agulhas Rings disappear from altimetry maps in the Cape Basin preventing their subsequent tracking. This may be due to their subduction in the ocean interior and not necessarily to eddy dissipation because, in this region, Agulhas Rings release large amounts of heat in the atmosphere and become denser [Arhan et al. 2011]. Indeed, evidence of their subduction has been observed by Arhan et al. [1999] and Garzoli et al. [1999]. Based on these observations, Herbette et al. [2004] used an idealized numerical simulation to show that the surface signature of such eddies can decrease considerably while they are still propagating in the ocean interior.

The AREN that we can still track in the Southwest Atlantic, follow a quasi-zonal path, about 5° wide along the 35°S parallel which widens further when passing the Mid-Atlantic Ridge. They eventually reach the South American continental slope where the majority of them propagates southward with the South Brazil Current. Here, they often merge with other anticyclones flowing south with the current and originating north of 20°S. Some AREN eddies can be detected along the western slope of the South Atlantic as far south as the Zapiola gyre.

Our results suggest that Agulhas Rings can live longer than expected. The longest main (i.e., 0-order AREN) trajectory is more than 4 years old whereas, if we compute the travel time of the network through lines C to G, we find a median time of 5 years for the trajectories connecting the eddies of the Southeast Indian Ocean to their furthest destination in the Southwest Atlantic.

Our study reveals a different view of the Agulhas Rings from that provided in previous studies. However, it does not necessarily disagree with their conclusions. Indeed, TOEddies is able to reconstruct a longer and more complete history of these eddies that encompasses the various Agulhas Rings segments of trajectories discussed in the literature.

The most important outcome of our study is probably the assessment of numerous eddy splitting and merging events involving Agulhas Rings but also anticyclonic eddies of different origins, which leads to the formulation of the AREN. This is essential for a better understanding of ocean dynamics. Indeed, eddy separations and coalescences must induce a vigorous mixing of water masses advected in the core of the eddies, which has an important impact on the overall redistribution of the physical and biogeochemical water properties. As suggested by Wang et al. [2015], Agulhas Rings cannot be considered as coherent and isolated structures advecting the same water masses along their path. Therefore, our results provide a different perspective on eddies from most published studies that do not account for eddy separations and merging events [e.g. Chelton et al. 2011; Haller and Beron-Vera 2013; Faghmous et al. 2015; Duacs/AVISO+ 2017]. However, if TOEddies can deduce the surface signature of eddies, it is still limited because it cannot access the exact processes involved in the evolution of eddies nor their subsurface structure.

Agulhas leakage plays an important role in the climate system, as a mechanism for transporting heat and salt between basins and closing the large scale overturning circulation [Gordon 1985; Beal et al. 2011]. In the context of global warming and early evidences of a changing Agulhas Current system and leakage [Biastoch et al. 2008a; Rouault et al. 2009; Beal and Elipot 2016] our results highlight the role of Agulhas Rings as an important, albeit complex, vector for Indo-Atlantic exchange. They reveal a new long route for these eddies, unequivocally connecting the western boundary currents of the Indian and South Atlantic oceans.

However, although modeling studies using Lagrangian techniques suggest a direct connection between the Agulhas Leakage and the AMOC [van Sebille et al. 2011; Rühs et al. 2013] with more than 50% of the Agulhas Leakage reaching the North Atlantic, our study does not show such a direct link for the Agulhas Rings as most of them recirculate southward with the South Brazil Current. Yet, a small number of these eddies appear to veer northward, crossing the Cruzeiro do Sul and the Vitoria-Trinidade seamounts chains. These results leave open the question of how the connection between the Agulhas leakage and the AMOC, as seen by the models, is achieved. Is the volume transport of these few eddies north of 20° intense enough to close the AMOC transport budget? Are all these eddies the ones that make the connection or are most of them invisible from altimetry because they flow northward at depth, as subsurface eddies? Finally, do the Agulhas Rings really make the connection with the AMOC or is this achieved by circulating water around the mesoscale field?

Although this study describes a much more complex Agulhas leakage made by Agulhas Rings than previously observed, our results are still incomplete because they cannot go beyond the limits of satellite altimetry. Indeed, altimetry maps are reconstructed from scattered observations that most probably affect the number of objectively recoverable eddies and trajectories. Moreover, these results are limited to the surface description of certain kinematic and dynamic properties. For a more in-depth description of these eddies and a quantitative estimate of the Agulhas leakage, future work should focus both on the variable three-dimensional structure of the Agulhas Rings and understanding all the processes that govern the connection of the Agulhas Current system with the AMOC.

4

Évolution de la structure thermohaline d'un Anneau des Aiguilles

Sommaire

4.1 Résumé de l'article 73
4.2 Evolution of the thermohaline structure of one Agulhas Ring reconstructed from satellite altimetry and Argo floats 74
4.2.1 Introduction 74
4.2.2 Data and Methods 78
4.2.3 Results 83
4.2.4 Comparison with Agulhas Rings identified in the literature 103
4.2.5 Summary and conclusion 110

4.1 Résumé de l'article

Le réseau des trajectoires des Anneaux des Aiguilles (AR) présenté dans le chapitre précédent nous a permis de décrire une dynamique des tourbillons des Aiguilles plus complexe que précédemment décrite. De nombreuses interactions entre anticyclones ont été identifiées ainsi qu'une grande variété des parcours suivis. Cependant, la description des tourbillons à partir des champs d'altimétrie satellitaires reste partielle car elle ne nous permet pas d'identifier les modifications que peuvent subir ces structures dans la colonne d'eau.

Nous proposons dans ce chapitre, actuellement au deuxième tour de révision pour le "Journal of Geophysical Research : Ocean" [Laxenaire et al. UR a], de tirer profit des profils de flotteur Argo en les colocalisant avec les Anneaux des Aiguilles détectés dans le chapitre précédent. Cela nous permet d'étudier l'évolution et la structure thermohaline d'un de ces tourbillons au cours d'une année et demie. Nous avons constaté qu'au cours de cette période, l'anneau évoluait selon deux phases différentes: une en hiver au cours de laquelle la couche de mélange dans le tourbillon se creusait de manière significative et une deuxième phase où le tourbillon subducte sous les couches chaudes de l'Atlantique Sud alors qu'il se propage vers l'ouest. La déconnexion de ce tourbillon profond de la surface de la mer pourrait expliquer la diminution de sa signature de surface dérivée de l'altimétrie satellitaire. Cela suggère que de tels changements ne sont pas dus à un processus global de dissipation des tourbillons. L'anneau est très grand s'étendant, après la subduction, de 200 à 1200 m de profondeur et est caractérisé par deux noyaux d'eaux modales. Ces deux noyaux concentrent la plus grande anomalie de chaleur des tourbillons et de sel par rapport aux eaux environnantes de l'Atlantique Sud. En calculant son impact sur un an, la propagation de cet anticyclone de longue durée vers le nord-ouest induit un flux de 2,3 Sv d'eau, 0,008 PW de chaleur et 2,3 kg/s de sel. Une comparaison poussée de ce tourbillon avec ceux décrits dans la littérature nous permet de mettre en évidence qu'il n'est pas hors norme tout en étant parmi ceux associés aux plus grosses anomalies de chaleur. Ainsi, ces résultats confirment que les Anneaux des Aiguilles jouent un rôle très important dans l'échange interocéanique indo-atlantique de chaleur et de sel.

4.2 Evolution of the thermohaline structure of one Agulhas Ring reconstructed from satellite altimetry and Argo floats

4.2.1 Introduction

Mesoscale eddies are ubiquitous in the World Ocean [Chelton et al. 2007; 2011]. Their energy generally exceeds that of the mean flow by an order of magnitude or more [Stammer 1997; Wunsch 1999] and they are thought to have a major impact on the spreading of hydrological properties by advecting them for far-reaching distances and during long times. In particular, their influence is seen as key in the transfer of heat, salt, mass and biogeochemical properties across the World Ocean [McWilliams 1985].

Over the last 25 years, satellite altimetry has provided a global, high-resolution, regular monitoring of sea level and ocean circulation variations [Morrow and Le Traon 2012]. These data constitute a precious time series with regular spatial sampling capable of recovering around 60 % of the variability in the 65 to 300 km mesoscale

band [Pujol et al. 2016]. For this reason, they allows us to quantitatively investigate the upper ocean dynamics, and they have been shown to be particularly well suited for the study of mesoscale eddies [e.g. Chelton et al. 2011].

Since the early period of satellite altimetry, because of their large extent and intense altimetric signal, various studies have focused on Agulhas Rings (AR) and their spatio-temporal evolution [e.g. Byrne et al. 1995; Gründlingh 1995; Schouten et al. 2000; Dencausse et al. 2010a; Guerra et al. 2018; Nencioli et al. 2018]. Agulhas Rings are mesoscale anticyclones spawn south of Africa by the South Indian western boundary current, the Agulhas, at its Retroflection. They are large (100 to 400 km diameter) rings of Agulhas Water that enter the Cape Basin, southwest of Africa, before moving westward across the South Atlantic Ocean [e.g. Byrne et al. 1995; Schouten et al. 2000; Biastoch et al. 2009; Guerra et al. 2018; Laxenaire et al. 2018]. The evolution and fate of AR are important aspects, since these rings are thought to account for an important fraction of Indian water leakage into the Atlantic [e.g. Gordon and Haxby 1990; Goni et al. 1997; Doglioli et al. 2006]. This leakage impacts the Atlantic Meridional Overturning (MOC) and the related meridional transport of heat, freshwater, and biogeochemical properties, by influencing its strength [Weijer et al. 1999; 2002; van Sebille and van Leeuwen 2007], stability [Weijer et al. 2001] and variability [Biastoch et al. 2008a; Biastoch and Böning 2013].

Satellite data give access to the evolution of surface properties of these eddies [e.g. Byrne et al. 1995; Schouten et al. 2000; Lehahn et al. 2011; Souza et al. 2014; Laxenaire et al. 2018]. In particular, these works show that Agulhas Rings (AR) surface signature decreases dramatically west of the Agulhas Retroflection and across the southern Cape Basin, and it continues to decrease gradually across the South Atlantic Ocean [e.g. Guerra et al. 2018; Laxenaire et al. 2018]. However, most of the previous studies based on satellite altimetry to recover the complete trajectories of one or more AR were not able to track all of them back from their area of Retroflection documenting their first detection in the vicinity of the Cape Basin [e.g. Byrne et al. 1995; Schouten et al. 2000; Lehahn et al. 2011; Souza et al. 2014]. Others tracked anticyclonic eddies in the South Atlantic without clearly identifying them as Agulhas Rings spawn at the Agulhas Retroflection [Guerra et al. 2018]).

This is most likely due to the non consideration by previous studies of the complex nature of Agulhas Ring trajectories that undergo to many eddy splitting and merging events [Laxenaire et al. 2018]. For example, studying Agulhas Rings in the Cape Basin, Dencausse et al. [2010a] showed that the number of these eddies entering the Cape Basin is multiplied by a factor of two when considering eddy splittings. Moreover, when focusing on the evolution and dissipation of three specific Agulhas rings, Nencioli et al. [2018] observed a merging of one of them in the vicinity of the South Atlantic Ocean. Consequently, these interactions, impacting the description of the eddy evolution and dissipation, are important to understand the mechanisms of the ocean circulation and how AR influence the Earth climate. Indeed, in the published literature, Agulhas Ring surface properties changes and they disappearance from satellite altimetry maps are often associated to eddy

dissipation processes, albeit direct observations of the latter are lacking. On the other hand, when these eddies are tracked for longer distances and times and by taking into account explicitly eddy mergings and splittings [Laxenaire et al. 2018], intense variations of their surface properties appear to be intimately correlated with such events.

Another limitation of satellite observations is that they do not inform on the eddy vertical structure and how it evolves *in route*. Agulhas Rings have only been occasionally sampled by *in situ* observations from ships in the Cape Basin [e.g. Gordon et al. 1987; Duncombe Rae et al. 1992; van Ballegooyen et al. 1994; Duncombe Rae et al. 1996; Arhan et al. 1999; Garzoli et al. 1999; McDonagh et al. 1999; Schmid et al. 2003; Gladyshev et al. 2008; Arhan et al. 2011; Casanova-Masjoan et al. 2017] and in the Southeast Atlantic [McCartney and Woodgate-Jones 1991; Arhan et al. 1999], and from Argo profiling floats [Souza et al. 2011a; Nencioli et al. 2018]. However, with the exception for the observations reported in Nencioli et al. [2018], Souza et al. [2011a] and Arhan et al. [1999], Agulhas Rings have not been sampled by *in situ* observations further west of the Southeast Atlantic, nor it has been possible to evaluate accurately their internal evolution from the Agulhas Retroflection onward. Concerning the last point, only, Schmid et al. [2003] and Nencioli et al. [2018] reported on the *in route* evolution of Agulhas Rings. Schmid et al. [2003] discussed of an Agulhas Ring sampled two times, at six months of interval, in the southern Cape Basin showing an intense change of the upper-layer eddy properties (essentially in terms of temperature and density, very likely due to strong seasonal air-sea interactions) and a freshening of intermediate waters. Nencioli et al. [2018] also considered the intense variation of properties in the upper 200 m of an Agulhas Ring crossing the South Atlantic and discussed the modifications in the internal structure of this eddy. Moreover, the internal structure of this eddy was characterized by a subsurface core of homogeneous water, that the authors identified as Mode Waters (MWs) in agreement with previous observations of subsurface intensified structures discussed by Arhan et al. [1999].

MWs are thick layer of homogeneous subsurface waters whose existence is thought to depend, as a precondition, on the formation of deep mixed layer [e.g. Hanawa and Talley 2001]. MWs have been identified in every ocean basin, always on the warm side of a current or front [e.g. McCartney 1977; 1982; Hanawa and Talley 2001]. They are generally distributed below the surface far beyond their formation areas. Among these are Western Subtropical Mode Waters (WSTMW) that usually are associated to subtropical gyres, and Subantarctic Mode Water (SAMW) associated with the subpolar fronts on the poleward boundaries of the southern hemisphere subtropical gyres [e.g. McCartney 1977; Hanawa and Talley 2001]. MWs are correlated with large surface heat loss from the ocean and their low potential vorticity arises as a result of convection [e.g. Hanawa and Talley 2001]. In the South Atlantic various MWs are discussed in the literature. Among these, Provost et al. [1999] documented from repeated hydrographic cruises two types of MWs: the South Atlantic Subtropical Mode Water (SASTMW) found in the western subtropical gyre and the South Atlantic Eastern Subtropical Mode Water

(SAESTMW) observed at th eastern edge of the subtropical gyre. Sato and Polito [2014] introduced a new definition of SASTMW by analyzing Argo float data. Using a clustering method they found three different varieties of SASTMW that differ in their hydrological properties and geographical location. These do not correspond completely with Provost et al. [1999] SASTMWs definition as they are defined from many more vertical profiles and over a larger area of the South Atlantic. To be noted here that, using the eddy database from Chelton et al. [2011], Sato and Polito [2014] checked if SASTMWs are correlated with the presence of mesoscale eddies. They did not find a high correspondence. However, when these authors observed a correspondence of SASTMW with eddies, 75 % of them were anticyclones.

Very recently, de Souza et al. [2018] described the origin of South Atlantic MWs by decomposing thermocline waters as a product of mixing of different MW varieties. They identified, among other, a particular SASTMW which is located along the Agulhas Rings main route where they are an important contributor of the thermocline water. In addition, de Souza et al. [2018] identified a westward deepening of SASTMW where it mixes with MWs originating from the Indian Ocean. They attributed such a deepening to a sinking of the core of Agulhas rings during they crossing of the South Atlantic. This echo with the works of Herbette et al. [2004] which numerically demonstrated that Agulhas Rings can subduct below a front. Taking into account these works we can wonder if Agulhas Rings might be an active process of MWs formation as speculated by de Souza et al. [2018] and if the variations of surface properties observed in the altimetry maps are linked with lateral mixing of waters between the eddy core and the environment or they result from a different process acting on the internal properties of eddies. Finally, by using *in situ* data, numerous authors [Gordon et al. 1987; McCartney and Woodgate-Jones 1991; Duncombe Rae et al. 1992; van Ballegooyen et al. 1994; Duncombe Rae et al. 1996; Arhan et al. 1999; Garzoli et al. 1999; McDonagh et al. 1999; Schmid et al. 2003; Gladyshev et al. 2008; Arhan et al. 2011; Casanova-Masjoan et al. 2017] have provided various point estimates of Agulhas Rings volume, heat and salt transports. It would be interesting to examine how this collection of observed Agulhas Rings compare together and if any general information Agulhas Rings distribution can be derived.

In order to provide an additional step forward in the assessment of Agulhas Rings dynamics and changes across the Atlantic, we discuss here the evolution of one of these eddies in the South Atlantic sampled by an high number of vertical profiles during more than one year. By making sure that the Argo profiles we used were meaningful observations of the eddy core, we isolated a period of the eddy lifetime during which the eddy subducted below the upper-ocean layer and whose thermohaline properties remained steady. During such a period of time, the eddy structure might be considered stationary enough to envisage a meaningful three-dimensional reconstruction. By undertaking a comprehensive comparison with Agulhas Rings properties discussed in the literature, we proved the robustness of our results and highlighted the role of specific MWs responsible of important heat and salt content anomalies with regards of the surrounding waters.

The paper is organized as follows. In Section 2, the data we have used are described and the methods we have developed are presented. The evolution of the surface and vertical eddy characteristics derived from satellite altimetry and Argo profiles, as well as the reconstruction of the South Atlantic mean three-dimensional structure are presented in Section 3. Section 4 discusses the results we obtained in the context of previous studies and assessments. A summary and the conclusions on the results presented in this article are provided in Section 5.

4.2.2 Data and Methods

The South Atlantic Eddy Atlas

We selected Agulhas Rings from the South Atlantic eddies we identified and tracked in time with the Tracked Ocean Eddies (TOEddies) automatic detection algorithm [Laxenaire et al. 2018] applied on more than 24 years (01/1993 to 05/2017) of the "all-sat-merged" series [Duacs/AVISO+ 2015] of delayed time daily satellite altimetry maps gridded at 1/4° in the South Atlantic and Southeast Indian oceans [70°W-65°E; 55°S-15°S]([Laxenaire et al. 2018], see Figure 4.1a). The TOEddies method is an evolution of the algorithm proposed and developed by Chaigneau et al. [2008; 2009] and Pegliasco et al. [2015]. The eddy detection algorithm is a two-step process: it identifies the occurrences of eddies before deriving their trajectories.

The key assumption of eddy detection by the TOEddies algorithm is that mesoscale eddies satisfy the geostrophic balance. Therefore, the instantaneous eddy streamlines should coincide with the closed isolines of the daily Absolute Dynamic Topography (ADT) maps. First, TOEddies identifies the local extrema (maxima and minima) of ADT, by comparing each ADT grid point to its eight neighbors, as possible eddy centers in the same way other methods defined extrema from Sea Level Anomaly (SLA) maps [e.g. Chelton et al. 2011; Faghmous et al. 2015]. Next, it looks for the outermost closed ADT contour around each extremum. The module of the ADT difference between the extremum and this contour defines the amplitude of the detected eddy, which is considered a proxy of the eddy (surface) intensity. To filter out weak extrema we require that the extremum amplitude is larger than a threshold of 1×10^{-3} m. This value, which is small in comparison with the precision of satellite altimetry maps, was obtained by Laxenaire et al. [2018] to improve the coherence between the TOEddies Atlas and eddies identified from surface drifting buoys by Lumpkin [2016]. The requirement to take into account eddies associated to amplitude lower than 1×10^{-2} m was also demonstrated by Faghmous et al. [2015].

In addition to the outer closed ADT contour, TOEddies also identifies the contour where the azimuthal velocity of the eddy is maximum. This contour, associated to the gradient of the ADT, is expected to be less dependent on the external field and easier to compare with *in situ* data. TOEddies uses for this purpose the geostrophic velocity derived from ADT maps and computes along each

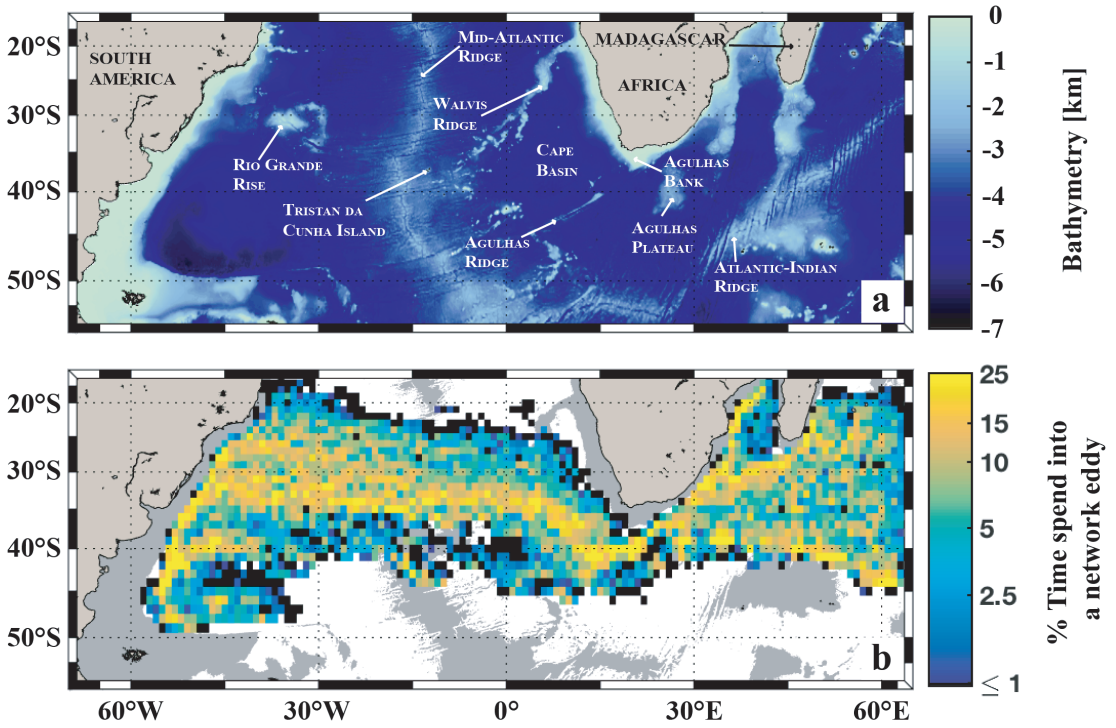


Figure 4.1: The study domain presented in terms of a) the local bathymetry from the ETOPO2 data set [Smith and Sandwell 1997] and b) the percentage of time each 2°x2° grid cell is occupied by the core of an eddy occurrence taking part to the Agulhas Ring Eddy Network [Laxenaire et al. 2018]. Figure modified from Laxenaire et al. [2018].

closed contour the mean azimuthal velocity $< V >$. The contour, corresponding to $V_{max} = max(< V >)$, is called the characteristic eddy contour. The area of the eddy within this contour defines what we designate as the eddy-core. The mean radius, R_{Vmax}, of this eddy-core area, A_{Vmax}, is derived according to the following equation:

$$R_{Vmax} = \sqrt{\frac{A_{Vmax}}{\pi}} \tag{4.1}$$

We called it the speed radius because it is associated to V_{max}. In the same way, TOEddies defines the maximum radial extent R_{out} associated to the outer closed contour of the eddy. This limit is important as the eddy-core defined by R_{Vmax} cannot be used alone to define neither the area of influence of the eddy nor the surface limiting the portion of the eddy where waters are trapped within the structure. This can be better understood by considering the ratio between the eddy azimuthal and drift speeds. This ratio is a nonlinear parameter delimiting the area of water trapped in a coherent structures [Flierl 1981; Chelton et al. 2011]. For example, Agulhas Rings are characterized by a drifting speed of about 5-8 $\times 10^{-2}$ m s^{-1} [e.g. Casanova-Masjoan et al. 2017; Nencioli et al. 2018; Guerra et al. 2018]

whereas V_{max} is of the order of several 10^{-1} m s^{-1} [e.g. Casanova-Masjoan et al. 2017]. This suggests that not only waters within the limit of R_{Vmax} are trapped within these eddies. This is confirmed by Souza et al. [2011a] who identified, in the South Atlantic, an horizontal extension of the eddy-trapped waters region larger than 150 km whereas the typical R_{Vmax} of Agulhas Rings is, in this area, 60-80 km [Guerra et al. 2018; Nencioli et al. 2018; Laxenaire et al. 2018].

At this step of the TOEddies algorithm sequences, the eddy center corresponds to the local extremum of ADT, which corresponds to a defined AVISO map grid point that might not coincide with the position of the eddy center. To avoid such constraint, TOEddies computes the centroid of the eddy-core area to determine the geometrical center of the eddy. Finally, the TOEddies algorithm computes the vortex Rossby number (Ro) that we use to quantify the (surface) eddy intensity [e.g. Chelton et al. 2011; Mkhinini et al. 2014; Le Vu et al. 2018; Laxenaire et al. 2018]. Ro given by the following equation:

$$Ro = \frac{V_{max}}{f R_{Vmax}} \tag{4.2}$$

where f is the Coriolis parameter.

In order to follow the position of each detected structure, TOEddies uses an algorithm based on the overlapping of eddy contours at consecutive time steps [Laxenaire et al. 2018]. Taking advantage of the daily AVISO fields, the method relies on the fact that mesoscale eddies move slowly (displacements of less than 10 km/day [e.g. Garzoli et al. 1999; Chelton et al. 2011; Laxenaire et al. 2018]) relative to their typical radii which span the range 20-200 km [Carton 2001]. Consequently, the areas occupied by an eddy for two consecutive days overlap which can be used to track eddies [Pegliasco et al. 2015]. Laxenaire et al. [2018] determined that the optimal percentage of the eddy area overlapping between two consecutive days was equal to or larger than 50% of the smallest area among the two eddies. This parameter reduces the number of spurious identifications [Laxenaire et al. 2018]. If no eddy satisfies the condition of area overlapping for consecutive time steps, the research is extended in time up to 5 consecutive days (i.e. half of the 10 days used by Le Vu et al. [2018]), while keeping the same value for the overlapping parameter.

The main advantage of the TOEddies tracking method is that it also allows to take into account the merging of eddies, that is when two or more eddies coalesce together to form one eddy, as well as the splitting of one eddy in two or more smaller eddies. Laxenaire et al. [2018] and Le Vu et al. [2018] have shown that merging and splitting events strongly impact the reconstruction of eddy trajectories and lifetimes. When these events occur, the segments of trajectories are reconstructed by associating pairwise eddies. In the case of a splitting, a cost function (CF), modified from Pegliasco et al. [2015] and Le Vu et al. [2018] and presented in equation 4.3, is applied to the eddy parent and the two or more eddy descendant. The CF compares changes (Δ) in the position of the eddy center ($Center$), Rossby

number (Ro) and radius of maximum speed (R_{Vmax}) of the eddies where, $\overline{\Delta\alpha}$ and $\sigma_{\Delta\alpha}$ denote, respectively, the mean and the standard deviation of the differences of a variable α. The two trajectory segments that minimize CF are identified as the main trajectories whereas the remaining segments are identified as the product of the splitting and referred to higher order trajectories ([Laxenaire et al. 2018]). Similarly, main trajectories are identified in the case of a merging.

$$CF = \sqrt{\left(\frac{\Delta Center - \overline{\Delta Center}}{\sigma_{\Delta Center}}\right)^2 + \left(\frac{\Delta Ro - \overline{\Delta Ro}}{\sigma_{\Delta Ro}}\right)^2 + \left(\frac{\Delta R_{Vmax} - \overline{\Delta R_{Vmax}}}{\sigma_{\Delta R_{Vmax}}}\right)^2} \tag{4.3}$$

In this study, we consider trajectories whose lifetime is equal or longer than 4 weeks. This reduces the size of the database by considering only eddies that are coherent for times longer than one month. This selection is reasonable in the case of Agulhas Rings that have, on average, a lifespan of a few months to several years [Souza et al. 2011a; Laxenaire et al. 2018].

Sea Surface Temperature

It was showed by Lehahn et al. [2011] and Souza et al. [2014] that Agulhas Rings crossing the Atlantic Ocean can be associated with specific surface properties. In this framework, we will use Sea Surface Temperature (SST) data to characterize the eddies. For this purpose we retrieved the level 4 ODYSSEA SST daily database [Autret and Piolle 2011] produced by the Group for High Resolution Sea Surface Temperature (GHRSST) at Ifremer/CERSAT (France). These daily cloud-free SST maps are obtained using an optimal interpolation on a global scale gridded at 1/10° over the full globe merging both microwave and infrared satellite SST.

Argo profiles data and eddy collocation

While altimeter measurements are representative of the vertically integrated effect of variations in temperature and salinity over the whole water column, ADT maps do not allow to directly obtain the vertical hydrological structure of the water column. To gain insights on this, we collocated the Agulhas Rings (AR) identified by TOEddies with *in situ* observations obtained from vertical profiles of the Argo floats international program which started in 2000. Argo floats provide a large number of CTD (Conductivity, Temperature and Depth) vertical profiles (i.e. more than 1.5 million profiles) over the upper 2000 m of the global ocean. These data are collected and made freely available by the International Argo Program, taking part to the Global Ocean Observing System, and the national programs that contribute to it (doi: <http://doi.org/10.17882/42182>). Argo Data Centers provide delayed mode data for each vertical profile. These data are validated and calibrated by the

data assembly centers [e.g. Owens and Wong 2009; Cabanes et al. 2016] against the most updated global climatology (computed with both full depth CTD from oceanographic research cruises and validated Argo floats) to estimate errors for each Argo profile. However, because mesocale eddies can have the ability to advect water from remote regions, the water trapped in the eddy core might have a distinct hydrological signature from the surrounding climatological environment. Indeed, Argo profiles close to an eddy center significantly differ from the environment [e.g. Chaigneau et al. 2011; Pegliasco et al. 2015]. Therefore, in this study, we use the Argo data downloaded from the Coriolis Global Data Center (Coriolis GDAC; url: <http://www.coriolis.eu.org>) that are not in the delayed mode but with control quality flags equal to 1 and 2, which refer to "good observation" and "probably good observation".

Because data from Argo profiles are usually not recorded at constant pressure levels, we have built an homogeneous data-set by interpolating the temperature and salinity on a constant vertical grid of 10 m step. Furthermore, we applied an additional selection of Argo profiles, following Chaigneau et al. [2011] and Pegliasco et al. [2015], to ensure the consistency of the interpolation. First, we kept a profile if it contained at least one measure between the surface and 20 m and one below 1500 m. Then, we prescribed that the vertical distance between two consecutive measurements should not exceed a given threshold depending on the depth interval. These limits are 25, 50, 75, 100 and 200 m between, respectively, the depth intervals 0-100 m, 100-300 m, 300-500 m, 500-1000 m and below 1000 m. This procedure removes about 40% of the profiles. Finally, we used the Gibbs SeaWater (GSW) Oceanographic Toolbox of the Thermodynamic Equation of SeaWater TEOS-10 [McDougall and Barker 2011] to compute the recommended hydrological variables which are the Conservative Temperature (CT), the Absolute Salinity (AS) and the potential density anomalies referenced to the ocean surface(σ_0).

Lebedev et al. [2007] showed that every Argo float moves at the surface, in average, about 4 km in 8 hours while sending 8 messages to the satellite (for the Argos system). Consequently, a typical lag of 1 hour can occur between the time the Argo float reaches the surface and the time its position is recorded by an Argos satellite. This time lag may induce an error in the position of the hydrological profile of the order of 500 m, which is small compared to the typical radii of mesoscale eddies [Carton 2001] as well as the resolution of satellite altimetry from which eddy centers and shapes are identified. It is therefore possible to determine if a given hydrographic profile is located inside a detected eddy [e.g. Chaigneau et al. 2011; Pegliasco et al. 2015]. The outer limit R_{out} is used for this determination as the trapped water in the eddy are not expected to be limited to the R_{Vmax} contour as previously discussed.

The collocation of Argo profiles and the TOEddies eddies results in the separation of such profiles into three groups: those sampling a cyclonic or anticyclonic eddy and those falling outside any of them. We define the latter as profiles sampling the environment within which the eddies propagate. In order to quantify the

hydrological anomalies associated to each eddy, we computed a climatological profile characteristic of the environment outside that eddy that is then substracted from the vertical profile sampling the core of the eddy. The climatological profile is the average of all the profiles falling out of the eddy and located in a rectangular box of $\pm 2.5°$ both in longitude and latitude centered on the eddy and whose date is in a maximum temporal range of ± 30 calendar days from the date of the Argo profile sampling the eddy. We tested both, the spatial and time thresholds, in order to find the best fit while keeping enough profiles and being sufficiently restrictive by not considering different hydrological regions or season to characterize the environment. Finally, we estimated the distance between each profile and the geometrical center of the eddy. This distance from the center will be referred as Dc in the following

4.2.3 Results

We followed Laxenaire et al. [2018] creating the eddy network associated to the Agulhas Ring (AR) identified in the South Atlantic Eddy Atlas. For that, AR are defined as the anticyclonic eddies which are initially detected in the Southeast Indian Ocean and then enter and propagate into the South Atlantic. The limit used to separate these two basins is an imaginary line connecting specific topographic structures, such as the Agulhas Ridge, that defines the southeastern limit of the Cape Basin (4.1a). As shown by Dencausse et al. [2010a], Agulhas Rings generally experience numerous mergings or splittings during their lifetime. Hence, several segments and bifurcations of trajectories have to be associated to correctly depict the whole lifespan for these eddies. In the following, we will make use of the concept of Agulhas Ring Eddy Network (AREN) of trajectories introduced by Laxenaire et al. [2018] that includes all the trajectories undertaken by any eddy, parent and descendant, that has merged with or split from a particular eddy or group of eddies originating in the Indian Ocean and traveling across the Indo-Atlantic limit.

The total Agulhas Ring network is composed of 730 481 eddy occurrences (i.e. eddies detected in daily maps) that cluster into 6 363 trajectories. The percentage of time each ADT grid point is inside the characteristic eddy contour of an eddy occurrence taking part to the AREN is presented in Figure 4.1b. The total AREN was sampled by 7 419 Argo profiles of which 826 sample Agulhas Ring main trajectories (i.e. a trajectory of an Indian anticyclone that flows into the South Atlantic basin).

We identified the Argo float that was trapped for the longest period by an AR. It corresponds to the float No. 5902281 which offers a long time series (from May 2012 to November 2013) that is composed of 54 vertical profiles sampling a single Agulhas Ring propagating from the Cape Basin to the Mid-Atlantic Ridge. The long trapping of this Argo float suggests that AR found in this region might behave as coherent eddies, at least at 1000 m which is the parking depth of these floats. This was also confirmed by other float trapping by such eddies described in the literature. In particular, a comparable long trapping of an Argo float by

an Agulhas Ring in this area was identified between February 2014 and August 2015 by Nencioli et al. [2018].

The AREN associated to the selected AR is presented in Figure 4.2 The AR main trajectory, as defined by the Cost Function, is composed of segments 2, 5 and 6. The network, decomposed in the seven segments, is a general example representing the relatively complex history of Agulhas Rings. It includes the various eddies and related segments of trajectory that have merged with and split from this Agulhas Ring during the 4 years and 7 months of its lifespan (from January 2011 to July 2015). Only the segments that interact directly with the main trajectory that trapped the Argo float No. 5902281 are discussed in the following. It is important to emphasize that as the TOEddies Atlas could contain some spurious eddy merging and splitting events, we manually validated the particular Agulhas Ring trajectory we analyze in this study by not considering those eddies that initially merge with and then split from this trajectory during times shorter than one week. The various eddies associated to this Agulhas Ring trajectory were sampled in total by 117 profiles from 19 different Argo floats. The number of the profiling floats together with their complete trajectories are presented in Figure D.1 in the Appendix.

The specific Agulhas Ring trajectory network that we analyze in this study starts with the shedding at the Agulhas Retroflection of three independent Agulhas Rings. The first shedding, which occurred on the 8 of January 2011, results in an eddy moving south and entering the Cape Basin by crossing the Agulhas Ridge (dark blue Segment 1 in Figure 4.2) and following the Southern Agulhas Rings Route defined by Dencausse et al. [2010a]. The second and third shedding occur, respectively, in August and November 2011. The second shedding gives rise to an eddy whose trajectory (in blue, Segment 2 in Figure 4.2) follows the Agulhas Rings Central Route [Dencausse et al. 2010a] whereas the third one (light blue, Segment 3 in Figure 4.2) takes the Northern Agulhas Rings Route [Dencausse et al. 2010a]. These two trajectories merge together in the eastern part of the Cape Basin forming the Segment 4 of the AREN (in green in Figure 4.2). The latter merges with the Southern Route eddy (Segment 1) in the northwestern part of the Cape Basin close to the Walvis Ridge. It results in Segment 5 (yellow line) that interacts with some other Agulhas Rings and anticyclones along its route but without any consistent merging and splitting events during 56 months until it reaches the South American Margin. There, it splits into two eddies in March 2015 that move south along the American continental slope until they disappear from the satellite altimetry field in July 2015.

In this study, we focus on the period of time spanning from May 2012 to November 2013, during which, the Agulhas Ring did not merge nor split while relatively well sampled by Argo floats (a profile sampled the structure at least every 10 days: see the black crosses in Figure 4.2). The dataset combines 531 days of eddy detection from ADT maps and 70 Argo vertical profiles located within the core of the eddy and achieved by 5 different Argo floats. During this period of time, the anticyclone associated to Segment 5 leaves the Cape Basin crossing

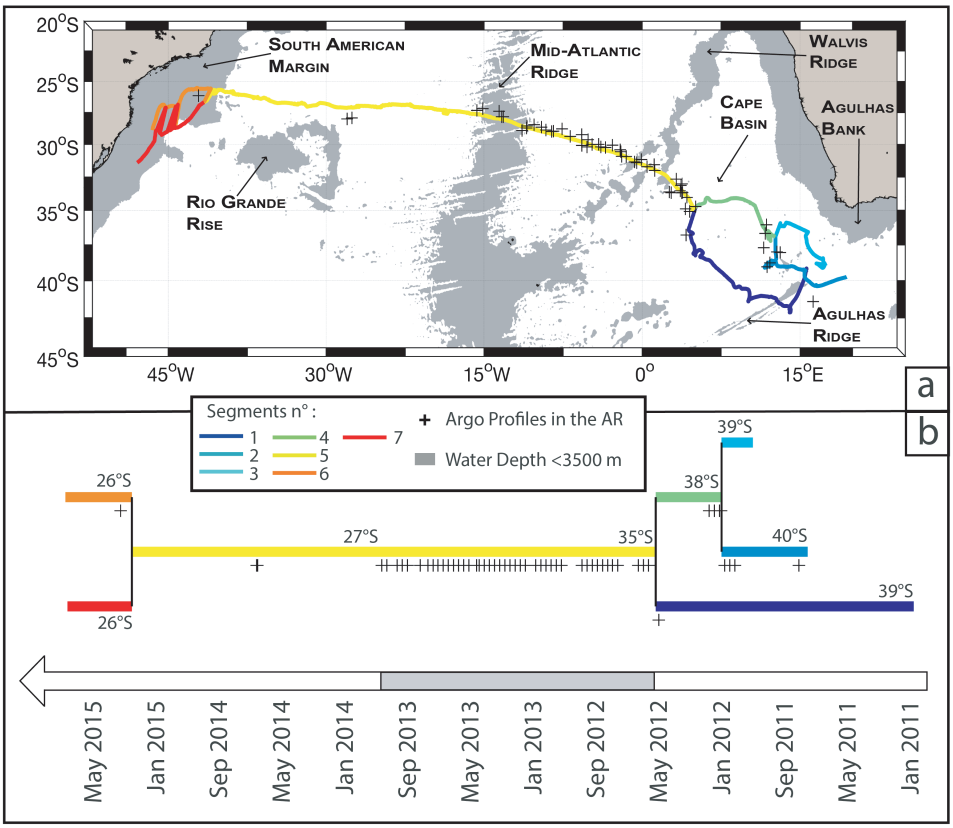


Figure 4.2: a) Geographical distribution of the segments (in colors) taking part to the network of trajectories for the Agulhas Ring sampled for the longest period by Argo profiling float. The positions of the Argo profiles sampling the whole set of eddies that composed this particular network are represented by the black crosses; b) A sketch displaying the various segments together with the eddy merging and splitting events and Argo profiles position as a function of time. The gray shading patches in (a) represents water depth shallower than 3500 m in the ETOPO2 data set [Smith and Sandwell 1997].

the Walvis Ridge between October 2012 and January 2013, it then propagates in the eastern part of the South Atlantic before crossing the highest points of the Mid-Atlantic Ridge between August and October 2013. The bathymetry profile below this trajectory is presented in Figure D.2 of the Appendix to allow a clear positioning of the Lagrangian segment with respect to the local topography.

Evolution of the Agulhas Ring surface dynamics

The temporal evolution of the surface signature of this Agulhas Ring (i.e., size and surface intensity) computed by TOEddies from ADT maps, is presented in Figure 4.3. While R_{Vmax} of this eddy is rather constant during the entire period with a median value of 64 km associated to a weak 8 km standard deviation (STD), R_{out} shows important variations (between 75 and 150 km and a STD of 23 km). To

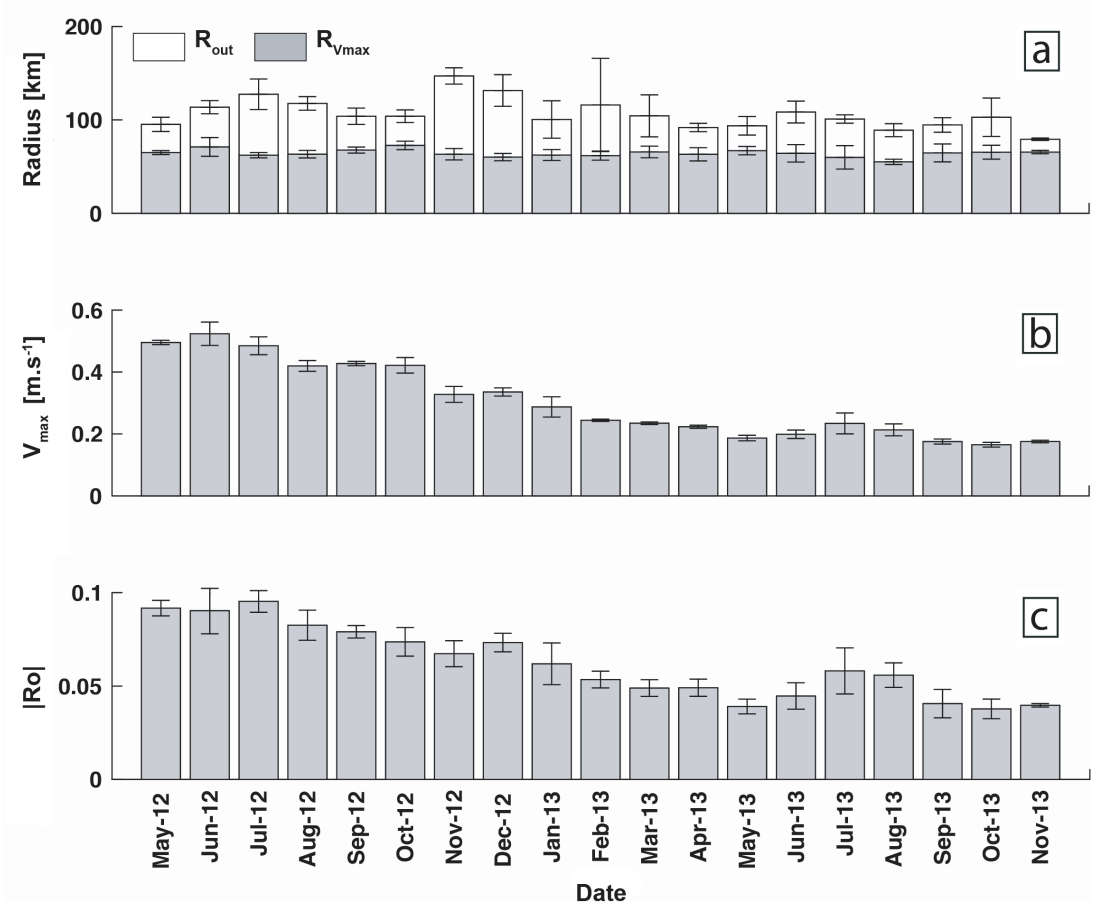


Figure 4.3: Temporal evolution of a) the monthly averaged equivalent radius of the outer contour (R_{out}) and the eddy core contour where the azimuthal velocity is maximum (R_{Vmax}), b) the maximum of azimuthal velocity (V_{max}) and c) the absolute Rossby number of the core ($|Ro|$) as derived from the altimetry maps. The error bars correspond to the monthly STD of these parameters.

emphasize these differences, the evolution of the outer and characteristic contours (the latter is associated to V_{max}), are presented in Figure 4.4. Each contour is drawn in the translating frame of the Agulhas Ring where the position of the center of each figure corresponds to the centroid of the eddy core area. The contrast between the highly variable structure of the outer contour, that takes very complex shapes, and the characteristic contour that remains coherent and keeps a relatively circular shape during the whole period of study appears clearly. his might be due to the distortion of the edge of the eddy by the strain of neighbor eddies and external flow field or to the small signal-to-noise ratio of the ADT outside of the eddy. In any case, we prefer to use the characteristic eddy contour and the corresponding speed radius R_{Vmax} to estimate the size of the structure similarly to other algorithms [e.g. Nencioli et al. 2010; Duacs/AVISO+ 2017; Le Vu et al. 2018].

The evolution of the monthly mean V_{max} and Ro are shown in the lower panels

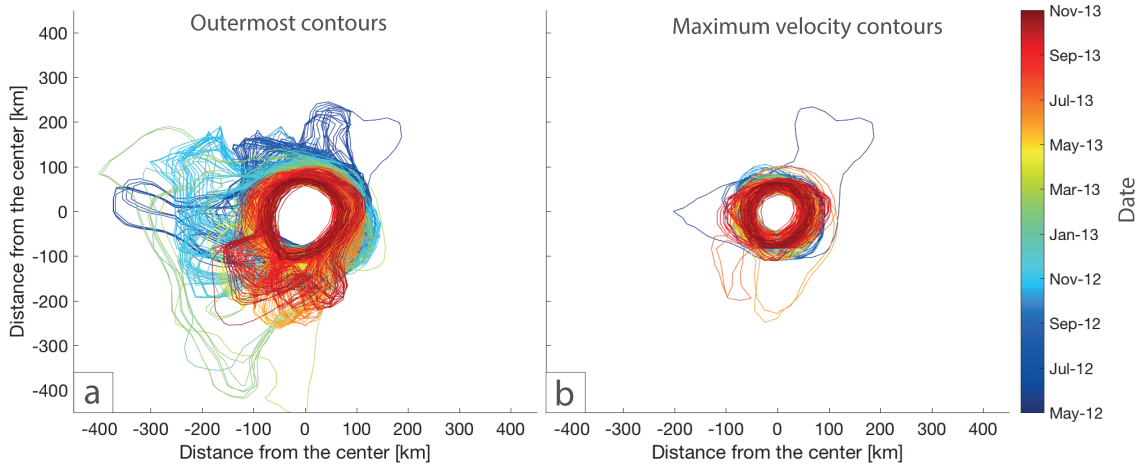


Figure 4.4: a) The outer contours and b) the characteristic contours (associated to the maximum of azimuthal speed) in the referential of the Agulhas Ring at times when an Argo float sample it.

of Figure 4.3. The maximum value of V_{max} is about 50 $\times 10^{-2}$ m s^{-1} in spring 2012. It then decreases gradually and reaches smaller values, below 20 $\times 10^{-2}$ m s^{-1}, almost one year later. Figure 4.3 shows a similar decay for Ro. This is very likely due to the variation of V_{max} as the eddy size is constant and the meridional displacement is limited. One might argue that this decrease of surface intensity is related to the change of environment. However, the Amplitude of the AR also decreases from 0.4 m to 0.1 m (not shown) during its journey while the variation of the MDT interpolated at the AR center are lower than 0.1 m. A similar decay of surface intensity across the South Atlantic has been already documented by several authors [e.g. Byrne et al. 1995; Schouten et al. 2000; Guerra et al. 2018; Laxenaire et al. 2018]. During the whole period, Agulhas Ring $|Ro|$ remains small (below 0.1) which confirms that this eddy is balanced geostrophycally and therefore we do not need to apply the cyclo-geostrophic correction [see Ioannou et al. 2017 ; for an example of such correction]. A short period of intensification is visible in winter during July and August 2013 and a final decay of the surface signature is visible during the two last months of the period under study.

Evolution of the internal structure

In order to estimate the evolution of the Conservative Temperature (CT), Absolute Salinity (AS) and potential density (σ_0) inside the Agulhas Ring, we first divided the time period in 10-day intervals. For each of this 10-day intervals we selected the CTD profiles closest to the eddy center. The selected vertical profiles are presented in the left panels (a, c and e) of Figure 4.5 whereas the associated anomalies, computed as the difference with the mean environmental profiles, are

presented in the right panels (b, d and f) of the same Figure. Taking into account that the hydrological anomaly associated to the Agulhas Ring strongly depends on the distance Dc of the Argo profile from the eddy center, we also present the latter (black crosses and lines) at the bottom of every panel were anomalies are plotted in the Figure 4.5.

The climatologic profiles used to compute the anomalies as well as the number of profiles used to compute the first 1500 meters of each climatological profile at each time step are presented in Figure 4.6. We selected in this study only Argo profiles associated to a maximum depth larger than 1500 m. Indeed, the number of profiles sampling the upper layer of the water column is higher than that reaching depths deeper than 1500 m. The minimum of available profiles within the eddy core close to the surface is 40 whereas it decreases to 28 for profiles reaching 1800 m of depth (not shown). The maximum number of profiles is 118 for the upper 1500 m of depth, and 93 for profiles reaching 1800 m (not shown). In the climatological profiles, the upper 200 meters appear as the most variable. A surface layer of low density appears in October 2012 concomitant to the onset of the summer seasonal stratification as well as the drifting of the eddy into warmer waters. This limit, characterized by the isopycnal 26.2 kg m^{-3}, appears to continuously thickens during a period longer than a full year. The layers below this isopycnal show more steady characteristics during the full period, albeit a relatively small down-lift of the isolines appears between 200 and 400 m of depth and an up-lift below 400 m. Very likely, this is due to the westward thinning of the Antarctic Intermediate Water (AAIW) layer marked by a minimum of salinity around 1000 m as discussed by Rusciano et al. [2012].

Figure 4.5 presents the hydrological characteristics of the Agulhas Ring as provided by the Argo profiles sampling the eddy. They show that important variations in the eddy properties occur in the upper 200 m. Here, a shallow and low density layer (limited by the 26 kg m^{-3} isopycnal) is visible in May 2012 (during the early austral fall). This layer is eroded at the beginning of the austral winter (from June 2012) and reappear in October 2012 during the austral spring. This layer might be associated to the seasonal cycle with the formation and erosion of a seasonal thermocline. However, similarly to the behavior shown by the climatological profiles (Figure 4.6), this layer continues to thicken from October 2012 to November 2013, not showing anymore a winter erosion. This suggests that the upper eddy layer is not only associated to the seasonal cycle but it is also affected by the displacement of the eddy into a different hydrological region (the South Atlantic subtropical gyre) characterized by a shallow permanent stratification.

The Argo data also show a relatively high correlation between vertical properties and the distance Dc of the profile from the eddy center (see, for instance, the variations of Dc together with those of the isolines 10 °C, 34.7 $g.kg^{-1}$ and 27 kg m^{-3} in Figure 4.5a,d,e). As expected for a warm and salty core anticyclone such as an Agulhas Ring, the isolines are deeper close to the center of the structure than at its edges. The correlation among the eddy hydrological properties and Dc is particularly evident from the vertical CT, AS, and σ_0 anomalies (Figure 4.5b,d

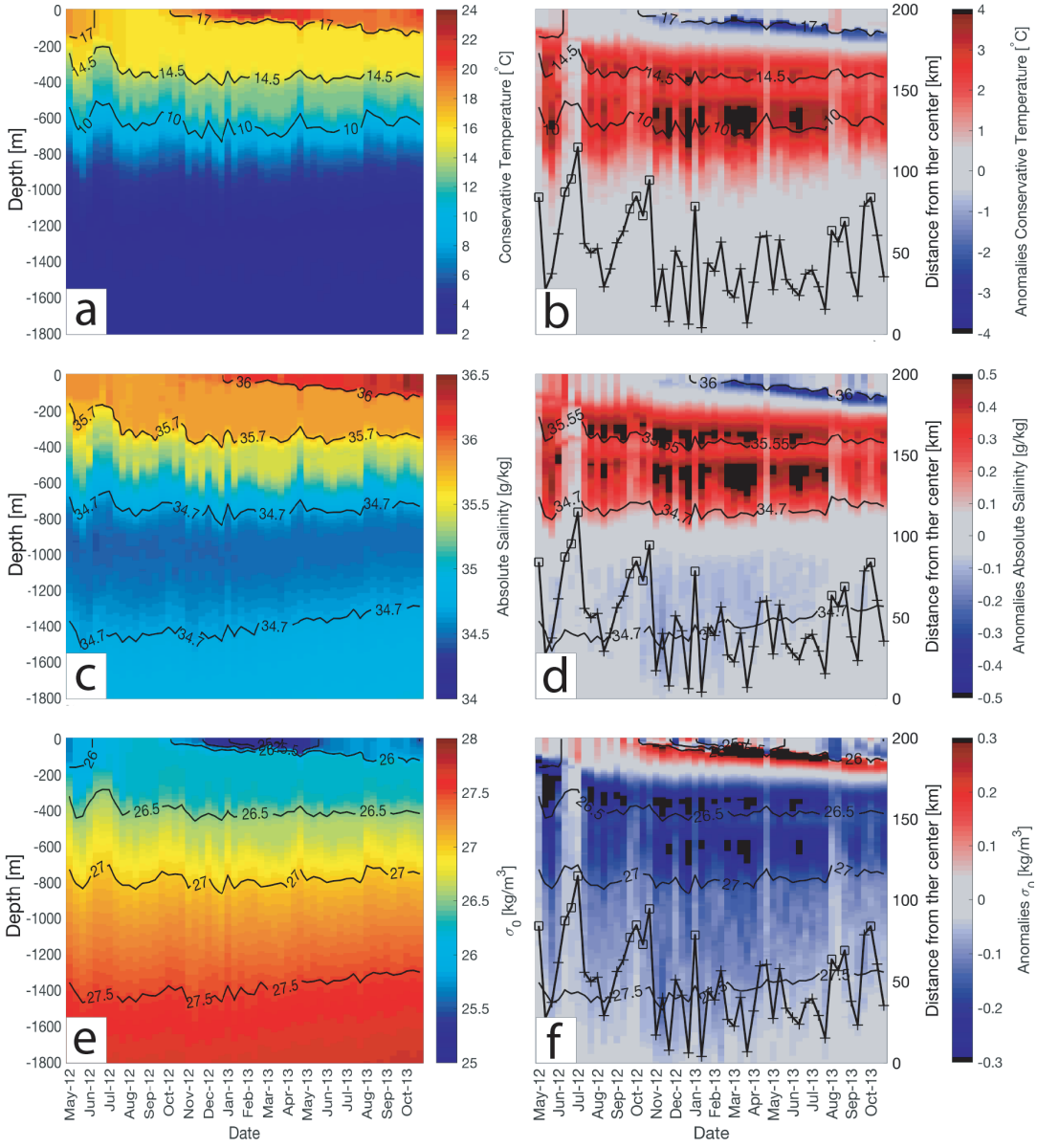


Figure 4.5: a) Conservative Temperature, b) Conservative Temperature Anomaly, c) Absolute Salinity, d) Absolute Salinity Anomaly, e) Potential Density and f) Potential Density Anomaly for the closest Argo profiles to the Agulhas Rings center for every 10-day intervals as a function of time and depth. Black lines with markers in each right panel represent the distance of each profile from the eddy center (Dc) whose scale is presented in the y-axis on the right of panels b, d and f. The marker is a cross for profiles inside the characteristic contours otherwise it is indicated as a square. Selected isotherms, isohalines and isopycnals levels are added to the corresponding panels for both, the full fields and the anomalies.

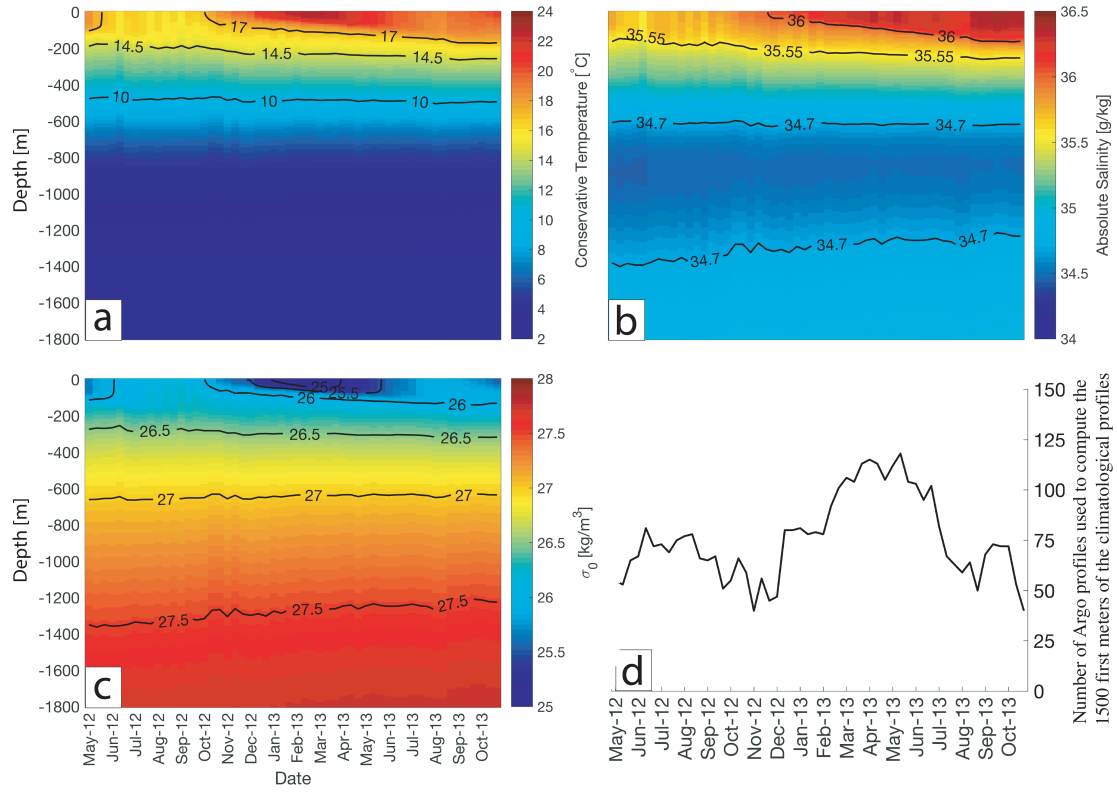


Figure 4.6: a) Conservative Temperature, b) Absolute Salinity and c) σ_0 for the environment climatological profiles we used to compute the Agulhas Ring vertical property anomalies in Figure 4.5; d) Number of averaged Argo profiles used to produce the environment climatology.

and f). Their amplitude variations are indeed intimately linked with Dc variability and this through the whole water column. In particular, Figure 4.5b,d and f show clearly a strong reduction in the anomaly amplitude when Dc is larger than 65 km. This corresponds to the periods of time June-July 2012, October 2012, January 2013 and, later on, in August and October 2013.

The eddy property anomalies (Figure 4.5b,d and f) show that the Agulhas Ring is warmer, saltier and less dense than the environment. A marked positive anomaly in AS (> 0.2 g kg^{-1}) and CT (> 1 °C) down to, at least, 800 m appears clearly for small Dc ($Dc < 50$ km). Moreover, theses anomalies exhibit a striking vertical pattern characterized, from November 2012 to August 2013, by two well separated extrema roughly located at -350 m and -650 m depth. Such a vertical structure strongly suggest the presence, within the eddy, of two cores of water masses very different from the environment. To be noted here that σ_0 anomaly for the two distinct water-mass cores is about -0.3 kg m^{-3}, a value six times higher than the STD of the environment σ_0 (0.05 kg m^{-3} (not shown)). It is worth noting that, after November 2012, negative anomalies of AS are found, within the eddy, below 1000 m of depth.

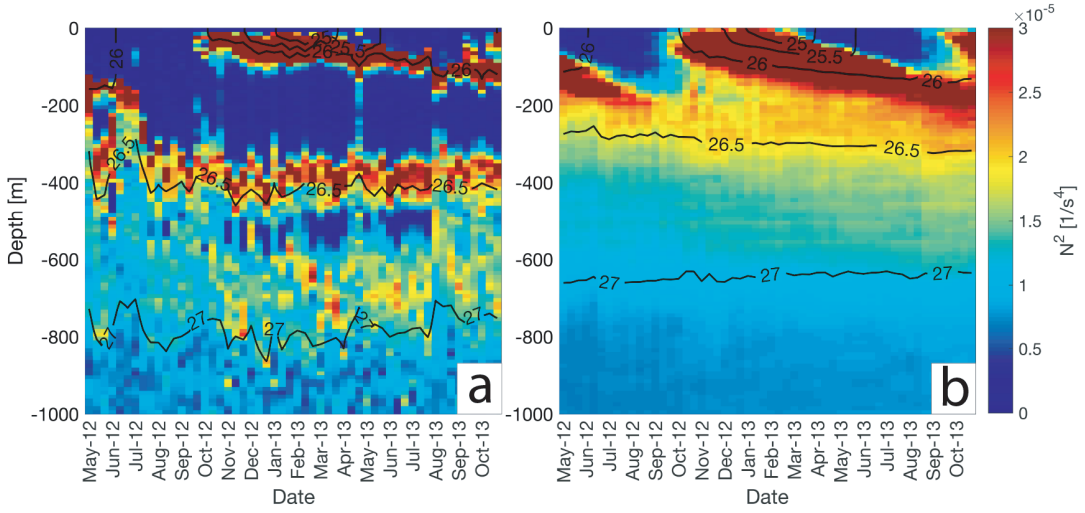


Figure 4.7: Time evolution of the Brunt Väisälä frequency computed for the Argo float No. 5902281 profiles a) within the Agulhas Ring and b) for the environment climatology. Isopycnals levels separated by a 0.5 $kg.m^{-3}$ interval are added to the corresponding panels.

To better understand the vertical structure of the Agulhas Ring, we plotted the Brunt Väisälä frequency squared N^2 in the Argo profiles plotted in the Figure 4.5, and the climatological environment in Figure 4.7. N^2 is computed from equation 4.4, where g is the gravitational acceleration and ρ_0 the density of reference set to 1000 kg m^{-3}. The environment profiles exhibit a seasonal cycle characterized by the development of a winter mixed layer (low values of N^2, below $1\,10^{-5}s^{-4}$) extending, on average, to 150 m of depth in August-September (Figure 4.7b). On the other hand, the eddy core is characterized by a considerably deeper mixed layer, that develops during the first five months of the time series and that reaches 350-400 m of depth in August-September 2012. During this period, the eddy upper layers are connected to the sea surface and the atmosphere through this deep mixed layer. Later on, from October 2012 to March 2013, the summer restratification seems to isolate the eddy homogeneous cores from the atmosphere and prevents any heat or momentum transfer between the surface layers and the eddy. Below this layer lies the uppermost of the two cores whose properties correspond to the previous winter mixed layer. Its properties are homogeneous over more than 200 m, suggesting that this core belongs to MWs.

$$N^2 = \frac{-g}{\rho_0}\frac{\partial \rho}{\partial z} \tag{4.4}$$

Figures 4.5 and 4.7 suggest, therefore, that the main hydrological core of the eddy was connected with the sea surface and exposed to air-sea interactions during the first part of the time series and that it became a subsurface core, isolated by the presence of an upper stable and relatively thick (200 m) warm layer, while

leaving the Cape Basin and entering the South Atlantic Ocean by crossing the Walvis Ridge (see Figure 4.2). This analysis is, of course, restricted by the limited availability of profiles close to the eddy center before July 2012. To corroborate our results, we undertook a satellite SST data analysis to try to assess the surface signature of the eddy and to characterize its connection with the ocean surface layer in an independent way. This is in line with the works of both, Assassi et al. [2016] and Schütte et al. [2016], who used surface SST anomalies to discriminate surface and sub-surface intensified eddies. Indeed, anticyclonic eddies are associated to positive Sea Level Anomalies. If they are surface eddies, they are expected to correspond to positive SST anomalies, whereas if they are subsurface eddies, they should be associated to negative SST anomalies as a consequence of the dooming of the isotherm above their hydrological core.

For this purpose, we used the ODYSSEA SST dataset [Autret and Piolle 2011] that we have interpolated at the position of the eddy center during the period of interest (see Figure 4.8). For each date, we computed the average of the SST field for all the points within 150 km from the eddy center (i.e. the maximum R_{out}) that we subtracted from the SST value at the eddy center to obtain SST anomalies. These anomalies are presented in Figure 4.8. It appears from this figure that they change sign between September and October 2012. This is simultaneous to what we identified as the beginning of the isolation of the Agulhas Ring from the ocean surface, as previously discussed by analyzing Figures 4.5 and 4.7. Such change of sign can be due to the modification of the background environment while the eddy moves into subtropical waters. Yet, the absolute SST (blue line in Figure 4.8) clearly shows a seasonal cycle which is not consistent with a fixed patch of constant temperature drifting into another environment. However, Souza et al. [2014] discussed the presence of negative SST anomalies related with Agulhas Rings still connected with the ocean surface. They explained this by a modification of the Ekman pumping due to the presence of the eddy and that it may induce dipole SST anomalies with the center of an Agulhas Ring associated to a negative SST anomaly whereas a positive anomaly would correspond to the eddy boundaries.

To assess the geographical pattern of SST anomalies, we computed monthly SST anomaly maps in the moving frame of the Agulhas Ring. They are presented in Figure D.3 in the Appendix. These maps show that, in July 2012, the Agulhas Ring core is associated to positive SST values lower than at its boundaries which might confirm the conclusions of Souza et al. [2014]. However, since the date we identified the isolation of the main hydrological core of the eddy from the ocean surface, in October 2012, the SST dipole-like anomaly disappears and the Agulhas Ring core becomes to be associated to a strong patch of negative SST anomalies, confirming the subsurface nature of the eddy and the generic results of Assassi et al. [2016] and Schütte et al. [2016]. Positive anomalies still exist close to the eddy boundary but are localized at the eddy western side, a feature that can be explained by the stirring of the environment due to the anticlockwise rotation of the Agulhas Ring in the presence of a north-south gradient of temperature.

The results we obtained by analyzing two independent datasets (Argo vertical profiles and satellite SST) corroborate that the Agulhas Ring, initially connected to the surface, subducted into the ocean interior while leaving the Cape Basin and penetrating into the South Atlantic subtropical gyre. We follow here the definition of subduction by Williams [2001] who defined it as the transfer of fluid from the mixed layer to the stratified thermocline (i.e. below the seasonal Mixed Layer). It is clear that the winter mixed layer developing between March 2013 and September 2013 stays separated from the shallower eddy-core of homogeneous water. However, it is difficult to select the main process generating the subduction between the modification of upper layer due to atmospheric forcing or the drifting of the eddy below the lighter water. To answer this question, the TS diagram of the Argo profiles with a $Dc < 25$ km (red) and those with a $150 < Dc < 200$ km (blue) sampling the segment 5 between November 2012 and November 2013 after the subduction are plotted in the Figure D.4 in the appendix. We see from this figure that the water masses in the upper layer in the eddy are different than those in the environment. Knowing that the non-linearity parameter for trapping water parameter [Flierl 1981; Chelton et al. 2011] is verified at the surface over all the time series where the minimum of V_{max} is larger than 0.2 m s^{-1} (see Figure 4.3) while the drifting speed of the eddy is smaller than 0.1 m s^{-1} and knowing that the water masses at the surface of the eddy are significantly different than the environment, this subduction seems to be the results of surface modification of advected water in the AR which are then detached from the main hydrological core. Using very high-resolution numerical simulations in the Cape Basin, Capuano et al. [2018a] showed that submesoscale instabilities (of different type) generate deep mixing layer formation during winter and the upper layer restratification during summer that might explain the detachment of the sub-surface core.

Between October 2012 and August 2013, Figure 4.7 reveals the presence of a second, albeit thinner, homogeneous layer located at greater depth than the first one (between 500 and 600 m of depth). It corresponds to the second thermohaline anomalies core that appears in the Argo vertical profiles sampling the Agulhas Ring (Figure 4.5). After August 2013, the Argo profiles sample the eddy farther from the eddy center. This prevents any conclusion on the reason making this deeper core of MW disappear. Indeed, on August 2013, the eddy is located over the Mid-Atlantic Ridge. It might be that the interaction between the eddy and the topography caused an intense mixing at depth with neighboring waters. Or, it might be that, because of the larger distance of the sampled profiles from the eddy center after August 2013, this core of MW that was probably small in its lateral extent, was not sampled by the Argo floats.

To prevent the interference of the varying position of Argo floats while attempting to determine the eddy evolution in time, we select, in the following, only those Argo profiles located within the eddy core (i.e., $Dc < R_{Vmax}$). The density anomalies associated to four profiles separated by three or four months between June 2012 and August 2013 are shown as solid lines in Figure 4.9a. All these profiles are located inside the eddy and close to its center (15 km $< Dc <$ 30 km), albeit it is

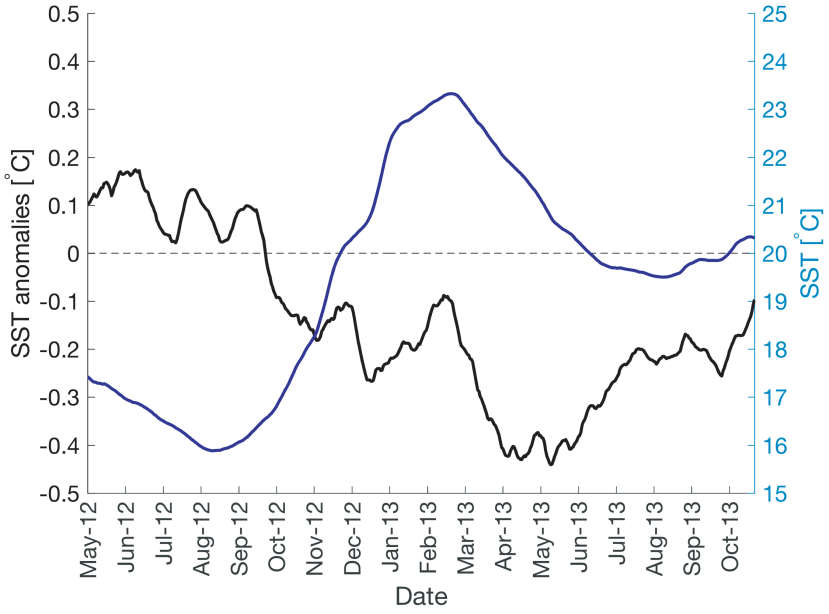


Figure 4.8: Sea Surface Temperature (blue) and associated anomalies (black) interpolated from the ODYSSEA SST dataset [Autret and Piolle 2011] at the position of the center of the AR. The anomalies are computed subtracting the mean SST computed in the region at less than 300 km from the eddy center to the SST at the center. All the data were smoothed by a moving average associated to a monthly window.

worth mentioning that the accuracy on the determination of the eddy center from ADT maps is limited and this might induce significant errors in Dc estimates. For comparison, Figure 4.9a presents, in dashed line, a vertical profile undertook in January 2013 by an Argo float far from the eddy center ($Dc = 151$ km). From this figure, it appears clearly that this profile does not sample any of the eddy MW cores.

Figure 4.9b shows the depth of the two Agulhas Ring MW cores as a function of Dc computed by taking a large number of Argo profiles, all located near the eddy center ($Dc < 40$ km) and defined as the vertical maxima of thermohaline anomalies. The vertical location of the two thermohaline anomaly maxima varies weakly with time and with the distance of the Argo profile from the eddy center. We also computed the STD of the residual between each extremum and the linear regression obtained between Dc and the depth of the two anomaly peaks. We considered as outliers those profiles whose residuals are larger than the STD (Figure 4.9b). From this, it appears that two of the three profiles that sampled the eddy before it subsided below the surface in November 2012 differ significantly from the others. For the latter, the density anomaly of the core seems to keep roughly the same depth for several months.

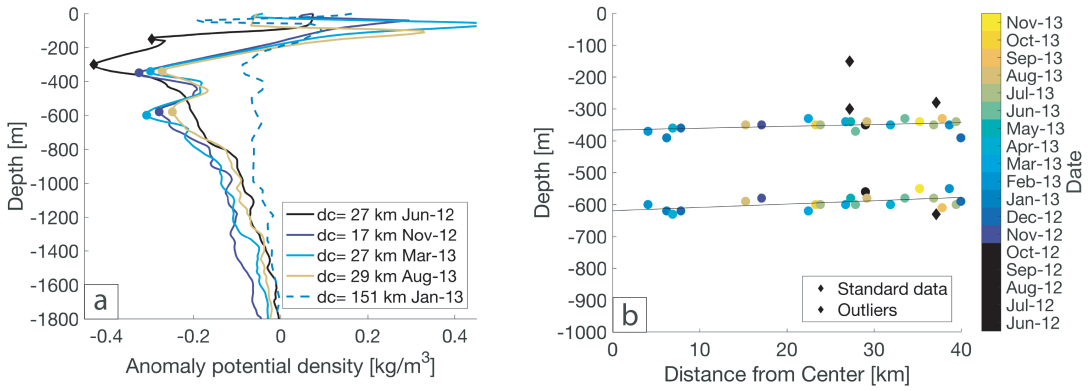


Figure 4.9: a) Argo vertical profiles of density anomaly. 4 lye close to the eddy center and show the two Mode Waters thermohaline extrema (plain lines) and 1 is located farther (dashed lines) and does not display these two Mode Waters related extrema. b) Depth of the two Mode Water cores as a function of Dc for all the profiles lying at less than 40 km from the eddy center. An outlier is identified if both extrema in a profile are at a distance from the black lines larger than the STD associated to the determination of each extremum.

Reconstruction of the subsurface structure of an Agulhas Ring

Figures 4.5 and 4.7 show that, from November 2012 to November 2013, the upper 150 m layer of water within the Agulhas Ring limits were characterized by a strong seasonal variability whereas, below it, the thermohaline properties undergo small variations. We therefore assumed, at the first order of approximation, that the Agulhas Ring, below 150-200 m of depth, was in a quasi-steady state and that the upper 150 m layer of water did not belong anymore to the eddy main hydrological core.

Similarly to the assumptions of Souza et al. [2011a] and Nencioli et al. [2018], we also hypothesized that the eddy had a quasi-circular symmetry. The amplitude of the subsurface anomaly will then depend only on the distance Dc between the Argo float position and the geometrical eddy center. As discussed previously, R_{Vmax} can be considered constant during, at least, the period November 2012 – November 2013 (with a median and mean radius of 64 km and a STD of 8 km). However, to test the validity of a quasi-circular eddy assumption, we estimated the ellipticity (ϵ) of the characteristic eddy contours derived from the daily ADT maps, from equation 4.5 where a is the semi major and b the semi minor axes.

$$\epsilon = 1 - \frac{b}{a} \tag{4.5}$$

The ellipticity remains small from November 2012 to November 2013, with a median value of 0.11, a mean of 0.12 and a STD of 0.07. We, therefore, restricted

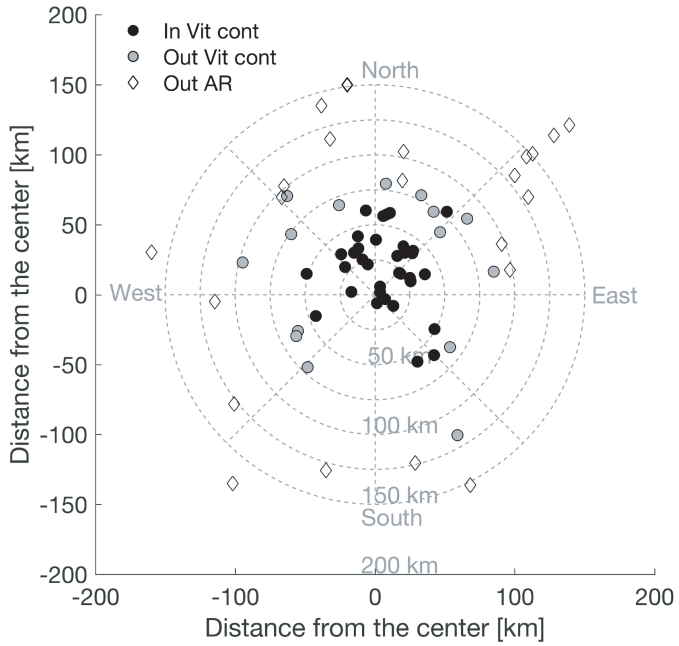


Figure 4.10: Position of the Argo profiles in the moving frame of the Agulhas Ring. The center of the frame corresponds to the centroid of the characteristic eddy contour delimited by R_{Vmax} and computed from ADT maps. The filled circles indicate Argo profiles inside the characteristic eddy contour, the gray circles those inside outer eddy edge and the empty diamond those outside the Agulhas Ring and any other neighboring eddy and lying in a 160 km radius from the Agulhas Ring center.

our analysis to this period of one year to ensure the validity of the axisymmetry hypothesis for the eddy which would otherwise not be valid for large ellipticity values.

In order to reconstruct the Agulhas Ring axisymmetric structure, we use 71 Argo profiles that were located within a distance of 185 km (i.e. $\sim 3 \times R_{Vmax}$) from the geometrical eddy center (Figure 4.10) during the November 2012 – November 2013 time period. More than 54% of the profiles were achieved by the Argo float No. 5902281, whereas 46% were undertaken from five other floats that surfaced sporadically inside the eddy. Overall, during the given one year time, the eddy was sampled by 52 profiles within a distance of 100 km from the eddy center.

Different techniques have been used in the literature to attempt a reconstruction of the vertical structure of mesoscale eddies from sparse *in situ* observations. Most of them employed a composite eddy reconstruction approach [e.g. Schütte et al. 2016; Amores et al. 2017], others tried to recover the structure of specific eddies. For example, Chaigneau et al. [2011] objectively mapped observations onto a 10 km grid assuming an isotropic Gaussian covariance decorrelation scale of 100 km or Souza et al. [2011a] fitted to a 7th order one-dimensional Lagrange polynomial. However, the Gaussian method smooths out horizontal gradients, whereas high

order polynomials often induce an overshooting of the hydrological variables at the outer edge of the reconstructed eddies. To avoid these drawbacks, we used a generic function tending towards zero outside the eddy.

The generic function we used to fit the (CT, AS) anomalies we defined previously at each depth (see equation 4.6) is that of an α-Gaussian vortex [see for example Carton 2001; Le Vu et al. 2018]. The parity of this generic function ensures the axisymmetry of the reconstructed eddy and an exponential decrease of its anomalies far from the center. The $A_0(z)$ profile represents the maximal core anomaly inside the eddy. To suggest a first guess for $A_0(z)$, we use the mean of the three Argo profiles closest to the eddy center while the parameters α and $R_0(z)$ are set initially to 2 (i.e. a purely Gaussian shape as used by Nencioli et al. [2018]) and R_{Vmax}= 64 km respectively. Then, the three parameters (A_0, R_0 and *alpha*) associated to the generic function 4.6 are adjusted at each depth level minimizing the residuals between the fitting of the equation and the observations using the Trust Region Reflective algorithm [Branch et al. 1999] with the function lsqcurvefit of the MATLAB Library. Below 200 m, the values obtained for the various parameters by fitting the function 4.6 are $\alpha = 2$ with a STD of 0.4 and $R_0 = 69$ km with a STD of 16 km.

$$Anom(r,z) = A_0(z)e^{-\frac{1}{\alpha}\left(\frac{r}{R_0(z)}\right)^{\alpha}} \tag{4.6}$$

Finally, to obtain a first estimation of the thermohaline structure of the Agulhas Ring ($Anom(r,z)$), we added the average of all the profiles of the environment computed for each vertical level to the reconstructed anomalies.

In Figure 4.11 are present the isolines of CT, AS, and σ_0 for the reconstructed Agulhas Ring (defined with the acronym RecAR in the following) superimposed over the raw Argo profile data plotted as a function of *Dc*. A more detailed examination of the σ_0 reconstruction is shown in Figure D.5 in the Appendix. Both figures show, below the surface, a particularly good agreement between the isocontours of RecAR and the raw Argo data.

Figure 4.11 shows clearly two layers of homogeneous thermohaline properties. A first one is centered around 250 m of depth, between the isolines 17°C - 15°C, 35.9 g kg^{-1} - 35.7 g kg^{-1}, and 26.1 kg m^{-3} - 26.3 kg m^{-3}. The maximal thickness of this layer is ~350 m at the eddy center. The second homogeneous layer is centered at 500 m of depth, and it is characterized by the isolines intervals 13°C - 11°C, 35.5 g kg^{-1} - 35.3 g kg^{-1}, and 26.5 kg m^{-3} - 26.7 kg m^{-3}.

In order to test the accuracy of the three-dimensional reconstruction, we computed the root mean square (RMSE) of the difference between the *in situ* measurements provided by every Argo profiles and RecAR (Figure 4.11d). The values of RMSE vary between 0.01 and 0.05 kg m^{-3} which is six times less than the maximum σ_0 anomalies. This gives us confidence in the eddy properties reconstruction.

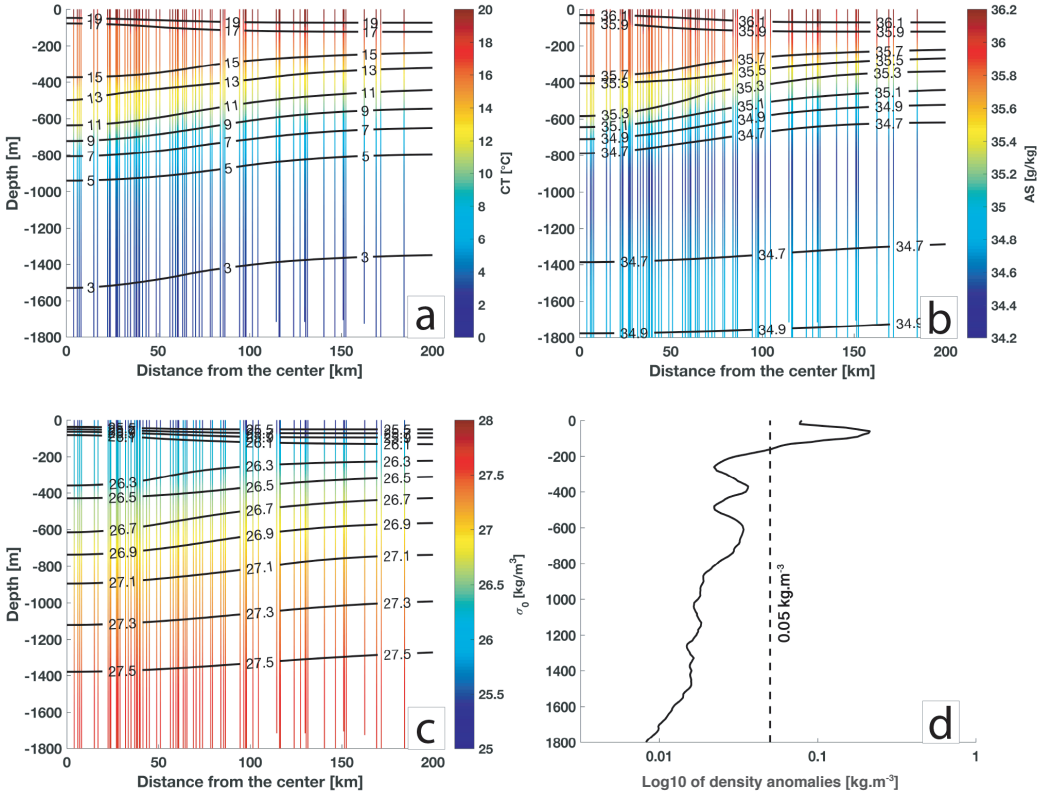


Figure 4.11: Superposition of the observed (background color) and the reconstructed (black contours) Agulhas Ring of the a) Conservative Temperature, b) Absolute Salinity, c) σ_0, and d) root-mean-square error between the observed σ_0 anomalies and the reconstructed values computed at each depth.

The two local maxima at 400 and 700 m of depth in Figure 4.11 correspond to the region of strong variation of properties when moving from the eddy center outward along a same depth. However, near the surface the errors are considerably larger. The RMSE value of 0.05 kg m^{-3} lies between 150 and 160 m of depth whereas the largest RMSE value (0.2 kg m^{-3}) is found at 60 m. At these depths waters undergo to a strong seasonal forcing and therefore we cannot consider that the thermohaline properties of the eddy remain here constant for the whole year. As discussed previously, the Agulhas Ring has subducted below the subtropical gyre upper 150 m of warm waters. Hence, we assumed that the eddy upper limit is below this layer. We choose as such limit for RecAR a specific isopycnal, the 26.2 kg m^{-3} isopycnal which corresponds to the specific limit identified in the Figure 4.5 as the separation between the part of the water column that evolves over time and the one which is steady below it, rather than a fixed depth. It is important to note here that the depth of this isopycnal varies between 150 m near the eddy center and 170 m away from it. In what follows, we will consider as RecAR the waters lying below the 26.2 kg m^{-3} isopycnal surface.

By using RecAR as the reference, we computed the error associated to the

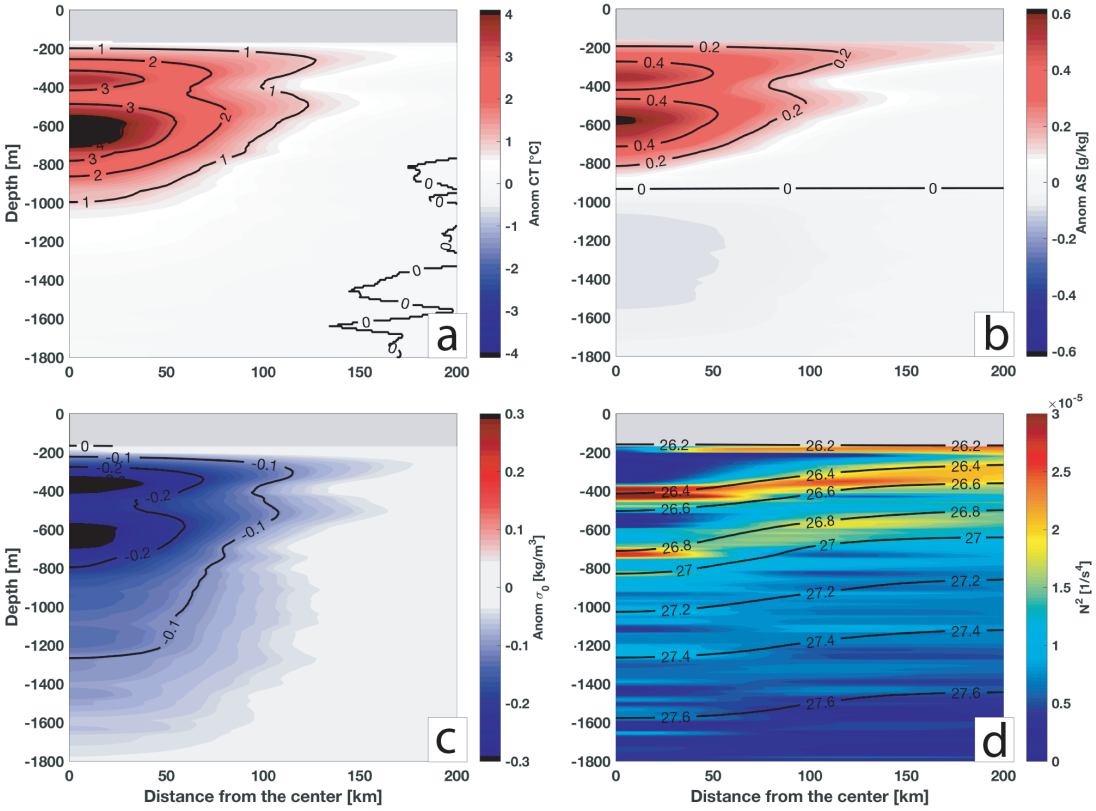


Figure 4.12: Anomalies of a) Conservative Temperature, b) Absolute Salinity, c) σ_0, and d) Brunt Väisälä frequency squared (N^2) for the Reconstructed Agulhas Ring. Contours in d) are isopycnals of the Reconstructed Aulhas Ring. The grey patch near the surface in each panel corresponds to the region above the isopycnal surface 26.2 kg m^{-3} which marks the separation between the subtropical gyre upper warm waters and the eddy upper limit.

values of *Dc* obtained in collocating the Argo profiles with the eddy as detected by the TOEddies algorithm. A distance is computed between each observation on the σ_0 levels, between 200 m and 1000 m of depth, from the Argo profiles and the corresponding value in the RecAR. This corresponds to the distance between each observation and the RecAR isoline taken at the same depth as shown in the Figure D.5. The lower-limit depth of 1000 m was fixed as the horizontal gradient of σ_0 is weak below this depth. This would have impacted the accuracy in the determination of *Dc*. From the ~5000 estimates we computed a median and mean values for *Dc* that resulted to be identical and equal to 14 km associated to a STD of 17 km.

Figure 4.12 shows the CT, AS, and σ_0 anomalies of RecAR as well as the Brunt Väisälä frequency squared (N^2). Such reconstruction clearly shows for RecAR a dual core structure. This is particularly discernible from the two low stratification blobs in Figure 4.12d). The anomalies are important as they materialize the eddy

content and transport of properties, such as heat and salt. The upper core lies at 350 m with peak anomalies of 3.7 °C, 0.56 g kg^{-1} and -0.35 kg m^{-3} for, respectively, Conservative Temperature, Absolute Salinity and Potential Density. The lower core lies around 550 m of depth and is characterized by anomalies of 4.4 °C, 0.62 g kg^{-1} and -0.31 kg m^{-3}. The anomalies of conservative temperature and absolute salinity are more intense within the lower core but, due to their inverse effect on density, the density anomalies are nearly equal for both cores.

In order to estimate the three-dimensional velocity structure (i.e. $V(r, z)$) for RecAR we use the non-linear thermal wind equation 4.7 [see Ioannou et al. 2017 ; for example]:

$$\frac{1}{r}\frac{\partial V^2}{\partial z} + f\frac{\partial V}{\partial z} = \frac{-g}{\rho_0}\frac{\partial \rho}{\partial r} \tag{4.7}$$

To solve this partial differential equation, the velocity field is set to 0 at 1800 m of depth (i.e. $V(r, z = -1800) = 0$). The resulting velocity field is shown in Figure 4.13a. The maximum value of the azimuthal velocity is equal to 31 $\times 10^{-2}$ m s^{-1}. It is located at 200 m of depth and at a distance of 66 km from the eddy center. This value is very close to the mean maximum speed radius, R_{Vmax} = 64 km, estimated from the surface geostrophic velocity field during the one year period. In comparison to the grid resolution of ADT maps (1/4 °), this difference in values is negligible.

In order to estimate the limits of the volume of water trapped within RecAR, we computed the translation speed of the eddy during the period of time of interest. For this we used the trajectory of the geometrical center of the eddy computed by TOEddies. The resulting mean translation speed is 5.9 ± 1.4 $\times 10^{-2}$ m s^{-1} where ± indicates the STD. We then identified the line delimiting the trapped water inside RecAR (called separatrix hereafter following De Steur et al. [2004]) by hypothesizing that the eddy is circular and is moving at constant speed. Here we followed Flierl [1981], who defined the volume of trapped water in an eddy as the envelop of depths enclosed within the outer eddy limit, where the azimuthal speed is equal or higher than the translating speed of the eddy.

The black solid line in Figure 4.13a indicates the approximate location of the separatrix at each depth and the two black dashed lines delimit the STD (± 1.4 $\times 10^{-2}$ m s^{-1}) of the mean translation speed. The separatrix is located below 1000 m of depth at less than ~100 km from the eddy center. To be noted here that 1000 m is the parking depth for most of the core Argo floats. The fact that the eddy is coherent at this depth explains why the Argo float No. 5902281 remained trapped within the structure for so long.

We also compared the steady horizontal velocity structure of RecAR with the eddy evolving surface geostrophic velocities derived from satellite altimetry. Figure 4.13b shows the various surface geostrophic velocity profile derived from

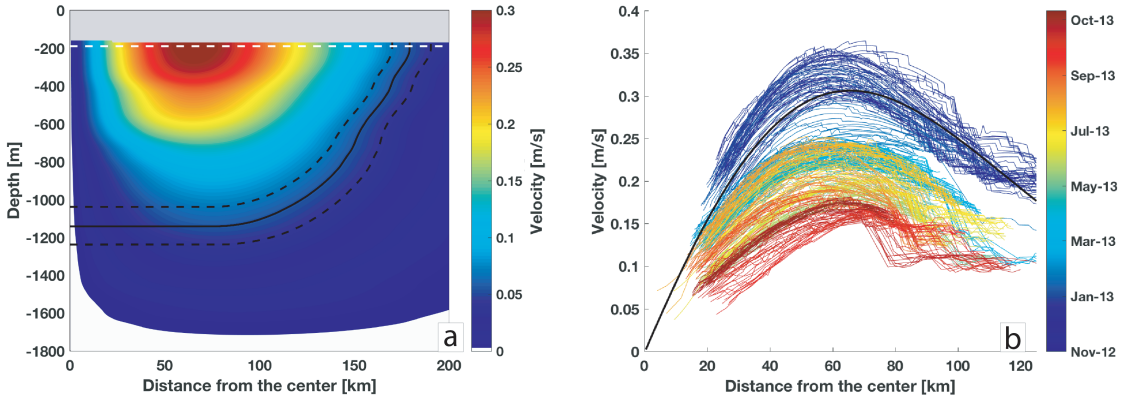


Figure 4.13: a) Velocity field of the Reconstructed Agulhas Ring computed from hydrographic data and b) evolution of the geostrophic currents derived from satellite altimetry maps as a function of the distance from the center. The black line in b) is the velocity derived from hydrographic data at -200 m (i.e. where this velocity is maximum). A dashed white line is added at this depth in panel a). The black line in panel a) corresponds to the separatrix where the velocity is equal to 5.7×10^{-2} m s^{-1} which is the median translation speed during the period November 2012 - November 2013. The two dashed lines correspond to this value ± a STD of 1.4×10^{-2} m s^{-1}. The grey patch in panel a corresponds to the region above the isopycnal surface 26.2 kg m^{-3} which marks the separation between the upper subtropical gyre waters and the upper limit of the eddy.

satellite altimetry and provided by AVISO (in colors, starting in November 2012 with the blue color and ending in Oct. 2013 with the red color) as well as the velocity profile at 200 m of depth (black solid line). The latter corresponds to the white dashed line in Figure 4.13a and it depicts the position where the azimuthal velocities reach a maximum. During the given period of time, the V_{max} derived from satellite altimetry decreases with time from 35 $\times10^{-2}$ m s^{-1} to 15 $\times10^{-2}$ m s^{-1}while R_{Vmax} remain approximately constant (Figure 4.3a). Therefore, in less than a year, the surface geostrophic velocity corresponding to the eddy position dropped to half the value of the mean RecAR subsurface geostrophic velocity intensity. Given the large extent of the Agulhas Ring (both horizontally and vertically) and its intense thermohaline signature, we suggest that the observed decrease in the surface velocity is not due to a mechanism of dissipation of the eddy, but to the decorrelation of the structure main core from the upper water layer attributable to its subduction happening during the Fall 2012. This is confirmed by the hydrological anomalies being, near the ocean surface, of opposite sign than those in the eddy subsurface core as suggested by Assassi et al. [2016] and Schütte et al. [2016]. As a consequence, the surface layer has an inverse effect on the vertically integrated properties (such as dynamic height, the eddy geostrophic velocity, etc) than that of the eddy at its core. This can explain, at least partially, the observed decrease in such variables observed since the subduction of the Agulhas Ring.

Integral properties of the subsurface Agulhas Ring

We used the separatrix and the 26.2 kg m^{-3} isopycnal surface to identify both the eddy lower (z_s) and upper (z_0) limits to compute the RecAR volume. This amounts to $7.2\times10^{13} \pm 1.5\times10^{13}$ m^3 where the confidence interval is computed using the STD of the eddy translation speed (as it impacts the volume integration). The temperature and salinity anomalies integrated between z_s and z_0 for both, the Argo profiles and RecAR, are presented in Figure 4.14. Here again, a clear relationship appears between these values and the distance Dc from the eddy center. Moreover, the anomalies computed for RecAR and directly from the Argo profiles are in good agreement which give confidence to our results and methodology.

$$HCA = 2\pi \int_0^{R_s} \int_{z_s}^{z_0} \rho C_p \Delta T r d_r d_z \tag{4.8}$$

$$SCA = 2\pi \int_0^{R_s} \int_{z_s}^{z_0} \rho \Delta S r d_r d_z \tag{4.9}$$

We estimated the eddy anomalies of heat (HCA) and salt (SCA) contents from the temperature and salinity anomalies we computed for RecAR and by integrating the equations 4.8 and 4.9 where, $C_p(T)$ is the heat capacity, $\rho(r, z)$ the density, $\Delta T(r, z)$ the conservative temperature anomalies and $\Delta S(r, z)$ the absolute salinity anomalies of RecAR whereas $R_s(z)$ is the radius of the separatrix. It is then possible to integrate, along the vertical, such anomalies to assess the total integrated HCA and SCA for RecAR. The values we obtained are, respectively, $2.6\times10^{20}\pm 1.3\times10^{19}$ J and $7.3\times10^{12}\pm 5.8\times10^{10}$ kg where the STD values comes from the ring translation speed to have an indication of the confidence interval as it directly impacts the eddy volume of integration.

To be able to compare to simpler estimates not depending on a precise determination of the eddy volume defined by the separatrix, we integrated the RecAR temperature and salinity anomalies from 1800 to 150 m of depth over the 200 km area around the eddy center. The values we obtained are 3.0×10^{20} J for HCA and 5.2×10^{12} kg for SCA. The estimates obtained by the two approaches are very close for HCA whereas the differ significantly for SCA. This is very likely due to the presence of a negative patch of AS anomalies that does not enter into account in the estimates obtained from the first approach as this patch lies below the eddy trapping depth (Figure 4.12b).

Finally, the instantaneous volume, heat and salt transport anomalies are computed following the method introduced by Olson and Evans [1986] and also used by Doglioli et al. [2007]. These physical quantities are obtained by multiplying the integrated eddy properties with the translation speed divided by the diameter of the structure. They account for the transport generated by an eddy crossing an imaginary section. The resulting volume, heat and salt transports are, respectively,

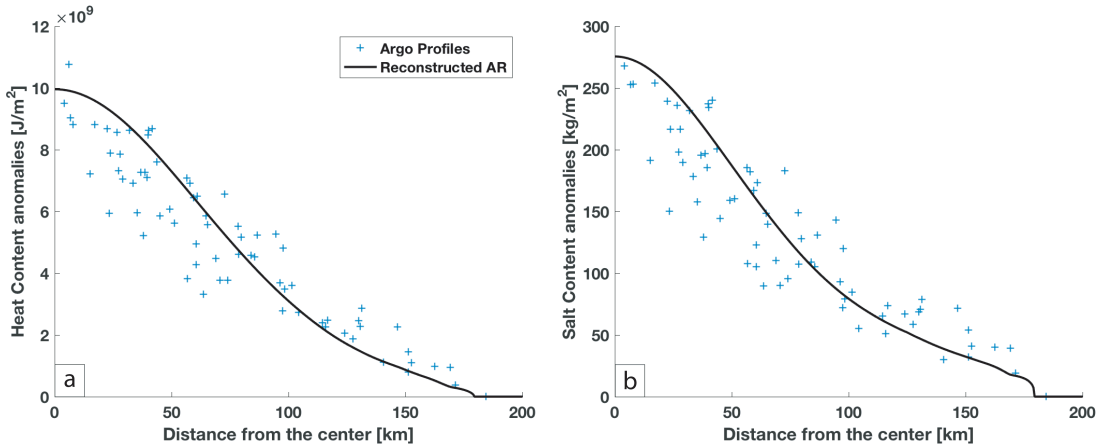


Figure 4.14: Anomalies of a) Heat Content and b) Salt Content as a function of the distance from the eddy center derived for both, the reconstructed Agulhas Ring and the Argo profiles sampling the eddy. These values are obtained by integrating vertically from the eddy separatrix up to 200 m equations 4.8 and 4.9.

11 ± 1 Sv, 0.04 ± 0.01 PW, and $1.2\times10^6\pm 3.5\times10^5$ kg.s^{-1}. These fluxes estimates are large as they correspond to the instantaneous transport of an Agulhas Ring. However, they cannot be used to compare directly with most estimates given in the literature as these estimate the generic impact of Agulhas Rings by dividing the volume, heat and salt contents of each ring by the number of second in one year [e.g. van Ballegooyen et al. 1994; Garzoli et al. 1999]. By using this generic approach, the transport of volume, heat, and salt would amount to, respectively, 2.3 Sv, 8.2×10^{-3} PW, and 2.3×10^5 kg s^{-1}.

4.2.4 Comparison with Agulhas Rings identified in the literature

Since more than two decades, numerous Agulhas Rings were sampled by *in situ* data and described in the literature. In this section, we compare the subsurface properties of RecAR with 27 different Agulhas Rings described in the literature (see Table 4.1 for a list of all these studies).This database constitutes an important frame of reference to test the robustness of the properties and characteristics we derived for RecAR (as, for example, the presence of MWs in its core, or its subsurface nature since it crossed the Walvis Ridge). In the following, we first introduce the general structure of the observed Agulhas Rings, then we focus on MWs properties with an emphasis on those found within the rings and, finally, we compare estimates of their volume as well as heat and salt contents.

Table 4.1: List of all the studies that described at least one Agulhas Ring in depth during dedicated oceanographic cruises. To be noted here that the list is limited to those Agulhas Rings that were sufficiently documented in the referenced studies.

Article	Number of Eddy
Gordon et al. [1987]	2
McCartney and Woodgate-Jones [1991]	1
Duncombe Rae et al. [1992]	1
van Ballegooyen et al. [1994]	4
Duncombe Rae et al. [1996]	6
Arhan et al. [1999]	3
Garzoli et al. [1999]	3
McDonagh et al. [1999]	2
Schmid et al. [2003]	1
Gladyshev et al. [2008]	1
Arhan et al. [2011]	1
Casanova-Masjoan et al. [2017]	1
Guerra et al. [2018]	1
TOTAL	27

Agulhas Rings general vertical structure and classification

The Agulhas Ring described in this study is characterized by two cores of MWs that concentrate the essential fraction of the ring anomalies when compared to surrounding waters. In the following we wish to verify if this is a common if not general vertical water masses organization for Agulhas Rings. Out of the 27 referenced eddies, 23 were sufficiently described in the literature to be used for the comparison [Gordon et al. 1987; McCartney and Woodgate-Jones 1991; Duncombe Rae et al. 1992; van Ballegooyen et al. 1994; Duncombe Rae et al. 1996; Arhan et al. 1999; Garzoli et al. 1999; McDonagh et al. 1999; Schmid et al. 2003; Gladyshev et al. 2008; Arhan et al. 2011; Casanova-Masjoan et al. 2017; Guerra et al. 2018]. We identified single or double core MWs eddies those Agulhas Rings whose vertical structure displays one or two homogeneous layers thicker than 100 m and separated by, at least, two isotherms of θ<1°C and two isohalines of PSU<.2°. These eddies were observed during a synoptic cruise each. Thus they can be associated to a single center position whereas the Agulhas Ring we analyze in this study has been sampled by various Argo profiles along a segment of its trajectory. Hence, it cannot be associated to a single position for its center. Consequently, hereinafter we will refer to the averaged location of the segment of trajectory that we reconstructed as the position of RecAR.

In the group of the 24 Agulhas Rings we analyzed (i.e. 23 from the literature and RecAR), all of them show at least a core of water with homogeneous hydrological properties, and 4 of them exhibit two of such cores (see Figure 4.15a). Three of them were observed northwest of the Cape Basin, as it was the case for RecAR,

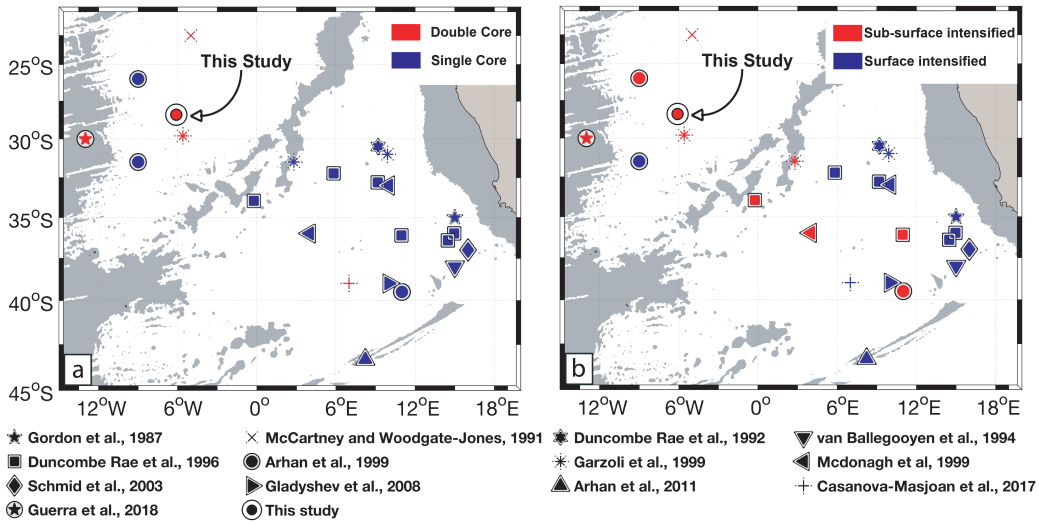


Figure 4.15: Number of a) cores and b) type of internal structure of the Agulhas Rings described in the literature. Each article is associated to a unique marker type. The gray shading patches in a) represent water depth shallower than 3500 m in the ETOPO2 data set [Smith and Sandwell 1997].

whereas the other one is found inside this basin.

We also tried to distinguish, among the documented rings in the literature, those eddies that could be considered surface intensified and those (if any) that could be described as subsurface structures. The classification of eddies as surface or subsurface intensified structures is difficult from sparse CTD data. Indeed, due to air-sea interactions a seasonal thermocline can appear near the ocean surface that might not, necessarily, isolate the eddy structure from the mixing layer during the entire annual cycle. Consequently, we have characterized as subsurface intensified eddies according to their shape. Following the schematic view presented by Assassi et al. [2016], subsurface intensified Agulhas Rings are defined as those anticyclones showing a lenticular shape with isopycnals on the top of the homogeneous core shallower at the eddy center and deeper at the eddy edge. Among such categorization of subsurface eddies, an exception is the eddy described in Guerra et al. [2018] whose structure was derived from a single profile. The first homogeneous core documented by Guerra et al. [2018] lies below 100 m. We associated it to a sub-surface eddy even if the horizontal structure of the eddy is not provided.

Among the 23 Agulhas Rings we selected from the literature, 10 of them (i.e. ~40 %) are subsurface intensified and they are indicated with red markers in Figure 4.15b. In general, they align along the southeast-northwest diagonal in the center of the Cape Basin following the main Agulhas Rings route [Dencausse et al. 2010a; Guerra et al. 2018; Laxenaire et al. 2018 ; e.g.] whereas the surface intensified ones (in blue in Figure 4.15b) lie closer to the Agulhas Retroflection area and the continental slope of the Cape Basin. It is worth noting that the eddy described by Arhan et al. [2011] that was observed while sitting above the Agulhas

Ridge is also a surface intensified eddy associated to a surface mixed layer depth of ~30 m which capped an homogeneous layer of more than ~500 m of thickness Arhan et al. [2011]. Consequently, his characterization as surface or subsurface eddy is not straightforward. Similarly, the eddy described by Casanova-Masjoan et al. [2017] shows a lenticular shape in salinity but not in temperature nor in potential density (see Figure 3 in Casanova-Masjoan et al. [2017]). Consequently, its classification as either surface or subsurface eddy was also difficult. As its upper part lies very close to the ocean surface we categorized it as surface intensified eddy. Three among the subsurface intensified eddies show a double core with homogeneous properties with a very similar vertical structure as RecAR. Two of them were found in the Southeast Atlantic, as RecAR.

In conclusion, we categorized the whole set of Agulhas Rings in four different categories according to the number of cores with homogeneous properties and if they were or not surface intensified eddies.

Agulhas Rings Mode Waters

The two-dimensional axisymmetric structure of RecAR has two distinct core with homogeneous water properties that fall in the MWs category. As these waters are responsible of the essential part of the eddy heat and salt anomalies (with reference to the environmental waters), it is important to compare the RecAR properties with similar structures documented in the literature to estimate the commonalities of their properties as well as their origins. Among the 27 Agulhas Rings identified in previous studies (see Table 4.1) that show one or two cores of MWs, 5 (i.e. ~20 %) have their upper limit shallower than 50 m. For these 5 eddies, the subsurface homogeneous layer has been described as a deep mixed layer by the authors of the related studies. Deep homogeneous layer are indeed thought to be the first and necessary phase of MWs formation [e.g. Alfultis and Cornillon 2001; Joyce 2012; Sato and Polito 2014]. This deep mixed layer have been shown to be common in eddies, and they appear to occur preferentially in anticyclones than in cyclones [Kouketsu et al. 2012; Sato and Polito 2014].

The hydrological properties of the documented Agulhas Rings MW cores are presented in Tables D.2 and D.3 in the Appendix and the position where these eddies were sampled and their θ-S characteristics are shown in panels a and b of Figure 4.16. Figure 4.16b shows that their properties range from 25.4 to 26.8 kg m^{-3} in σ_0, from 12 to 19 °C in potential temperature and from 35.08 and 35.75 in (practical) salinity units.

As discussed in the Introduction, various MWs are described in the literature. We have summarized their properties in Table D.1 in the appendix. Even if very similar, they all show small property differences. Recently de Souza et al. [2018] discussed a possible contribution of distinct MWs to South Atlantic Central Water (SACW). However, as they decomposed SACW by MWs contribution, the specific

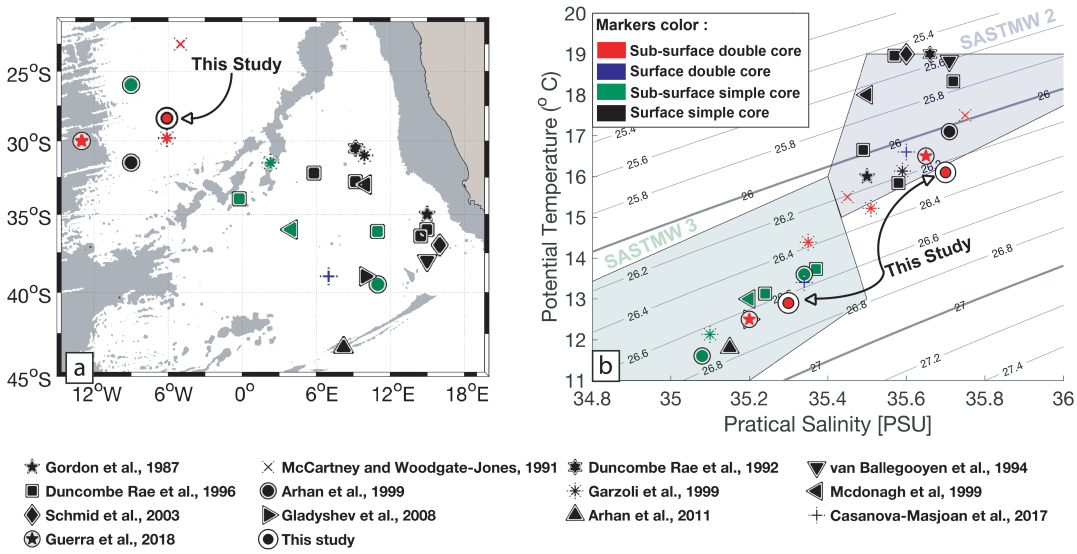


Figure 4.16: a) Position and b) hydrological properties in the Mode Water cores of the Agulhas Rings described in the literature. Each study discussing one or more of these eddies is associated to a specific marker and the color correspond to a particular type of eddy. Double Mode Water core eddies have two similar markers. The gray shaded patches in a) represent water depth shallower than 3500 m in the ETOPO2 data set [Smith and Sandwell 1997]. The background lines in b) represent isopycnals of potential density anomalies referenced to the surface pressure (σ_0). The blue and green shaded patches highlight the hydrological properties of, respectively, SASTMW2 and SASTMW3 as described by Sato and Polito [2014].

hydrological properties of de various SATMWs cannot be derived directly from that publication.

Here, we compared the whole set of Agulhas Ring MWs (that includes RecAR and all those found in the literature) to Sato and Polito [2014] SATMWs. Figure 4.16 presents the Sato and Polito [2014] SATMWs hydrological distributions as areas shaded in blue (SASTMW2) and green (SASTMW3). We do not consider here SASTMW1 which is only found west of 30°W whereas SASTMW2 and SASTMW23 occupy the eastern South Atlantic sector. SASTMW2 and SASTMW3 are separated by the 35°S parallel (see Figure 4 in Sato and Polito [2014]).

Agulhas Rings MW cores properties fall in the range of SASTMW2 and SASTMW3. Moreover, more than 50% of these Agulhas Rings MW cores have properties within the generic SASTMW characteristics (see Table D.1 in the appendix). In particular, nearly all the surface Agulhas Rings that have a single MW core (in black) are in the range of SASTMW2 whereas the whole set of subsurface Agulhas Rings with a simple MW core (green) fall in the SASTMW1 category. The only exception is the eddy described by Arhan et al. [2011] which shows a particularly thick homogeneous layer capped by a narrow surface layer. We identified it as a surface intensified eddy as the surface layer was only 30 m

thick. However, this eddy that was observed by the 2008 GoodHope cruise in late February, was clearly in the beginning of a subduction phase as it disappeared from the altimetry few months later (at the beginning of April 2008, [Arhan et al. 2011]). Given the size and energy of this Agulhas Ring, it is improbable that it just dissipated so quickly.

When looking at the spatial organization of sinngle MW core Agulhas Rings in Figure 4.16a, those that are surface intensified mainly lie near the African continental slope covering the eastern part of the Cape Basin. The subsurface ones, on the other hand, are essentially found in the central part of basin, along the AR central path [Laxenaire et al. 2018].

Double MW core Agulhas Rings have a simpler distribution. Most (4) subsurface double MW core rings were observed north/north-west of the the Cape Basin. That described by McCartney and Woodgate-Jones [1991] shows SASTMW2 characteristics, whereas the others three (Garzoli et al. [1999], Guerra et al. [2018] and RecAR) have properties falling in both varieties of SASTMW (see Figure 4.16b). Only one surface double-core eddy was identified in the literature so far (by Casanova-Masjoan et al. [2017]) lying in the center of the Cape Basin. The MW cores of this show both, SASTMW2 and SASTMW3 properties.

Arhan et al. [1999] and Arhan et al. [2011] have suggested that Agulhas Rings hydrological properties are intimately linked to their past history. Indeed, these studies have suggested that depending on the route undertaken by these eddies (northern, central or southern according to Dencausse et al. [2010a]), the time they spend within the subantarctic regions, if they experience a wintering or not, are factors that determine the water properties of the upper 1000 m of these structures, mediated by strong air-sea interactions and mixing with environmental water. This might explain why, even if some correspondence between geographical regions and Agulhas Rings characteristics appear, there seem to be a not clear pattern. On the other hand, Garzoli et al. [1999] and Gladyshev et al. [2008] have suggested that Agulhas Rings displaying a multiple core structure might be explained either through the merging of two rings with distinct histories or by two consecutive mode water formation during consecutive years.

Our study cannot resolve completely the origins and diversity of Agulhas Rings MW properties and structure. Indeed, while the formation of the upper MW core was well captured by the profiles achieved by the Argo float No. 5902281 during the time it was trapped within the eddy core, we do not have any information on the MW ventilation of the second and deeper one. The whole set of profiles that sampled Segments 1, 2 and 3 before they merged into Segments 4 and 5 (see Figure 4.2) did not sample the eddy structures close to the center so they cannot be assumed as characterizing the inner eddy vertical structure. It should be noted that Segment 1 spent an entire winter south of 40°S, in the strong westerlies blowing in the subantarctic region, before its merging with Segment 4 to form Segment 5. Segment 1 is very close albeit it crossed the Walvis Ridge slightly northward to the eddy observed by Arhan et al. [2011]. The latter could explain the fact that

both eddies display SASTMW2 characteristics, but the deeper core of RecAR is relatively warmer and saltier than the homogeneous layer of the eddy discussed by Arhan et al. [2011] suggesting that RecAR underwent to less intense air-sea interactions. Other published studies have suggested that MWs observed within Agulhas Rings are or might derive from modified (Indian) SAMW [e.g. Arhan et al. 1999; Gladyshev et al. 2008] or Subtropical Indian MW [de Souza et al. 2018]. However, the definitions of both of these two MWs are not precisely defined (see Tab D.1 in the appendix) which prevent any clear conclusion. We can just suggest that Agulhas Rings are large coherent structures advecting, south of Africa, Agulhas Current waters (i.e., Subtropical Indian waters). These waters are transformed underway by ocean-atmosphere interactions. As suggested by Arhan et al. [2011], these exchanges, when occurring during winter, give rise to episodes of intense convection that have to be accompanied by lateral mixing with environmental water to explain the observed characteristics within the observed eddies. Indeed, the large cooling and freshening of the homogeneous layer waters can be explained only by taking into account both processes. Moreover, the intenser the convection, the larger should be the mixing and therefore the cooling and freshening. This can elucidate why the eddy observed by Arhan et al. [2011], that was observed southward of the Segment 1 actual trajectory, showed lower temperature and salinity than RecAR.

Concerning the description of the precise processes achieving the formation of relatively deep mixed layer within Agulhas Rings and how these layers transforms into MW cores, they have not been directly observed. However, by using very high-resolution numerical simulations, Capuano et al. [2018a] showed that submesoscale instabilities (of differet type) are responsible of both, deep mixing layer formation during winter and the upper layer restratification during summer as discussed in former sections describing possible mechanisms of the subduction. Moreover, these type of instabilities lead to mixing layer water subduction and the formation of a local variety of mode water that the authors defined as Agulhas Ring Mode Water (ARMW) whose properties depend on the eddy history. These numerical results as well as our analyses on the observed Agulhas Rings MW properties would suggest that MWs found in Agulhas Ring cores are formed within these eddies and not a regional variety of SASTMW issued by a more classical and larger scale definition of water mass subduction. Yet, from the *in situ* data we have analyzed we are not able to reconstruct the entire evolution of RecAR, neither we are able to demonstrate uniquivocally that ARMWs are the same water masses as SASTMW2 and SASTMW3, nor that they can be found only within eddies.

Agulhas Rings volume transport, and heat and salt contents

In Table 4.2 are presented the estimates of the volume as well the heat and salt content anomalies for 17 of the 27 Agulhas Rings found in the literature for which at least one of these values was provided by the authors of the related studies. When the authors give more than one value for these variables for one eddy, we only provide those estimates that use in the computation the closest boundaries

of integration to ours.

The average Agulhas Rings volume, HCA and SCA in the literature are, respectively, $3.4\times10^{13}\pm\ 1.6\times10^{13}$ m^{-3} $1.0\times10^{20}\pm\ 0.7\times10^{20}$ J whereas these are $5.2\times10^{12}\pm\ 3.6\times10^{12}$ kg for RecAR where, again, $\pm$ indicates the STD. Hence RecAR results to be among the strongest and largest AR ever observed. The estimated volume is more than the double of Agulhas Ring documented values, and HCA and SCA are the largest out of all except one to which they compare (the ring A4 studied by van Ballegooyen et al. [1994]).

All rings, with the exception of RecAR and two others [McCartney and Woodgate-Jones 1991; Garzoli et al. 1999], were found in the Cape Basin. It might therefore be possible that the large values of RecAR for both, HCA and SCA, are due to a lateral mixing with surrounding waters. However, the fact that the waters trapped within the eddy shows different properties from the environment and that the MW cores are similar to those found in others Agulhas Rings, it gives us confidence that RecAR is a coherent mesoscale eddy advecting modified Indian waters into the South Atlantic. To go beyond these conjectures, we can compare assessments of these integrated properties for RecAR and the rings documented in the literature achieved by using the same approach than those used in the related articles. The results are presented in Table D.4 in the Appendix where the values given in the articles are expressed in percentage of the values for the same variables obtained for RecAR. This comparison shows that, even if we do not consider for RecAR the upper 200 m of the water column, it results in the largest volume. It is also among the rings containing the higher HCA as only 4 of the 16 other eddies are characterized by larger values. However, these 4 rings were observed close to the Agulhas Retroflection area. Finally, RecAR SCA is among the lowest value observed for Agulhas Rings. The only other AR showing lower SCA values was described by Duncombe Rae et al. [1996], however, we cannot explain why as we do not have its history nor a clear spatial pattern emerges.

To conclude on this comparison, RecAR is clearly among the largest AR observed from *in situ* data. It is also associated to large HCA whereas it shows the lowest SCA. We think that this anomaly is concentrated to the AAIW layer and it is due to the slow in-route mixing of Indian Ocean AAIW with Atlantic Ocean AAIW documented by Rusciano et al. [2012] and Capuano et al. [2018b].

4.2.5 Summary and conclusion

We have analyzed the evolution of a long-lived Agulhas Ring (AR) during 1.5 years of its lifespan by using simultaneously a new eddy-tracking algorithm TOEddies applied to satellite altimetry maps and the collocation with Argo floats to uncover the eddy hydrological properties. This eddy was sampled by a large number of Argo profiles (71), and this between the northern region of the Cape Basin and the Mid-Atlantic Ridge similarly to the eddies discussed by Souza et al. [2011a] and

Table 4.2: Integrated properties of Agulhas Rings described in the literature. The reference for the bottom limit of integration are given in the last column. The integration are either achieved from an isotherm, for a fixed depth or by identifying the coherent part of the eddy assessed, by following Flierl [1981], as the volume of the eddy where eddy velocities are lower than the eddy drifting speed. The upper limit of integration is the surface for all eddies except for RecAR for which the integration is limited to σ_0=26.2 kg m^{-3}.

Article	Eddy	Volume [m^3]	HCA [J]	SCA[kg]	Reference
McCartney & Woodgate-Jones, (1991)	Eddy	3.6×10^{13}			Trap 5×10^{-2} m s^{-1}
van Ballegooyen et al., (1994)	A3	4.31×10^{13}	1.5×10^{20}	8.74×10^{12}	T > 8° C
van Ballegooyen et al., (1994)	A4	$3.94\ 10^{13}$	2.36×10^{20}	13.1×10^{12}	T > 8° C
van Ballegooyen et al., (1994)	A5	1.53×10^{13}	0.73×10^{20}	4.35×10^{12}	T > 8° C
van Ballegooyen et al., (1994)	A6	2.45×10^{13}	1.06×10^{20}	4.59×10^{12}	T > 8° C
Duncombe Rae et al., (1996)	B1-1		0.19×10^{20}	1.21×10^{12}	800 m
Duncombe Rae et al., (1996)	B2-1		0.24×10^{20}	1.52×10^{12}	800 m
Duncombe Rae et al., (1996)	B2-2		0.57×10^{20}	3.8×10^{12}	800 m
Duncombe Rae et al., (1996)	B2-3		0.55×10^{20}	3.72×10^{12}	800 m
Duncombe Rae et al., (1996)	B2-4		0.42×10^{20}	1.67×10^{12}	800 m
Duncombe Rae et al., (1996)	B3-1		0.6×10^{20}	3.88×10^{12}	800 m
McDonagh et al, (1999)	R1	1.5×10^{13}	0.39×10^{20}	2.43×10^{12}	T > 10° C
McDonagh et al, (1999)	R2	4.7×10^{13}	0.44×10^{20}	2.71×10^{12}	T > 10° C
Garzoli et al., (1999)	R-1	2.8×10^{13}	1.33×10^{20}	8×10^{12}	1100 m
Garzoli et al., (1999)	R-2	4.18×10^{13}	1.31×10^{20}		1100 m
Garzoli et al., (1999)	R-3	1.88×10^{13}	0.77×10^{20}		1100 m
Schmid et al., (2003)	JAR	2.8×10^{13}	1.71×10^{20}	10.7×10^{12}	1100 m
This study	RecAR	7.2×10^{13}	2.6×10^{20}	7.3×10^{12}	Trap 6×10^{-2} m s^{-1}

Nencioli et al. [2018]. In particular, one of the Argo float (No. 5902281) remained trapped within the eddy core during 14 months (from October 2012 to November 2013) which provided a vertical snapshot of the eddy every 10 days. We also selected all additional Argo profiles lying at less than 200 km from the ring center. However, we made a careful distinction between the profiles sampling the eddy within its boundaries and those characterizing the environment. This has been possible as the TOEddies method automatically computes, for every detected eddy, its outer and characteristic contours together with the evolution of its surface properties.

The AR we discussed in this study corresponds to a segment of an Agulhas Ring main trajectory (according to the definition of Laxenaire et al. [2018]) that has been tracked by TOEddies for 4 years and 7 months (from January 2011 to July 2015). This segment was generated by the merging, in the Cape Basin, of three different Agulhas Rings. Along this segment the eddy showed to be particularly coherent in its shape whereas its surface ADT anomaly, velocity and $|Ro|$ decreases with time as previously observed for other rings [e.g. Byrne et al. 1995; Schouten et al. 2000; Guerra et al. 2018; Laxenaire et al. 2018].

The subsurface observations of the eddy were characterized by two distinct periods: one, in austral winter, during which the mixing layer in the eddy deepened significantly, and a second period, in austral summer, during which the upper hydrological core of the eddy subsided while propagating west. We showed that the eddy, when capped by surface warmer layers, is characterized by negative SST anomalies which support, according to Assassi et al. [2016], its characterization as subsurface intensified eddy. Consequently, this study represents, to our knowledge, the first Lagrangian evidence of the subduction of an Agulhas Ring. However a subducted AR has been already observed [Arhan et al. 1999] and a possible mechanism at play studied numerically by Herbette et al. [2004] simulating the subduction of one AR below a front. However, in this study, the significantly different water masses in the AR and in the environment as well as the important variations of the upper layer hydrological properties rather indicate a detachment of the upper layer from the lower layers due to atmospheric forcing which results into a less coherent upper layer that can mix with the surrounding water [e.g. Wang et al. 2015]. It might results into an upper core of the AR composed of modified water of Indian-Atlantic origins instead of the background subtropical gyre modified locally by a completely subducted AR.

The transition from a surface to a subsurface intensified eddy concomitant to the trapping of a profiling float is of a great interest in the light of the question about the ability of eddy detection methods to detect coherent eddies [e.g. Abernathey and Haller 2018] from a surface field. In the same way as other previous studies [Souza et al. 2011a; Nencioli et al. 2018], the TOEddies eulerian detection algorithm showed to successfully identify and track a coherent eddy as it is able to trap a profiling float for more than one year. However, the observation of the subduction of the eddy enabled us to go beyond these results as it documented that a decrease in the eddy surface intensity is not associated to the global dissipation of the structure,

but to its subsidence in the ocean interior. Indeed, the subducted eddy conserves its size and properties, and the maximum geostrophic velocity seems to move, while subducting, from the ocean surface to 200 m of depth. In this case, the velocities at the surface still satisfy the non-linearity parameter for trapping water of Flierl [1981] and Chelton et al. [2011] but we might expect that it is not always the case resulting in a non coherent eddy in the surface field while it is the case in the water column. Moreover, as the surface geostrophic velocity decreases, we can expect the signal over noise ratio to increase in satellite altimetry maps. This ratio is particularly important for Lagrangian eddy detection techniques [e.g. Beron-Vera et al. 2013; Abernathey and Haller 2018] very sensible to absolute values of the surface velocities. Therefore we suggest caution when analyzing eddies coherence from surface fields only and, in particular, to estimate the Agulhas Leakage achieved by the AR [e.g. Wang et al. 2015; 2016] as we shown that the sub-surface layers can be more coherent than the surface one.

Another possible consequence of the subduction process, might be the formation of Mode Water layer cores. Indeed, the eddy we studied presented two cores of Mode Waters. One very likely linked to the last winter convection as described by Capuano et al. [2018a]. A second one, located deeper, probably linked with a merging of an Agulhas Ring that took, after being spawned by the Agulhas Retroflection, the Southern Route defined by Dencausse et al. [2010a] and experienced intenser winter conditions.

Given the long time coherence of the structure after subduction which shielded the eddy from any further air-sea exchanges, we assumed it was steady and axisymmetric. This allowed us to reconstruct its three-dimensional hydrological vertical structure by fitting an alpha Gaussian function [see for examples Carton 2001; Le Vu et al. 2018]. We defined the eddy thermohaline anomalies in relation with the surrounding environment. These anomalies turned out to be very intense and concentrated within the two Mode Waters layers, and they concentrate the majority of the anomaly signal distinguishing this eddy from the surrounding South Atlantic waters. Our reconstruction is similar to the approach of Nencioli et al. [2018] who studied a different eddy. However, it diverges in the choice of the variables of integration and in the definition of the eddy boundaries. Indeed, we carefully considered only profiles falling strictly within the eddy limits (lateral and vertical) in seeking to represent accurately the eddy thermohaline structure.

A comparisons with 27 other Agulhas Rings described in the literature from oceanographic cruises shows that we can subdivide them among surface and subsurface intensified eddies. The surface intensified ones mainly lie in the Cape Basin, along the Southern Africa slope. Those that are located along the main rings path that occupies the central part of the Cape Basin [Laxenaire et al. 2018] are predominantly subsurface intensified eddies. Moreover, the rings for which we have found in the literature a vertical section of their thermohaline properties are all characterized by the presence of, at least, one core of Mode Waters. Some of them shows two Mode Water cores (including the ring we focus on in this study).

For these, all except one are located in the South Atlantic, north of the Cape Basin. Hence, the results of the comparison suggest that the subsurface eddy we reconstructed in this work which is composed of two homogeneous cores is not an exception. Moreover, this analysis provides indications that Agulhas Rings follow a geographical pattern according to their history and water masses properties. Such a distribution needs to be investigate further from updated data, complementary modeling studies and by applying reproducible quantitative method.

The Mode Waters found in Agulhas Rings show very variable properties that fall in the range of two varieties of SASTMW [Sato and Polito 2014] and in the upper (warmer and saltier) range of SAMW [McCartney and Woodgate-Jones 1991]. However, the continuity of their θS properties would rather suggest that these eddies are associated to one specific variety of Mode Water formed within Agulhas Rings during the austral winter (the so called ARMW as suggested from modeling studies by Capuano et al. [2018a]) and not to different types of Mode Waters formed remotely. Indeed, south of Africa the ocean is submitted to intense wind forcing and buoyancy exchanges that affect in particular the warm and salty Agulhas Current and Agulhas Rings [e.g. van Ballegooyen et al. 1994; Arhan et al. 1999; 2011]. The assorted properties observed for ARMW might be due to the different amplitude of such air-sea fluxes as they vary according to the path undertaken by the rings as well to the synopticity of the atmospheric forcing that can vary from one week to the other as well as one year from the following, or according to the time the rings spend in the area as they can be blocked for several months by the interaction with the local topography [e.g. Arhan et al. 1999; 2011]. Yet, our study cannot assess if the formation of the observed Mode Waters are restricted to Agulhas Rings only, nor it can define the origin of the observed Mode Waters for the double-core AR. The latter might indeed be the result of convection within an eddy during two consecutive winters or the merging of two rings that took different routes and underwent different weather conditions [Garzoli et al. 1999]. Also, the deeper Mode Water core could be a remnant of SAMW advected within the Agulhas Current from the Indian Ocean and already present in the eddy at the moment it was spawned from that current.

We recovered the geostrophic velocity of the reconstructed eddy from the nonlinear thermal wind relation. The maximal value of the azimuthal velocity (0.3 m s^{-1}) was found at 200 m and had the same radius as the speed radius derived from satellite altimetry. The surface maximum azimuthal velocity was more intense (up to 0.35 m s^{-1}) than its subsurface expression from Nov 2012 to January 2013. After this period it decreased steadily down to 0.15 m s^{-1} at the end of the Argo float No. 5902281 observing period. This is a consequence of the eddy subduction that implies a disconnection, at least partial, of the eddy from the ocean surface. Our analysis suggest that the eddy extended, after subduction, from 200 to 1200 m of depth. We estimated its volume to $7.2\times10^{13}\pm 1.5\times10^{13}$ m^{-3}. The heat and salt anomalies transported by the eddy amounted to, respectively, 4 °C and 0.6 g kg^{-1} at -600 m and the total integrated Heat Content (HCA) and Salt Content (SCA) anomalies were estimated to $2.6\times10^{20}\pm 0.1\times10^{20}$ J and $7.3\times10^{12}\pm 0.6\times10^{12}$ kg,

respectively. Both the volume and the HCA resulted to be particularly large when compared with comparable estimates for Agulhas Rings found in the literature. Only Agulhas Rings close to the Agulhas Retroflection show comparably large HCA [e.g. van Ballegooyen et al. 1994; Arhan et al. 1999; 2011]. On the other hand, the eddy SCA is among the lowest. As the eddy was found already far from the Retroflection, and the anomaly being concentrated in the deeper layer of the eddy, we suggest that the SCA has been affected by the in-route mixing of Indian AAIW with the Atlantic AAIW variety as discussed by Rusciano et al. [2012] and Capuano et al. [2018b].

Our analysis enlightens the complex evolution of Agulhas Rings that split and merge, undergo to intense ventilation, subduct but remain intense while crossing the South Atlantic basin. They advect very large quantity of water, heat and salt from the Indian Ocean. South of Africa, Agulhas Ring waters are (at least partially) modified by winter convection that produces thick cores of Mode Waters. It is in these Mode Water cores that seem to reside the strongest heat anomaly of these intense eddies when they are advected in the South Atlantic Ocean. This, together with the numerous eddy merging and splitting occurrences, strongly suggest that the use of exclusively satellite altimetry maps to characterize the coherence of eddies has limitations and coupling with ARGO is very useful.

5

Contenu thermique et transport de chaleur des Anneaux des Aiguilles dans l'Atlantique Sud

Sommaire

5.1 Résumé de l'article 117
5.2 Agulhas Rings heat content and transport in the South Atlantic estimated by combining satellite altimetry and Argo profiling floats data 118
5.2.1 Introduction 118
5.2.2 Data and Methods 121
5.2.3 Hydrological properties of Indian Water AREN 125
5.2.4 Discussion 146
5.2.5 Conclusion 149

5.1 Résumé de l'article

Dans la section précédente, nous avons mis en évidence la transformation d'un Anneau des Aiguilles d'une structure intensifiée en surface dans le bassin du Cap en un tourbillon détaché de l'atmosphère dans l'océan Atlantique. Cette subduction se traduit par la création de deux cœurs d'eau modale dans l'Atlantique Sud. Une fois sous la thermocline saisonnière, la partie de subsurface de ce tourbillon s'est révélée être relativement cohérente nous permettant d'en faire sa reconstruction

thermohaline et de calculer le transport de chaleur qu'il effectuait. Afin de mettre nos résultats en perspective, nous les avons comparés avec ceux décrits dans la littérature. Une régionalisation du type de tourbillon ainsi qu'une similitude des propriétés des eaux modales ont été mises en avant. Cependant, le faible nombre de tourbillons décrits ainsi que l'inhomogénéité des calculs effectués dans la littérature ont limité les conclusions.

Nous proposons dans ce chapitre, soumis dans le "Journal of Geophysical Research : Ocean" [Laxenaire et al. UR b], d'utiliser tous les flotteurs Argo collocalisés avec les Anneaux des Aiguilles identifiés dans le chapitre 3 afin d'essayer d'obtenir des estimations quantitatives des observations effectuées dans le chapitre 4. Pour cela, nous développons une méthode permettant d'identifier le type de tourbillon (i.e. intensifié en surface ou en subsurface) à partir des anomalies de densité calculées sur les profils Argo. Cela nous permet de clairement mettre en évidence la plongée des tourbillons des Aiguilles lorsqu'ils quittent le bassin du Cap. Nous nous focalisons ensuite sur leur contenu thermique afin d'identifier l'intervalle de profondeur où la plus grosse anomalie de chaleur est présente. Nous développons ensuite une méthode de reconstruction des anomalies du contenu de chaleur le long de segments de trajectoires que nous comparons aux méthodes de création de tourbillon composite afin d'obtenir une nouvelle estimation des transport de chaleur engendrés par les tourbillons des Aiguilles.

5.2 Agulhas Rings heat content and transport in the South Atlantic estimated by combining satellite altimetry and Argo profiling floats data

5.2.1 Introduction

Ocean dynamics is highly nonlinear and is characterized by dynamical processes across a broad range of spatial scales, from ~1000 km down to ~1 km and even smaller scales. Among them, mesoscale eddies refer to coherent structure which, generally, have space scales of 20-200 km and time scales of 10-100 days [Carton 2001; Chelton et al. 2011; Morrow and Le Traon 2012]. The energy of these processes, which are omnipresent in the upper ocean layers [Stammer 1997], typically exceeds that of the larger and smaller-scale flow by an order of magnitude or more. In particular, they are associated with a peak in the kinetic energy spectrum in the subinertial frequency band [see Ferrari and Wunsch 2009 ; for a review]. They are generated by instabilities of larger-scale currents and they can feed energy and momentum back into the mean flow. They impact all the different dynamical components of the ocean from the air-sea fluxes [e.g. Frenger et al. 2013] to the ventilation of the ocean deep interior [Sallée et al. 2010] as well as the large-scale

ocean circulation [Morrow et al. 1994; Lozier 1997]. Moreover, they are suspected to play a major role in the transport of heat, salt, carbon, and chemical components as they propagate in the ocean, and therefore represent a key dynamical element in the global budgets of these tracers [Morrow and Le Traon 2012].

Since the last 25 years and the advent of satellite altimetry many studies have been dedicated to the general assessment of upper-ocean mesoscale characteristics and propagation properties [e.g. Chelton et al. 2007; Chaigneau et al. 2008; Chelton et al. 2011]. However, over the last few years, an interest was given to the consideration of the merging and splitting events [e.g. Du et al. 2014; Li et al. 2014; Yi et al. 2014; Le Vu et al. 2018; Laxenaire et al. 2018]. It revealed, by accurately accounting these events, a more complex eddy dynamic than previously documented. In particular, it showed that mesoscale eddies cannot be associated to a unique eddy and a single trajectory but more realistically to various eddies linked in a complex network [Laxenaire et al. 2018]. Yet, the description of these eddies from satellite altimetry maps is not complete as only their surface signature can be characterized.

To deepen the knowledge on global ocean eddies, recent studies have attempted to systematically combine satellite altimetry observations of eddies with vertical profiles from Argo floats to provide eddy three-dimensional reconstructions [e.g. Chaigneau et al. 2011; Souza et al. 2011a; Yang et al. 2013; Pegliasco et al. 2015; Nencioli et al. 2018]. Those studies have confirmed that mesoscale eddies can advect large amounts of water, heat, and salt by trapping and transporting water masses within their core as they propagate. However, an accurate estimate of their properties as well as the generalization to the same family of eddies (i.e., eddies of the same polarity, generated in the same region) is a complicated task. Indeed, *in situ* data coverage are still sparse at the ocean mesoscale despite it has much improved in the last 15 years with the advent and development of the Argo profiling floats international program.

In particular, previous studies, have tried to estimate eddies properties and transport using *in situ* and satellite altimetry via two types of approaches. The composite one is the most widely used approach. It is based on the computation of eddy composites within box areas [e.g. Chaigneau et al. 2011; Yang et al. 2013]. This method relies on the two following hypotheses: 1) Eddies of the same polarity in a given geographical area are similar to each others; 2) The eddy-composite hydrological properties are representative of the average of such properties for the eddies of the same polarity populating a given region. Other authors reconstructed one or more eddies when they were sufficiently sampled by *in situ* observations along their trajectories, and tried to generalize they results by assuming that eddy properties and trajectories are representative of a specific family of eddies in a given region [e.g. Souza et al. 2011a; Nencioli et al. 2018; Laxenaire et al. UR a]. This approach gains in robustness with the number of eddies it reconstructs. Indeed, as we will show in the present study, a family of eddies can display a relative broad diversity in properties that need to be accounted of.

Using one of these approaches, it is possible to estimate the transport of volume, heat and salt by the eddies (composite or individual reconstruction) by combining their hydrological properties with the eddy trajectories derived from satellite altimetry [Souza et al. 2011a; Nencioli et al. 2018; Laxenaire et al. UR a]. The transport of water masses and heat by mesoscale eddies is particularly important for large eddies such as the Agulhas Rings [Lutjeharms 2006]. Agulhas Rings are shed from the Agulhas Current, the western boundary current of the south Indian Ocean, at its retroflection south of Africa [Olson and Evans 1986; Lutjeharms and Gordon 1987; Gordon and Haxby 1990; Duncombe Rae 1991; Bang 1970].

These eddies are thought to materialize most of the so called Agulhas Leakage [De Ruijter et al. 1999a; Lutjeharms 2006]. The Agulhas Leakage is a relatively substantial transfer (about 15 Sv) of Southwest Indian Ocean thermocline waters into the South Atlantic via the Cape Basin (a basin lying at the southwestern tip of Africa) [Ballegooyen et al. 1994; Garzoli et al. 1999; Arhan et al. 1999; 2011]. The Agulhas Leakage it has been shown to impact the regional climate of South Africa [Cheng et al. 2018] as well the climate at global scale by substantially influencing the Atlantic Meridional Overturning Circulation (AMOC) [Dong et al. 2011b; Biastoch et al. 2009; Lampitt et al. 2010; Beal et al. 2011]. However, despite many advances in the assessment on mesoscale eddies, and on Agulhas Rings in particular, an adequate quantitative characterization of their 3D subsurface structure, of the phenomenological understanding of their role in the global ocean circulation and of properties they transport (heat, salt, and biogeochemical variables) are still essentially uncovered.

In this work, we explore and discuss a novel and relatively general Agulhas Rings characterization inferred by the TOEddies eddy detection method applied to satellite altimetry maps [Laxenaire et al. 2018] and their collocation with vertical Argo profiles. In particular, we provide a novel assessment on the heat transport achieved by Agulhas Rings in the South Atlantic Ocean that comes from a more complete and complex network of eddy trajectories and a higher number of profiling floats than previous studies using a similar approach [Souza et al. 2011a; Nencioli et al. 2018]. Moreover, we propose here to compare different types of reconstructed subsurface eddy properties and associated transports by computing eddy subsurface structure according to various published methods applied to our data. To do so, we provide a relatively precise assessment on the vertical extension of Agulhas Rings that needs to be taken into account to correctly evaluate their heat content and associated transport. We then estimate Agulhas Rings heat content anomalies and we conclude the study with an assessment of heat transport associated with Agulhas Rings by using the whole set of trajectories identified from 17 years (from 2000 to 2016) of altimetry Absolute Dynamic Topography (ADT) maps concurrent with the Argo profiling floats program.

The manuscript is organized as follows. In Section 2, we introduce the data and the method used to define Agulhas Ring trajectories and their collocation with Argo vertical profiles. In Section 3 we present the characterization of surface and

sub-surface Agulhas Rings following Assassi et al. [2016] as well as the determination of the depth levels needed to correctly estimate the heat anomalies associated with AR. Section 4 focuses on the assessment of the Agulhas Rings heat content and associated heat transport. Discussions of these results follow in Section 5. In Section 6 we provide our conclusion to this work.

5.2.2 Data and Methods

Eddy detection and the Agulhas Ring Eddy Network

Under the geostrophic approximation, closed contours of Sea Surface Height (SSH) correspond to closed stream functions which can be used to detect geostrophic eddies. This property explains the great interest gained by the availability since the 1990s of gridded altimetric maps to enable the identification and tracking of mesoscale eddies [we refer the readers to the chapter 10 of Stammer and Cazenave 2017 ; for an up-to-date review on the subject]. The availability of these maps allowed the development of systematic eddy detection and the derivation of their trajectory via the development of various algorithms [e.g. Isern-Fontanet et al. 2006; Doglioli et al. 2007; Nencioli et al. 2010; Chaigneau et al. 2011; Chelton et al. 2011; Mason et al. 2014; Faghmous et al. 2015; Pegliasco et al. 2015; Ashkezari et al. 2016; Matsuoka et al. 2016; Qiu-Yang et al. 2016; Le Vu et al. 2018; Laxenaire et al. 2018].

However, most of the previous approaches did not take into account the fact that mesoscale eddies often experience episodes during which the eddies split in two or more mesoscale structures or merge with neighboring eddies. This is particularly true for Agulhas Rings as it is documented from both, *in situ* and remote sensing studies [Byrne et al. 1995; Arhan et al. 1999; Boebel et al. 2003a; Dencausse et al. 2010b; Baker-Yeboah et al. 2010; Nencioli et al. 2018; Laxenaire et al. 2018; UR a]. While previous works did not take into account this complex behavior of Agulhas Rings, we developed a novel eddy detection and tracking algorithm, TOEddies [Laxenaire et al. 2018], that identifies and records every separation and coalescence of eddies. TOEddies is based on the eddy-tracking method developed by Chaigneau et al. [2011] that was subsequently improved by Pegliasco et al. [2015] and Laxenaire et al. [2018]. TOEddies is based on the identification of eddies as closed contour of ADT in daily altimetry maps [Duacs/AVISO+ 2015] and uses the superposition of the areas occupied by one eddy between two consecutive days to reconstruct its trajectories.

The TOEddies South Atlantic database contains more than 24 years (from January 1993 to May 2017) of eddies identification and trajectories in the South Atlantic and the Southeast Indian oceans [70 W-65 E; 55 S-15 S] [Laxenaire et al. 2018]. This database contains only eddies associated with a persistence parameter (a parameter linked to the eddy amplitude defined as the ADT difference between the

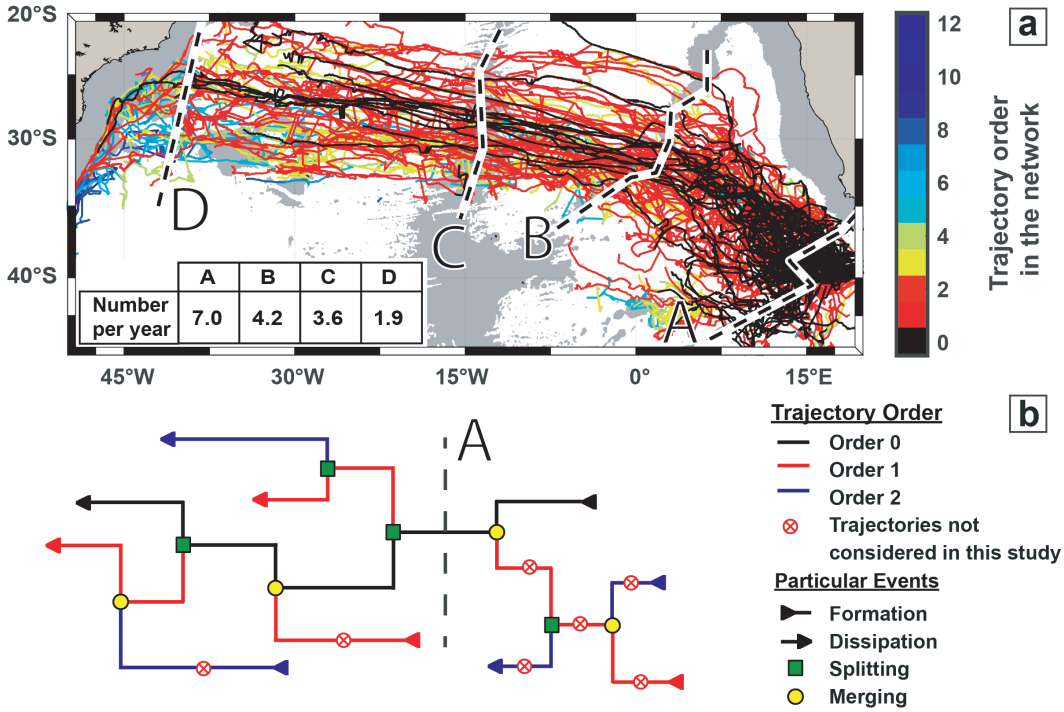


Figure 5.1: a) Indian water Agulhas Ring Eddy Network (AREN) trajectories. The color of the trajectories is related to their order. The black color is for order 0, which we defined as Agulhas Rings "main trajectories". Seven sections (A–D) were used to derive the number of Indian water AREN trajectories crossing per year during the period 01/01/2000 – 31/12/2016. The gray shading in each figure represents water depths less than 3,500 m in the ETOPO2 data set [Smith and Sandwell 1997]. b) Schematic of the reconstructed Indian water AREN where the segments not considered in this study are indicated by a red cross.

center and the outer closed contour of the eddy) higher than 1 mm and trajectories lasting for at least 4 weeks. Following Laxenaire et al. [2018], we defined, for each eddy, its dynamical core that corresponds to the eddy area encompassed by the ADT closed contour associated with the maximum of the azimuthal geostrophic velocities derived from ADT maps [Duacs/AVISO+ 2015]. The area of this characteristic core (A_{Vmax}) is used to define an equivalent radius (R_{Vmax}) as $R_{Vmax} = \sqrt{A_{Vmax}/\pi}$ as well as the eddy center corresponding to the centroid of this area. We refer to Laxenaire et al. [2018] for a complete description of the eddy tracking method and the eddy database. To be noted here that TOEddies has been extensively validated with the independent looping surface drifters dataset provided by Lumpkin [2016] and compared to the AVISO eddy database.

Following the definition of Laxenaire et al. [2018], we identified Agulhas Rings as those anticyclonic eddies whose trajectories enter the Cape Basin by crossing its southern limit, materialized by the A-line drawn in Figure 5.1a. To ensure the consistency of the recovered trajectories, we only use, for the eddy detection,

the time period spanning from 01/2000 to 12/2016. This ensures a complete reconstruction of the associated eddy trajectories [Laxenaire et al. 2018]. Indeed, Agulhas Rings span very long distances and life-time (up to 4 years). This definition allows us to classify Agulhas Rings as those anticyclonic eddies whose trajectories originate in the Southwest Indian Ocean and enter the South Atlantic. These set of eddies and associated trajectories are called order-0 Agulhas Rings Eddy Network (AREN0) of trajectories [Laxenaire et al. 2018]. Such trajectories would coincide with those obtained with more classical eddy detection algorithms that do not take into account eddy splittings and mergings.

To recover the whole set of trajectories linked with Agulhas Rings, we included the AREN trajectories at higher-order, such order being determined by flagging the number of eddy splittings and mergings needed to be taken into account to link that specific trajectory to an AREN0 trajectory. Details on how AREN have been computed can be found in Laxenaire et al. [2018]. A schematic on how the more comprehensive higher order AREN trajectories have been constructed is provided in Figure 5.1b. However, the aims of the present study being the assessment of the heat content and transport achieved by Agulhas Rings, in the following we will only take into account the whole set of AREN0 and those higher-order AREN whose trajectories that participate to the inter-ocean exchange. Therefore, we only consider here the set of higher-order AREN segments that are a product of splitting of AREN0 in the Atlantic Ocean and higher order AREN in the same domain. Very likely, this results in missing some of the higher-order AREN that cannot be tracked back directly to the Indian Ocean (i.e., east of line A in Figure 1). We preferred to be as restrictive as possible to not include eddies containing South Atlantic water before their merging with an AREN containing Indian waters. The AREN we will refer to in the present study are composed of 122 AREN0 and 553 higher-order AREN. In the following, we will define them as Indian Water AREN and refer to them, in the following (for sake of simplicity) as Agulhas Rings (AR). Indeed, we think they are, among the whole set of AREN, those that best represent the hydrological entity and fate of these eddies. Moreover, one can argue that it complicates the comparison with previous works but, not taking into account merging and splitting, many of the previous studies might have identified as AR the anticyclonic eddies crossing the Atlantic Ocean without any consideration of their interactions with other structures after their shedding.

Argo profiles data and eddy collocation

Argo floats provide a large number of CTD (Conductimetry, Temperature and Depth) vertical profiles for the upper 2000 m of the global ocean. These data were collected and made freely available by the International Argo Program and the national programs that contribute to it (doi: <http://doi.org/10.17882/42182>) as part of the Global Ocean Observing System. Argo Data Centers provide delayed mode data for each vertical profile. These data are validated and calibrated by the data assembly centers [e.g. Owens and Wong 2009; Cabanes et al. 2016] against

the most updated global climatology (computed with both full depth CTD from oceanographic research cruises and validated Argo floats) to estimate errors for each Argo profile.

In this study, we used the Argo data obtained from the Coriolis Global Data Center (Coriolis GDAC; url: <http://www.coriolis.eu.org>) that are in the delayed mode with control quality flags equal to 1 and 2, which refer to "good observation" and "probably good observation" and that contain at least one observation in the upper 20 m and one below 1200 m of depth. We did a further selection within these profiles following Chaigneau et al. [2011]. We selected those profiles whose minimum vertical resolution were within 25, 50, 75, 100 and 200 m for, respectively, the depth intervals 0-100 m, 100-300 m, 300-500 m, 500-1000 m and below 1000 m of depth. The data for the profiles satisfying all these criteria were interpolated vertically at a 10 m depth-step.

Following Laxenaire et al. [UR a], we collocated the selected Argo profiles with the mesoscale eddies contained in the TOEddies South Atlantic database[Laxenaire et al. 2018]. We separated these Argo profiles in three groups: one associated with anticyclonic eddies, one with cyclonic eddies and those falling outside of any detected features. We used the latter to characterize the environment (i.e., waters that are not part of a mesoscale eddy). Similarly to Laxenaire et al. [UR a], we estimated a climatological profile for each Argo profile to derive the associated hydrological anomalies. For this, we averaged all the Argo profiles characterizing the environment located in a square box ($\pm 1^\circ$ in longitude and latitude) centred on the given profile position and whose date were $\leqslant 30$ calendar days from the date of the given profile. This box is two times smaller than the one used in Laxenaire et al. [UR a] as it proved to provide better results in regions of intense hydrological gradients. Indeed, a manual inspection of the variations of hydrological properties in the argo profiles selected to create climatologic profiles was defined as too large close to the Agulhas retroflection.

The collocation of Argo floats with the South Atlantic eddies resulted in identifying 2267 profiles lying within Agulhas Rings. The distribution of these profiles as a function of the order of Agulhas Rings (alias Indian Water AREN) is presented in Figure 5.2a. It shows that more than half of the profiles (i.e. 67%) lie within Agulhas Rings of order $\leqslant 2$. For Agulhas Rings of order 4, the percentage of Argo profile captured within one of these eddies increases to 92%. The histogram of the distance (Dc) between each profile and the eddies center is presented in Figure 5.1b. It shows that less than 4% of the Argo profiles lie within a distance of 20 km from the eddy center. This value reaches 22% and 48% for, respectively, $\pm Dc = 50$ and $\pm Dc = 80$ km. These results point out that Argo profiling floats better sample the outer area than the inner core of the eddies as already discussed by, for example, Chaigneau and Pizarro [2005]. However, our statistics show that about half of the profiles (49%) fall within the eddy dynamical cores (which is delimited by the maximum of azimuthal velocities, R_{Vmax}, depicted by the darker bars in Figure 5.2; see Laxenaire et al. [2018] for more details).

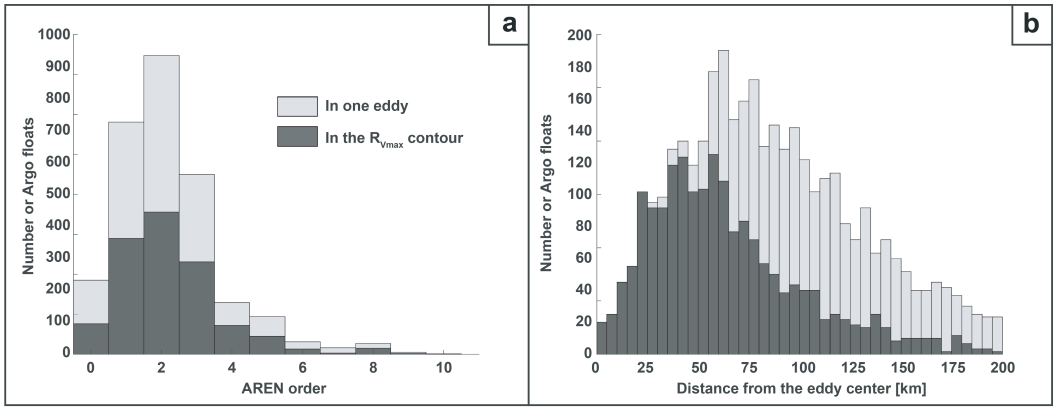


Figure 5.2: Histogram showing the number of Argo profiles sampling Indian Water AREN according to a) the AREN order and b) the distance (Dc) of the profiles position from the eddy centers. Each bar is colored in dark gray when the Argo profiles lie within the eddy core or in light gray otherwise.

Among all Agulhas Rings identified from ATD maps, 245 (i.e. ~31 %) were sampled, at least once, by an Argo profile. This number decreases drastically when looking at Agulhas Rings sampled by more than one Argo profile. Indeed, 102, 32 and 12 Agulhas Rings are sampled by, respectively, 5, 20 and 40 profiles. However, these profiles are not necessarily close in time and space as Agulhas Rings can have life-time of several years [e.g. Byrne et al. 1995; Laxenaire et al. 2018].

5.2.3 Hydrological properties of Indian Water AREN

Here we use the total dataset of Argo profiles collocated within Agulhas Rings to assess their hydrological properties via a Semi-Eulerian framework. We use this terminology because eddies are studied regionally but their selection is achieved by identifying and tracking their trajectories using, in this step, a Lagrangian approach.

Type of eddy

Arhan et al. [1999] and Garzoli et al. [1999] observed subsurface intensified anticyclonic eddies in the Cape Basin and in the eastern part of the Atlantic Ocean. These authors qualified these features as “modified Agulhas Rings" that were propagating as subsurface eddies. Herbette et al. [2004] showed numerically that this type of eddies could evolve from surface to subsurface vortices via lateral advection subducting below lighter waters. In a recent study, Laxenaire et al. [UR a] achieved a Lagrangian reconstruction of an Agulhas Ring from Argo profiles which provided the evidence of the in route modification of an AR, transitioning

from a surface to a subsurface intensified eddy. Comparing the TS properties of the surface layers in the subducted AR and in the environment, these authors showed that the AR contains modified water close to the surface which would indicate a subduction due to the restratification of the AR instead of a lateral advection.

In the same study, Laxenaire et al. [UR a] qualitatively identified from historical observations the horizontal shape of the pycnocline above the hydrological core of some Agulhas Rings referenced in the literature flagging as sub-surface eddies those showing a dooming of isopycnals in their upper layers. This comparison qualitatively supports the existence, in the Cape Basin and beyond, in the South Atlantic Ocean, of subsurface modified-AR.

To learn further on Agulhas Rings hydrological properties, we implemented an objective method applied to the Argo profiles sampling these eddies to discriminate them as surface or subsurface intensified vortices. While the previous study of Laxenaire et al. [UR a] used isopycnal shape for such a characterization, single Argo profiles only give access to only the vertical hydrological properties at the position of the Argo float. To overcome this difficulty, we used hydrological anomalies in the upper layers to quantify the difference between the density within the eddy and that of the environment. This way, a positive (negative) anomaly of potential density is associated with the shallowing (deepening) of isopycnals outward of the eddy. This is similar to the index implemented by Assassi et al. [2016] and the procedure developed by Schütte et al. [2016] applied to surface properties from in situ observations and numerical models in two different regions of the global ocean to classify eddies as surface or subsurface intensified. Their index consisted in flagging as subsurface (surface) eddies those structures characterized by a positive deviation of the sea surface and sea surface density anomalies of the same (opposite) sign.

The method we implemented is similar, except that we looked at the sign of the density anomaly in the eddy layers below the mixed layer (ML). This because the shallowest Argo float observations lies generally at about 7-15 m of depth and not at the sea surface. Also, by analyzing the eddy properties below the ML we can filter out seasonal and higher frequency variability characterizing the upper layers. The mixed layer depth (MLD) is computed from density profiles using the hybrid method developed by Holte and Talley [2009]. When applied to Argo profiles, this method showed to be more accurate than the one developed by de Boyer Montégut et al. [2004] [Holte et al. 2017]. The present study is focused on anticyclonic eddies that are, by definition, associated with positive SLA. We compute the density anomalies (σ_0') below the MLD for the identified Agulhas Rings. When, for these eddies $\sigma_0' < 0$ ($\sigma_0' > 0$), they are classified as surface (subsurface) eddies.

The magnitude of such density anomalies are expected to be stronger for profile lying close to the eddy center. This reduces the number of Argo profiles available for such eddy characterization. We chose to only use the profiles sampling at a distance from the eddy center, Dc, smaller than half of the R_{Vmax}. This restriction aims to take into account structures of different size while ensuring the profile to be close to (and sampling) the eddy center as this is the region representing the

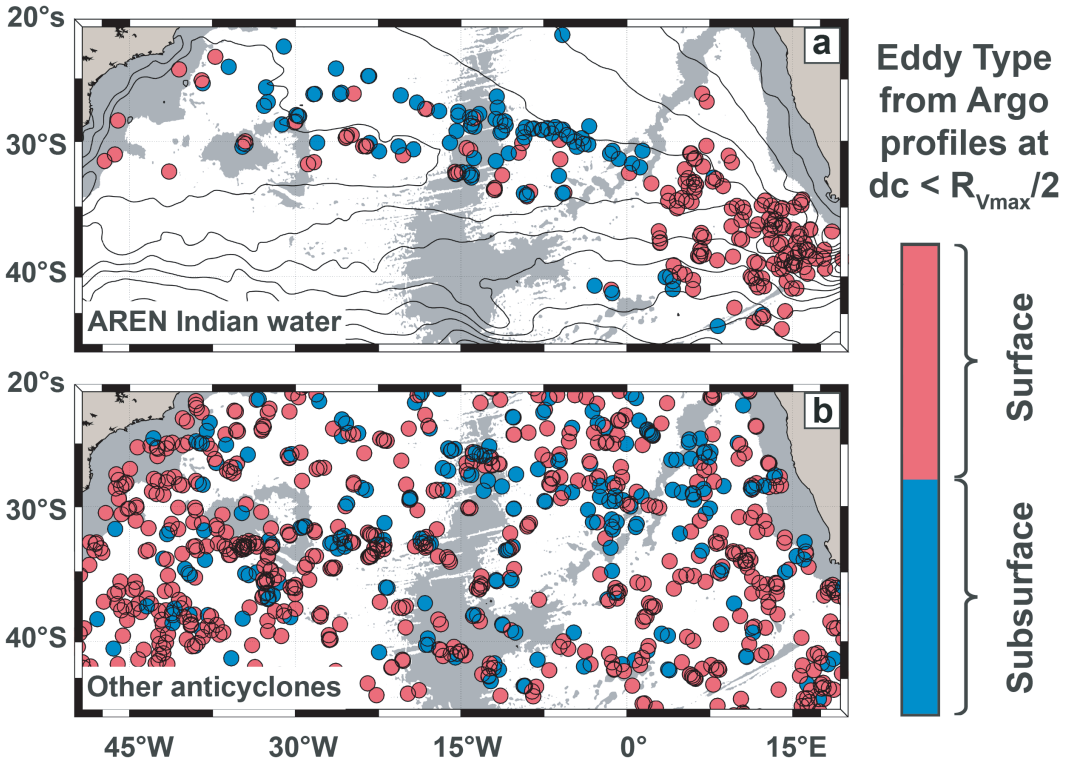


Figure 5.3: Type of anticyclonic eddies (surface and subsurface intensified) for a) Agulhas Rings and b) all other anticyclonic eddy identified in the region. Only Argo profiles sampling an anticyclone at a distance from the center lower than half of its instantaneous R_{Vmax} are considered. The Mean Dynamic Topography (MDT, [Duacs/AVISO+ 2014]) contours spaced by 10 cm are superposed to indicate the large-scale mean circulation in the area. The gray shading in each figure represents water depths less than 3,500 m in the ETOPO2 data set [Smith and Sandwell 1997].

eddy core and the coherent part of the eddy. The type of eddies identified from the Argo profiles satisfying this criterion are presented in Figure 5.3 for Agulhas Rings (Figure 5.3a) and for all other anticyclonic eddy identified in the region by the TOEddies algorithm (Figure 5.3b).

From Figure 5.3a two main regions stand out for Agulhas Rings: The Cape Basin which is strongly dominated by surface intensified structures, whereas in the South Atlantic Ocean sub-surface intensified eddies prevail. The transition seems to take place in the Cape Basin upstream of or in top of the Walvis Ridge as five of the six Argo profiles sampling one of these eddies as they were lying on the top of this ridge were categorized as subsurface features. The regional upper-layer density field estimated from the World Ocean Database [Boyer et al. 2013] (see Figure E.1 in the Appendix) shows that Agulhas Rings cross outcropping isopycnals as they drift northwestward in the Cape Basin.

To be noted that Agulhas Rings located in the southwestern corner of the

Cape Basin are identified as subsurface eddies. These eddies are part of the "Southern Route" [Dencausse et al. 2010a], that passes very close to if not within the subantarctic frontal zone. These eddies undergo to very intense air-sea interactions that result in important eddy heat loss inducing an intense cooling of the eddy cores [Arhan et al. 2011]. These air-sea exchanges are responsible for, within the core of these eddies that are originally characterized by relatively salty Indian Ocean waters, deep mixed layer and upper-layer density increase [Arhan et al. 2011]. These denser eddies appear therefore to subduct relatively rapidly after they injection into the Cape Basin.

Agulhas Rings identified by the TOEddies Atlas cross the South Atlantic basin along two major branches, that were defined as the "southern" and the "northern" branches [Laxenaire et al. 2018]. The northern branch lies along the north-westward branch of the subtropical gyre as indicated by the contours of the AVISO Mean Dynamic Topography in Figure 5.3a, as it has already been discussed by Byrne et al. [1995]. It is worth noting that nearly all the Agulhas Rings along this branch are subsurface eddies, whereas both, surface and subsurface eddies are found along the southern branch. Agulhas Rings reaching the American Margin and the South Brazil Current become surface intensified eddies. This suggests the merging of Agulhas Rings with South Brazil Current waters or other anticyclonic eddies in this region.

Figure 5.3b shows that no clear pattern emerges for the rest of anticyclonic eddies (i.e., those not identified as Agulhas Rings) present in this region: both types of eddies, surface and subsurface, fill the different areas of the regional domain. This is particularly true in the region north of 30°S and east of the Atlantic Ridge. Here nearly all Agulhas Rings are subsurface eddies (Figure 5.3a) whereas the rest of the detected anticyclonic eddies are of any of the two categories (Figure 5.3b).

However, it must be noted that some of the subsurface eddies among those that were not identified as Agulhas Rings by our definition (i.e., as Indian Water AREN) might be still linked to Agulhas Rings. Indeed, numerous authors [e.g. Souza et al. 2011a; Guerra et al. 2018] identified Agulhas Rings as anticyclonic eddies formed in the Cape Basin (and therefore not as eddies originating from the Indian Ocean as we prescribed). Using this definition, these authors identified the formation of Agulhas Rings north of 30°S in the Cape Basin. Hence, at least some of the subsurface eddies found in this region, can be associated with such type of structures. On the other hand, Pegliasco et al. [2015] showed that anticyclonic eddies formed in the Benguela Upwelling can either be surface or subsurface intensified. These authors also showed that these eddies can be tracked west to 10°W and north of 30°S which also makes them strong candidates for the subsurface eddies found in this geographical area.

Spatial distribution of Agulhas Rings Heat Content Anomaly

To estimate the heat content and transport achieved by Agulhas Rings we first need to assess their Heat Content Anomaly (HCA). To do this, we computed the Heat Content (HC) for both, Argo profiles falling within Agulhas Rings and those associated to the climatology, following equation 5.1:

$$HC_{z_{inf}}^{z_{sup}}(r) = \int_{z_{inf}}^{z_{sup}} \rho(z) C_p T(z) dz \tag{5.1}$$

where, $C_p(T)$ is the heat capacity, $\rho(r, z)$ the density and $T(r, z)$ the conservative temperature in Kelvin. The HC(r) computed is not the total HC of the eddy but the vertically integrated one at a fixed distance r from the center of the eddy. Finally, the HCA(r) is then obtained by subtracting the climatological HC from the HC(r) computed in the eddy.

As discussed in the previous section, Agulhas Rings can be either surface or subsurface intensified eddies. In the reconstruction of such structures by Nencioli et al. [2018] and Laxenaire et al. [UR a], these authors limited their analyses to the subsurface portion of the eddies, namely below about 200 m of depth. Indeed, at shallower depths, the eddies properties were observed to vary at seasonal and higher frequency, while below 200 m they showed to be highly coherent in time. Hence, the depth of 200 m seems to lie below the regional seasonal thermocline as suggested by the seasonal MLD maps produced by de Boyer Montégut et al. [2004]. Consequently, we prescribed the upper limit of the vertical integration of HC to 200 m of depth (i.e. $z_{sup} = 200$ m). This allows, in particular, to compare the HCA(r) for eddies sampled at different period of the year and eddies located in different regions of the domain. We also fixed 1200 m (i.e. $z_{inf} = 1200$ m) as the lower limit for the HC integration, (i.e. the depth minimum we prescribed when selecting Argo profiles) to maximize the number of Argo profiles available without the need to extrapolate data below the deepest measurement.

Finally, as the temperature anomalies decrease rapidly far from the eddy center [Souza et al. 2011a; Nencioli et al. 2018; Laxenaire et al. UR a], we present in Figure 5.4 only Argo profiles sampling an Agulhas Rings at a distance Dc smaller than half of the instantaneous value of R_{Vmax}. It is worth noting here that Agulhas Rings property anomalies are computed relatively to the environment. However, the hydrological properties of the environment vary from area to area of the larger domain (see Figure E.2 in the Appendix). Consequently, a direct comparison of HCA between remote regions have to be achieved cautiously.

The $HCA_{1200}^{200}(r)$ (hereafter $HCA(r)$) computed for Agulhas Rings is presented in Figure 5.4a. It shows that all the surface intensified eddies lying in the southeastern corner of the Cape Basin (and therefore close to the Agulhas Current retroflection) have high $HCA(r)$ values (up to $1 \times 10^{10} J.m{-}2$). On the other hand, in the western part of this basin, subsurface eddies show values among the lowest for this area. This

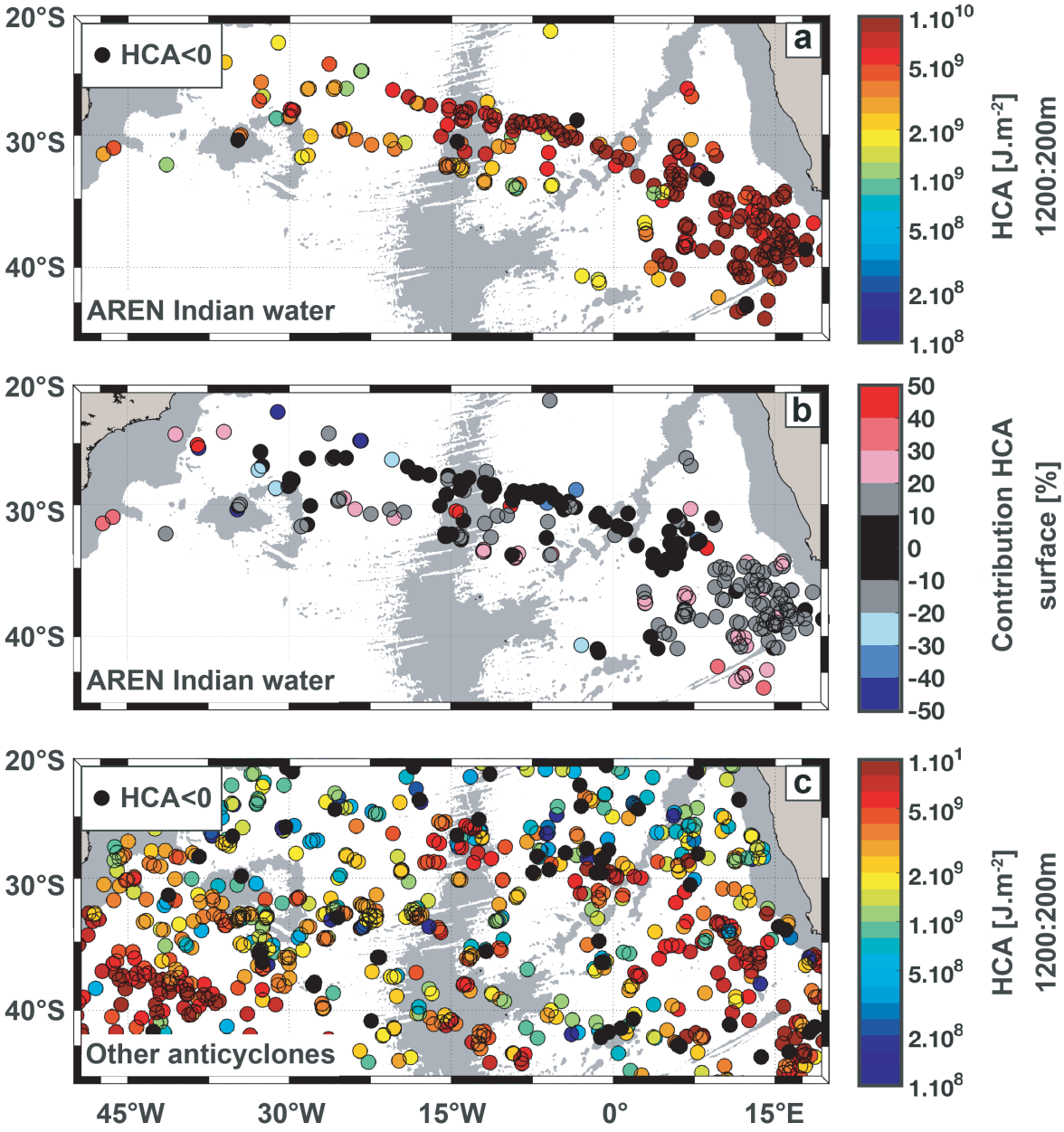


Figure 5.4: Heat Content Anomalies (HCA) for the profiles sampling an Agulhas Ring integrated between a) 1200 m to 200 m of depth and b) the contribution to HCA for the upper 200 m layer ($ContribHCA^0_{200}$) expressed as percentage of the total HCA following equation 5.2. c) HCA for anticyclonic eddies non identified as Agulhas Rings from the TOEddies Atlas. Negative values of HCA(r) are indicated in black in panels a and c. The gray shading in each figure represents water depths less than 3,500 m in the ETOPO2 data set [Smith and Sandwell 1997].

might indicate that these eddies also originating from the Agulhas Current, have undergone to intense heat loss before subducting in then ocean interior as discussed in the previous section. The difference of $HCA(r)$ is particularly important across this basin as the environment Heat Content is lower in the western Cape Basin than in its center (see Figure E.2 in the Appendix).

The high $HCA(r)$ values found in the central part of the Cape Basin are organized in such a way they form a continuous band across the Cape Basin, the Walvis and the Mid-Atlantic ridges following the northern branch of the Agulhas Rings corridor that extends across the South Atlantic basin. The southern branch of this corridor is characterized by significantly lower $HCA(r)$ (down by an order of magnitude). From Figure 5.4a it appears that the northern route is composed of Agulhas Rings with the highest subsurface $HCA(r)$ values and seems to materialize the major route for the Agulhas Rings heat transport in the South Atlantic Ocean. No clear pattern emerges in the western South Atlantic Ocean were both large and small values of $HCA(r)$ are found. Finally, only a very small fraction (i.e. $< 4\%$) of $HCA(r)$ is negative. It coincides with subsurface Agulhas Rings. This might indicate errors of detection as Agulhas Rings are expected to have positive temperature anomalies at depths deeper than 200 m.

The fact that the layers below the seasonal thermocline are stable during the whole year motivated us to only take into account the subsurface fraction (below 200 m) of $HCA(r)$. However, we need to assess the percentage of the neglected surface fraction of HCA(r). With this aims, we computed the percentage of the total $HCA(r)$ contribution is stored in the upper 200 m defining $z_{sup} = 0$ m and $z_{inf} = 200$ m in the equation 5.2:

$$ContribHCA_{z_{inf}}^{z_{sup}} = \frac{HCA_{z_{inf}}^{z_{sup}} \times 100}{|HCA_{z_{inf}}^{z_{sup}}| + |HCA_{1200}^{200}|} \tag{5.2}$$

The results are presented in Figure 5.4b. The lowest contribution (in black in Figure 5.4b) are mainly found in the northern portion of the Cape Basin and along the northern route, between the Walvis and the Mid-Atlantic ridges, characterized by subsurface Agulhas Rings. The highest upper 200 m HCA(r) contributions are found close to the Agulhas retroflection area and along the American margin. For 38 % (79 %) of the profiles, the upper 200 m layer contribute to less than 10 % (20 %) of HCA(r). This percentage remains unchanged by taking into account Argo profiles with Dc larger than half of the R_{Vmax} (not shown).

This figure also shows that subsurface Agulhas Rings contain a lower contribution of $HCA(r)_{200}^{0}$ that surface intensified ones. Indeed, when taking into account only these structures, the percentages given previously become 66 % and 84 % for, respectively, 10 % and 20 % of the $HCA(r)$. Consequently, in most cases, by not including the upper 200 m layer in the $HCA(r)$ estimate we neglect less than 20 % of its total value. It is worth noting that the $ContribHCA_{200}^{0}$ can be negative

for subsurface eddies as these structures are associated to positive σ_0' in the upper layers (as discussed previously).

Another strong assumption we made is to fix 1200 m of depth as the lower limit of the heat content vertical integration. In doing so, we neglected the fraction of $HCA(r)$ below this depth in contradiction with estimates of Agulhas Rings vertical extension reaching greater depths near their area of formation [e.g. Schmid et al. 2003; Arhan et al. 2011]. To evaluate the error, we introduce by neglecting this deep contribution to $HCA(r)$, we computed the fraction of $HCA(r)$ for the depth range 1200-1800 m ($ContribHCA(r)_{1800}^{1200}$) defining $z_{sup} = 1200$ m and $z_{inf} = 1800$ m in the equation 5.2. To be noted that ~80 % of Argo profiles within AR reach depths greater than 1800 m. In contrast with the distribution for $HCA(r)$ in the upper 200 m, the deep $HCA(r)$ contribution does not show a clear spatial pattern (Figure not shown). The results show unambiguously that the deepest layer affects less the total value of $HCA(r)$ than the upper 200 m layer does. Indeed, $HCA(r)_{1800}^{1200}$ contributes to less than 5 % (10 %) of the $HCA(r)_{1800}^{200}$ in 59 % (95 %) of Agulhas Rings. Surprisingly, subsurface eddies seem to contain a lower proportion of their $HCA(r)$ in the deepest layers than in the upper 200 m. Indeed for these, the contribution to $HCA(r)$ decreases to, respectively, 76 % and 98 % when only considering these structures. Finally, only two among the whole set of Agulhas Rings have $|ContribHCA(r)_{1800}^{1200}| > 20\%$. These are surface eddies showing a $HCA(r)_{1200}^{200} < 0$.

Similarly to what was done for the determination of the type of eddy (i.e., surface versus subsurface), it is important to compare Agulhas Rings $HCA(r)$ with that of other anticyclonic eddies detected in the domain of study. Figure 5.4c shows the $HCA(r)$ for the latter. It appears clearly that in the area where most of Agulhas Rings are sampled, the $HCA(r)$ for other anticyclones is lower in magnitude. This is particularly true between the Walvis and the Mid-Atlantic ridges along the Agulhas Rings northern branch. Here, all except four Argo profiles shows $HCA(r)$ values lower than the typical $HCA(r)$ value for Agulhas Rings ($1 \times 10^{10} J.m^{-2}$).

To have a more quantitative view for the whole domain, we computed the mean and standard deviation (STD) of $HCA(r)$ in 4°x4° grid cells from the HCA(r) computed in the anticyclonic eddies which are not AR as showed in Figure 5.4c (not shown). 9% of the Argo profiles not sampling an AR have a $HCA(r) < 0$. As this might indicate error of detection, only profiles associated to a $HCA(r) > 0$ are considered to create this grid. It is then possible to compare HCA(r) computed in the AR and the created grid. The results suggest that $HCA(r)$ in the Agulhas Ring is higher than the $HCA(r)$ mean (mean + STD) computed in the other anticyclonic eddies found in the region in 80 % (62 %) of cases.

Integration of the Agulhas Rings Heat Content Anomaly

In the previous section, we showed that the main contribution to $HCA(r)$ for Agulhas Rings lies within 1200 and 200 m of depth and its value is higher than for the environment. However, to obtain the total HCA associated to every eddy, the values of $HCA(r)$ needs to be integrated across the entire surface of the eddy following equation 5.3.

$$HCA_{r=0}^{r_{integ}} = 2\pi \int_{r=0}^{r_{integ}} HCA_{1200}^{200}(r) r d_r \tag{5.3}$$

Because Argo profiles do not sample the entire surface of the eddy structure, we need to extrapolate the values of $HCA(r)$ across the entire width of the eddy, or, alternatively, we need to extrapolate the values of the hydrological properties for the whole eddy. The most widely used approach is to define several geographical boxes in which composite eddies are computed [e.g. Chaigneau et al. 2011; Yang et al. 2013; Schütte et al. 2016]. This method relies heavily on the assumption that eddies properties and their structure are homogeneous in a specific region. This hypothesis has profound impacts on the estimates of eddy integrated variables such as the heat content anomaly. Indeed, considering n eddies, we might expect that $\frac{1}{n}\sum_{i=1}^{n}\left(\int_{r=0}^{r_{integ}} HCA_i(r) r dr\right) \neq \int_{r=0}^{r_{integ}} \frac{1}{n}\sum_{i=1}^{n}\left(HCA_i(r)\right) r dr$. This is particularly important if eddies of different size are integrated in the composite estimate. This can be shown considering, as an example, two different eddies: one with a radius larger than 200 km associated with a $HCA(r) = 1$ everywhere, and a smaller eddy with a 150 km radius, also characterized by $HCA(r) = 1$. In this case, for the second eddy, observations farther than 150 km from its center are not considered as they do not characterize the eddy properties but, instead, the environment. As a consequence, $\frac{1}{2}\sum_{i=1}^{2} HCA_i(r)$ would be equal to 1 instead of 0.5 for $r > 150$ km. In this example, the integration in terms of eddy composite results in an overestimation of HCA of about 30 % for $r_{integ} = 200$ km when compared to the estimate obtained by taking the average values of HCA integrated separately for each eddy.

Diversity of $HCA(r)$ in selected boxes

In this study, by selecting Agulhas Rings we choose eddies whose structure and properties should be closely related. This might suggest that, in selected geographical boxes, their vertical properties might be rather homogeneous. As we focus on anomalies, we need to take into account the local environment climatology. Knowing that such a climatology varies across the domain, the geographical boxes have to be selected carefully by trying to define the regions where the hydrological properties might be relatively homogeneous.

In Figure 5.5a are presented the four geographical boxes we selected. They are positioned along the Agulhas Rings corridor and they are subdivided according to the main topographic features (the Agulhas, Walvis and Mid-Atlantic ridges) of the domain as they are expected to have a strong impact on the eddy structure

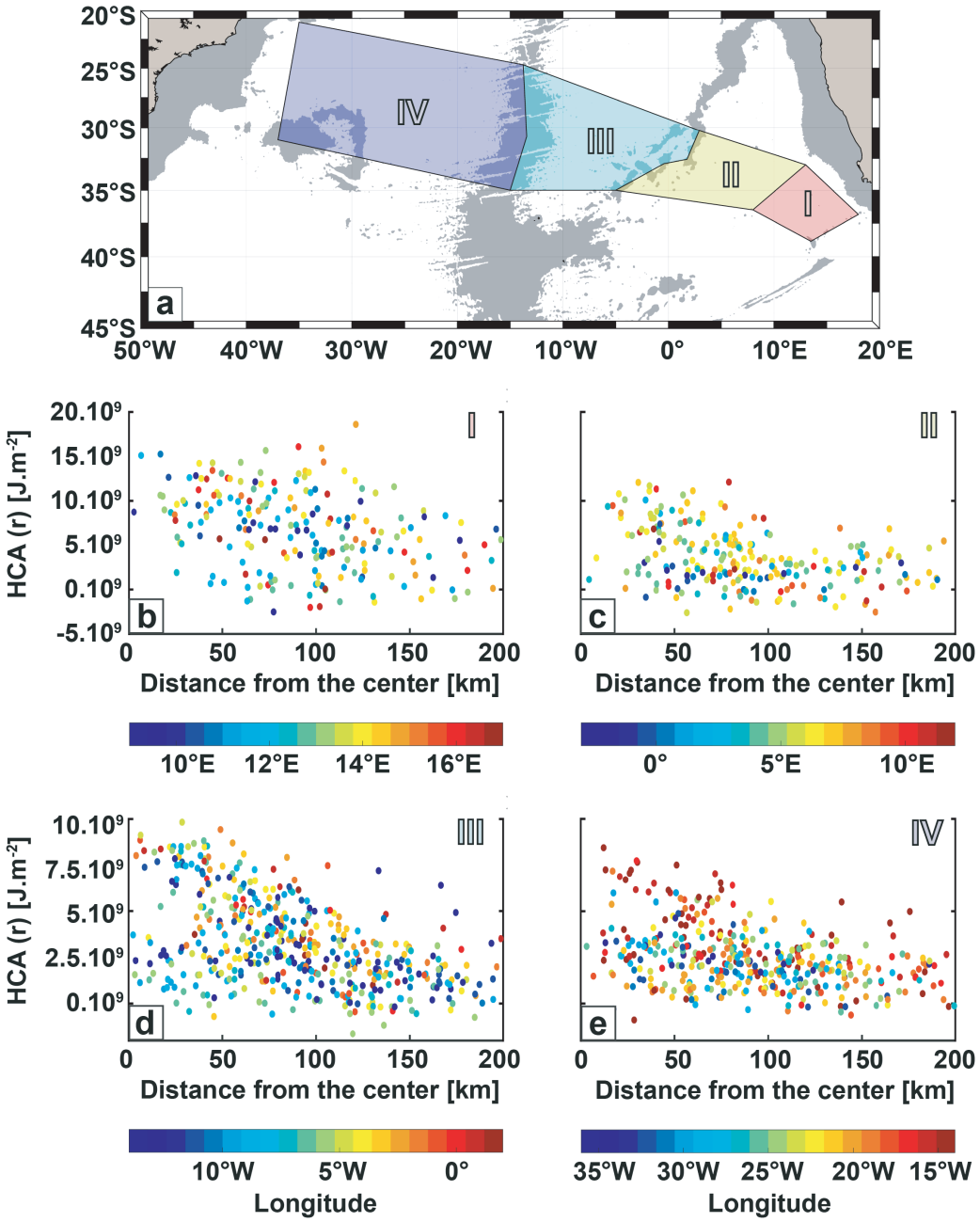


Figure 5.5: (b to d) $HCA^{200}_{1200}(r)$ computed for all the Argo profiles sampling an Indian Water AREN as estimated in the four boxes presented in panel a. The color of each point in the two lower panels corresponds to the longitude of the sampling.

and properties (by inducing diapycnal mixing for example) as discussed by different authors [e.g. Beismann et al. 1999; Nencioli et al. 2018]. We have divided the Cape Basin in two separated boxes: one representing the southeastern sector where eddy activity is very intense (the so called Cape Cauldron [Boebel et al. 2003a]) and where $HCA(r)$ has particularly high values. The other corresponds to the northwestern sector of the Cape Basin that is further away from the Agulhas Ridge and the Agulhas Current retroflection. Here Agulhas Rings are older and have already traveled across the Cape Cauldron area. The two Cape Basin boxes are relatively small compared to the size of the basin as well as to that of the other two South Atlantic boxes. This is because the Cape Basin exhibits the largest variations in the environment properties as shown in Figure E.2 in the Appendix.

Figure 5.5b presents the value of $HCA(r)$ computed for every Argo profile falling within an Agulhas Ring for each box. The results are plotted as function of (Dc), the distance of the profile from the eddy center. Here we made the assumption that eddies are axis-symmetric. This figure shows clearly that, in the Cape Basin, $HCA(r)$ in Agulhas Rings (box b to c) has higher magnitude than in the Atlantic basin (box d and e). However, the dispersion of $HCA(r)$ values is very large in all boxes. This suggests that $HCA(r)$ is highly variable within the different geographical areas and a clear correlation with Dc does not stand out. One might argue that these boxes are too large. Still, as shown by the color of the circles representing the longitude for each profile, no clear regional dependency emerges. Similar figures where circles are colored according both latitude and longitude (not shown) give similar results except for box I where, in the Cape Cauldron area, the latitude seems to have an impact as expected by the large variations of HCA in this box (see Figure E.2 in the Appendix). These results suggest that, even by selecting eddies that should be similar in hydrological properties, they still show highly variable properties.

The reconstruction of $HCA(r)$ in individual AR

One approach to estimate the total HCA for Agulhas Rings is to reconstruct individual structures that are sufficiently sampled by Argo profiles along their trajectory. This type of approach has been already implemented to reconstruct one or more AR hydrological structures [e.g. Souza et al. 2011a; Nencioli et al. 2018; Laxenaire et al. UR a].

Here we applied this approach to estimate the total HCA of several Agulhas Rings in each box. This assessment should allow us to better characterize the geographical distribution of HCA. However, to achieve such a reconstruction, we need to provide some assumptions on the eddy shape to be able to extrapolate sparse profiles into a full structure. For example, it is very common to assume that Agulhas Rings have an axi-symmetric configuration without any vertical tilt. This assumption has been validated from both, observations [Van Aken et al. 2003] and numerical simulations [Bettencourt et al. 2012].

A second assumption is to prescribe the horizontal variations of the hydrological

properties of Agulhas Rings in terms of a generic function that does not depend on depth. This assumption has been verified, at least at the first order, from observations of eddies in the global ocean by Zhang et al. [2013] and for some Agulhas Rings by Nencioli et al. [2018].

In this study, therefore, we sake the most appropriate horizontal function characterizing $HCA(r)$ for Agulhas Rings at any vertical level between 200 m and 1200 m of depth. This type of horizontal function has been already used in past studies to characterize the eddy hydrological properties (i.e. temperature, salinity and density anomalies) [e.g. Laxenaire et al. UR a], the Sea Surface Height Anomalies (SSHA) [e.g. Chelton et al. 2011] and the pressure anomaly [e.g. Zhang et al. 2013; Nencioli et al. 2018].

As, to our knowledge, the horizontal dependence between $HCA(r)$ and a fixed horizontal function has not yet been tested, in the following we tried to validate our approach. For this purpose, we computed, for every Argo profile within an Agulhas Ring, the correlation between $HCA^{200}_{1200}(r)$ and the local Dynamical Height Anomaly (DHA), a proxy of SSHA, computed for the same depth interval. The DHA is estimated using the "*geo_strf_dyn_height*" MATLAB function from the Gibbs SeaWater (GSW) Oceanographic Toolbox of the Thermodynamic Equation of SeaWater TEOS-10 [McDougall and Barker 2011]. The results show a strong linear correlation between these two variables with a coefficient of determination (R^2) equal to 0.95. This correlation, which is very likely related to the impact of the thermal expansion of water on DHA, gives us confidence in using a function to describe the horizontal shape of the eddies, similarly to the assumptions for SSHA by Chelton et al. [2011]. This allows us to use the same type of function for Agulhas Rings at any depth levels within the 200 - 1200 m range of depth.

$$HCA(r) = HCA(r=0)e^{-\frac{1}{2}\left(\frac{r}{R_0}\right)^2} \tag{5.4}$$

Many horizontal functions have been suggested to appropriately describe the horizontal shape of eddies. The class of functions most widely found in the literature is the α-Gaussian vortex [Carton 2001] which is, in general, simplified to a simple Gaussian vortex, where $\alpha = 2$ [e.g. Zhang et al. 2013; Nencioli et al. 2018] which showed to be a good approximation by Laxenaire et al. [UR a]. Consequently, an α-Gaussian dependence on r is used on $HCA(r)$ as shown in equation 5.4. It is then possible to fit this function for every segment of AR trajectories sampled by, at least, two profiles to reconstruct the full $HCA(r)$ for every eddy. However, to prevent large error in the extrapolation, we have prescribed that the horizontal reconstruction of $HCA(r)$ along a segment of Agulhas Rings trajectory is possible only if some criteria are verified. These criteria require for each AR segment that:

- The eddy has been sampled by more than 6 Argo profiles and, among these, at least 3 should be located at a distance $Dc < \frac{R_{Vmax}}{2}$;

- At least one of the profile must lie in each of the following Dc intervals: [center,50 km[, [50 km,100 km[and [100 km,R_{out}];
- The Argo profiles should be spaced in time by less than 20 consecutive days (i.e. two Argo cycles);
- The maximum difference of eddy weekly averaged R_{Vmax} (ΔR_{Vmax}) should not exceed 40 km;
- The eddy should not cross any of the limit of the 4 geographical boxes presented in Figure 5.1a.

sing these criteria, we were able to identify 32 segments of Agulhas Ring trajectories. For these, we computed, for each profile, the $HC(r)$ and the related climatology of the environment. The obtained values for $HCA(r)$ are more coherent along the identified segments of trajectories when they are referred to the mean $HC(r)$ of the environment climatology instead of the $HC(r)$ computed in the associated climatological profile This is particularly true for the longest segments that can cross slightly different hydrological environments.

We also assumed that anomalies associated with an eddy reduce to zero far from the structure. To ensure this, we added artificial $HCA(r = 200km) = 0$ values. We choose a distance of 200 km as it is larger than the horizontal extension of the observed Agulhas Rings size which varies between 65 and 150 km [e.g. Garzoli et al. 1999; Arhan et al. 1999; Casanova-Masjoan et al. 2017]. Also, according to Souza et al. [2011a] and Laxenaire et al. [UR a], the eddy core radius for Agulhas Rings is ˜ 150 km. To give an equivalent weight to these artificial points in the different reconstructions, we added n artificial values of $HCA(r = 200) = 0$, where n is the number of observations used for the reconstruction.

We computed the horizontal function for $HCA(r)$ by minimizing the fitting of equation 5.4 to the observations. For this we made use of the Trust Region Reflective algorithm [Branch et al. 1999] with the function lsqcurvefit of the MATLAB Library. For each reconstruction, the initial value of R_0 is fixed to the average R_{Vmax} and it is constrained by $R_{Vmax} \pm 20km$ which corresponds to the criterion of the maximum of ΔR_{Vmax} used for the identification of the Agulhas Rings segments that could be reconstructed. This choice is motivated by the fact that, when used on the satellite altimetry SSH field and by assuming the geostrophic approximation, one can easily show that R_0 in equation 5.4 is equal to the R_{Vmax} obtained from the altimetry maps. A local minimum of the residuals obtained from the least-square method is often derived when fitting this function. To prevent this, five different fitting are tested where the initial value of $HCA_{r=0}$ increases from 2×10^9 to 18×10^9 J.m^{-2}. The coefficient providing the lowest squared 2-norm of the residual is conserved.

For different reasons, such as the occurrence of eddy splitting and merging events, the $HCA(r)$ measured in the various profiles sampling a segment can be not completely coherent. Consequently, we used the coefficient of determination (R^2) to

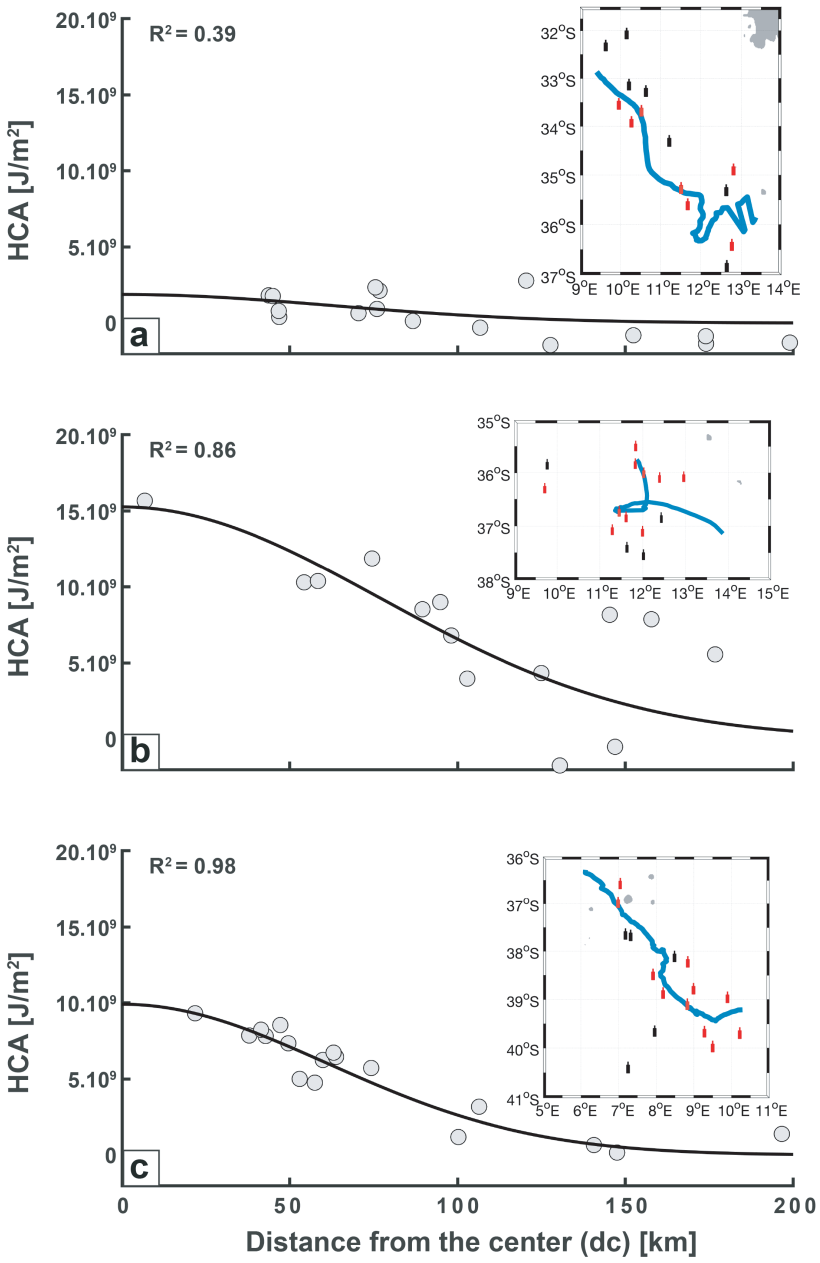


Figure 5.6: Three examples (panels a to c) of reconstructed $HCA(r)$ and their associated coefficient of determination (R^2) for eddies lying in close-by regions. The $HCA(r)$ values directly derived from observations are presented as grey circles while the Lagrangianly reconstructed $HCA(r)$ values are shown as black lines. The trajectories (in blue) and the position of the associated Argo profiles are presented in a map on the right top corner of each panel. The position of the Argo profiles are drawn in red if they sample the Agulhas Rings within their R_{Vmax} contours and black otherwise.

validate the reconstruction following Nencioli et al. [2018]. This coefficient is applied to a non-linear fitting which prevent to use it to validate a null-hypothesis but it allows to qualitatively evaluate the robustness of the fit. Figure 5.6 shows three examples of $HCA(r)$ reconstruction for close-by segments with a similar number of Argo profiles (between 14 and 17).

Figure 5.6a presents the poorest reconstruction among the three cases. Here, observations show a large dispersion compared to the relatively low $HCA(r)$ of the eddy. Figure 5.6b shows a better reconstruction but, still, a large dispersion appears away from the center of the eddy. The effect of these points, which might sample a close-by structure for example, and therefore not representing the core of the eddy under study, is reduced using the artificial $HCA_{1200}^{200}(r = 200) = 0$. However, it should be noted here that if $HCA(r)$ is integrated over the surface of the eddy, the values lying in the outer ring of the eddy affect the result and attention should be paid to those peripheral points that might lead to large errors in the estimates. Figure 5.6c shows an example of a particularly adequate reconstruction for $HCA(r)$.

Among the 32 segments for which we implemented the Lagrangian reconstruction of $HCA(r)$, 75% are associated with a $R^2 > 0.9$ and 44% with a $R^2 > 0.95$. For a comparison, the R^2 obtained fitting the equation 5.4 for $HCA(r)$ in the four boxes shown in panels b to d of Figure 5.5, ranges only between 0.61 and 0.73. After a careful examination of the $HCA(r)$ reconstruction for each of the 32 segments, the limit of $R^2 > 0.9$ seems sufficient to grant an adequate functional fitting with the observations. This threshold allowed us to select 24 segments. To be mentioned here that this value is more restrictive than the $R^2 = 0.7$ used by Nencioli et al. [2018].

By examining the values of Dc associated with the closest profile to the eddy center for each of the selected 24 segments, we found that for 13 segments $Dc<$ 20 km and only in one case $Dc > 40$ km. The median number of Argo profiles used to reconstruct the $HCA(r)$ for the selected Agulhas Ring segments is 16. The most sampled eddy accounts for 43 Argo profiles. The median number of profiles achieved by a same float in one eddy is 10 (i.e. ~3 months), the maximum number is 32 (i.e. ~10 months) and the minimum is 4 (i.e. ~1 month).

The eddy integrated HCA and the total HC obtained by adding the HC of reference to $HCA(r)$ for the 24 selected segments are shown in Figure E.3 of the Appendix. It is then possible to identify the reconstructed segments crossing a box to obtain, if there are enough segments in the given area, the geographical distribution of HCA. In the Cape Basin, one segment can cross two boxes (see Figure 5.1a). For this reason, we prescribed that each of the 24 segments is associated with a box area if it spends more than one third of its lifetime in it. By doing so, none of the segments is associated to more than one box.

The composite reconstruction of the HCA and comparisons of the two approaches

To compare the results of the composite and individual reconstructions, we integrated the $HCA(r)$ into composite eddies computed over a fixed grid of 1 km in the radial distance and 10 m in the vertical following five different methods [Chaigneau et al. 2011; Souza et al. 2011a; Yang et al. 2013; Schütte et al. 2016; Laxenaire et al. UR a].

Chaigneau et al. [2011] and Yang et al. [2013] developed a similar method. They computed the eddy properties value at each grid point by averaging all the observations weighted by an isotropic Gaussian function centred on the grid point. We followed this approach by identifying as outliers the observations that are more than 3 times the interquartile interval from either the first or the third quantile. The difference between the approaches of Chaigneau et al. [2011] and Yang et al. [2013] is the Gaussian covariance decorrelation scale used (100 km in Chaigneau et al. [2011] and 60 km in Yang et al. [2013]).

Souza et al. [2011a] and Laxenaire et al. [UR a] used an approach based on the fitting of a function to the observations by using a least-square method. A 7^{th} order polynomial is used in Souza et al. [2011a] while Laxenaire et al. [UR a] applied an α-Gaussian function (similar to the equation 5.4 with α =2).

In their approach, Schütte et al. [2016] implemented a moving-average window of 0.2 *x the normalized radius*. In this method, the eddy radius was defined according to detection algorithm developed by Nencioli et al. [2010] which is equivalent to the R_{Vmax} given by the TOEddies algorithm. Knowing that the mean R_{Vmax} value for Agulhas Rings is 60-80 km [e.g. Guerra et al. 2018; Laxenaire et al. 2018], we choose a 15 km window to apply the Schütte et al. [2016] method in our region of study.

Figure 5.7 presents the different estimates for HCA computed according the various techniques for each of the four boxes. We initially compared the results issued from the different methods of eddy composites computation as they turn out to have similar relative ranges and distribution in all four boxes (see Figure 5.7). The methods of Souza et al. [2011a] and Laxenaire et al. [UR a] give very similar results (they nearly overlap everywhere). This might be due to the fact that, in both methods, the reconstruction is obtained by a least-square fitting of a function to the observations. However, they differ substantially in how they take into account the outer area of the eddy. Indeed, the method of Laxenaire et al. [UR a] prescribes that HCA is zero far from the eddy center, whereas it is not necessarily the case for higher order polynomials as in Souza et al. [2011a].

Chaigneau et al. [2011] and Yang et al. [2013] provides also similar results to each, that can be explained as the only difference between the two methods is the value of the Gaussian scale, which is higher in Chaigneau et al. [2011] resulting in flatter shapes for the HCA reconstructions. Schütte et al. [2016] shows the the most contrasting results due to the approach which apply a milder smoothing.

In comparison, the results obtained using the individual reconstruction method are significantly different than any of the eddy-composite methods. In general, the

individual reconstruction provide HCA values at the center of the eddies that are higher than for the eddy-composite approach, whereas they are smaller in the outer rim of the eddies. However, the number of the eddies HCA reconstructed with the individual reconstruction approach, and therefore their representativeness in terms of eddy varieties, is not homogeneous for all boxes. They are relatively well distributed in boxes II and III where, respectively, 5 and 6 Agulhas Ring segments were reconstructed. However, only 2 reconstructions were possible in each one of the other two boxes (i.e., boxes I and IV).

To obtain a more quantitative comparison between the different approaches, we integrated the HCA values across the first 200 km for each eddy following the equation 5.3. The results are presented in Table 5.1. Among all the HCA values obtained by applying the eddy-composite approaches, the method of Chaigneau et al. [2011] always results in the highest HCA whereas Laxenaire et al. [UR a] in the lowest. However, all the results come out to be very close to each other as the associated standard deviation is $\sim$10$-$15 % of the HCA mean value in all boxes.

The HCA mean value obtained by applying the individual reconstruction are, in general, lower than for the eddy-composite approaches. However, the latter are, in most of case, in the range of the standard deviation obtained for the Lagrangian reconstruction. This is not the case in Box IV but results have to be considered with precaution as we were able to reconstruct the HCA for only two segments which are associate to the highest values of the observed $HCA(r)$ (see Figure 5.7). Moreover, in Box I (the Cape Cauldron area), the eddy-composite approaches provide higher values for HCA than the average of the Lagrangian reconstructions albeit the latter estimate comes from only two segments and might not sufficiently robust to draw any conclusion. Boxes II and III, that account for at least 5 different segment reconstructions, suggest that the eddy-composite estimate in these regions are rather coherent with the Lagrangian approach. In particular, the eddy-composite approaches that apply a fitting of the observations to a function such as Souza et al. [2011a] and Laxenaire et al. [UR a], provide the closest estimate to those obtained with the Lagrangian method.

The HCA estimates represent anomalies. These estimates are therefore very sensitive to the heat content estimate for the environment. The latter evolves geographically and in time. Therefore, it is not possible to directly compare the the HCA estimates for the different box areas. We also cannot compare truthfully the Total HC values as the eddies are not expected to be barotropic and cylindrical in structure. Hence, especially far from the eddy centers, we expect that only a small fraction of the water column is impacted by the eddy presence. This is not a constraint for HCA estimates themselves as anomalies should go to zero below and above the eddy, but it prevents any simple integration with the local average value of the environment HC, and therefore any robust comparison among remote eddies.

However, close to the eddy-center, Agulhas Rings are expected to extend, at least, from 200 to 1200 m of depth within the Cape Basin [e.g. Duncombe Rae et al. 1996; McDonagh et al. 1999] and in the South Atlantic Ocean [e.g. Souza et al. 2011a;

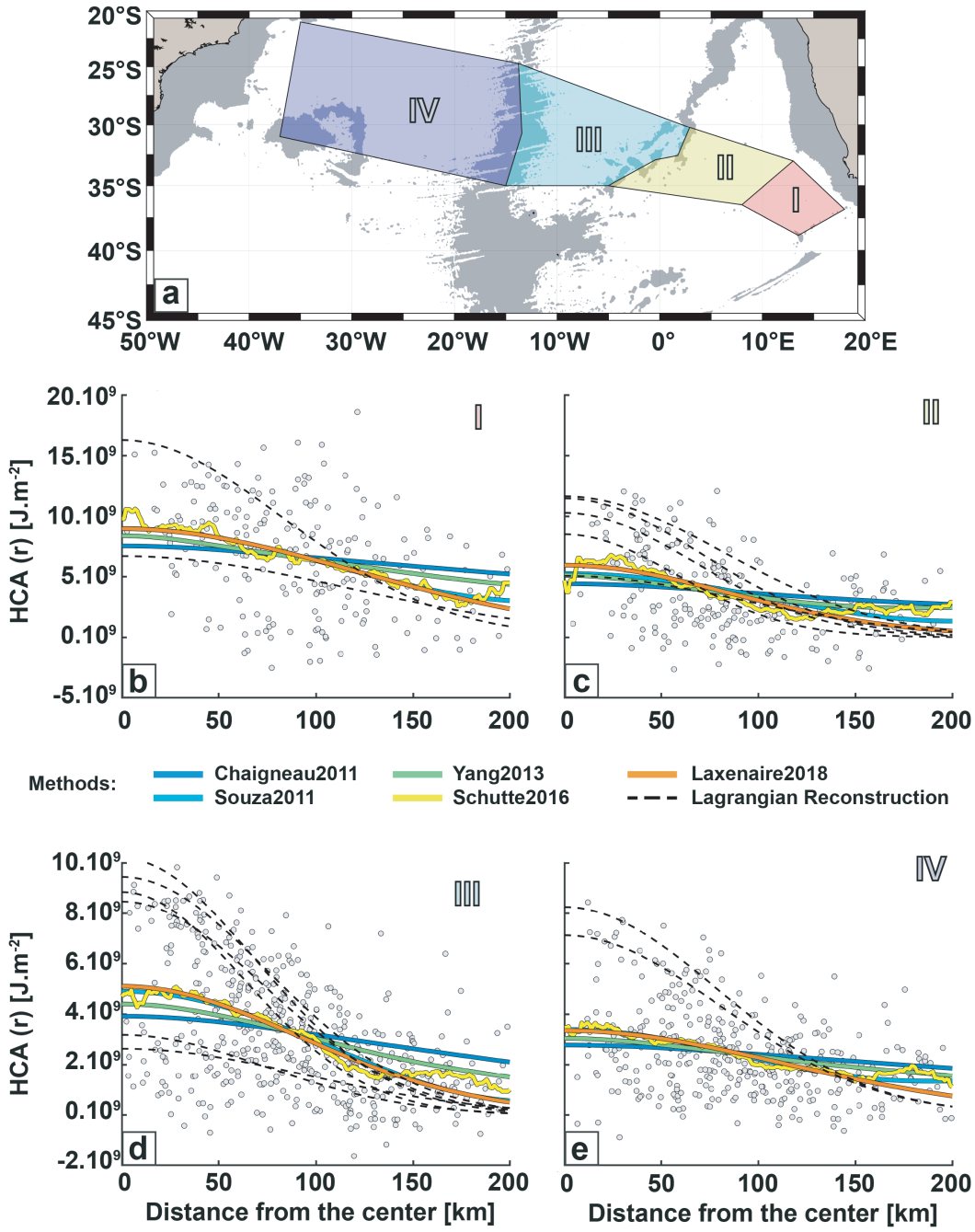


Figure 5.7: Reconstruction of HCA_{1200}^{200} using the whole set of Argo profiles sampling an Indian Water AREN (b to e) in the four geographical boxes presented in a). Each colored thick lines in b) to e) is associated with a different eddy-composite method of reconstruction whereas the dashed black lines represent the various Lagrangian reconstructions.

Table 5.1: Eddy integrated HCA_{1200}^{200} obtained by applying different approaches (eddy-composite and Lagrangian) in each of the four geographical boxes presented in Figure 5.7a.

Type of Reconstruction	Box I	Box II	Box III	Box IV
Chaigneau2011	$77\,10^{19}J$	$41\,10^{19}$J	$35\,10^{19}$J	$28\,10^{19}$J
Souza2011	$63\,10^{19}$J	$33\,10^{19}$J	$25\,10^{19}$J	$23\,10^{19}$J
Yang2013	$71\,10^{19}$J	$37\,10^{19}$J	$31\,10^{19}$J	$26\,10^{19}$J
Schutte2016	$64\,10^{19}$J	$34\,10^{19}$J	$27\,10^{19}$J	$24\,10^{19}$J
Laxenaire2018	$62\,10^{19}$J	$27\,10^{19}$J	$25\,10^{19}$J	$22\,10^{19}$J
Lagrangian	$55 \pm 16\,10^{19}$J	$30 \pm 11\,10^{19}$J	$23 \pm 9\,10^{19}$J	$29 \pm 2\,10^{19}$J
Number of Reconstruction	2	5	6	2

Nencioli et al. 2018; Laxenaire et al. UR a]. Therefore, a qualitative comparison among Agulhas Rings lying in different regions can be undertaken by correlating their $HC(r = 0)$. The resulting $HC(r = 0)$ values for the eddies and those for the environment are presented in Table 5.1. The $HC(r = 0)$ values decrease gradually along the Agulhas Rings route, from the Cape Basin to the Atlantic Ocean. This is in agreement with two possible processes: i) a gradual dissipation of the eddy and its properties as discussed recently by Nencioli et al. [2018] ii) the splitting or the merging of eddies and the subsequent decrease in Indian waters volume they contain or the mixing of Indian waters with waters of South Atlantic origins.

The results issued by applying the Schütte et al. [2016] method provides the only contrasting estimate with the in-route eddy-heat content decrease. This might be due to a possible sensitiveness of the method on observations (it uses a 15 km window averaging). A contrasted value appears also for the Lagrangian reconstruction in box IV, very likely due to an insufficient number of Agulhas Rings appropriately sampled by Argo profiles.

In general, the eddy-composite results suggest a more important $HC(r = 0)$ transition than the Lagrangian reconstruction between boxes I and II. The opposite is true for boxes II and III, where enough segments are available for the Lagrangian reconstruction.

Heat transport across the South Atlantic Ocean

Finally, the reconstructed total HCA can be used to compute the heat transport achieved by Agulhas Rings. This cannot be robustly undertaken in the Cape Basin as the geographical boxes we defined do not cover this basin entirely. However, its seems legit to do this in the South Atlantic Ocean as the boxes cover the entire path of Agulhas Rings as depicted in Figure 5.1.

The classical heat transport estimates for Agulhas Rings documented in the literature is achieved by multiplying one or two eddies observed or reconstructed temperature and volume by the average number of eddies spawn at the Agulhas retroflection (see Souza et al. [2011a] for example). However, as shown in Figure 5.1a, the number of Agulhas Rings crossing a specific geographical line across the Cape Basin and the South Atlantic Ocean per year, decreases far from the Agulhas Ridge. For example, according to the detected trajectories, 4.2 Agulhas Rings enter in box III every year and 3.6 leaves it. Hence, in average, 0.6 Agulhas Rings per year disappear from the altimetric field in this region. Interpreting this disappearance as the dissipation of the AR in this box and taking the values of HCA obtained using the 6 Lagrangian reconstruction, the dissipation of the AR results into a transfer of $0.4 \pm 0.2 \times 10^{-2} PW$ to the ocean interior in this box.

Another possible estimate of Agulhas Rings heat transport can be achieved considering the average between the number of Agulhas Rings entering and exiting each box per year. This amounts to a mean value of ~4 Agulhas Rings crossing box III each year that account for a heat transport of $2.8 \pm 1 \times 10^{-2} PW$. It is

Table 5.2: $HC(r=0)$ computed from the $HCA(r=0)$ for the reconstructed Indian Water AREN and the environment local average HC. Values are expressed as $1\,1\,10^{11}$ J.m^{-2}

Type of Reconstruction	Box I	Box II	Box III	Box IV
Chaigneau2011	$55.7\,10^9$ J.m^{-2}	$53.7\,10^9$J.m^{-2}	$53.5\,10^9$J.m^{-2}	$53.4\,10^9$J.m^{-2}
Souza2011	$57.1\,10^9$ J.m^{-2}	$54.6\,10^9$J.m^{-2}	$54.5\,10^9$J.m^{-2}	$54.1\,10^9$J.m^{-2}
Yang2013	$56.6\,10^9$ J.m^{-2}	$54.4\,10^9$J.m^{-2}	$54.0\,10^9$J.m^{-2}	$53.7\,10^9$J.m^{-2}
Schutte2016	$58.0\,10^9$ J.m^{-2}	$54.0\,10^9$J.m^{-2}	$54.3\,10^9$J.m^{-2}	$54.1\,10^9$J.m^{-2}
Laxenaire2018	$57.1\,10^9$ J.m^{-2}	$55.3\,10^9$J.m^{-2}	$54.7\,10^9$J.m^{-2}	$54.0\,10^9$J.m^{-2}
Lagrangian	$59.8 \pm 3.2\,10^9$ J.m^{-2}	$58.7 \pm 2.7\,10^9$J.m^{-2}	$56.7 \pm 3.3\,10^9$J.m^{-2}	$58.3 \pm 0.8\,10^9$J.m^{-2}
Number of Reconstruction	2	5	6	2
Reference	$48.4\,10^9$ J.m^{-2}	$49.2\,10^9$J.m^{-2}	$49.5\,10^9$J.m^{-2}	$50.7\,10^9$J.m^{-2}

not possible to do the same computation for box IV where it was only possible to reconstruct 2 individual AR.

Among the various estimates using different reconstruction approach for HC, the methods of Laxenaire et al. [UR a] and Souza et al. [2011a] are those providing the closest estimates to the Lagrangian reconstruction in boxes II and III. Using these two methods, we obtain a heat transport of $3.1 \times 10^{-2} PW$ across box III and of $2.0 \pm 0.2 \times 10^{-2} PW$ across box IV. Finally, with these two methods, it is also possible to compute the transfer of heat from the eddies to the ocean interior due to dissipation, that amounts to $0.5 \times 10^{-2} PW$ for box III and $1.2 \times 10^{-2} PW$ for box IV.

5.2.4 Discussion

In this study we used the recently developed TOEddies eddy-detection and tracking method [Laxenaire et al. 2018] and collocated Argo vertical profiles of temperature, salinity and pressure to attempt to characterize Agulhas Rings properties and evolution along their path across the Cape Basin and the South Atlantic Ocean.

By using this technique and by applying a modified version of the method of Assassi et al. [2016] and Schütte et al. [2016], we were able to provide a regional characterization in terms of surface and sub-surface intensified eddies. The resulting pattern compares well with the literature that documents a relatively sparse set of surface intensified Agulhas Rings in the Cape Basin and sub-surface eddies in the Southeast Atlantic. See, for example, Laxenaire et al. [UR a] who used a qualitative method to identify surface and sub-surface intensified eddies from historical observations of Agulhas Rings documented in different articles [Gordon et al. 1987; Duncombe Rae et al. 1996; Schmid et al. 2003; McCartney and Woodgate-Jones 1991; Arhan et al. 1999; Gladyshev et al. 2008; Duncombe Rae et al. 1992; Garzoli et al. 1999; Arhan et al. 2011; van Ballegooyen et al. 1994; McDonagh et al. 1999; Casanova-Masjoan et al. 2017].

Overall, the present study and Laxenaire et al. [UR a] results suggest that Agulhas Rings in the central Cape Basin are surface intensified eddies while in the South Atlantic Ocean (between the Walvis and the Mid-Atlantic ridges) and in the southern Cape Basin they are, in general, subsurface intensified eddies. Agulhas Rings located on top of the Walvis Ridge fall in the category of subsurface eddies. However, Laxenaire et al. [UR a] identified, in the literature, the case of a couple of subsurface eddies in the Cape Basin. One of these eddies was discussed by Duncombe Rae et al. [1996] that described it as an eddy of Brazilian Current origins. This hypothesis seems to us not robust as none of such structures has been documented in any other published work. Moreover, while it might be possible that this eddy was formed in a different region than the Agulhas retroflection, yet the hydrological properties of that eddy are within the range characterizing Agulhas

Rings (see Laxenaire et al. [UR a]).

In the present work we show that in the Cape Basin both, surface and subsurface Agulhas Rings can coexist, with the latter located essentially in the southern part of the basin. In addition, Laxenaire et al. [2018] showed that a large number of Agulhas Rings disappear from altimetry maps very shortly after these eddies leave the Agulhas retroflection area and enter the Cape Basin. Hence, it might be that the very strong local air-sea exchanges south of Africa induce a more generalized Agulhas Rings subduction within the Cape Basin than what we could assess by tracking eddies from altimetry data. Our study also shows that surface and subsurface anticyclonic eddies with different origins than Agulhas Rings populate the Cape Basin. Still, the overall similarities in the results of the present study with those issued from all historical observations of Agulhas Rings discussed in Laxenaire et al. [UR a] suggest that Agulhas Rings are mainly surface intensified eddies in the central part of the Cape Basin whereas they subduct quickly in its southwestern portion. Subduction occurs also when Agulhas Rings cross the Walvis Ridge and enter the South Atlantic Ocean. These results strongly suggest that Agulhas Rings at one point all subduct along their route and in the South Atlantic they propagate as subsurface eddies. Near the American continent, anticyclones that have a connection with an origin in the Agulhas Current show properties of surface eddies. This might be linked with the merging of Agulhas Rings with anticyclones formed locally as observed from altimetry maps [Laxenaire et al. 2018].

A second aspect of Agulhas Ring characteristics that emerges from this work is that the majority of their Heat Content Anomalies are located within the 200-1200 m depth interval. Indeed, the upper 200 m of water account only for less than 10 % (20 %) of the 0-1200 m water column Heat Content Anomalies for subsurface (surface) intensified eddies and the deepest layers (1200-1800 m of depth) only for ~5%. In the case of subsurface eddies, the upper 200 m are often associated to a negative Heat Content Anomaly. Moreover, when in the South Atlantic, Agulhas Rings account for a smaller Heat Content Anomaly in the lower layers than in the Cape Basin. This might be linked to their age, distance from the area of their formation, a higher number of splitting and merging events experienced or to the interaction of barotropic Agulhas Rings with strong topographic barriers such as the Walvis Ridge as suggested by Beismann et al. [1999] and De Steur and Van Leeuwen [2009]. Also, this work provides an estimate of the heat loss by Agulhas Rings along their route. Agulhas Rings loose heat both in the upper layers (to the atmosphere) but also in the subsurface (to the ocean interior), confirming results by Nencioli et al. [2018], as showed by the study of the changes of the first 1200 meters at their center.

For sake of exhaustiveness, in this study we tested different approaches to assess the total Agulhas Rings Heat Content Anomaly. These included various eddy-composite estimates [e.g. Chaigneau et al. 2011; Yang et al. 2013; Schütte et al. 2016] as well as computations based on reconstruction of individual eddies in four regions spanning the Agulhas Rings route across the Cape Basin and the South

Atlantic Ocean. Overall, in the regions sufficiently sampled by Argo vertical profiles, the various estimates provide rather similar results and they compare well with the novel Lagrangian approach we propose. Yet, the eddy-composite approaches tend to underestimate the Heat Content Anomaly at the eddy center and to overestimate it at the eddy periphery.

From these estimates, we computed the heat transport associated with these eddies that results in $3 \times 10^{-2} PW$ and $2 \times 10^{-2} PW$ for, respectively, the eastern and western South Atlantic areas. These values are lower than the $7 \times 10^{-2} PW$ proposed by Souza et al. [2011a] and they correspond to the lower range of the $3 \times 10^{-2} - 8 \times 10^{-2} PW$ estimates by Gründlingh [1995]. However, comparisons are difficult as Gründlingh [1995] and Souza et al. [2011a] values were obtained by computing the number of Agulhas Rings entering the Cape Basin per year whereas in this study we focused specifically on tracking and accounting for Agulhas Rings leaving the Cape Basin and entering the South Atlantic only. These eddies have undergone to merging and splitting events, strong air-sea exchanges as well as interactions with topography. Is therefore reasonable that they account for a lower heat transport than Agulhas Rings just spawned by the Agulhas retroflection.

One limit of such estimation is the number of Agulhas Rings we are able to detect from satellite altimetry. However, when comparing to the results obtained in previous studies and, in particular, those discussed in the recently published work by Guerra et al. [2018], our estimate accounts for a larger number of eddies crossing the South Atlantic Ocean. For example, Guerra et al. [2018] enumerate 2.5 and 1.7 Agulhas Rings crossing, respectively, the meridian 10 and 20°W whereas our calculation suggests that, in average, 3.6 Agulhas Rings cross the Mid-Atlantic ridge near 15°W.

Another possible shortcoming of this work lies in the definition we adopted for the eddy heat transport that we associated to the advection of water masses within the moving eddies identified as coherent structures (known as "eddy drift transport", [Hausmann and Czaja 2012]). Indeed, recent studies suggested that other processes might impact such a transport. For example, some authors [e.g. Roemmich and Gilson 2001; Souza et al. 2011a; Hausmann and Czaja 2012; Amores et al. 2017] have suggested that the non alignment between the eddy azimuthal speeds and hydrological anomalies can results to a net meridional transport (defined as the "swirl heat transport" by Hausmann and Czaja [2012]). By comparing these two type of transport by reconstructing 16 different Agulhas Rings, Souza et al. [2011a] obtained comparable values for "eddy drift transport" and "swirl heat transport". Recently, the "eddy drift transport" has been revisited and its amplitude slightly reduced [e.g. Wang et al. 2015; 2016]. However, it is worth noting here that these results are based on algorithms that are strongly dependent on the absolute values of the azimuthal velocities associated to the eddy. In particular, the surface signature of the eddy velocities might not be representative of the eddy-core velocities if the eddy is a subsurface intensified structure [e.g. Laxenaire et al. UR a] as is the general case for Agulhas Rings as we discussed previously. Besides, Agulhas Rings show

a clear coherent eddy behavior as they advect in their course numerous drifting buoys and Argo floats [Laxenaire et al. 2018; UR a]. In particular, we showed here that within each eddy we were able to track and reconstruct at least one Argo float was captured within its core for more than one month. We also estimated that Argo floats spent a median time of 3 months within Agulhas Rings. These results agree also with the values proposed by Souza et al. [2011a], Nencioli et al. [2018] and Laxenaire et al. [UR a].

5.2.5 Conclusion

In this work we made use of TOEddies [Laxenaire et al. 2018], a new eddy detection and tracking method, to identify Agulhas Rings from the AVISO daily satellite absolute dynamic topography maps. By collocating the identified eddies with every available *in situ* Argo floats profiles we aimed to investigate their vertical structure and associated heat content and transport.

While Argo floats have improved drastically the upper 2000 m sampling of the world ocean, their spatio-temporal coverage is not yet sufficient to document the mesoscales. Therefore, any three-dimensional eddy reconstruction is possible only if there are a sufficient number of vertical profiles sampling individual structures. In this study we showed that a number of 6 for such profiles with, at least, 3 profiles falling in the first inner half region of the eddy core (which is delimited by R_{Vmax}) was providing a sufficient base for a robust estimate of eddy three-dimensional structure. We also pointed out that the stability of the results is achieved only if we take into account profiles lying within the eddy core and if we compute properties in terms of anomalies with respect to the environment to ensure they go to zero at the eddy outer edge.

With this setting and by being able to track eddies from altimetry maps, we have been able to isolate highly coherent Agulhas Rings that carry warm and salty water over large distances. However, we demonstrated that the AR detected from satellite altimetry maps are not unequivocally surface eddies. In particular, our results showed that Agulhas Rings are mostly subsurface eddies from the Walvis Ridge westward whose main thermohaline anomaly signature lies within the 200-1200 m depth range.

We were able to estimate the heat content anomalies for some of these eddies across the South Atlantic basin. This allowed us to provide the average heat content associate to such eddies in separate regions of this basin, as well as the heat they transport. For sake of completeness, we compared our estimates with different approaches published in the literature by implementing our data in the computation. While our individual reconstruction technique shows that Agulhas Rings are very diverse in their thermohaline properties, the estimates obtained by the different methods do not differ sensibly within the large uncertainties in the estimates that are due to the limited availability of *in situ* data. All methods when applied to our

data show a step decrease in the heat content anomaly of Agulhas Rings across the Cape Basin and the South Atlantic Ocean. Such a diminution might be associated to both, air-sea interactions, heat release in the ocean interior but also to the increase of environmental heat content.

Finally, this study points out that observations are still limited in coverage to allow a complete eddy tracking (that include subsurface and deep eddies) and accurate estimates of the three-dimensional properties transported by eddies and how they evolve in route. Complementary studies implementing similar techniques applied to high-resolution ocean simulation three-dimensional fields could be used to corroborate the results we obtained and further deepen our knowledge and estimates on eddy dynamics, heat and salt transports.

6

Conclusions et perspectives

Sommaire

6.1 Conclusions 151
6.2 Perspectives 155

6.1 Conclusions

Bien qu'offrant une vision parcellaire de la dynamique océanique, l'analyse des champs altimétriques journaliers nous a permis d'accéder à une description de la dynamique des tourbillons des Aiguilles (AR) plus complexe que tout autre étude publiée jusqu'ici. Nos résultats, obtenus via la méthode de détection et suivi des tourbillons TOEddies développée dans le cadre de cette thèse, montrent que ces tourbillons ne sont pas des structures cohérentes uniques associées à une seule trajectoire entre le moment de leur naissance et celui de leur disparition. Cela a été mis en exergue par la création du concept de réseau de trajectoires qui, tel un arbre généalogique, relie la plupart des tourbillons identifiés à une multitude d'autres structures. Ce réseau est donc constitué de nombreuses branches connectées entre elles par des nœuds marquants des épisodes de séparation d'un tourbillon en plusieurs structures ("splitting") ou, au contraire, de fusion de tourbillons ("merging").

De tels épisodes ont déjà été décrits par des travaux qui ont documenté quelques événements particuliers dans des zones délimitées de notre région d'étude [e.g. Arhan et al. 1999; Schouten et al. 2000; Dencausse et al. 2010a; Nencioli et al. 2018]. Le

réseau de trajectoire que nous avons reconstruit permet l'intégration de ces événements dans une vision globale de ces interactions rendant possible l'identification des régions où ces phénomènes ont lieu de manière plus fréquente. Ainsi, les tourbillons se déplaçant dans l'océan Atlantique subissent peu d'interactions alors que le Courant des Aiguilles, le bassin du Cap, les barrières bathymétriques et le courant du Brésil sont des zones où les AR subissent des nombreuses séparations (splitting) et fusions (merging).

De ce fait, il est possible de suivre le devenir de tout tourbillon entre sa naissance et ses multiples séparations/fusions pendant les années où il est observable sur les champs altimétriques AVISO. Cela se traduit par la mise en évidence d'un lien étroit entre des tourbillons anticycloniques formés dans l'océan Indien et d'autres aux abords du courant du Brésil. Une confirmation de la capacité des AR à interagir avec ce courant a été apportée très récemment par Guerra et al. [2018]. Ils ont pour cela analysé l'interaction d'un AR avec le courant du Brésil et deux tourbillons cycloniques à partir de champs altimétriques et de mesures in-situ. Le tripôle ainsi formé est advecté vers le sud par le courant ce qui est en accord avec nos résultats où les AR peuvent être suivis jusqu'au gyre Zapiola, au sud-ouest du bassin d'Argentine.

D'un autre côté, l'advection des tourbillons anticycloniques formés dans le canal du Mozambique ou dans le courant Est-Malgache jusqu'à la zone de la rétroflection du courant des Aiguilles est assez novatrice puisque seuls Schouten et al. [2002] avaient identifié ce genre de structure. Cependant, le récent travail de Braby et al. [2016] indique la dissipation de ces tourbillons dans le Courant des Aiguilles. Leurs résultats pourraient être dûs à la non-considération des interactions entre tourbillons lors de leurs reconstructions des trajectoires. On peut ainsi s'attendre, comme il est effectivement la cas pour la grande majorité des méthodes de détection et suivi des tourbillons publiées à ce jour, à ce que des trajectoires soient terminées prématurément lors d'épisodes de merging ou que de nouvelles détections soient associées à des épisodes de splitting. Bien que cela ne puisse pas être utilisé directement comme une validation de nos résultats, on peut noter que des tourbillons anticycloniques advectés jusqu'à la zone de rétroflection peuvent être visuellement identifiés dans des simulations numériques telles que dans l'animation intitulée "Ocean Surface Vorticity" mise en ligne par la NOAA (`https://sos.noaa.gov/datasets/ocean-surface-vorticity`).

La description des tourbillons à partir des champs d'altimétrie satellitaire est très instructive mais reste partielle car elle ne nous donne pas accès à leur structure thermohaline tridimensionnelle. Nous avons ainsi collocalisé les tourbillons détectés à partir des champs altimétriques avec les profils verticaux mesurés par les flotteurs Argo. Cela nous a permis de caractériser la structure verticale de plusieurs Anneaux des Aiguilles dans une région donnée du domaine d'étude et aussi nous avons pu suivre, pour l'un d'entre eux nommé RecAR, son évolution le long d'une partie de sa trajectoire. Nous avons aussi pu mettre nos résultats dans un contexte plus large d'observations in-situ historiques discutées dans la littérature scientifique [Gordon

et al. 1987; McCartney and Woodgate-Jones 1991; Duncombe Rae et al. 1992; van Ballegooyen et al. 1994; Duncombe Rae et al. 1996; Arhan et al. 1999; Garzoli et al. 1999; McDonagh et al. 1999; Schmid et al. 2003; Gladyshev et al. 2008; Arhan et al. 2011; Casanova-Masjoan et al. 2017; Guerra et al. 2018].

En particulier, nous avons vu que la perte d'intensité sur les champs altimétriques du tourbillon RecAR lors de sa traversée de l'océan Atlantique est étroitement liée à sa subduction. En effet, les structures de subsurface se déplacent telles des lentilles dans l'océan et sont associées à des isopycnes convexes au-dessus de leur cœur hydrologique. On peut donc s'attendre à ce que cette géométrie réduise l'effet intégré des anomalies de densité sur la hauteur de l'eau. Ors, une telle perte de signature en surface des tourbillons des Aiguilles lors de leur traversée de l'océan Atlantique a été décrite et interprétée comme un attribut témoignant de leur dissipation [e.g. Byrne et al. 1995; Guerra et al. 2018]. Ainsi, bien que les Anneaux des Aiguilles soient suspectées de se dissiper dans cet océan [Nencioli et al. 2018], notre étude quantitative a mis en évidence que les AR sont, en grande majorité, intensifiés en surface dans le bassin du Cap alors que de nombreuses structures de subsurface peuplent l'océan Atlantique. Ainsi, notre étude indique clairement la subduction de ces structures dans l'océan Atlantique qui, au moins partiellement, explique leur perte de signature. En particulier, une branche nord a été identifiée dans cet océan où la très grande majorité des AR sont en subsurface alors que la route sud est suivie par les deux types de structures. Cette observation est en accord avec l'identification d'un tourbillon en subsurface dans la route nord et en surface dans celle sud par Arhan et al. [1999] et avec les simulations numériques effectuées par Herbette et al. [2004] où des tourbillons subductent sous des fronts océaniques. De plus, ces épisodes de subduction pourraient être une des raisons qui explique leur capacité à traverser l'océan Atlantique en diminuant leur perte d'énergie vers l'atmosphère dans cet océan alors qu'elle est intense dans le bassin du Cap [e.g. Arhan et al. 2011; Messager and Swart 2016].

De plus, des AR composés de plusieurs cœurs hydrologiques homogènes à différentes profondeurs ont été identifiés dans nos résultats ainsi que dans la littérature [McCartney and Woodgate-Jones 1991; Garzoli et al. 1999; Casanova-Masjoan et al. 2017; Guerra et al. 2018]. Des questions subsistent sur l'origine de ces doubles cœurs d'eau modale. Ceux-ci peuvent être la conséquence d'épisodes d'intense ventilation hivernale pendant deux années successives ou, plus probablement d'après Garzoli et al. [1999], de l'appariement de tourbillons ayant des cœurs à différentes profondeurs comme cela a déjà été observé dans d'autres régions du monde [e.g. Cresswell 1982; Schultz Tokos et al. 1994; Garreau et al. 2018]. La reconstruction, à partir de plus de 50 profils hydrologiques combiné à l'identification par satellite,du réseau de tourbillons associé à une structure ayant ce double cœur nous laisse penser que cela est le résultat de la fusion de deux tourbillons ayant vécu plus d'un an depuis leur éjection de la retroflection des Aiguilles. Un de ces tourbillons est resté, en moyenne, 5° de latitude plus au sud que l'autre, dans la région de la route "sud" de Dencausse et al. [2010a] ce qui pourrait expliquer une importante différence de ventilation dans leur cœur et donc leur différence de densité. En effet, les intenses

échanges océan-atmosphère dans la partie sud du bassin du Cap donnent lieu à la formation d'épaisses couches de mélange homogènes qui peuvent atteindre les 600 m de profondeurs [Arhan et al. 2011].

Une fois que ces tourbillons subductent en subsurface durant leur trajectoire en entrant dans l'océan Atlantique, ces couches d'eau homogènes sont définitivement isolées de la surface océanique et des interactions air-mer. Elles constituent donc d'importantes poches d'eau modale. Les caractéristiques hydrologiques de cette eau modale dépendent de l'histoire des AR aussi bien en terme de région source, d'interactions entre tourbillons que d'échanges avec l'atmosphère. Cette subduction est donc un acteur important de transfert des eaux de surfaces ver l'océan intérieur. Capuano et al. [2018a] ont montré que des instabilités agissent sur les tourbillons dans le bassin du Cap modifiant les propriétés des eaux de la thermocline de l'océan Indien en donnant naissance à une nouvelle masse d'eau. Nos résultats confirment les conclusions de cette étude. Nous avons désigné cette eau modale avec le terme d'eau modale des Anneaux des Aiguilles (ARMW pour "Agulhas Ring Mode Water") qui est une variété d'eau modale subtropicale (STMW pour "Subtropical Mode Water"). Sato and Polito [2014] ont effectivement décrit des variétés de STMW le long de la route des AR, mais ces auteurs n'ont pas trouvé de présence préférentielle dans les tourbillons.

Le résultat le plus significatif de ce travail est probablement l'identification des ARMW en tant que réceptacle de la plus importante fraction d'anomalie de chaleur transportée par ces tourbillons dans l'intérieur de l'océan Atlantique. Nous avons ainsi pu mettre en évidence que l'intervalle entre 200 et 1200 m contient, en moyenne, plus de 85 % des anomalies de contenus de chaleur (HCA pour "Heat Content Anomalies") de la colonne d'eau au-dessus de 1800 m dans les AR subductés dans l'océan Atlantique. Cela confirme que les Anneaux des Aiguilles sont des agents efficaces dans le transport de chaleur entre l'ocean Indien et Atlantique. Ce transport n'est pas associé à des eaux de la thermocline de l'Océan Indien mais à des eaux modales qui ont été formées par modification des eaux Indiennes via les intenses échanges air-mer au sud de l'Afrique et à la subduction des tourbillons le long de leur trajectoire.

Le calcul des flux de HCA engendrés par ces tourbillons à partir d'observations est une travail difficile. La dispersion des profils des flotteurs Argo est telle que nous ne pouvons pas reconstituer finement le volume tridimensionnel de tous les tourbillons des Aiguilles. De fait, il nous est impossible d'évaluer précisément les transports de chaleur associés à l'ensemble de ces tourbillons. Cependant, nous avons pu estimer l'anomalie du contenu de chaleur le long d'un segment de trajectoire des AR qui ont été suffisamment échantillonnés. Nous disposons ainsi d'estimations du contenu de chaleur d'un certain nombre de tourbillons dans différentes régions de l'Atlantique Sud ce qui nous a permis d'attribuer une valeur de transport de chaleur accompli par ces structures pour chaque zone. Notre approche combinant les trajectoires des tourbillons et une description par région est donc semi-lagrangienne.

La plupart des travaux publiés qui ont cherché à estimer les transports effectués

par les tourbillons ont pallié à l'éparpillement des données in-situ en travaillant par une approche en "tourbillon composite" où plusieurs tourbillons sont moyennés. Nous avons appliqué certains de ces calculs [Chaigneau et al. 2011; Yang et al. 2013; Schütte et al. 2016] à nos données afin de les comparer entre elles ainsi qu'à la moyenne des tourbillons que nous avons pu reconstruire pour chaque zone géographique à partir de notre méthode semi-lagrangienne. Cela a seulement été possible dans l'océan Atlantique où les interactions entre tourbillons sont moins nombreuses ce qui permet de reconstruire des trajectoires des tourbillons cohérentes néccessaire à notre méthode semi-lagrangienne. Ainsi, en combinant les deux approches, nous avons obtenu des transferts de chaleur en subsurface plus faibles que les estimations précédentes alors que notre méthode de suivi est celle qui, dans la littérature, donne le plus grand nombre d'AR dans l'océan Atlantique.

6.2 Perspectives

Cela doit être le propre d'un travail de thèse mais ces trois années se terminent avec plus de questions qui se posent à nous que lors de l'amorce de ce projet. Nous souhaitons présenter ici quelques-unes de ces interrogations et des pistes pour les aborder sous forme de perspectives.

Nous omettons celles liées aux avancées attendues par l'arrivée de nouvelles technologies puisque nous voulons nous concentrer sur des pistes que l'on pourrait imaginer explorer dès à présent. Cependant, il semble indispensable, dans le cadre d'une thèse traitant la détection des tourbillons océaniques à partir des champs altimétriques, de mentionner le très prometteur satellite SWOT ("Surface Water and Ocean Topography", `https://swot.cnes.fr/`). Cette mission prévue pour 2021 devrait permettre d'obtenir des champs altimétriques sur une fauchée d'environs 150 km avec une résolution spatiale comparable à celle des mesures satellite de température de surface et un cycle de répétition des traces 10 à 20 jours. Cette bande à haute résolution permettra d'offrir une cartographie 2D instantanée des tourbillons sur cette fauchée ce qui, de nos jours, n'est possible qu'après la construction des cartes.

En attendant cette nouvelle technologie, il est important de définir quelle confiance nous pouvons avoir dans les détections que nous obtenons. Un effort a été placé sur cet aspect dans le cadre de cette thèse où nous avons clairement mis en évidence que, statistiquement, les tourbillons détectés à partir de bouées dérivantes par Lumpkin [2016] sont en accord avec ceux obtenus par TOEddies. Cependant, cette méthode ne permet ni de quantifier la proportion d'artefacts dans les tourbillons identifiés ni de valider les propriétés dynamiques et géométriques obtenues. Or, lors d'une étude récente, Amores et al. [2018] ont mis en évidence les limites de l'altimétrie pour la détection des tourbillons. Pour se faire, ils ont développé une OSSE ("Observing System Simulation Experiment") où des champs synthétiques de produits grillés altimétriques ont été produits à partir

de champs de sortie de simulations numériques. Ainsi, ces auteurs ont montré que l'océan est envahi par des tourbillons qui ne sont pas résolus par l'altimétrie. Cela se traduit, entre autre, par l'agrégation de plusieurs tourbillons en un seul sur les champs altimétriques ("aliasing"). Ce dernier résultat est clairement une limitation de notre étude puisque l'on peut s'attendre à ce que des interactions de merging ou de splitting puissent être la signature de tel phénomène d'"aliasing". Une des possibles solutions à ces limitations serait de mettre en place une OSSE afin d'essayer de déterminer des critères de validation des détections pour pouvoir qualifier les épisodes de fusion et séparation des tourbillons en fonction de la confiance que l'on peut avoir sur les tourbillons détectés. C'est une procédure qui est déjà envisagée et débutée dans le cadre de l'ANR ASTRID-Maturation DYNED-Atlas (`https://www1.lmd.polytechnique.fr/dyned/`) et qui pourrait grandement améliorer la confiance que nous avons dans les différents proxys obtenus sur les champs altimétriques. Bien que ne permettant pas d'améliorer les détections à proprement dit, un tel critère permettrait de sélectionner les détections à utiliser pour obtenir des champs statistiques des tourbillons.

Nous avons montré dans cette étude que la propagation des tourbillons dans l'océan Atlantique est, en majorité, non pilotée par les courants océaniques. Or, lors des longues périodes d'observation d'animation de suivi de tourbillons, nous avons remarqué que de nombreux cyclones semblent suivre les AR à travers cet océan. De plus, des études basées sur des mouillages dans le bassin du Cap par Kersalé et al. [2018] et dans le courant du Brésil par Guerra et al. [2018] indiquent clairement des interactions entre des AR et des tourbillons cycloniques. Nous pensons donc qu'il serait important d'aller plus loin sur le suivi des tourbillons en analysant les interactions qui peuvent exister entre des tourbillons de différentes polarités. Il nous semble que ces interactions devraient permettre de mieux comprendre les trajectoires des AR. On peut donc imaginer des traitements de trajectoires afin d'identifier les tourbillons qui restent pendant de longues périodes dans la périphérie d'autres structures.

Nous avons vu que la définition de tourbillon de surface et subsurface est possible à partir des mesures dans la colonne d'eau. Cependant, la transition d'un AR de surface en structure de subsurface a aussi été identifiée à partir des données SST. Pour cela, il a fallu calculer les anomalies de SST au centre de la structure puis de les moyenner mensuellement. Ainsi, cela semble difficile d'identifier les structures à partir d'images instantanées mais possible à partir de variables dites de "proxy" moyennés sur les trajectoires. Nous pourrions donc imaginer discrétiser les segments de trajectoires entre les tourbillons de surface et ceux de subsurface en appliquant la méthode de Assassi et al. [2016]. Il nous semble que cela devient particulièrement important lorsque l'on s'intéresse aux méthodes lagrangiennes de détection des tourbillons. En effet, ces méthodes nécessitent une bonne définition des vitesses associées aux tourbillons qui, comme nous l'avons montré, peuvent être en partie sous-estimées sur les champs de surface lors d'une subduction ce qui s'ajoute aux biais déjà présents pour les tourbillons de surface [e.g. Ioannou et al. 2017]. Au contraire, les vitesses de translations moyennes des tourbillons doivent

être assez précises et ne pas dépendre de la profondeur du cœur du tourbillon. Or, la définition de la région où l'eau est advectée est liée au ratio entre ces deux types de vitesses [Flierl 1981]. On peut donc s'attendre à ce que des tourbillons intensifiés en surface associés à des gradients de hauteur d'eau peu intenses ne seront pas détectés comme des structures advectant des masses d'eau alors que cette advection peut avoir lieu en subsurface. Nous pensons donc qu'une séparation des tourbillons de surfaces et ceux de sub-surface en parallèle avec des algorithmes lagrangiens pourrait permettre de mieux caractériser ces limitations. Il est à noter que cela est loin d'être triviale puisque des tourbillons de subsurface, tel que les Meddies, peuvent engendrer des structures de surface secondaires en perturbant les couches supérieures [e.g. Bashmachnikov et al. 2009].

Plus généralement, nous pensons qu'effectuer une étude similaire à celle entreprise dans cette thèse sur des sorties de simulations numériques aiderai à comprendre nos observations. Nous avons, en parallèle à ce travail de thèse, appliqué avec succès les algorithmes de détection sur des champs numériques [Capuano et al. 2018b]. Cela nous a permis de mettre en évidence des trajectoires des tourbillons des Aiguilles proches de celles obtenues à partir des observations satellitaires. Ces sorties ont ensuite été explorées par Capuano et al. [2018a] afin d'étudier les types d'instabilités agissant dans les tourbillons des Aiguilles. Nous pensons qu'il serait intéressant d'utiliser de telles sorties pour développer une détection tridimensionnelle des tourbillons océaniques similairement au travail de Doglioli et al. [2007]. Cela serait possible, par exemple, en effectuant des détections à chaque niveau en replaçant l'ADT par des lignes de courants ou par des champs de hauteur dynamique avec l'algorithme TOEddies ou directement à partir des champs de vitesses avec des méthodes telles que AMEDA [Le Vu et al. 2018]. D'un point de vue méthode, cela permettrait d'utiliser des mesures hydrologiques artificielles afin de tester les méthodes de reconstruction de tourbillons et d'essayer de caractériser l'erreur faite sur les calculs de gradients. De plus, cela permettrait de mieux caractériser la subduction des tourbillons ainsi que mieux définir leur transport de chaleur. En particulier, une augmentation du contenu de chaleur en subsurface est clairement visible dans l'environnement le long de la trace des tourbillons. Cela semble indiquer deux choses : qu'une dissipation graduelle des AR impacte l'environnement ou qu'une quantité importante de tourbillons n'est pas identifiée sur les champs altimétriques (ou du moins retracée jusqu'à leur origine). Cette dernière est d'autant plus probable d'après les limites de la détection des tourbillons mises en évidence par Amores et al. [2018] et par la possible perte de signal des tourbillons en cas de subduction rapide et profonde lors d'intense ventilation dans le bassin du Cap. Or, nous pensons qu'il serait important de caractériser au mieux la quantité de chaleur contenue dans l'environnement puisqu'elle a une influence directe sur les calculs d'anomalies et donc sur nos estimations de flux de chaleur.

Finalement, nous avons développé et utilisé des détections automatiques pour le support de campagnes et opérations en mer. Cela s'est traduit par une détection et un envoi des données de manière automatique à plusieurs missions océanographiques pendant ce travail. En parallèle, nous avons pu utiliser ces détections pour définir

si des flotteurs ARGO communicant via le protocole Iridium étaient dans des tourbillons. Ainsi, grâce à l'aide de Romain Cancouët à Euro-Argo, nous avons pu modifier les paramètres d'échantillonnage. Il est donc possible d'imaginer une définition automatique des cycles des flotteurs Argo que l'on adapterait s'ils se trouvent dans des tourbillons océaniques. En vue de la réussite obtenue sur des détections en temps réel (NRT pour "Near Real Time") lorsqu'on vise les structures intenses et en utilisant des critères de fiabilité comme cités plus haut, il serait ainsi possible de réduire le nombre de mauvaises détections et optimiser au mieux le temps de vie des profileurs tout en augmentant la fréquence d'échantillonnage dans des structures tourbillonnaires. Nous pensons donc que l'implémentation d'un tel outil en NRT pourrait, même si non parfait, être de grand intérêt pour l'océanographie opérationnelle.

Appendices

A

Activités scientifiques pendant la thèse

Articles scientifiques

Publications en 1er auteur

- **Laxenaire, R.**, Speich, S., Blanke, B., Chaigneau, A., Pegliasco, C., & Stegner, A. (2018). Anticyclonic eddies connecting the western boundaries of Indian and Atlantic Oceans. Journal of Geophysical Research: Oceans, 123. https://doi.org/10.1029/2018JC014270
- **Laxenaire, R.**, Speich, S., & Stegner, A. (2^{e} soumission après une révision). Evolution of the thermohaline structure of one Agulhas Ring reconstructed from satellite altimetry and Argo floats. Journal of Geophysical Research: Oceans
- **Laxenaire, R.**, Speich, S., & Stegner, A. (1er soumission). The heat transports in the South Atlantic achieved by the Agulhas Rings as estimated combining satellite altimetry and Argo profiles. Journal of Geophysical Research: Oceans

Autres publications

- Capuano, T. A., Speich, S., Carton, X., & **Laxenaire, R.** (2018). Indo-Atlantic exchange, mesoscale dynamics, and Antarctic intermediate water. Journal of Geophysical Research: Oceans, 123. https://doi.org/10.1002/2017JC013521

- Kersalé, M., Lamont, T., Speich, S., Terre, T., **Laxenaire, R.**, Roberts, M. J., van den Berg, M. A., & Ansorge, I. J. (2018). Moored observations of mesoscale features in the Cape Basin: characteristics and local impacts on water mass distributions, Ocean Sci., 14, 923-945. https://doi.org/10.5194/os-14-923-2018,

- Liebrand, D., Raffi, I., Fraguas, Á., **Laxenaire, R.**, Bosmans, J. H. C., Hilgen, F. J., et al. (2018). Orbitally forced hyperstratification of the Oligocene South Atlantic Ocean. Paleoceanography and Paleoclimatology, 33. https://doi.org/10.1002/2017PA003222

- Sauzede, R., Martinez, E., Maes, C., Dufois, F., Mignot, A., **Laxenaire, R.**, Maamaatuaiahutapu, K., & Petrenko, A. (En Préparation). Impact of eddy activity on the vertical distribution of phytoplankton biomass in the South Pacific Subtropical Gyre.

Communications scientifiques

- 2016 Ocean Science Meeting, février 2016, La Nouvelle-Orléans , Louisiane, États-Unis (Poster présenté par S. Speich)

- 2016 International Liege Colloquium - Submesoscale Processes: Mechanisms, Implications and new Frontiers, mai 2016, Liège, Belgique (Poster)

- Séminaire au LACY suite à l'invitation de K. Lamy, novembre 2016, Saint-Denis (île de la Réunion), France (Présentation orale)

- 2018 Ocean Science Meeting, février 2018, Portland, Oregon, États-Unis (Présentation orale)

- "25 Years of Progress in Radar Altimetry" Symposium, septembre 2018, Ponta Delgada, Açores, Portugal (Poster)

Missions océanographiques et expérimentales

- 2016 MOOSE-GE : LEG 2 de 10 jours en juin 2016 sur le R/O "L'Atalante" en Méditerranée Nord Occidentale. Chef de mission : L. Coppola (LOV-UPMC). Campagne océanographique annuelle dévolue à un réseau hydrologique du bassin nord-occidental de la Méditerranée et la maintenance de lignes de mouillage. Ma participation : Quart de prélèvement CTD et Biogéochimiques ainsi que détection opérationnelle des tourbillons océaniques.

- MD 205 / SOCLIM : 1 mois en octobre 2016 sur le Marion Dufresne dans la région du plateau de Kerguelen. Chef de mission : S. Blain (OOB-UPMC). Déploiement de mouillages et de flotteurs dérivants novateurs afin d'améliorer les connaissances sur l'océan Austral avec un accent particulier sur les flux

de carbone. Ma participation : Préparation au déploiement et suivi des relevés Bathysondes, mise en place d'expériences numériques d'advection de particules lagrangiennes pour définir les points de déploiements de certaines bouées dérivantes ainsi que détection opérationnelle des tourbillons océaniques pour cibler l'échantillonnage.

- Projet SLOCET : 1 mois en février-mars 2017 sur la Plateforme tournante Coriolis au LEGI à Grenoble. Projet porté par E. R. Johnson (UCL Mathématics) et A. Stegner (LMD-CNRS) financé par "l'EuHIT". Ce projet a pour but d'étudier l'impact d'une variation de la pente continentale océanique sur la propagation d'ondes de Rossby topographiques, de courant côtier et de front côtier. Ma participation : Préparation et réalisation des expériences puis traitements préliminaires des données PIV et celles issues des capteurs hydrologiques.

Participation active à l'encadrement de stages, de projets et de recherches bibliographiques

- Stage d'Emmanuel Herpin (M1 du Master Mécaniques des Fluides de l'Université Paris-Saclay), mai-juillet 2017, encadré par B. Deremble (LMD-CNRS). Sujet : Simulation et analyse de l'interaction océan-atmosphère pour les tourbillons du courant des Aiguilles

- Stage d'Emma Bent (L3 du Parcours Géoscience de l'ENS), juin-juillet 2017, co-encadré avec S. Speich (LMD-ENS). Sujet : Eddy dynamics in the North Atlantic Ocean

- Tuteur de l'étude bibliographique d'Aurélien Domeau (cadre technique 2^e année du CNAM-Intechmer), septembre 2017-janvier 2018. Sujet : Le rôle des tourbillons océaniques sur la production primaire

- Stage découverte de Jérémy Pinto (3^e du collège Pierre Sémard de Drancy), 1 semaine de janvier 2018, co-encadré avec C. Rault (Laboratoire de Géologie-ENS). Sujet : Découverte du Département de Géosciences de l'ENS

- Stage de Léa Olivier (césure après le M1 du Master Géoscience de l'ENS), janvier-juin 2018, co-encadré avec S. Speich (LMD-ENS). Sujet : Mesoscale variations in the Tropical Atlantic Ocean

- Stage de Soren François (M2 du Master Océan, Atmosphère, Climat et Observations Spatiales de l'UPMC), mars-aout 2018, encadré par S. Speich (LMD-ENS). Sujet : Analyse de la variabilité du niveau de la mer

- Stage d'Ulysse Vigny (1er année du parcours ingénieur de l'INSA de Rouen), juin 2018, co-encadré avec S. Speich (LMD-ENS). Sujet : Tourbillons océaniques et formation des eaux modales

- Stage de Natacha Le Grix (césure après le M1 du Master Géoscience de l'ENS), juin 2018, co-encadré avec S. Speich (LMD-ENS). Sujet : Caractérisation des tourbillons océaniques du "TOEddies" Atlas

Enseignement et médiation scientifique

- 2015-2017 Médiateur scientifique dans des collèges de Seine-Saint-Denis dans le cadre du plan départemental "La Culture et l'Art au Collège" du Centre de Culture Scientifique et Technique F93. Les projets s'articulent autour de 20 heures de présence en classe et de 2 sorties sur une journée :
  - Projet "Sous la surface" (2015-2016), en partenariat avec le Laboratoire de Géologie de l'École Normale Supérieure, axé sur le cycle des roches avec la classe de 4^e F du collège Jean-Vigo d'Epinay-sur-Seine. Sorties : échantillonnage du Lutécien à Compiègne (Oise) et visite de la cartothèque et de la galerie de Minéralogie et Géologie du Muséum national d'Histoire naturelle de Paris
  - Projet "Histoire de climats" (2016-2017), en partenariat avec le SIRTA, axé sur la physique de l'atmosphère et l'étude du bilan radiatif avec la classe de 3^e option "science" du collège Jean-Jaurès de Pantin. Sorties : découverte du SIRTA et restitution des travaux devant les chercheurs du Laboratoire Météorologie Dynamique
- 2017-2018 Moniteur des étudiants de L3 et M1 du Master Géoscience de l'École Normale Supérieure (Paris). Préparation et encadrement de TD/TP/examens en Mécanique des fluides, Océanographie, Calculs numériques et Télédétection pour un total de 68 heures

Formations, Workshops et Cours de l'École Doctorale

- Cours de Biogéochimie Marine pour le climat et l'écologie de l'École Doctorale 129, du 26 au 30 avril 2016 à Banyuls sur Mer
- Formation "High Performance Computing" de l'Université Paris Saclay, du 2 au 10 mai 2016 à Palaiseau
- École d'été "Fluid Dynamics of Sustainability and the Environment" organisée par l'École Polytechnique et "l'University of Cambridge", du 2 au 14 juillet 2017 à Palaiseau
- "Workshop Ocean Mesoscale Eddy Interactions with the Atmosphere" organisé par "l'US Clivar", du 17 au 18 février 2018 à Portland, Oregon, États-Unis

B

Validation of the TOEddies method and parameters

Sommaire

B.1 Sensitivity of the algorithm on the persistence parameter 165
B.2 Validation of the Eddy Detection Algorithms 168
B.3 Validation of tracking filtering 170

In this appendix, we describe in detail some aspects of the analyses and cross-validation presented in the core of the chapter 3.

B.1 Sensitivity of the algorithm on the persistence parameter

To assess the skill of the method, we developed a systematic procedure that tests the presence and properties of eddies against the "loopers", the independent eddy data set derived from surface drifting buoys by Lumpkin [2016] (LU16 in the following). This was used in the manuscript to infer the efficiency of the algorithm and to compare it to the database distributed by Duacs/AVISO+ [2017] and based on Chelton et al. [2011] method and modified by Schlax and Chelton [2016].

This procedure was also used to test the sensitivity of TOEddies to its parameters

and their value. These sensitivity studies have shown that the "persistence" is the most important parameter of the algorithm. This parameter, which prescribes a minimum value as an eddy amplitude threshold, is based on topological simplification studies [Edelsbrunner et al. 2002; Edelsbrunner and Harer 2010]. It is applied to isolate the local extremes of altimetric fields whose value is high enough to be considered robust in terms of signal-to-noise ratio. It can be compared to the minimum amplitude threshold often used in eddy detection algorithms found in the literature [e.g. Chelton et al. 2011]. However, while the latter is applied to eddies after they have been identified, the persistence parameter is integral part of the eddy identification step of the TOEddies algorithm because it is used to select the altimetry extremes to be considered as eddies. This is to ensure, for example, the detection of the merging of two or more eddies, or the growth of a large eddy. Indeed, if the algorithm finds in a relatively large area more than one extreme, the TOEddies algorithm automatically identifies more than one eddy because it requires that the eddies should contain one and only one extreme. This is true unless all but one of the extremes have values below the threshold limit. In this case, TOEddies identifies a single large eddy and not two or more.

Four eddy data sets are presented in Table B.1 that lists the number of eddies identified by each of them and their detection efficiency expressed as a percentage of the total number of collocations with LU16 eddies. These datasets were created by varying the minimum amplitude threshold (i.e., the persistence) for the identified ADT extremes and are labelled accordingly: ADT_MinPersistenceThreshold. No tracking considerations were applied on them. Hence, ADT_01 corresponds to the ADT_raw data set presented in the core of the Article.

This parameter directly influences the number of eddies: when it is not zero, the higher is its value, the lower the number of detected eddies (Table B.1). We observed that this parameter has the greatest impact when it goes from a value of 0 mm to 1 mm, and less for values greater than 1 mm (see rows for ADT_00 and ADT_01 in Table B.1). In fact, a non-zero value, as small as 1 mm, for persistence increases the number of eddies detected. This is explained by the fact that it takes at least four grid points for an eddy to be defined as such by the method. When examining the effectiveness of matching TOEddies with LU16 loopers, a value of 1 mm compared to zero for the persistence parameter increases the matching by up to 8%. For threshold values greater than 1 mm there is no significant increase in the matching.

While a non-zero threshold value for persistence increases the number of detections, as well as the total area occupied by eddies and the efficiency of detecting eddies associated with LU16 loopers, it also increases the number of erroneous detections (computed as the mismatch in polarity between TOEddies and loopers) by a large fraction (up to 50%, see Table B.1). These errors increase with the threshold value. However, for a threshold value of 1 mm, they are negligible for eddies larger than 25 km (see Figure 3.8 in the main text). For these reasons, we chose the threshold value of 1 mm when applying TOEddies to altimetry maps.

Table B.1: Eddy detection and collocation statistics with LU16 loopers for 4 data sets for the persistent threshold from 0 to 10 mm. The "max" annotation refers to the eddy contours associated with the maximum eddy azimuthal speed while the "out" annotation refers to the outer eddy contours. The percentages indicate the fractions of eddies by polarity as defined in LU16. Anti and Cyclo stand for respectively anticyclonic and cyclonic eddies.

Dataset	Number Eddies anti/cyclo 10^6]	Sum Area max anti/cyclo [10^{10} km^2]	Sum Area out anti/cyclo [10^{10} km^2]	Match Anti max / out [%]	Mismatch Anti max / out [%]	Match Cyclo max / out [%]	Mismatch Cyclo max / out [%]
ADT_00	3.1 / 3.2	2.7 / 2.4	4.1 / 3.8	63 / 66	1 / 2	69 / 71	1 / 1
ADT_01	3.2 / 3.3	3.2 / 2.8	5.2 / 4.6	66 / 71	2 / 3	71 / 75	1 / 2
ADT_05	3.1 / 3.2	3.1 / 2.8	5.2 / 4.6	66 / 71	2 / 3	71 / 75	1 / 2
ADT_10	2.8 / 2.9	3.1 / 2.7	5.2 / 4.6	66 / 71	2 / 3	70 / 75	1 / 2

B.2 Validation of the Eddy Detection Algorithms

The results of the cross-validation between LU16 and the different eddy satellite altimetry databases listed in Table 3.1 are discussed in detail below. Table 3.2 shows the number of eddies identified in each dataset and their detection efficiency expressed as percentages of the total number of collocations with LU16 eddies. To assess the skill of the method and provide quantitative comparisons between the different eddy datasets, a matching percentage is computed. It represents the proportion of each polarity of the LU16 eddies that were successfully cross-detected with eddies of the same polarity in each dataset (Table 3.2). Cross-detection errors are also defined as mismatches in eddy polarity or when several eddies detected by altimetry have been assigned to the same LU16 eddy.

The TOEddies detection algorithm was tested on the SLA and ADT maps (without applying an eddy lifetime threshold) to evaluate the most relevant altimetry dataset for automatic eddy detection. Table 3.2 shows that the TOEddies algorithm (referred to SLA_raw and ADT_raw) detects 34% (36%) more anticyclonic (cyclonic) eddies when SLA instead of ADT maps are used. The total area occupied by eddies derived from SLA is larger than that resulting from the use of the ADT field. This area is 31% (50%) higher than the surface encompassed by the eddy contour defined by R_{Vmax} for anticyclones (cyclones) and by 48% (65%) when the eddy boundary contour is defined by R_{out}.

When comparing the effectiveness of the results with LU16 and using the outer contour as eddy edge (Table 3.2), the ADT maps show a slightly better agreement for anticyclones (by about 2%) while the SLA maps give a slightly better result for cyclones (by about 3%). On the other hand, when the contour of maximum velocity is taken as the eddy boundary, the differences in detection efficiency between the SLA and ADT maps decrease in the case of cyclones while, for anticyclones, the ADT shows better results (4% more effective).

To validate the robustness of the TOEddies threshold requiring a minimum longevity of 4 weeks for a trajectory segment, the results of ADT_raw and TOEddies are compared. Table 3.2 shows that such a threshold reduces both the number and total extent of eddies. The number of eddies decreases by 25% and the total area they occupy by 10%. This is mainly due to the fact that the threshold over the eddy lifespan reduces the number of small eddies. In terms of validation compared to LU16, the number of collocations decreases for both cyclones and anticyclones when the time threshold is used (Table 3.2). This is particularly true for cyclones. Note here that the highest matching of the algorithm, independent of the time threshold or the altimetry field, is obtained for the eddy perimeters defined by the outer contour although there is a slight increase in errors.

As META2017 is probably the most widely used eddy atlas derived from satellite altimetry, in order to have another independent measure of the performance of our algorithm, we quantitatively compare META2017 and TOEddies overall statistics

and skills. Table 3.2 suggests that META2017 identify 25% fewer eddies but their overall extent is 41% larger. Figure 3.7 shows the statistical distribution of META2017 and TOEddies radii. The distribution maximum is positioned at about 40 km for TOEddies and 60 km for META2017. A clear difference between cyclones and anticyclones appears in TOEddies where cyclones are, on average, smaller than anticyclones. This difference is also noticeable in META2017, but less marked. In TOEddies, fewer than 1% of the eddies have a radius greater than 140 km while it corresponds to 5% of the structures for META2017.

To compare the size of eddies detected by satellite altimetry with an independent variable related to mesoscale ocean dynamics, we estimated the first Rossby baroclinic radius (L_R). L_R characterizes regionally the size of long-lived eddies in the open ocean. The average value of L_R was calculated using the definition of Chelton et al. [1998] and the seven-year average (i.e. 2005 to 2012) of the World Ocean Database [Boyer et al. 2013]. The resulting value is represented by the vertical dotted line in Figure 3.7. The shaded area represents L_R percentiles 10 and 90. This figure shows that TOEddies identifies structures whose size is comparable to L_R (around 60% of TOEddies radii are in the percentile range L_R 10 - 90) whereas this is not the case for META2017, for which less than 20% of radii are in this interval.

To ensure that the comparison of TOEddies and META2017 skill against LU16 loopers is as robust as possible in terms of measurement, TOEddies_rad statistics were used instead of TOEddies. Indeed, the TOEddies_rad and META2017 skills are obtained by considering equivalent eddy radii instead of eddy contours. Note here that the statistics for TOEddies and TOEddies_rad are very similar, only the skill decreases slightly. TOEddies_rad is 10% more efficient and its error in eddy detection is 3 times lower than META2017 in terms of eddy collocation with LU16. The ability of TOEddies_rad and META2017 to encompass LU16 eddy centers as a function of eddy size is shown in Figure 3.8. The percentage of matches with LU16 increases while the percentage of matching errors decreases for both atlases as the size of the LU16 vortex increases. Both datasets are more effective at detecting small cyclones than small anticyclones, and large anticyclones than large cyclones.

It can be expected that there will be a minimum size of eddies detected on satellite altimetry maps. The ability of the two atlases, TOEddies and META2017, to match LU16 eddies as function of LU16 size is presented in Figure 3.8. It shows that for a 25 km radius (which represents the average radius of the LU16 loopers, Figure 3.5 and the average grid size of the altimetry maps) more than 65% of the eddies are identified by TOEddies whereas they represent only 48% (52%) for the anticyclones (cyclones) in META2017. The 90% limit is reached for TOEddies for eddies with radii between 45 and 55 km, while it is 85-95 km (75-85 km) for anticyclones (cyclones) in META2017. In terms of detection errors (mismatching), they are less than 1% for anticyclones (cyclones) over 15 km (10 km) in the case of TOEddies, whereas for META2017, they become as small only for anticyclones (cyclones) larger than 30 km (70 km).

B.3 Validation of tracking filtering

In this section, we examine the ability of the two atlases, TOEddies and META2017, to track eddies. This ability is measured by looking at the proportion of the eddy collocation of the two atlases with LU16 loopers that participate in a trajectory that lasts more than a week. The total number of LU16 trajectories used in the comparison is 431 for anticyclones and 414 for cyclones. The comparison is presented here for the three versions of our atlas where we vary either the type of contours defining the eddy area (the outer contour and the maximum velocity contour) or by applying the same method in the collocation with LU16 as used for META2017.

Eddy trajectory comparison statistics are presented in Table B.2. Here, skill is measured by the overall percentage of matching between the TOEddies or META2017 and LU16 trajectories. The percentage of trajectories tracked is computed as the percentage of LU16 eddy trajectories of each polarity associated, for at least one day, with TOEddies or META2017 eddy trajectories of the same polarity. The "trajectory network" column shows the percentage of LU16 trajectories erroneously matched by more than one eddy in META2017 or by a first order network in TOEddies. The columns "> 50%" and "> 90%" indicate the number of LU16 trajectories collocated with the eddies defined by the other atlases during, respectively, more than 50 and 90 % of lifetime of the LU16 eddies. The "mean tracking time" column gives the average percentage of collocation time between LU16 eddies and those of the other atlases, expressed in terms of LU16 lifetime. The error estimates correspond to the collocation of eddies of different polarities for at least one day.

The results show that the TOEddies skill improves when the outer eddy contour (R_{out}) instead of the maximum velocity contour (R_{Vmax}) is used to define the eddy perimeter. However, the associated mismatches are somewhat larger. Taking into account both definitions of eddy limits, between 60% and 70% of LU16 trajectories are tracked by TOEddies and between 50 and 60% of them are tracked for more than 50% of their lifetime. The reconstruction of a higher order network is necessary for fewer than 10% of the trajectories successfully tracked. This could be a consequence of the LU16 filtering we performed before the validation processes. In fact, the merging and splitting of the eddies can cause sudden changes in the spin of the drifter and an increase in the radius of the LU16 loopers, a radius that can become greater than 300 km, the maximum limit we have set for them.

Using the radius for cross detection of structures gives results similar to those obtained using defined eddy perimeters. Table B.2 shows that the greatest difference in skill is obtained for META2017. Indeed, META2017 identifies between 5 and 10 % fewer trajectories than TOEddiesAtlas. Moreover, the percentages obtained for TOEddies indicate that trajectories that account for eddy merging and splitting are real and well reconstructed. On the other hand, the association of more than one META2017 trajectory with a LU16 trajectory suggests that META2017 sometimes loses the true eddy track. This is clear when considering the collocation time

with LU16 loopers. Indeed, while between 1/2 and 1/3 of the TOEddies network recovers almost all LU16 trajectories (i.e. > 90 %), this statistic is only 1/4 for META2017. Moreover, META2017 trajectories follow LU16 loopers 10% less than TOEddies. META2017 mismatch cases are also more numerous (by a factor of two) than TOEddies cases.

Table B.2: Tracking skill statistics for 4 collocated data sets with LU16 eddy trajectories (traj) that lasted at least 1 week. The percentage of trajectories tracked indicates the number of LU16 trajectories that are only associated with trajectories of the same polarity. The percentage of the trajectory network explains the percentage of trajectories poorly tracked in META2017 and properly tracked through the reconstruction of the first order network in TOEddies. The columns "> 50%" and "> 90%" indicate the number of LU16 trajectories collocated with the eddies defined by the other atlases during, respectively, more than 50 and 90 % of the life of LU16 eddies. The "mean tracking time" column gives the average percentage of collocation time between the LU16 loopers and the eddies of the other atlases expressed in terms of LU16 eddy life. The trajectory errors column indicates the number of trajectories associated, for at least one day, with an unmatched polarity eddy.

Dataset	limits	Traj tracked anti/cyclo [%]	Traj network anti/cyclo [%]	Followed > 50% anti/cyclo [%]	Followed > 90% anti/cyclo [%]	Mean % time tracked anti/cyclo [%]	Traj errors anti/cyclo [%]
TOEAtlas	out	67 / 68	7 / 4	58 / 60	44 / 49	84 / 88	8 / 6
TOEAtlas	max	61 / 65	4 / 1	52 / 57	37 / 43	81 / 85	5 / 3
TOEAtlas_rad	max	58 / 63	6 / 4	49 / 54	34 / 40	81 / 84	4 / 5
META2017	max	48 / 58	3 / 7	35 / 41	26 / 27	73 / 70	9 / 8

C

Supporting Information for "Anticyclonic eddies connecting the western boundaries of Indian and Atlantic oceans"

Sommaire

C.1 Introduction 173
C.2 Trajectories and frequency maps for five sub-groups of Agulhas Ring Eddy Network (AREN) trajectories . 174
C.3 Trajectories for eddies disconnected from AREN . . . 177
C.4 Detailed examples of order-0 trajectories 178
C.5 Ratio of the mean AREN propagation speed over the mean surface geostrophic velocity derived from satellite altimetry maps 179

C.1 Introduction

The supplementary materials presented here aim to complete some aspects of the analyses described in the core of the article. In the first section, we present the trajectories and frequency maps of five sub-groups of the Agulhas Ring Eddies Network (AREN). This will provide a clearer view on the trajectory partitions as function of the orders of the AREN which complements the information given in Figure 3.10 in the main article where the AREN trajectories are shown all together. We also present three examples of order-0 (or "main") AREN trajectories. Finally,

we present the trajectories of all the anticyclonic eddies that are not connected to the AREN.

C.2 Trajectories and frequency maps for five sub-groups of Agulhas Ring Eddy Network (AREN) trajectories

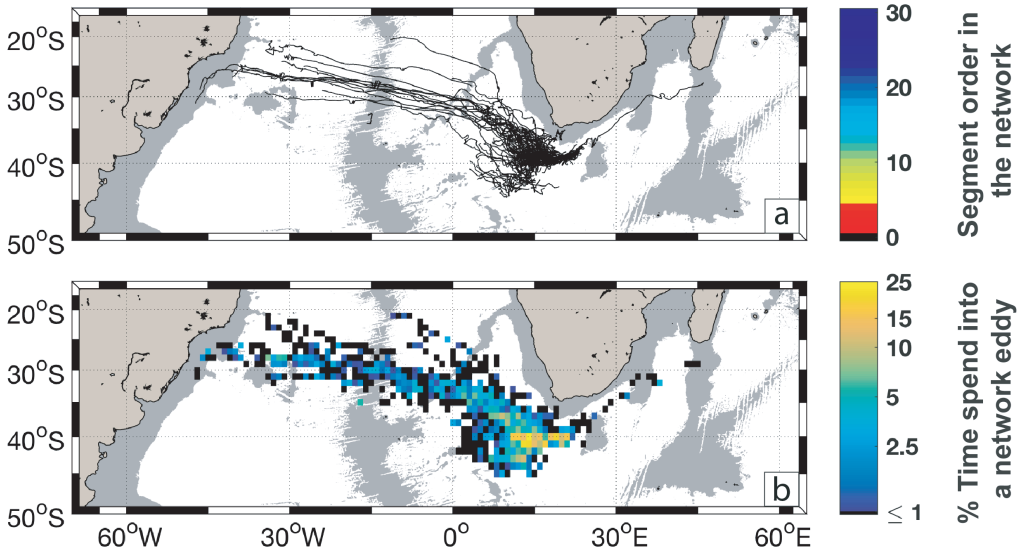


Figure C.1: a) The order-0 Agulhas Ring Eddy Network trajectories. The trajectories color is related to their order. b) Percentage of time each 2°x2° grid cell lies within an Agulhas Ring Eddy Network. The gray shading in each figure represents water depths less than 3500 m in the ETOPO2 data set [Smith and Sandwell 1997].

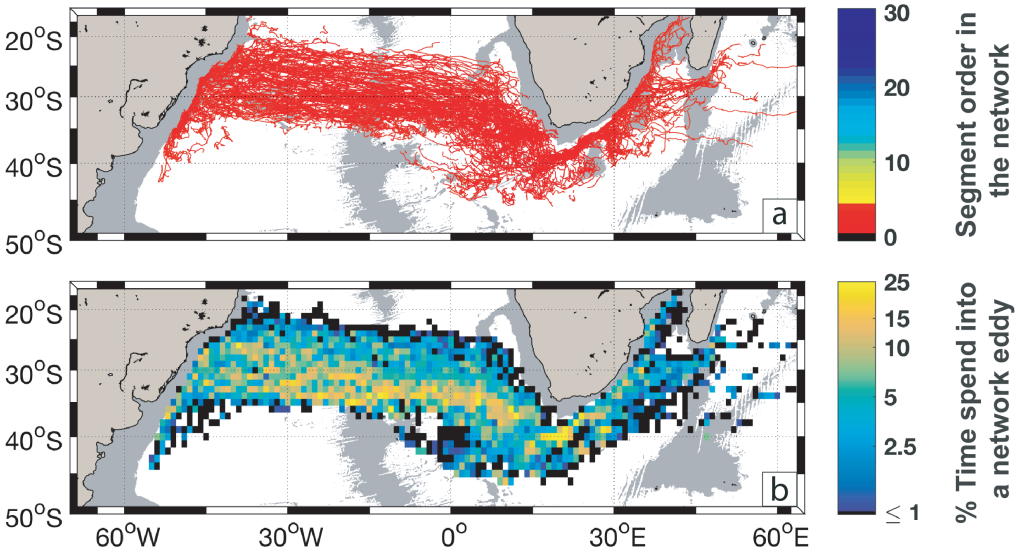


Figure C.2: a) Orders 1 to 4 of Agulhas Ring Eddy Network trajectories. The trajectories color is related to their order. b) Percentage of time each 2°x2° grid cell lies within an Agulhas Ring Eddy Network. The gray shading in each figure represents water depths less than 3500 m in the ETOPO2 data set [Smith and Sandwell 1997].

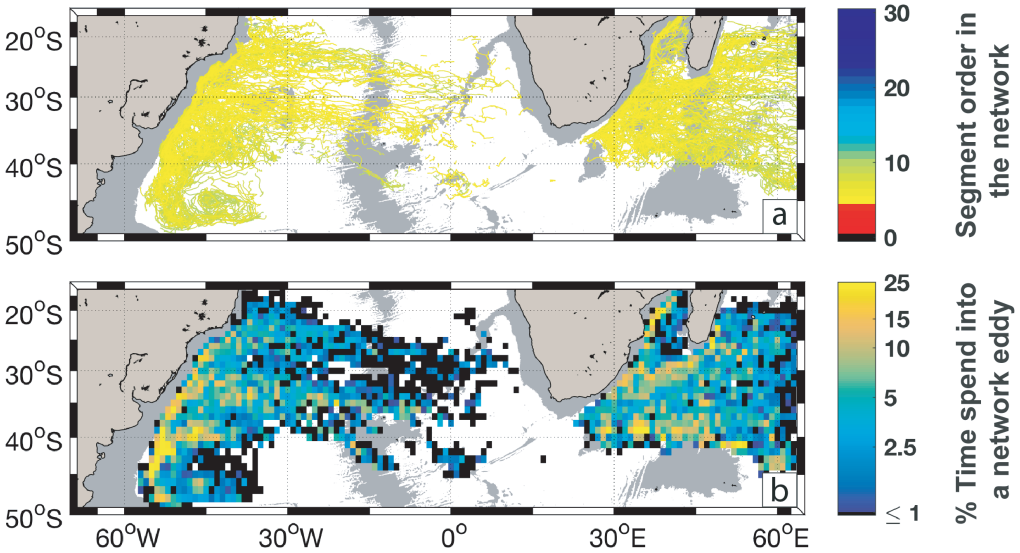


Figure C.3: a) Orders 5 to 10 of Agulhas Ring Eddy Network trajectories. The trajectories color is related to their order. b) Percentage of time each 2°x2° grid cell lies within an Agulhas Ring Eddy Network. The gray shading in each figure represents water depths less than 3500 m in the ETOPO2 data set [Smith and Sandwell 1997].

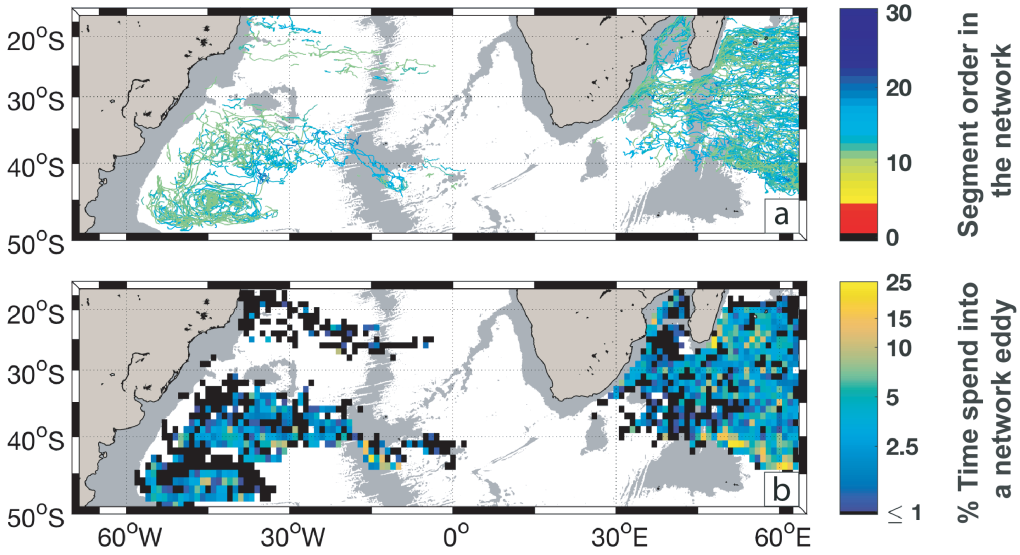


Figure C.4: a) Orders 11 to 20 of Agulhas Ring Eddy Network trajectories. The trajectories color is related to their order. b) Percentage of time each 2°x2° grid cell lies within an Agulhas Ring Eddy Network. The gray shading in each figure represents water depths less than 3500 m in the ETOPO2 data set [Smith and Sandwell 1997].

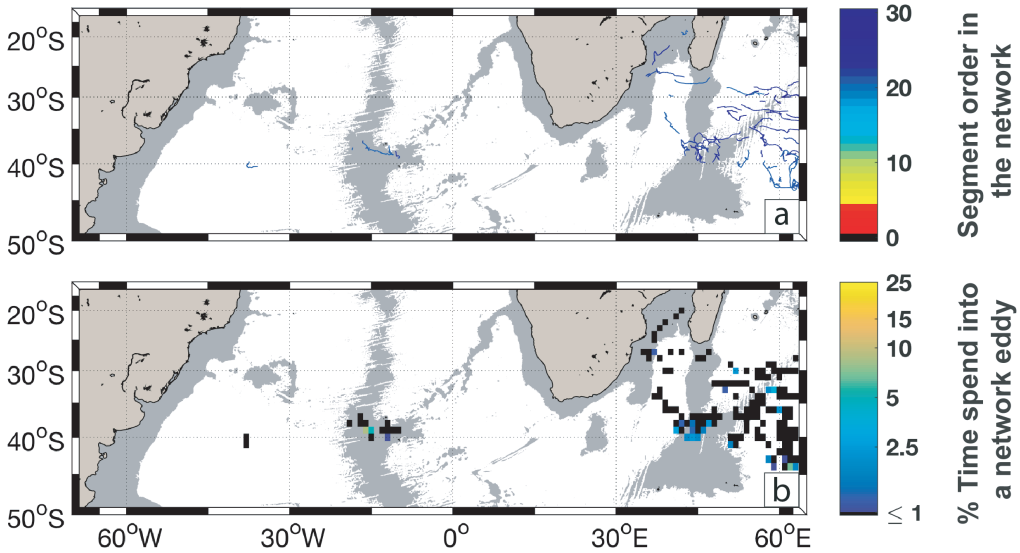


Figure C.5: a) Orders 21 to 29 of Agulhas Ring Eddy Network trajectories. The trajectories color is related to their order. b) Percentage of time each 2°x2° grid cell lies within an Agulhas Ring Eddy Network. The gray shading in each figure represents water depths less than 3500 m in the ETOPO2 data set [Smith and Sandwell 1997].

C.3 Trajectories for eddies disconnected from AREN

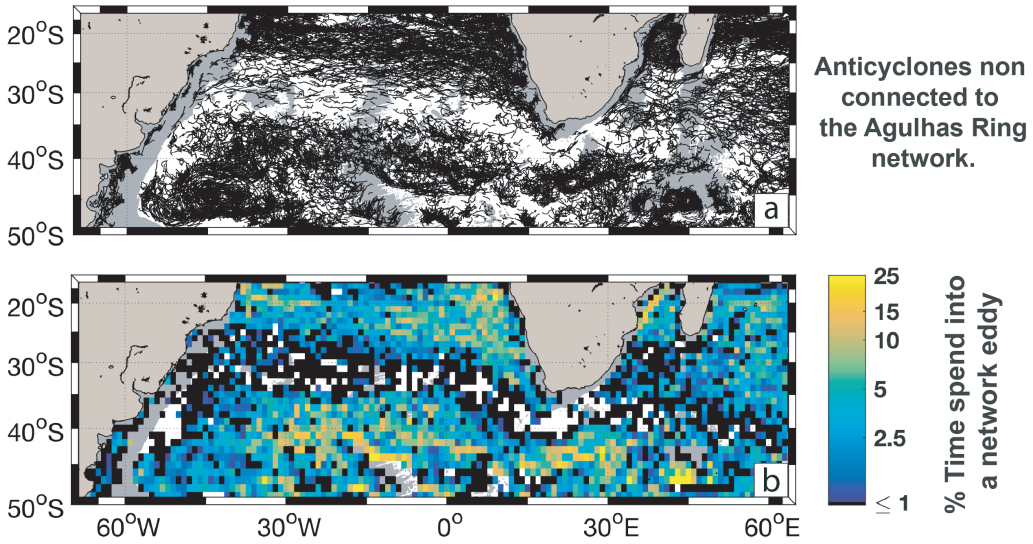


Figure C.6: a) Trajectories non connected with the Agulhas Ring Eddy Network. Percentage of time each 2°x2° grid cell lies within an Agulhas Ring Eddy Network. The gray shading in each figure represents water depths less than 3500 m in the ETOPO2 data set [Smith and Sandwell 1997].

C.4 Detailed examples of order-0 trajectories

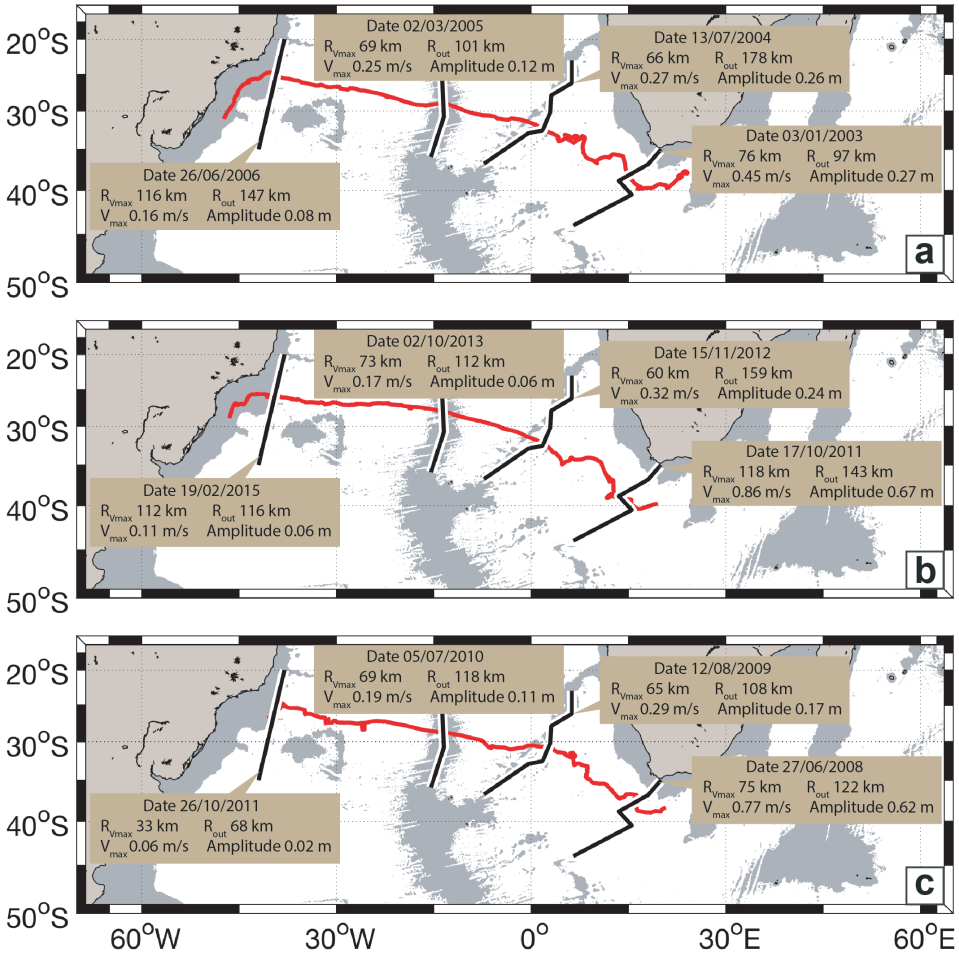


Figure C.7: Three order-0 Agulhas Ring Eddy Network trajectories with their properties specified at the crossing of the lines [C-F]. The gray shading in each figure represents water depths less than 3500 m in the ETOPO2 data set [Smith and Sandwell 1997].

C.5 Ratio of the mean AREN propagation speed over the mean surface geostrophic velocity derived from satellite altimetry maps

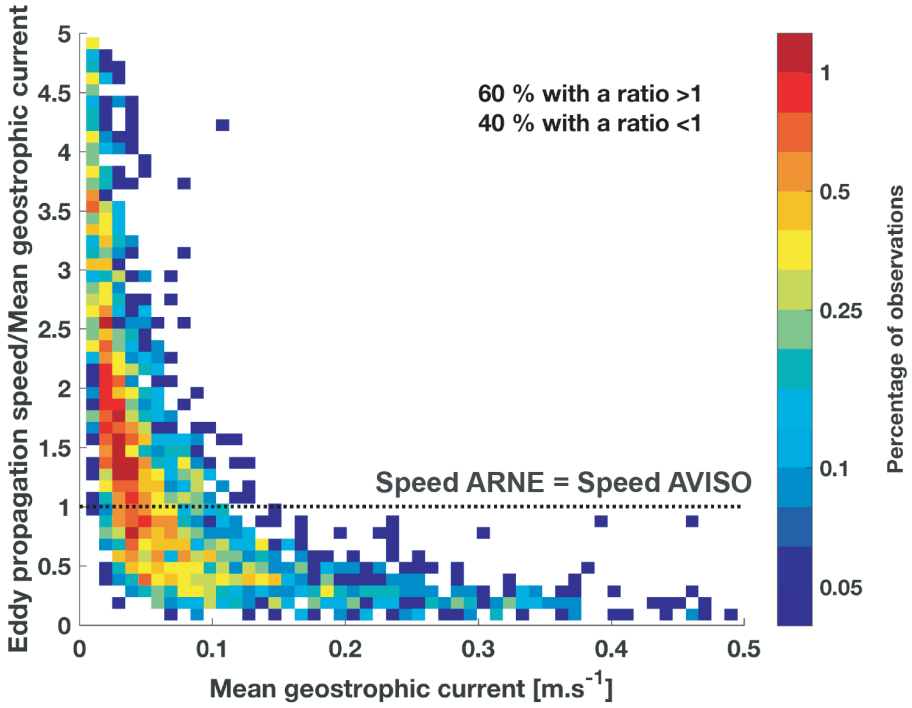


Figure C.8: Density plot of the ratio of the mean AREN speed of propagation over the mean surface geostrophic geostrophic velocity derived from AVISO maps. This ratio is obtained by dividing the 2°x2° averaged propagation speed (see Figure 12a in the main article) by the temporal and spatial averaged of the AVISO surface geostrophic velocity calculated in the same grid-cel (see Figure 13a in the main article).

D

Additional Figures for "Evolution of the thermohaline structure of one Agulhas Ring reconstructed from satellite altimetry and Argo floats"

Sommaire

D.1 Argo profiling float trajectories 182
D.2 Bathymetry below the fifth trajectory segment 182
D.3 SST anomalies 183
D.4 TS diagram 184
D.5 Examples of potential anomalies reconstruction 185
D.6 Hydrological properties of Mode Waters found in the South Atlantic as described in the literature. 186
D.7 Hydrological properties of the Agulhas Ring's cores described in the literature. 188
D.8 Integrated properties of the Agulhas Rings described in the literature. 191

In this appendix, we present few figures discussed in the core of the chapter 4.

D.1 Argo profiling float trajectories

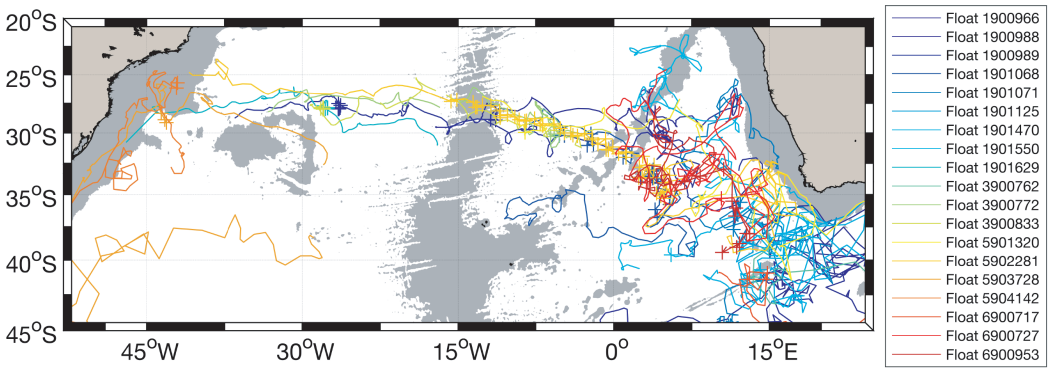


Figure D.1: Trajectories and name of the profiling floats that sampled the AREN of interest. The profiles which are used in this study are marked by crosses.

D.2 Bathymetry below the fifth trajectory segment

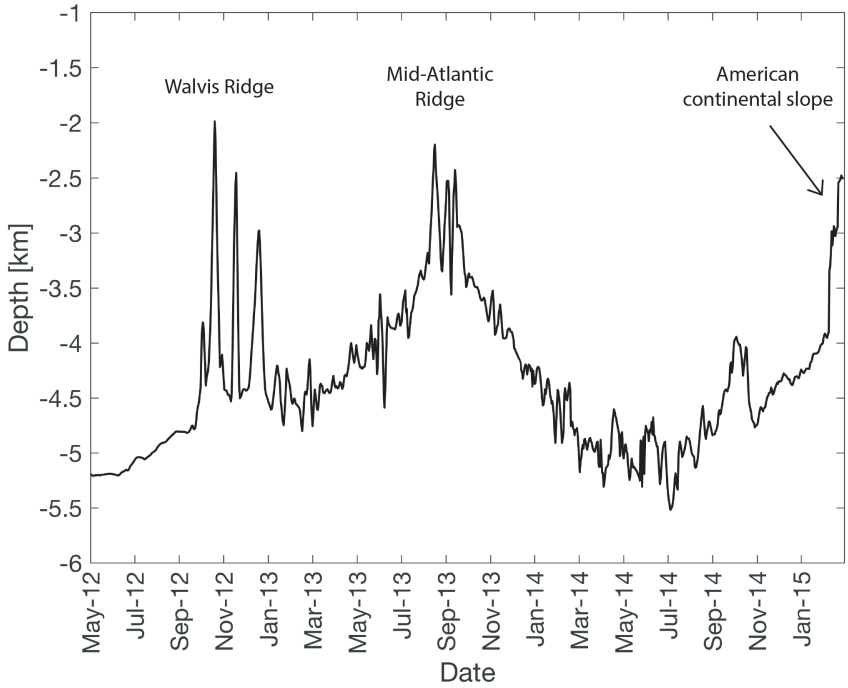


Figure D.2: Bathymetry below the fifth trajectory segment of the Agulhas Ring main trajectory studied in this work from the ETOPO2 data set [Smith and Sandwell 1997].

D.3 SST anomalies

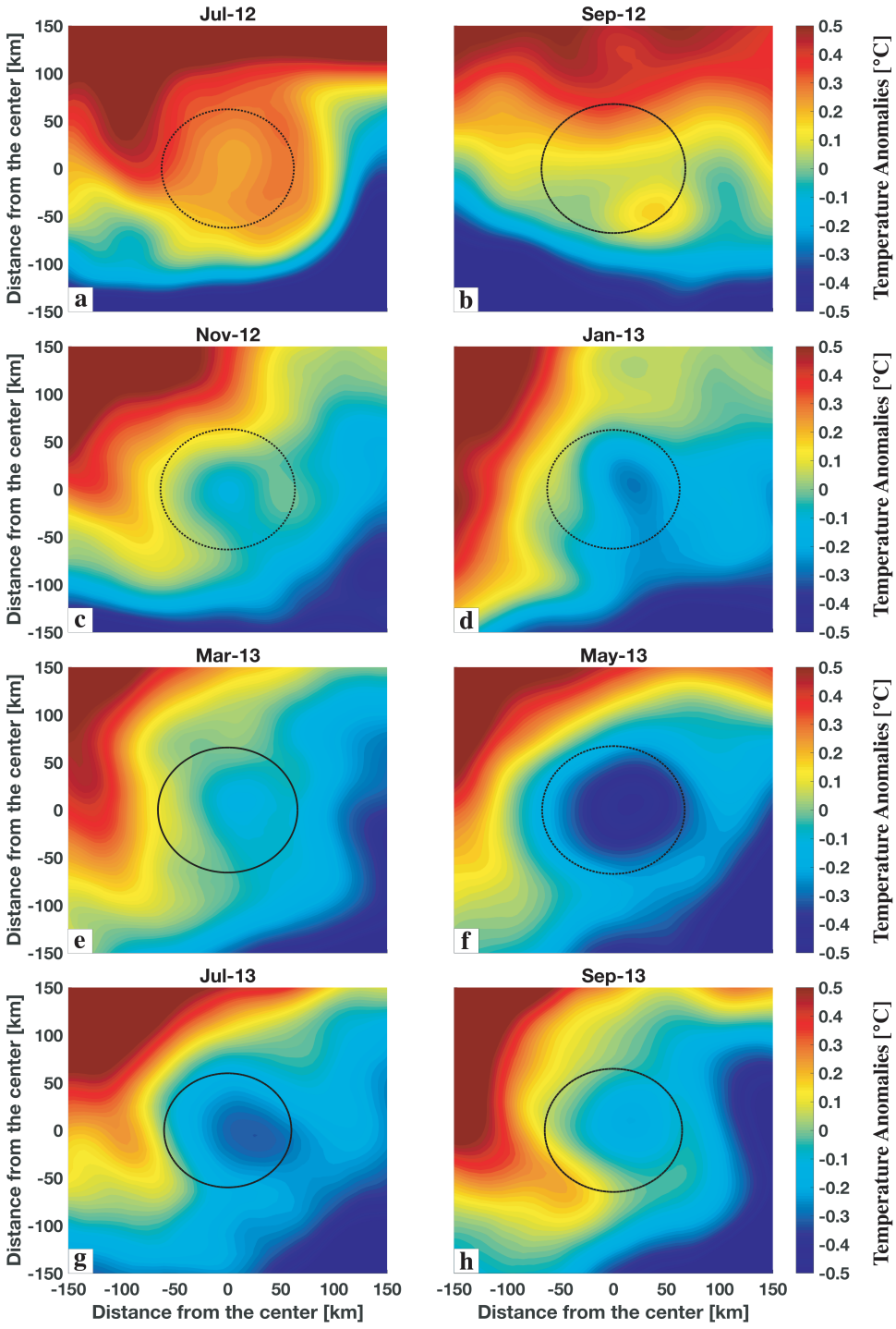


Figure D.3: Monthly averaged SST anomalies in the moving reference frame of the 5^{th} segment of the AREN interpolated from the ODYSSEA SST dataset [Autret and Piolle 2011]. These anomalies are computed subtracting the mean SST computed in each panels to the SST values at each point.

D.4 TS diagram

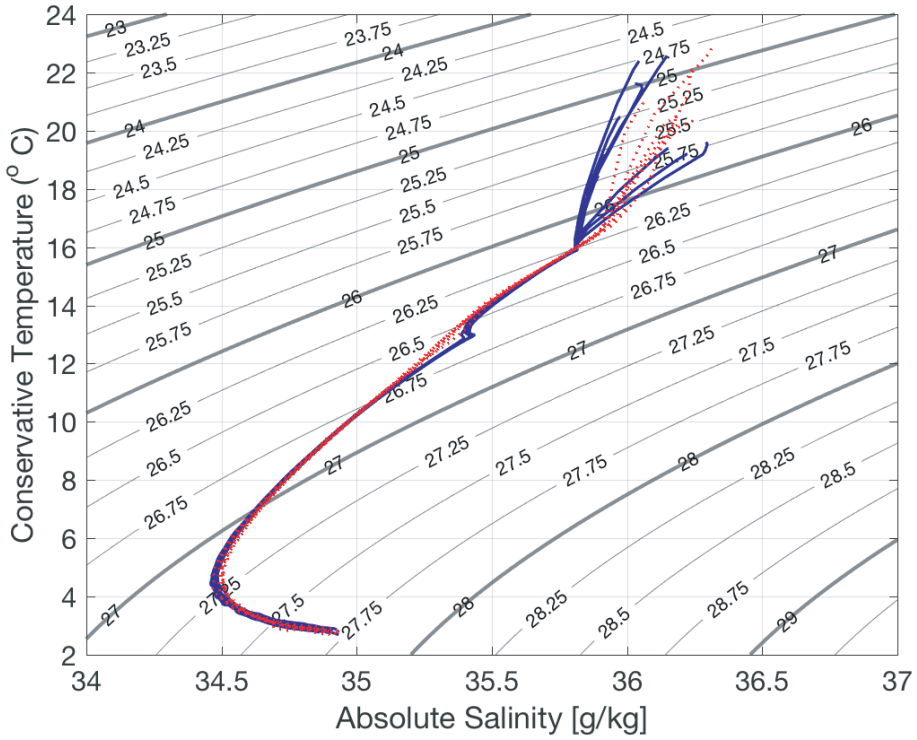


Figure D.4: TS diagram of Argo profiles with a $Dc < 25$ km in red and those with a $150 < Dc < 200$ km in blue sampling the segment 5 between November 2012 and November 2013.

D.5 Examples of potential anomalies reconstruction

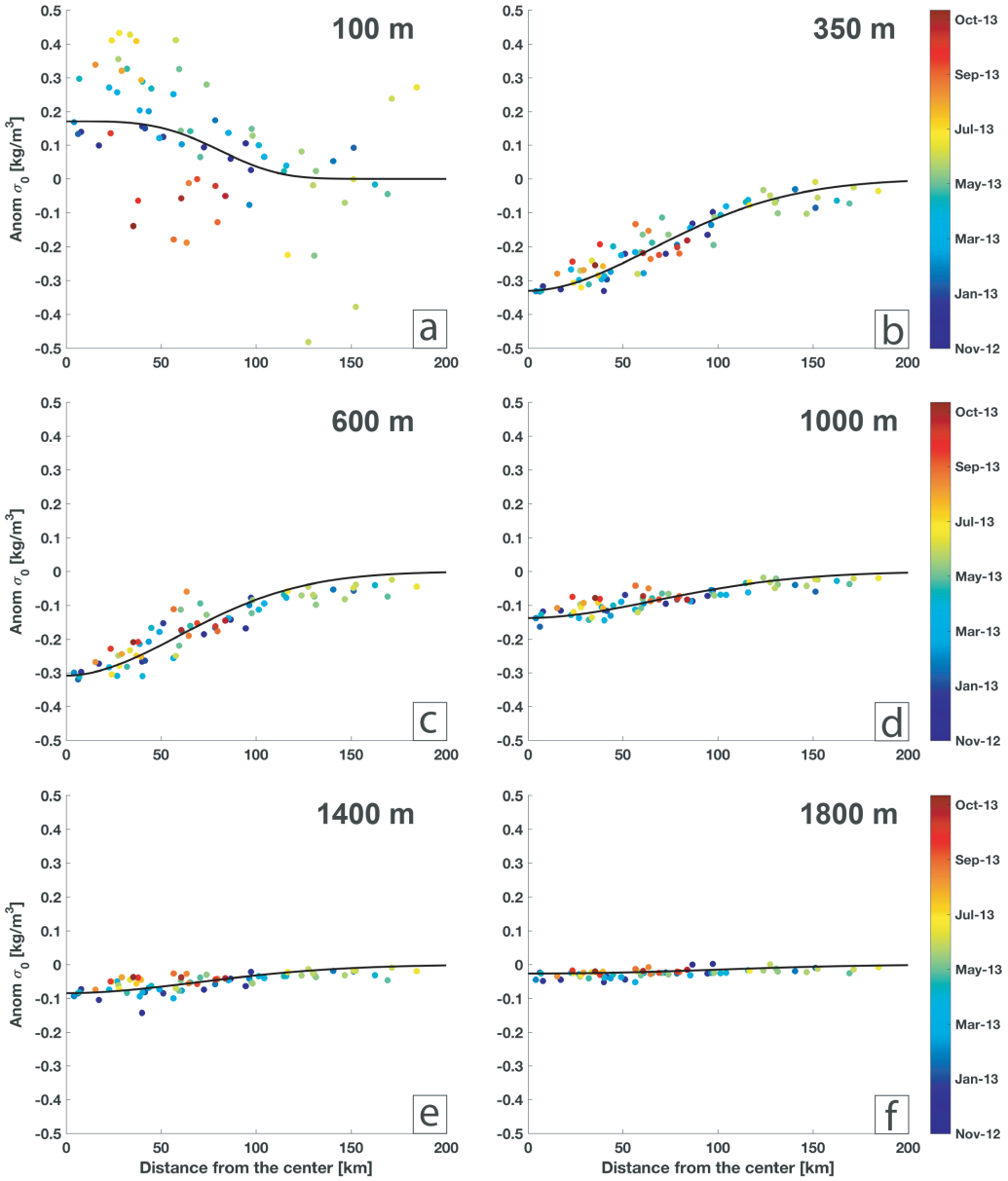


Figure D.5: σ_0 anomalies derived from Argo observations (circles) and from the Reconstructed Agulhas Ring (solid black lines) at 6 different depths as function of the distance from the eddy center (Dc). The date for every observation is indicated by the color of the circles.

D.6 Hydrological properties of Mode Waters found in the South Atlantic as described in the literature.

Table D.1: Hydrological properties Potential Temperature (θ), Practical Salinity and σ_θ) of Mode Waters found in the South Atlantic as described in the literature. The standard deviations ($\pm$ STD) is provided when it is explicitly supplied in the articles.

Acronym	Full Name	θ [°C]	PSU [psu]	σ_θ [kg m^{-3}]	Reference
SAMW	Subantarctic MW	4-15	34.2-35.8	26.5-27.1	McCartney [1977,1982]
SASTMW	South Atlantic STMW	12-18	35.2-36.2	26.2-26.6	Provost et al. [1999]
SAESTMW	South Atlantic Eastern STMW	15-16	35.4	26.2-26.3	Provost et al. [1999]
SASTMW1	South Atlantic STMW 1	15.0 ± 0.9	35.6 ± 0.2	26.4 ± 0.1	Sato & Polito [2014]
SASTMW2	South Atlantic STMW 2	16.7 ± 0.9	35.7 ± 0.2	26.1 ± 0.1	Sato & Polito [2014]
SASTMW3	South Atlantic STMW 3	13.2 ± 0.9	35.2 ± 0.2	26.5 ± 0.1	Sato & Polito [2014]
$STMW_{18}$	STMW θ=18	18 ± 0.56	35.8 ± 0.11	25.9	de Souza et al. [2018]
$STMW_{14}$	STMW θ=14	14 ± 0.53	35.40 ± 0.01	26.5	de Souza et al. [2018]
$STMW_{12}$	STMW θ=12	12 ± 0.50	35.03 ± 0.14	26.6	de Souza et al. [2018]
SIMW	Subtropical Indian MW	17 ± 0.28	35.57 ± 0.54	26.0	de Souza et al. [2018]

D.7 Hydrological properties of the Agulhas Ring's cores described in the literature.

Table D.2: Properties of the Agulhas Ring cores described in the literature. The precision of the variables is not fixed as it depends of each article.

Article	Eddy.Core Number	Depth [m]	Thickness [m]	θ [° C]	PSU []
Gordon et al., 1987	CTE.1	-230	200	16	35.5
McCartney and Woodgate-Jones, 1991	Eddy.1	-150	100	17.5	35.75
McCartney and Woodgate-Jones, 1991	Eddy.2	-250	100	15.5	35.45
Duncombe Rae et al., 1992	Ring.1	-50	100	19	35.66
van Ballegooyen et al., 1994	A4.1	-70	140	18.83	35.71
Duncombe Rae et al., 1996	B1-1.1	-150	300	16.65	35.49
Duncombe Rae et al., 1996	B2-1.1	-300	400	13.13	35.24
Duncombe Rae et al., 1996	B2-2.1	-100	200	15.84	35.58
Duncombe Rae et al., 1996	B2-3.1	-50	100	18.33	35.72
Duncombe Rae et al., 1996	B2-4.1	-100	200	18.96	35.57
Duncombe Rae et al., 1996	B3-1.1	-300	400	13.73	35.37
Arhan et al., 1999	R1.1	-325	350	11.6	35.08
Arhan et al., 1999	R2.1	-150	120	17.1	35.71
Arhan et al., 1999	R3.1	-350	300	13.6	35.34
McDonagh et al, 1999	R1.1	-325	450	13	35.2
McDonagh et al, 1999	R2.1	-150	100	18	35.5

Table D.3: Properties of the Agulhas Ring cores described in the literature. The precision of the variables is not fixed as it depends of each article.

Article	Eddy.Core Number	Depth [m]	Thickness [m]	Pt0 [° C]	PSU []
Garzoli et al., 1999	R-1.1	-100	200	16.13	35.59
Garzoli et al., 1999	R-2.1	-510	140	12.13	35.1
Garzoli et al., 1999	R-3.1	-270	100	15.22	35.51
Garzoli et al., 1999	R-3.2	-350	150	14.39	35.35
Schmid et al., 2003	JAR.1	-50	100	19	35.6
Gladyshev et al., 2008	E3.1	-400	500	12.5	35.2
Arhan et al., 2011	Eddy M.1	-380	550	11.8	35.15
Casanova-Masjoan et al., 2017	ACR.1	-145	170	16.6	35.6
Casanova-Masjoan et al., 2017	ACR.2	-400	100	13.4	35.34
Guerra et al., 2018	Lilian.1	-200	160	16.5	35.65
Guerra et al., 2018	Lilian.2	-480	240	12.5	35.2
This study	AR.1	-290	180	16.1	35.7
This study	AR.2	-560	100	12.9	35.3

D.8 Integrated properties of the Agulhas Rings described in the literature.

Table D.4: Integrated properties of the Agulhas Rings describe in the literature expressed as percentage of the same variables obtained in the RecAR. We do not compare volume for a fixed depth as there is no meaning to do that.

Article	Eddy	Volume	HCA	SCA	Reference
McCartney & Woodgate-Jones, (1991)	Eddy	50%			Trap 5 cm/s
van Ballegooyen et al., (1994)	A3	73%	150%	378%	T > 8° C
van Ballegooyen et al., (1994)	A4	67%	237%	567%	T > 8° C
van Ballegooyen et al., (1994)	A5	26%	73%	188%	T > 8° C
van Ballegooyen et al., (1994)	A6	42%	107%	199%	T > 8° C
Duncombe Rae et al., (1996)	B1-1		23%	46%	800 m
Duncombe Rae et al., (1996)	B2-1		30%	58%	800 m
Duncombe Rae et al., (1996)	B2-2		70%	144%	800 m
Duncombe Rae et al., (1996)	B2-3		68%	141%	800 m
Duncombe Rae et al., (1996)	B2-4		52%	63%	800 m
Duncombe Rae et al., (1996)	B3-1		74%	147%	800 m
McDonagh et al, (1999)	R1	31%	39%	105%	T > 10° C
McDonagh et al, (1999)	R2	98%	44%	117%	T > 10° C
Garzoli et al., (1999)	R-1		86%	195%	1100 m
Garzoli et al., (1999)	R-2		85%		1100 m
Garzoli et al., (1999)	R-3		50%		1100 m
Schmid et al., (2003)	JAR		110%	261%	1100 m

E

Additional Figures for "Agulhas Rings heat content and transport in the South Atlantic estimated by combining satellite altimetry and Argo profiling floats data"

Sommaire

E.1 Potential density (σ_0) in the upper ocean from the World Ocean Database 194
E.2 HC ref 195
E.3 Lagrangian Reconstruction 196

In this appendix, we present few figures discussed in the core of the chapter 5.

E.1 Potential density (σ_0) in the upper ocean from the World Ocean Database

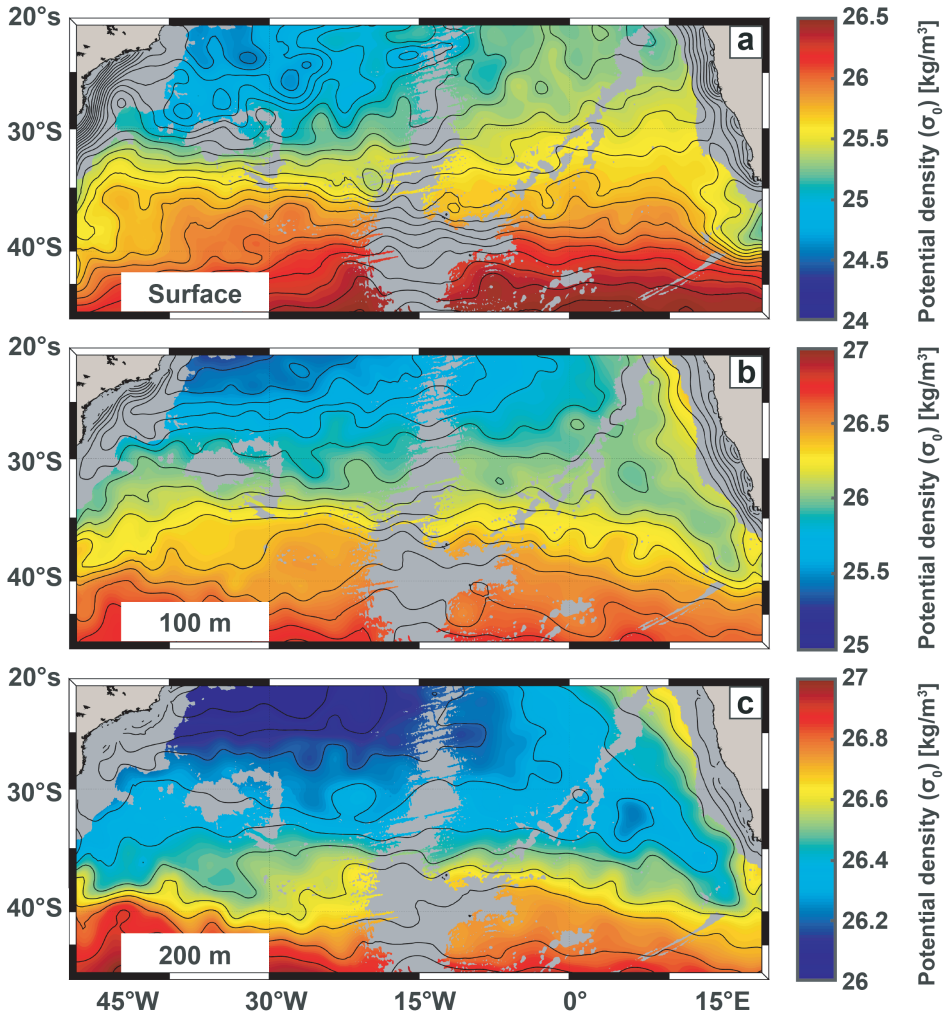


Figure E.1: Potential density (σ_0) at a) the surface, b) 100 m and c) 200 m from the World Ocean Database [Boyer et al. 2013] averaged over seven years (i.e. 2005 to 2012). Isopycnals levels are drawn every 0.1 kg.m^{-3}. The gray shading in each figure represents water depths less than 3500 m in the ETOPO2 data set [Smith and Sandwell 1997].

E.2 HC ref

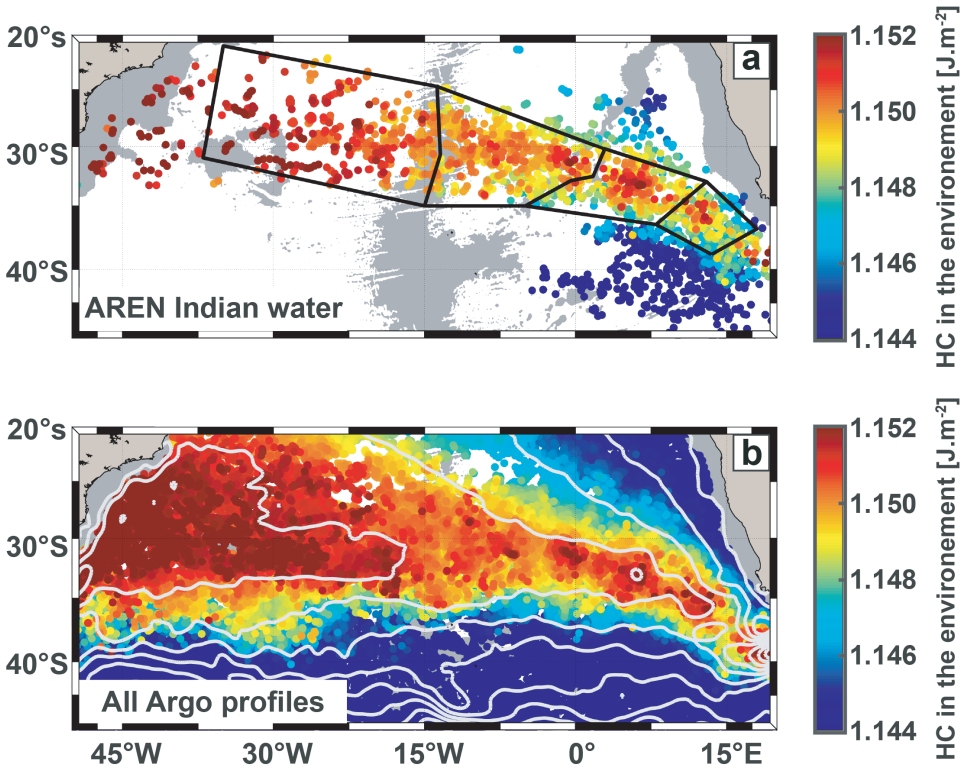


Figure E.2: Heat Content between 1200 and 200 m computed in the climatologic profiles associated to the Agulhas Ring (panel a) and those computed for all the Argo profiles extracted in this region (panel b)

E.3 Lagrangian Reconstruction

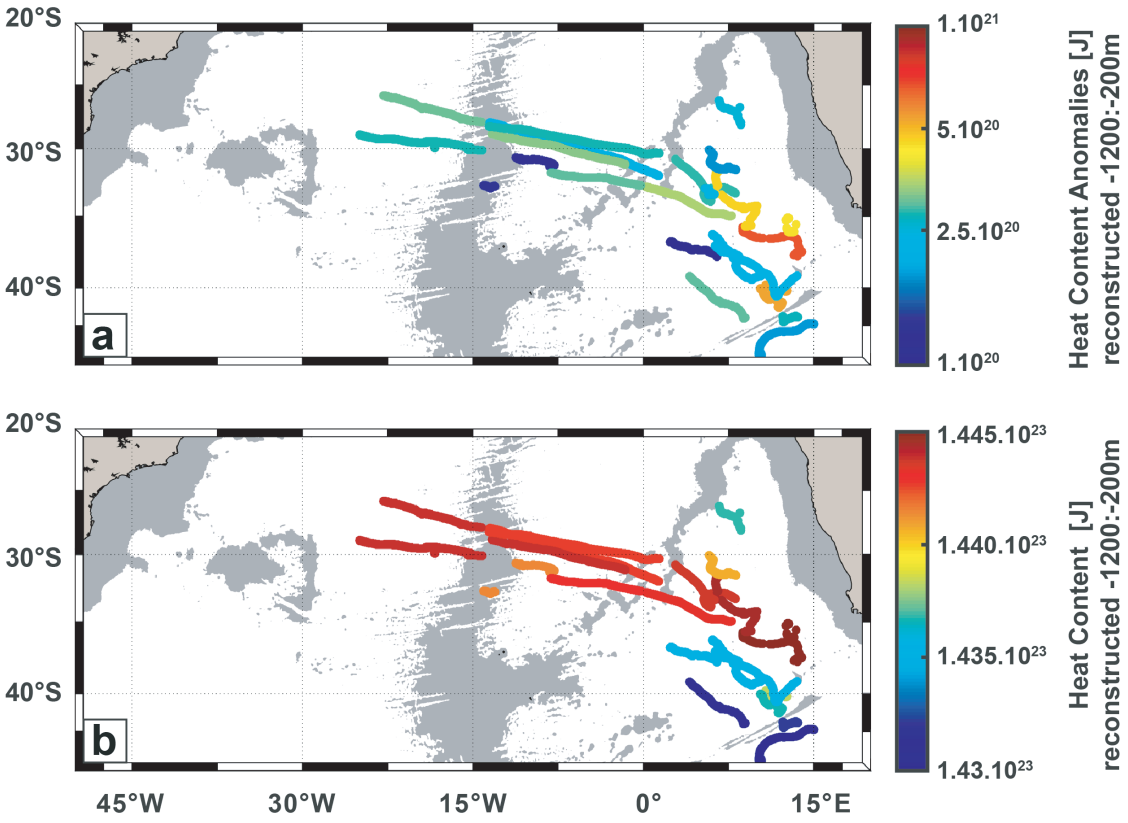


Figure E.3: Heat content Anomalies (panel a) and total Heat content (panel b), both between 1200 and 200 m, computed in the eddies reconstructed by the Agulhas Ring. The values obtained in the HCA are plotted at the position of the center derived from the altimetry.

Bibliographie

Abernathey, R. and Haller, G. (2018). Transport by Lagrangian Vortices in the Eastern Pacific. *Journal of Physical Oceanography*, 48(3):667–685.

Alfultis, M. A. and Cornillon, P. (2001). Annual and interannual changes in the North Atlantic STMW layer properties. *Journal of Physical Oceanography*, 31(8):2066–2086.

Amores, A., Jordà, G., Arsouze, T., and Le Sommer, J. (2018). Up to What Extent Can We Characterize Ocean Eddies Using Present-Day Gridded Altimetric Products? *Journal of Geophysical Research: Oceans*, 123(10):7220–7236.

Amores, A., Melnichenko, O., and Maximenko, N. (2017). Coherent mesoscale eddies in the North Atlantic subtropical gyre: 3-D structure and transport with application to the salinity maximum. *Journal of Geophysical Research: Oceans*, 122(1):23–41.

Arhan, M., Mercier, H., and Lutjeharms, J. R. E. (1999). The disparate evolution of three Agulhas rings in the South Atlantic Ocean. *Journal of Geophysical Research: Oceans*, 104(C9):20987–21005.

Arhan, M., Speich, S., Messager, C., Dencausse, G., Fine, R., and Boye, M. (2011). Anticyclonic and cyclonic eddies of subtropical origin in the subantarctic zone south of Africa. *Journal of Geophysical Research*, 116(C11).

Arístegui, J., Sangrá, P., Hernández-León, S., Cantón, M., Hernández-Guerra, A., and Kerling, J. (1994). Island-induced eddies in the Canary Islands. *Deep Sea Research Part I: Oceanographic Research Papers*, 41(10):1509–1525.

Armi, L., Hebert, D., Oakey, N., Price, J. F., Richardson, P. L., Rossby, H. T., and Ruddick, B. (1989). Two years in the life of a Mediterranean salt lens. *Journal of Physical Oceanography*, 19(3):354–370.

Armi, L. and Zenk, W. (1984). Large lenses of highly saline Mediterranean water. *Journal of Physical Oceanography*, 14(10):1560–1576.

Ashkezari, M. D., Hill, C. N., Follett, C. N., Forget, G., and Follows, M. J. (2016). Oceanic eddy detection and lifetime forecast using machine learning methods. *Geophysical Research Letters*, 43(23):12,234–12,241. 2016GL071269.

Assassi, C., Morel, Y., Vandermeirsch, F., Chaigneau, A., Pegliasco, C., Morrow, R., Colas, F., Fleury, S., Carton, X., Klein, P., et al. (2016). An Index to Distinguish Surface-and Subsurface-Intensified Vortices from Surface Observations. *Journal of Physical Oceanography*, 46(8):2529–2552.

Autret, E. and Piolle, J. (2011). Product User Manual for ODYSSEA Level 3 and 4 global and regional products. Technical report, MYO-PUM-SST-TAC-ODYSSEA, Ifremer/CERSAT.[Available online at: http://projets ....

Baker-Yeboah, S., Byrne, D. A., and Watts, D. R. (2010). Observations of mesoscale eddies in the South Atlantic Cape Basin: Baroclinic and deep barotropic eddy variability. *Journal of Geophysical Research: Oceans*, 115(C12). C12069.

Ballegooyen, R. C., Gründlingh, M. L., and Lutjeharms, J. R. (1994). Eddy fluxes of heat and salt from the southwest Indian Ocean into the southeast Atlantic Ocean: A case study. *Journal of Geophysical Research: Oceans*, 99(C7):14053–14070.

Bang, N. (1970). Dynamic interpretations of a detailed surface temperature chart of the Agulhas Current retroflexion and fragmentation area. *South African Geographical Journal*, 52(1):67–76.

Bashmachnikov, I., Machín, F., Mendonça, A., and Martins, A. (2009). In situ and remote sensing signature of meddies east of the mid-Atlantic ridge. *Journal of Geophysical Research: Oceans*, 114(C5).

Bashmachnikov, I., Neves, F., Calheiros, T., and Carton, X. (2015). Properties and pathways of Mediterranean water eddies in the Atlantic. *Progress in Oceanography*, 137:149–172.

Beal, L. M. and Elipot, S. (2016). Broadening not strengthening of the Agulhas Current since the early 1990s. *Nature*, 540(7634):570–573.

Beal, L. M., Ruijter, W. P. M. D., Biastoch, A., Zahn, R., Cronin, M., Hermes, J., Lutjeharms, J., Quartly, G., Tozuka, T., Baker-Yeboah, S., Bornman, T., Cipollini, P., Dijkstra, H., Hall, I., Park, W., Peeters, F., Penven, P., Ridderinkhof, H., and Zinke, J. (2011). On the role of the Agulhas system in ocean circulation and climate. *Nature*, 472(7344):429–436. Authors No 5 to 19 are members of the Working Group.

Beismann, J.-O., Käse, R. H., and Lutjeharms, J. R. (1999). On the influence of submarine ridges on translation and stability of Agulhas rings. *Journal of Geophysical Research: Oceans*, 104(C4):7897–7906.

Beron-Vera, F. J., Wang, Y., Olascoaga, M. J., Goni, G. J., and Haller, G. (2013). Objective detection of oceanic eddies and the Agulhas leakage. *Journal of Physical Oceanography*, 43(7):1426–1438.

Bettencourt, J. H., López, C., and Hernández-García, E. (2012). Oceanic three-dimensional Lagrangian coherent structures: A study of a mesoscale eddy in the Benguela upwelling region. *Ocean Modelling*, 51:73–83.

Biastoch, A. and Böning, C. W. (2013). Anthropogenic impact on Agulhas leakage. *Geophysical Research Letters*, 40(6):1138–1143.

Biastoch, A., Böning, C. W., and Lutjeharms, J. R. E. (2008a). Agulhas leakage dynamics affects decadal variability in Atlantic overturning circulation. *Nature*, 456:489–492.

Biastoch, A., Böning, C. W., Schwarzkopf, F. U., and Lutjeharms, J. (2009). Increase in Agulhas leakage due to poleward shift of Southern Hemisphere westerlies. *Nature*, 462(7272):495.

Biastoch, A., Lutjeharms, J. R. E., Böning, C. W., and Scheinert, M. (2008b). Mesoscale perturbations control inter-ocean exchange south of Africa. *Geophysical Research Letters*, 35(20). L20602.

Boebel, O., Lutjeharms, J., Schmid, C., Zenk, W., Rossby, T., and Barron, C. (2003a). The Cape Cauldron: a regime of turbulent inter-ocean exchange. *Deep Sea Research Part II: Topical Studies in Oceanography*, 50(1):57–86.

Boebel, O., Rossby, T., Lutjeharms, J., Zenk, W., and Barron, C. (2003b). Path and variability of the Agulhas Return Current. *Deep Sea Research Part II: Topical Studies in Oceanography*, 50(1):35–56.

Boyer, T. P., Antonov, J. I., Baranova, O. K., Coleman, C., Garcia, H. E., Grodsky, A., Johnson, D. R., Locarnini, R. A., Mishonov, A. V., O'Brien, T. D., et al. (2013). World Ocean Database 2013.

Braby, L., Backeberg, B. C., Ansorge, I., Roberts, M. J., Krug, M., and Reason, C. J. (2016). Observed eddy dissipation in the Agulhas Current. *Geophysical Research Letters*, 43(15):8143–8150.

Branch, M. A., Coleman, T. F., and Li, Y. (1999). A subspace, interior, and conjugate gradient method for large-scale bound-constrained minimization problems. *SIAM Journal on Scientific Computing*, 21(1):1–23.

Brundage, W. and Dugan, J. (1986). Observations of an anticyclonic eddy of 18 C water in the Sargasso Sea. *Journal of physical oceanography*, 16(4):717–727.

Bryden, H. (1979). Poleward heat flux and conversion of available potential energy in Drake Passage. *1979. 24 P.*

Burkov, V. A. and Ovchinnikov, I. M. (1960). Studies of the equatorial currents north of New Guinea. *Trudy Inst. Okeanol. Akad. Nauk SSSR*, 40:121–134.

Byrne, D. A., Gordon, A. L., and Haxby, W. F. (1995). Agulhas Eddies: A Synoptic View Using Geosat ERM Data. *Journal of Physical Oceanography*, 25(5):902–917.

Cabanes, C., Thierry, V., and Lagadec, C. (2016). Improvement of bias detection in Argo float conductivity sensors and its application in the North Atlantic. *Deep Sea Research Part I: Oceanographic Research Papers*, 114:128–136.

Capet, A., Mason, E., Rossi, V., Troupin, C., Faugère, Y., Pujol, I., and Pascual, A. (2014). Implications of refined altimetry on estimates of mesoscale activity and eddy-driven offshore transport in the Eastern Boundary Upwelling Systems. *Geophysical Research Letters*, 41(21):7602–7610.

Capuano, T. A., Speich, S., Carton, X., and Blanke, B. (2018a). Mesoscale and submesoscale processes in the Southeast Atlantic and their impact on the regional thermohaline structure. *Journal of Geophysical Research: Oceans*, 123(3):1937–1961.

Capuano, T. A., Speich, S., Carton, X., and Laxenaire, R. (2018b). Indo-Atlantic Exchange, Mesoscale Dynamics, and Antarctic Intermediate Water. *Journal of Geophysical Research: Oceans*.

Carton, X. (2001). Hydrodynamical Modeling Of Oceanic Vortices. *Surveys in Geophysics*, 22(3):179–263.

Carton, X. (2010). Oceanic vortices. In *Fronts, Waves and Vortices in Geophysical Flows*, chapter 3, pages 61–108. Springer.

Casanova-Masjoan, M., Pelegrí, J., Sangrà, P., Martínez, A., Grisolía-Santos, D., Pérez-Hernández, M. D., and Hernández-Guerra, A. (2017). Characteristics and evolution of an Agulhas ring. *Journal of Geophysical Research: Oceans*, 122(9):7049–7065.

Cazenave, A. and Massonnet, D. (2004). *La Terre vue de l'espace*. Belin.

Chaigneau, A., Eldin, G., and Dewitte, B. (2009). Eddy activity in the four major upwelling systems from satellite altimetry (1992–2007). *Progress in Oceanography*, 83(1):117–123.

Chaigneau, A., Gizolme, A., and Grados, C. (2008). Mesoscale eddies off Peru in altimeter records: Identification algorithms and eddy spatio-temporal patterns. *Progress in Oceanography*, 79(2):106–119.

Chaigneau, A., Marie, L. T., Gérard, E., Carmen, G., and Oscar, P. (2011). Vertical structure of mesoscale eddies in the eastern South Pacific Ocean: A composite analysis from altimetry and Argo profiling floats. *Journal of Geophysical Research: Oceans*, 116(C11).

Chaigneau, A. and Pizarro, O. (2005). Eddy characteristics in the eastern South Pacific. *Journal of Geophysical Research: Oceans*, 110(C6).

Chassignet, E. P., Olson, D. B., and Boudra, D. B. (1990). Motion and evolution of oceanic rings in a numerical model and in observations. *Journal of Geophysical Research: Oceans*, 95(C12):22121–22140.

Chelton, D. B., deSzoeke, R. A., Schlax, M. G., El Naggar, K., and Siwertz, N. (1998). Geographical Variability of the First Baroclinic Rossby Radius of Deformation. *Journal of Physical Oceanography*, 28(3):433–460.

Chelton, D. B., Schlax, M. G., and Samelson, R. M. (2011). Global observations of nonlinear mesoscale eddies. *Progress in Oceanography*, 91(2):167–216.

Chelton, D. B., Schlax, M. G., Samelson, R. M., and de Szoeke, R. A. (2007). Global observations of large oceanic eddies. *Geophysical Research Letters*, 34(15):n/a–n/a. L15606.

Cheng, Y., Beal, L. M., Kirtman, B. P., and Putrasahan, D. (2018). Interannual Agulhas Leakage Variability and Its Regional Climate Imprints. *Journal of Climate*, (2018).

Ciani, D. (2016). *Subsurface-intensified oceanic vortices: impact on the sea-surface and mutual interactions*. PhD thesis, Université de Bretagne occidentale-Brest.

Cipollone, A., Masina, S., Storto, A., and Iovino, D. (2017). Benchmarking the mesoscale variability in global ocean eddy-permitting numerical systems. *Ocean Dynamics*, 67(10):1313–1333.

Collins, C. A., Margolina, T., Rago, T. A., and Ivanov, L. (2013). Looping RAFOS floats in the California Current System. *Deep Sea Research Part II: Topical Studies in Oceanography*, 85:42–61.

Cresswell, G. R. (1982). The Coalescence of Two East Australian Current Warm-Core Eddies. *Science*, 215(4529):161–164.

Cushman-Roisin, B. and Beckers, J.-M. (2011). *Introduction to geophysical fluid dynamics: physical and numerical aspects*, volume 101. Academic press.

Cushman-Roisin, B., Tang, B., and Chassignet, E. P. (1990). Westward motion of mesoscale eddies. *Journal of Physical Oceanography*, 20(5):758–768.

Davis, R. W., Ortega-Ortiz, J. G., Ribic, C. A., Evans, W. E., Biggs, D. C., Ressler, P. H., Cady, R. B., Leben, R. R., Mullin, K. D., and Würsig, B. (2002). Cetacean habitat in the northern oceanic Gulf of Mexico. *Deep Sea Research Part I: Oceanographic Research Papers*, 49(1):121–142.

de Boyer Montégut, C., Madec, G., Fischer, A. S., Lazar, A., and Iudicone, D. (2004). Mixed layer depth over the global ocean: An examination of profile data and a profile-based climatology. *Journal of Geophysical Research: Oceans (1978–2012)*, 109(C12).

De Ruijter, W. (1982). Asymptotic analysis of the Agulhas and Brazil Current systems. *Journal of Physical Oceanography*, 12(4):361–373.

De Ruijter, W., Biastoch, A., Drijfhout, S., Lutjeharms, J., Matano, R., Pichevin, T., Van Leeuwen, P., and Weijer, W. (1999a). Indian-Atlantic interocean exchange: Dynamics, estimation and impact. *Journal of Geophysical Research: Oceans*, 104(C9):20885–20910.

De Ruijter, W. P., Van Leeuwen, P. J., and Lutjeharms, J. R. (1999b). Generation and evolution of Natal Pulses: solitary meanders in the Agulhas Current. *Journal of physical oceanography*, 29(12):3043–3055.

de Souza, A. G. Q., Kerr, R., and de Azevedo, J. L. L. (2018). On the influence of Subtropical Mode Water on the South Atlantic Ocean. *Journal of Marine Systems*, 185:13–24.

De Steur, L., Van Leeuwen, P., and Drijfhout, S. (2004). Tracer leakage from modeled Agulhas rings. *Journal of Physical Oceanography*, 34(6):1387–1399.

De Steur, L. and Van Leeuwen, P. J. (2009). The influence of bottom topography on the decay of modeled Agulhas rings. *Deep Sea Research Part I: Oceanographic Research Papers*, 56(4):471–494.

Dencausse, G., Arhan, M., and Speich, S. (2010a). Routes of Agulhas rings in the southeastern Cape Basin. *Deep Sea Research Part I: Oceanographic Research Papers*, 57(11):1406–1421.

Dencausse, G., Arhan, M., and Speich, S. (2010b). Spatio-temporal characteristics of the Agulhas Current retroflection. *Deep Sea Research Part I: Oceanographic Research Papers*, 57(11):1392–1405.

Dibarboure, G., Pujol, M.-I., Briol, F., Traon, P. L., Larnicol, G., Picot, N., Mertz, F., and Ablain, M. (2011). Jason-2 in DUACS: Updated system description, first tandem results and impact on processing and products. *Marine Geodesy*, 34(3-4):214–241.

Dickey, T. D. (2003). Emerging ocean observations for interdisciplinary data assimilation systems. *Journal of Marine Systems*, 40:5–48.

Doglioli, A., Veneziani, M., Blanke, B., Speich, S., and Griffa, A. (2006). A Lagrangian analysis of the Indian-Atlantic interocean exchange in a regional model. *Geophysical Research Letters*, 33(14).

Doglioli, A. M., Blanke, B., Speich, S., and Lapeyre, G. (2007). Tracking coherent structures in a regional ocean model with wavelet analysis: Application to Cape Basin eddies. *Journal of Geophysical Research: Oceans*, 112(C5). C05043.

Dong, C., Liu, Y., Lumpkin, R., Lankhorst, M., Chen, D., McWilliams, J. C., and Guan, Y. (2011a). A scheme to identify loops from trajectories of oceanic surface drifters: an application in the Kuroshio extension region. *Journal of Atmospheric and Oceanic Technology*, 28(9):1167–1176.

Dong, C., McWilliams, J. C., Liu, Y., and Chen, D. (2014). Global heat and salt transports by eddy movement. *Nature communications*, 5:3294.

Dong, S., Garzoli, S., and Baringer, M. (2011b). The role of interocean exchanges on decadal variations of the meridional heat transport in the South Atlantic. *Journal of Physical Oceanography*, 41(8):1498–1511.

Donners, J. and Drijfhout, S. S. (2004). The Lagrangian view of South Atlantic interocean exchange in a global ocean model compared with inverse model results. *Journal of physical oceanography*, 34(5):1019–1035.

Donohue, K. A., Firing, E., and Beal, L. (2000). Comparison of three velocity sections of the Agulhas Current and Agulhas Undercurrent. *Journal of Geophysical Research: Oceans*, 105(C12):28585–28593.

Drijfhout, S. S. (2003). Why anticyclones can split. *Journal of Physical Oceanography*, 33(8):1579–1591.

Du, Y., Yi, J., Wu, D., He, Z., Wang, D., and Liang, F. (2014). Mesoscale oceanic eddies in the South China Sea from 1992 to 2012: evolution processes and statistical analysis. *Acta Oceanologica Sinica*, 33(11):36–47.

Duacs/AVISO+ (2014). A new version of SSALTO/Duacs products available in April 2014. Version 1.1, CNES. *[Available at http://www.aviso.altimetry.fr/fileadmin/documents/data/duacs/Duacs2014.pdf.]*.

Duacs/AVISO+ (2015). SSALTO/DUACS user handbook:(M) SLA and (M) ADT near-real time and delayed time products. *CLS-DOS-NT-06-034*, 6:74.

Duacs/AVISO+ (2017). Mesoscale Eddy Trajectory Atlas Product Handbook . *SALP-MU-P-EA-23126-CLS*, page 17.

Ducet, N., Le Traon, P.-Y., and Reverdin, G. (2000). Global high-resolution mapping of ocean circulation from TOPEX/Poseidon and ERS-1 and-2. *Journal of Geophysical Research: Oceans*, 105(C8):19477–19498.

Dugan, J., Mied, R., Mignerey, P., and Schuetz, A. (1982). Compact, intrathermocline eddies in the Sargasso Sea. *Journal of Geophysical Research: Oceans*, 87(C1):385–393.

Duncan, C. (1968). An eddy in the subtropical convergence southwest of South Africa. *Journal of Geophysical Research*, 73(2):531–534.

Duncombe Rae, C., Garzoli, S., and Gordon, A. (1996). The eddy field of the southeast Atlantic Ocean: A statistical census from the Benguela Sources and Transports Project. *Journal of Geophysical Research: Oceans*, 101(C5):11949–11964.

Duncombe Rae, C., Shillington, F., Agenbag, J., Taunton-Clark, J., and Gründlingh, M. (1992). An Agulhas ring in the South Atlantic Ocean and its interaction with the Benguela upwelling frontal system. *Deep Sea Research Part A. Oceanographic Research Papers*, 39(11-12):2009–2027.

Duncombe Rae, C. M. (1991). Agulhas retroflection rings in the South Atlantic Ocean: an overview. *South African Journal of Marine Science*, 11(1):327–344.

Dussurget, R., Birol, F., Morrow, R., and Mey, P. D. (2011). Fine resolution altimetry data for a regional application in the Bay of Biscay. *Marine Geodesy*, 34(3-4):447–476.

Edelsbrunner, H. and Harer, J. (2010). *Computational topology: an introduction.* American Mathematical Soc.

Edelsbrunner, H., Letscher, D., and Zomorodian, A. (2002). Topological persistence and simplification. *Discrete Comput Geom*, 28:511–533.

Elipot, S. and Beal, L. M. (2015). Characteristics, Energetics, and Origins of Agulhas Current Meanders and Their Limited Influence on Ring Shedding. *Journal of Physical Oceanography*, 45(9):2294–2314.

Ertel, H. (1942). Ein neuer hydrodynamischer Erhaltungssatz. *Naturwissenschaften*, 30(36):543–544.

Escudier, R., Renault, L., Pascual, A., Brasseur, P., Chelton, D., and Beuvier, J. (2016). Eddy properties in the Western Mediterranean Sea from satellite altimetry and a numerical simulation. *Journal of Geophysical Research: Oceans*, 121(6):3990–4006.

Faghmous, J. H., Frenger, I., Yao, Y., Warmka, R., Lindell, A., and Kumar, V. (2015). A daily global mesoscale ocean eddy dataset from satellite altimetry. *Scientific Data*, 2:150028.

Feron, R., De Ruijter, W., and Van Leeuwen, P. (1998). A new method to determine the mean sea surface dynamic topography from satellite altimeter observations. *Journal of Geophysical Research: Oceans*, 103(C1):1343–1362.

Feron, R. C., De Ruijter, W. P., and Oskam, D. (1992). Ring shedding in the Agulhas Current system. *Journal of Geophysical Research: Oceans*, 97(C6):9467–9477.

Ferrari, R. and Wunsch, C. (2009). Ocean circulation kinetic energy: Reservoirs, sources, and sinks. *Annual Review of Fluid Mechanics*, 41.

Flierl, G. and McGillicuddy, D. J. (2002). Mesoscale and submesoscale physical-biological interactions. *The sea*, 12:113–185.

Flierl, G. R. (1981). Particle motions in large-amplitude wave fields. *Geophysical & Astrophysical Fluid Dynamics*, 18(1-2):39–74.

Foussard, A., Lapeyre, G., and Plougonven, R. (2018). Storm tracks response to oceanic eddies in idealized atmospheric simulations. *Journal of Climate*, (2018).

Frenger, I., Gruber, N., Knutti, R., and Münnich, M. (2013). Imprint of Southern Ocean eddies on winds, clouds and rainfall. *Nature geoscience*, 6(8):608.

Frenger, I., Münnich, M., Gruber, N., and Knutti, R. (2015). Southern ocean eddy phenomenology. *Journal of Geophysical Research: Oceans*, 120(11):7413–7449.

Garfield, N., Collins, C. A., Paquette, R. G., and Carter, E. (1999). Lagrangian exploration of the California Undercurrent, 1992–95. *Journal of Physical Oceanography*, 29(4):560–583.

Garreau, P., Dumas, F., Louazel, S., Stegner, A., and Le Vu, B. (2018). High-resolution observations and tracking of a dual-core anticyclonic eddy in the Algerian Basin. *Journal of Geophysical Research: Oceans*.

Garzoli, S. L. and Goni, G. J. (2000). Combining altimeter observations and oceanographie data for ocean circulation and climate studies. In *Elsevier Oceanography Series*, volume 63, pages 79–97. Elsevier.

Garzoli, S. L., Richardson, P. L., Duncombe Rae, C. M., Fratantoni, D. M., Goñi, G. J., and Roubicek, A. J. (1999). Three Agulhas rings observed during the Benguela Current Experiment. *Journal of Geophysical Research: Oceans*, 104(C9):20971–20985.

Gaube, P., Barceló, C., McGillicuddy Jr, D. J., Domingo, A., Miller, P., Giffoni, B., Marcovaldi, N., and Swimmer, Y. (2017). The use of mesoscale eddies by juvenile loggerhead sea turtles (Caretta caretta) in the southwestern Atlantic. *PloS one*, 12(3):e0172839.

Gaube, P., Braun, C. D., Lawson, G. L., McGillicuddy, D. J., Della Penna, A., Skomal, G. B., Fischer, C., and Thorrold, S. R. (2018). Mesoscale eddies influence the movements of mature female white sharks in the Gulf Stream and Sargasso Sea. *Scientific reports*, 8(1):7363.

Gill, A. E., Green, J. S. A., and Simmons, A. J. (1974). Energy partition in the large-scale ocean circulation and the production of mid-ocean eddies. *Deep Sea Research*, 21:499–528.

Gladyshev, S., Arhan, M., Sokov, A., and Speich, S. (2008). A hydrographic section from South Africa to the southern limit of the Antarctic Circumpolar Current at the Greenwich meridian. *Deep Sea Research Part I: Oceanographic Research Papers*, 55(10):1284–1303.

Goni, G., Garzoli, S., Roubicek, A., Olson, D., and Brown, O. (1997). Agulhas ring dynamics from TOPEX/POSEIDON satellite altimeter data. *Journal of Marine Research*, 55:861–883.

Gordon, A. L. (1985). Indian-Atlantic transfer of thermocline water at the Agulhas retroflection. *Science*, 227:1030–1034.

Gordon, A. L. (1986). Interocean exchange of thermocline water. *Journal of Geophysical Research: Oceans*, 91(C4):5037–5046.

Gordon, A. L. and Haxby, W. F. (1990). Agulhas eddies invade the South Atlantic: Evidence from Geosat altimeter and shipboard conductivity-temperature-depth survey. *Journal of Geophysical Research: Oceans*, 95(C3):3117–3125.

Gordon, A. L., Lutjeharms, J. R., and Gründlingh, M. L. (1987). Stratification and circulation at the Agulhas Retroflection. *Deep Sea Research Part A. Oceanographic Research Papers*, 34(4):565–599.

Gordon, A. L., Weiss, R., Smethie, W., and Warner, M. (1992). Thermocline and intermediate water communication between the South Atlantic and Indian Oceans. *J. Geophys. Res*, 97:7223–7240.

Griffa, A., Lumpkin, R., and Veneziani, M. (2008). Cyclonic and anticyclonic motion in the upper ocean. *Geophysical Research Letters*, 35(1).

Gruber, N., Lachkar, Z., Frenzel, H., Marchesiello, P., Münnich, M., McWilliams, J. C., Nagai, T., and Plattner, G.-K. (2011). Eddy-induced reduction of biological production in eastern boundary upwelling systems. *Nature geoscience*, 4(11):787.

Gründlingh, M. L. (1995). Tracking eddies in the southeast Atlantic and southwest Indian oceans with TOPEX/POSEIDON. *Journal of Geophysical Research: Oceans*, 100(C12):24977–24986.

Guerra, L. A. A., Paiva, A. M., and Chassignet, E. P. (2018). On the translation of Agulhas rings to the western South Atlantic Ocean. *Deep Sea Research Part I: Oceanographic Research Papers*, 139:104–113.

Haller, G. and Beron-Vera, F. J. (2013). Coherent Lagrangian vortices: The black holes of turbulence. *Journal of Fluid Mechanics*, 731.

Halo, I., Backeberg, B., Penven, P., Ansorge, I., Reason, C., and Ullgren, J. (2014). Eddy properties in the Mozambique Channel: A comparison between observations and two numerical ocean circulation models. *Deep Sea Research Part II: Topical Studies in Oceanography*, 100:38–53.

Hamon, B. (1965). The East Australian Current, 1960–1964. *Deep Sea Research*, 12(6):899–921.

Hanawa, K. and Talley, L. D. (2001). .4 Mode waters. In *International Geophysics*, volume 77, pages 373–386. Elsevier.

Harris, T. (1972). Sources of the Agulhas current in the spring of 1964. *Deep Sea Research and Oceanographic Abstracts*, 19(9):633 – 650.

Hausmann, U. and Czaja, A. (2012). The observed signature of mesoscale eddies in sea surface temperature and the associated heat transport. *Deep Sea Research Part I: Oceanographic Research Papers*, 70:60–72.

Herbette, S., Morel, Y., and Arhan, M. (2003). Erosion of a surface vortex by a seamount. *Journal of Physical Oceanography*, 33(8):1664–1679.

Herbette, S., Morel, Y., and Arhan, M. (2004). Subduction of a surface vortex under an outcropping front. *Journal of physical oceanography*, 34(7):1610–1627.

Hernandez, F., Le Traon, P.-Y., and Morrow, R. (1995). Mapping mesoscale variability of the Azores Current using TOPEX/POSEIDON and ERS 1 altimetry, together with hydrographic and Lagrangian measurements. *Journal of Geophysical Research: Oceans*, 100(C12):24995–25006.

Holte, J. and Talley, L. (2009). A new algorithm for finding mixed layer depths with applications to argo data and subantarctic mode water formation. *Journal of Atmospheric and Oceanic Technology*, 26(9):1920–1939.

Holte, J., Talley, L. D., Gilson, J., and Roemmich, D. (2017). An Argo mixed layer climatology and database. *Geophysical Research Letters*, 44(11):5618–5626.

Huang, R. X. (2010). *Ocean circulation: wind-driven and thermohaline processes*. Cambridge University Press.

Ioannou, A., Stegner, A., Le Vu, B., Taupier-Letage, I., and Speich, S. (2017). Dynamical Evolution of Intense Ierapetra Eddies on a 22 Year Long Period. *Journal of Geophysical Research: Oceans*, 122(11):9276–9298.

Iselin, C. and Fuglister, F. C. (1948). Some recent developments in the study of the Gulf Stream. *J. Marine Res*, 7(3):317–329.

Iselin, C. O. (1936). *A study of the circulation of the western North Atlantic*. Massachusetts Institute of Technology and Woods Hole Oceanographic Institution.

Isern-Fontanet, J., García-Ladona, E., and Font, J. (2006). Vortices of the Mediterranean Sea: An altimetric perspective. *Journal of physical oceanography*, 36(1):87–103.

Isoda, Y. (1994). Warm eddy movements in the eastern Japan Sea. *Journal of Oceanography*, 50(1):1–15.

Isoguchi, O., Shimada, M., Sakaida, F., and Kawamura, H. (2009). Investigation of Kuroshio-induced cold-core eddy trains in the lee of the Izu Islands using high-resolution satellite images and numerical simulations. *Remote Sensing of Environment*, 113(9):1912–1925.

Jiang, M., Zhou, M., Libby, S. P., and Anderson, D. M. (2011). Dynamics of a mesoscale eddy off Cape Ann, Massachusetts in May 2005. *Deep Sea Research Part I: Oceanographic Research Papers*, 58(11):1130–1146.

Johns, W. E., Baringer, M. O., Beal, L. M., Cunningham, S., Kanzow, T., Bryden, H. L., Hirschi, J., Marotzke, J., Meinen, C., Shaw, B., et al. (2011). Continuous, array-based estimates of Atlantic Ocean heat transport at 26.5 N. *Journal of Climate*, 24(10):2429–2449.

Joyce, T. M. (2012). New perspectives on eighteen-degree water formation in the North Atlantic. *Journal of oceanography*, 68(1):45–52.

Jullien, S., Marchesiello, P., Menkes, C. E., Lefèvre, J., Jourdain, N. C., Samson, G., and Lengaigne, M. (2014). Ocean feedback to tropical cyclones: Climatology and processes. *Climate dynamics*, 43(9-10):2831–2854.

Kamenkovich, V. M., Leonov, Y. P., Nechaev, D. A., Byrne, D. A., and Gordon, A. L. (1996). On the influence of bottom topography on the Agulhas eddy. *Journal of Physical Oceanography*, 26(6):892–912.

Kersalé, M., Lamont, T., Speich, S., Terre, T., Laxenaire, R., Roberts, M. J., van den Berg, M. A., and Ansorge, I. J. (2018). Moored observations of mesoscale features in the Cape Basin: characteristics and local impacts on water mass distributions. *Ocean Science*, 14(5):923–945.

Koshlyakov, M. N., Galerkin, L. I., and Hien, C. D. (1970). On mesostructure of geostrophic currents in the open ocean. *Oceanologia*, 10:805–814.

Koshlyakov, M. N. and Monin, A. (1978). Synoptic eddies in the ocean. *Annual Review of Earth and Planetary Sciences*, 6(1):495–523.

Kouketsu, S., Tomita, H., Oka, E., Hosoda, S., Kobayashi, T., and Sato, K. (2012). The role of meso-scale eddies in mixed layer deepening and mode water formation in the western North Pacific. *Journal of oceanography*, 68(1):63–77.

Kuhlbrodt, T., Griesel, A., Montoya, M., Levermann, A., Hofmann, M., and Rahmstorf, S. (2007). On the driving processes of the Atlantic meridional overturning circulation. *Reviews of Geophysics*, 45(2).

Kunze, E., Firing, E., Hummon, J. M., Chereskin, T. K., and Thurnherr, A. M. (2006). Global abyssal mixing inferred from lowered ADCP shear and CTD strain profiles. *Journal of Physical Oceanography*, 36(8):1553–1576.

Lambin, J., Morrow, R., Fu, L.-L., Willis, J. K., Bonekamp, H., Lillibridge, J., Perbos, J., Zaouche, G., Vaze, P., Bannoura, W., et al. (2010). The OSTM/Jason-2 mission. *Marine Geodesy*, 33(S1):4–25.

Lampitt, R., Favali, P., Barnes, C., Church, M., Cronin, M., Hill, K., Kaneda, Y., Karl, D., Knap, A., McPhaden, M., et al. (2010). In situ sustained Eulerian observatories. *Proceedings of the OceanObs*, 9:27.

Lankhorst, M. (2006). A self-contained identification scheme for eddies in drifter and float trajectories. *Journal of Atmospheric and Oceanic Technology*, 23(11):1583–1592.

Laxenaire, R., Speich, S., Blanke, B., Chaigneau, A., Pegliasco, C., and Stegner, A. (2018). Anticyclonic Eddies Connecting the Western Boundaries of Indian and Atlantic Oceans. *Journal of Geophysical Research: Oceans*, 123(11):7651–7677.

Laxenaire, R., Speich, S., and Stegner, A. (UR a). Evolution of the thermohaline structure of one Agulhas Ring reconstructed from satellite altimetry and Argo floats.

Laxenaire, R., Speich, S., and Stegner, A. (UR b). The heat transports in the South Atlantic achieved by the Agulhas Rings as estimated combining satellite altimetry and Argo profiles.

Le Traon, P. and Dibarboure, G. (1999). Mesoscale mapping capabilities of multiple-satellite altimeter missions. *Journal of Atmospheric and Oceanic Technology*, 16(9):1208–1223.

Le Traon, P., Faugère, Y., Hernandez, F., Dorandeu, J., Mertz, F., and Ablain, M. (2003). Can we merge GEOSAT Follow-On with TOPEX/POSEIDON and ERS-2 for an improved description of the ocean circulation? *Journal of Atmospheric and Oceanic Technology*, 20(6):889–895.

Le Traon, P.-Y. (2013). From satellite altimetry to Argo and operational oceanography: three revolutions in oceanography. *Ocean Science*, 9(5):901–915.

Le Vu, B., Stegner, A., and Arsouze, T. (2018). Angular Momentum Eddy Detection and tracking Algorithm (AMEDA) and its application to coastal eddy formation. *Journal of Atmospheric and Oceanic Technology*, 35(4):739–762.

Lebedev, K. V., Yoshinari, H., Maximenko, N. A., and Hacker, P. W. (2007). Velocity data assessed from trajectories of Argo floats at parking level and at the sea surface. *IPRC Technical Note*, 4(2):1–16.

Ledwell, J. R., Watson, A. J., and Law, C. S. (1998). Mixing of a tracer in the pycnocline. *Journal of Geophysical Research: Oceans*, 103(C10):21499–21529.

Legg, S. and Marshall, J. (1993). A heton model of the spreading phase of open-ocean deep convection. *Journal of physical oceanography*, 23(6):1040–1056.

Lehahn, Y., d'Ovidio, F., Lévy, M., Amitai, Y., and Heifetz, E. (2011). Long range transport of a quasi isolated chlorophyll patch by an Agulhas ring. *Geophysical Research Letters*, 38(16).

Li, Q.-Y., Sun, L., Liu, S.-S., Xian, T., and Yan, Y.-F. (2014). A new mononuclear eddy identification method with simple splitting strategies. *Remote Sensing Letters*, 5(1):65–72.

Lilly, J. M., Scott, R. K., and Olhede, S. C. (2011). Extracting waves and vortices from Lagrangian trajectories. *Geophysical Research Letters*, 38(23).

Lozier, M. S. (1997). Evidence for large-scale eddy-driven gyres in the North Atlantic. *Science*, 277(5324):361–364.

Lumpkin, R. (2016). Global characteristics of coherent vortices from surface drifter trajectories. *Journal of Geophysical Research: Oceans*, 121(2):1306–1321.

Lumpkin, R. and Pazos, M. (2007). Measuring surface currents with Surface Velocity Program drifters: the instrument, its data, and some recent results. *Lagrangian analysis and prediction of coastal and ocean dynamics*, pages 39–67.

Lutjeharms, J. (1981). Features of the southern Agulhas Current circulation from satellite remote sensing. *South African Journal of Science*, 77(5):231–236.

Lutjeharms, J. and Ansorge, I. (2001). The Agulhas return current. *Journal of Marine Systems*, 30(1-2):115–138.

Lutjeharms, J. and Cooper, J. (1996). Interbasin leakage through Agulhas Current filaments. *Deep Sea Research Part I: Oceanographic Research Papers*, 43(2):213–238.

Lutjeharms, J. and Gordon, A. (1987). Shedding of an Agulhas ring observed at sea. *Nature*, 325(6100):138–140.

Lutjeharms, J., Penven, P., and Roy, C. (2003). Modelling the shear edge eddies of the southern Agulhas Current. *Continental Shelf Research*, 23(11-13):1099–1115.

Lutjeharms, J. and Roberts, H. (1988). The Natal pulse: An extreme transient on the Agulhas Current. *Journal of Geophysical Research: Oceans*, 93(C1):631–645.

Lutjeharms, J. and Valentine, H. (1988). Eddies at the subtropical convergence south of Africa. *Journal of Physical Oceanography*, 18(5):761–774.

Lutjeharms, J. R., Boebel, O., and Rossby, T. (1997). KAPEX: an international experiment to study deep water movement around southern Africa. *South African journal of science*, 93:377–381.

Lutjeharms, J. R. E. (2006). *The Agulhas current*. Springer-Verlag.

Lutjeharms, J. R. E. and Ballegooyen, R. C. V. (1988). The Retroflection of the Agulhas Current. *Journal of Physical Oceanography*, 18(11):1570–1583.

Mahadevan, A. (2016). The impact of submesoscale physics on primary productivity of plankton. *Annual review of marine science*, 8:161–184.

Marshall, J. and Speer, K. (2012). Closure of the meridional overturning circulation through Southern Ocean upwelling. *Nature Geoscience*, 5(3):171.

Martin, A. (2003). Phytoplankton patchiness: the role of lateral stirring and mixing. *Progress in oceanography*, 57(2):125–174.

Mason, E., Pascual, A., and McWilliams, J. C. (2014). A New Sea Surface Height–Based Code for Oceanic Mesoscale Eddy Tracking. *Journal of Atmospheric and Oceanic Technology*, 31(5):1181–1188.

Matano, R. and Beier, E. (2003). A kinematic analysis of the Indian/Atlantic interocean exchange. *Deep Sea Research Part II: Topical Studies in Oceanography*, 50(1):229–249.

Matsuoka, D., Araki, F., Inoue, Y., and Sasaki, H. (2016). A New Approach to Ocean Eddy Detection, Tracking, and Event Visualization–Application to the Northwest Pacific Ocean. *Procedia Computer Science*, 80:1601–1611.

McCartney, M. (1977). Subantarctic Mode Water, A Voyage of Discovery, George Deacon: 70th Anniversary Volume M. Angel, 103–119.

McCartney, M. S. (1982). The subtropical recirculation of mode waters. *J. Mar. Res*, 40(427.4):64.

McCartney, M. S. and Woodgate-Jones, M. (1991). A deep-reaching anticyclonic eddy in the subtropical gyre of the eastern South Atlantic. *Deep Sea Research Part A. Oceanographic Research Papers*, 38:S411–S443.

McDonagh, E. L. and Heywood, K. J. (1999). The origin of an anomalous ring in the southeast Atlantic. *Journal of Physical Oceanography*, 29(8):2050–2064.

McDonagh, E. L., Heywood, K. J., and Meredith, M. P. (1999). On the structure, paths, and fluxes associated with Agulhas rings. *Journal of Geophysical Research: Oceans*, 104(C9):21007–21020.

McDonagh, E. L. and King, B. A. (2005). Oceanic fluxes in the South Atlantic. *Journal of physical oceanography*, 35(1):109–122.

McDougall, T. J. and Barker, P. M. (2011). Getting started with TEOS-10 and the Gibbs Seawater (GSW) oceanographic toolbox. *SCOR/IAPSO WG*, 127:1–28.

McGillicuddy Jr, D. (2016). Mechanisms of Physical-Biological-Biogeochemical Interaction at the Oceanic Mesoscale. *Annual review of marine science*, 8:125.

McWilliams, J. C. (1985). Submesoscale, coherent vortices in the ocean. *Reviews of Geophysics*, 23(2):165–182.

McWilliams, J. C. (2008). The nature and consequences of oceanic eddies. *Ocean Modeling in an Eddying Regime*, pages 5–15.

McWilliams, J. C. (2016). Submesoscale currents in the ocean. *Proc. R. Soc. A*, 472(2189):20160117.

Melander, M., Zabusky, N., and McWilliams, J. (1988). Symmetric vortex merger in two dimensions: causes and conditions. *Journal of Fluid Mechanics*, 195:303–340.

Messager, C. and Swart, S. (2016). Significant Atmospheric Boundary Layer Change Observed above an Agulhas Current Warm Cored Eddy. *Advances in Meteorology*, 2016:1–7.

Millot, C., Taupier-Letage, I., and Benzohra, M. (1990). The Algerian eddies. *Earth-Science Reviews*, 27(3):203–219.

Mkhinini, N., Coimbra, A. L. S., Stegner, A., Arsouze, T., Taupier-Letage, I., and Béranger, K. (2014). Long-lived mesoscale eddies in the eastern Mediterranean Sea: Analysis of 20 years of AVISO geostrophic velocities. *Journal of Geophysical Research: Oceans*, 119(12):8603–8626.

Morrow, R., Birol, F., Griffin, D., and Sudre, J. (2004). Divergent pathways of cyclonic and anti-cyclonic ocean eddies. *Geophysical Research Letters*, 31(24).

Morrow, R., Coleman, R., Church, J., and Chelton, D. (1994). Surface eddy momentum flux and velocity variances in the Southern Ocean from Geosat altimetry. *Journal of Physical Oceanography*, 24(10):2050–2071.

Morrow, R. and Le Traon, P.-Y. (2012). Recent advances in observing mesoscale ocean dynamics with satellite altimetry. *Advances in Space Research*, 50(8):1062–1076.

Müller, P., McWilliams, J., and Molemaker, M. (2005). Routes to dissipation in the ocean: The 2D/3D turbulence conundrum.

Munk, W. H. (1950). On the wind-driven ocean circulation. *Journal of meteorology*, 7(2):80–93.

Nel, D., Lutjeharms, J., Pakhomov, E., Ansorge, I., Ryan, P., and Klages, N. (2001). Exploitation of mesoscale oceanographic features by grey-headed albatross Thalassarche chrysostoma in the southern Indian Ocean. *Marine Ecology Progress Series*, 217:15–26.

Nencioli, F., Dall'Olmo, G., and Quartly, G. D. (2018). Agulhas ring transport efficiency from combined satellite altimetry and Argo profiles. *Journal of Geophysical Research: Oceans*, 123(8):5874–5888.

Nencioli, F., Dong, C., Dickey, T., Washburn, L., and McWilliams, J. C. (2010). A Vector Geometry–Based Eddy Detection Algorithm and Its Application to a High-Resolution Numerical Model Product and High-Frequency Radar Surface Velocities in the Southern California Bight. *Journal of Atmospheric and Oceanic Technology*, 27(3):564–579.

Nof, D. (1981). On the β-induced movement of isolated baroclinic eddies. *Journal of Physical Oceanography*, 11(12):1662–1672.

Nof, D. (1991). Fission of single and multiple eddies. *Journal of Physical Oceanography*, 21(1):40–52.

Nof, D. (2005). The momentum imbalance paradox revisited. *Journal of physical oceanography*, 35(10):1928–1939.

O'Brien, M. C., Melling, H., Pedersen, T. F., and Macdonald, R. W. (2011). The role of eddies and energetic ocean phenomena in the transport of sediment from shelf to basin in the Arctic. *Journal of Geophysical Research: Oceans*, 116(C8).

Okubo, A. (1970). Horizontal dispersion of floatable particles in the vicinity of velocity singularities such as convergences. In *Deep sea research and oceanographic abstracts*, volume 17, pages 445–454. Elsevier.

Olson, D. B. (1991). Rings in the ocean. *Annual Review of Earth and Planetary Sciences*, 19(1):283–311.

Olson, D. B. and Evans, R. H. (1986). Rings of the Agulhas current. *Deep Sea Research Part A. Oceanographic Research Papers*, 33(1):27–42.

Olson, D. B., Fine, R. A., and Gordon, A. L. (1992). Convective modifications of water masses in the Agulhas. *Deep Sea Research Part A. Oceanographic Research Papers*, 39:S163 – S181.

Owens, W. B. and Wong, A. P. (2009). An improved calibration method for the drift of the conductivity sensor on autonomous CTD profiling floats by θ-S climatology. *Deep Sea Research Part I: Oceanographic Research Papers*, 56(3):450–457.

Pachauri, R. K., Allen, M. R., Barros, V. R., Broome, J., Cramer, W., Christ, R., Church, J. A., Clarke, L., Dahe, Q., Dasgupta, P., et al. (2014). *Climate change 2014: synthesis report. Contribution of Working Groups I, II and III to the fifth assessment report of the Intergovernmental Panel on Climate Change*. IPCC.

Paul, M., van de Flierdt, T., Rehkämper, M., Khondoker, R., Weiss, D., Lohan, M. C., and Homoky, W. B. (2015). Tracing the Agulhas leakage with lead isotopes. *Geophysical Research Letters*, 42(20):8515–8521. 2015GL065625.

Pegliasco, C., Chaigneau, A., and Morrow, R. (2015). Main eddy vertical structures observed in the four major Eastern Boundary Upwelling Systems. *Journal of Geophysical Research: Oceans*, 120(9):6008–6033.

Penven, P., Echevin, V., Pasapera, J., Colas, F., and Tam, J. (2005). Average circulation, seasonal cycle, and mesoscale dynamics of the Peru Current System: A modeling approach. *Journal of Geophysical Research: Oceans*, 110(C10).

Penven, P., Lutjeharms, J. R. E., and Florenchie, P. (2006). Madagascar: A pacemaker for the Agulhas Current system? *Geophysical Research Letters*, 33(17). L17609.

Perrot, X. and Carton, X. (2010). 2D vortex interaction in a non-uniform flow. *Theoretical and Computational Fluid Dynamics*, 24(1-4):95–100.

Pichevin, T., Nof, D., and Lutjeharms, J. (1999). Why are there Agulhas rings? *Journal of physical oceanography*, 29(4):693–707.

Pinot, J.-M. and Ganachaud, A. (1999). The role of winter intermediate waters in the spring-summer circulation of the Balearic Sea: 1. Hydrography and inverse box modeling. *Journal of Geophysical Research: Oceans*, 104(C12):29843–29864.

Provenzale, A. (1999). Transport by coherent barotropic vortices. *Annual review of fluid mechanics*, 31(1):55–93.

Provost, C., Escoffier, C., Maamaatuaiahutapu, K., Kartavtseff, A., and Garçon, V. (1999). Subtropical mode waters in the South Atlantic Ocean. *Journal of Geophysical Research: Oceans*, 104(C9):21033–21049.

Pujol, M.-I., Faugère, Y., Taburet, G., Dupuy, S., Pelloquin, C., Ablain, M., and Picot, N. (2016). DUACS DT2014: the new multi-mission altimeter data set reprocessed over 20 years. *Ocean Science*, 12(5).

Qiu-Yang, L., Sun, L., and Sheng-Fu, L. (2016). GEM: a dynamic tracking model for mesoscale eddies in the ocean. *Ocean Science*, 12(6):1249.

Rahmstorf, S. (2002). Ocean circulation and climate during the past 120,000 years. *Nature*, 419(6903):207.

Renault, L., Molemaker, M. J., McWilliams, J. C., Shchepetkin, A. F., Lemarié, F., Chelton, D., Illig, S., and Hall, A. (2016). Modulation of wind work by oceanic current interaction with the atmosphere. *Journal of Physical Oceanography*, 46(6):1685–1704.

Rhein, M. a., Rintoul, S. R., Aoki, S., Campos, E., Chambers, D., Feely, R. A., Gulev, S., Johnson, G., Josey, S., Kostianoy, A., et al. (2013). Observations: ocean. *Climate change*, pages 255–316.

Rhines, P. B. (1975). Waves and turbulence on a beta-plane. *Journal of Fluid Mechanics*, 69(3):417–443.

Richardson, P. L. (1980). Benjamin Franklin and Timothy Folger's first printed chart of the Gulf Stream. *Science*, 207(4431):643–645.

Richardson, P. L. (1993). Tracking ocean eddies. *American Scientist*, 81(3):261–271.

Richardson, P. L. (2008). On the history of meridional overturning circulation schematic diagrams. *Progress in Oceanography*, 76(4):466–486.

Ridgway, K. and Dunn, J. (2007). Observational evidence for a Southern Hemisphere oceanic supergyre. *Geophysical Research Letters*, 34(13).

Rio, M., Guinehut, S., and Larnicol, G. (2011). New CNES-CLS09 global mean dynamic topography computed from the combination of GRACE data, altimetry, and in situ measurements. *Journal of Geophysical Research: Oceans*, 116(C7).

Rio, M.-H., Mulet, S., and Picot, N. (2014). Beyond GOCE for the ocean circulation estimate: Synergetic use of altimetry, gravimetry, and in situ data provides new insight into geostrophic and Ekman currents. *Geophysical Research Letters*, 41(24):8918–8925. 2014GL061773.

Roemmich, D., Church, J., Gilson, J., Monselesan, D., Sutton, P., and Wijffels, S. (2015). Unabated planetary warming and its ocean structure since 2006. *Nature climate change*, 5(3):240.

Roemmich, D. and Gilson, J. (2001). Eddy transport of heat and thermocline waters in the North Pacific: A key to interannual/decadal climate variability? *Journal of Physical Oceanography*, 31(3):675–687.

Rossi, V., López, C., Sudre, J., Hernández-García, E., and Garçon, V. (2008). Comparative study of mixing and biological activity of the Benguela and Canary upwelling systems. *Geophysical Research Letters*, 35(11).

Rouault, M., Penven, P., and Pohl, B. (2009). Warming in the Agulhas Current system since the 1980's. *Geophysical Research Letters*, 36(12). L12602.

Rühs, S., Durgadoo, J. V., Behrens, E., and Biastoch, A. (2013). Advective timescales and pathways of Agulhas leakage. *Geophysical Research Letters*, 40(15):3997–4000.

Rühs, S., Schwarzkopf, F. U., Speich, S., and Biastoch, A. (2018). Cold vs. warm water route - sources for the upper limb of the AMOC revisited in a high-resolution ocean model. *Ocean Science Discussions*, pages 1–38.

Rusciano, E., Speich, S., and Ollitrault, M. (2012). Interocean exchanges and the spreading of Antarctic Intermediate Water south of Africa. *Journal of Geophysical Research: Oceans*, 117(C10).

Sallée, J.-B., Speer, K., Rintoul, S., and Wijffels, S. (2010). Southern Ocean thermocline ventilation. *Journal of Physical Oceanography*, 40(3):509–529.

Sangrà, P., Pelegrí, J. L., Hernández-Guerra, A., Arregui, I., Martín, J. M., Marrero-Díaz, A., Martínez, A., Ratsimandresy, A. W., and Rodríguez-Santana, A. (2005). Life history of an anticyclonic eddy. *Journal of Geophysical Research: Oceans*, 110(C3). C03021.

Sato, O. and Polito, P. (2014). Observation of South Atlantic subtropical mode waters with Argo profiling float data. *Journal of Geophysical Research: Oceans*, 119(5):2860–2881.

Savchenko, V., Emery, W., and Vladimirov, O. (1978). A cyclonic eddy in the Antarctic Circumpolar Current south of Australia: results of Soviet-American observations aboard the R/V Professor Zubov. *Journal of Physical Oceanography*, 8(5):825–837.

Schlax, M. G. and Chelton, D. B. (2016). The "Growing Method" of Eddy Identification and Tracking in Two and Three Dimensions.

Schmid, C., Boebel, O., Zenk, W., Lutjeharms, J., Garzoli, S., Richardson, P., and Barron, C. (2003). Early evolution of an Agulhas Ring. *Deep Sea Research Part II: Topical Studies in Oceanography*, 50(1):141–166.

Schmitz Jr, W. J. (1995). On the interbasin-scale thermohaline circulation. *Reviews of Geophysics*, 33(2):151–173.

Schouten, M. W., de Ruijter, W. P. M., and van Leeuwen, P. J. (2002). Upstream control of Agulhas Ring shedding. *Journal of Geophysical Research: Oceans*, 107(C8):23–1–23–11.

Schouten, M. W., de Ruijter, W. P. M., van Leeuwen, P. J., and Lutjeharms, J. R. E. (2000). Translation, decay and splitting of Agulhas rings in the southeastern Atlantic Ocean. *Journal of Geophysical Research: Oceans*, 105(C9):21913–21925.

Schultz Tokos, K. L., Hinrichsen, H.-H., and Zenk, W. (1994). Merging and migration of two meddies. *Journal of physical oceanography*, 24(10):2129–2141.

Schütte, F., Brandt, P., and Karstensen, J. (2016). Occurrence and characteristics of mesoscale eddies in the tropical northeast Atlantic Ocean. *Ocean Science*, 12(3):663–685.

Seki, M. P., Lumpkin, R., and Flament, P. (2002). Hawaii cyclonic eddies and blue marlin catches: the case study of the 1995 Hawaiian International Billfish Tournament. *Journal of Oceanography*, 58(5):739–745.

Shapiro, G. and Meschanov, S. (1991). Distribution and spreading of Red Sea Water and salt lens formation in the northwest Indian Ocean. *Deep Sea Research Part A. Oceanographic Research Papers*, 38(1):21–34.

Shay, L. K., Goni, G. J., and Black, P. G. (2000). Effects of a warm oceanic feature on Hurricane Opal. *Monthly Weather Review*, 128(5):1366–1383.

Simmons, H. L. and Nof, D. (2000). Islands as eddy splitters. *Journal of marine research*, 58(6):919–956.

Smith, W. and Sandwell, D. (1997). Global Sea Floor Topography from Satellite Altimetry and Ship Depth Soundings. *Science*, 277(5334):1956–1962.

Southwick, O., Johnson, E., and McDonald, N. (2016). A simple model for sheddies: Ocean eddies formed from shed vorticity. *Journal of Physical Oceanography*, 46(10):2961–2979.

Souza, J., Chapron, B., and Autret, E. (2014). The surface thermal signature and air–sea coupling over the Agulhas rings propagating in the South Atlantic Ocean interior. *Ocean Science*, 10(4):633–644.

Souza, J. M. A. C., de Boyer Montégut, C., Cabanes, C., and Klein, P. (2011a). Estimation of the Agulhas ring impacts on meridional heat fluxes and transport using ARGO floats and satellite data. *Geophysical Research Letters*, 38(21). L21602.

Souza, J. M. A. C. D., De Boyer Montegut, C., and Le Traon, P.-Y. (2011b). Comparison between three implementations of automatic identification algorithms for the quantification and characterization of mesoscale eddies in the South Atlantic Ocean. *Ocean Science*, 7(3):317–334.

Spain, D. L. (1980). *SOFAR float data report of the POLYMODE Local Dynamics Experiment*. Graduate School of Oceanography, Narragansett Marine Laboratory, University of Rhode Island.

Speer, K., Rintoul, S. R., and Sloyan, B. (2000). The diabatic Deacon cell. *Journal of physical oceanography*, 30(12):3212–3222.

Speich, S., Blanke, B., and Cai, W. (2007). Atlantic meridional overturning circulation and the Southern Hemisphere supergyre. *Geophysical Research Letters*, 34(23).

Speich, S., Blanke, B., and Madec, G. (2001). Warm and cold water routes of an OGCM thermohaline conveyor belt. *Geophysical Research Letters*, 28(2):311–314.

Stammer, D. (1997). Global characteristics of ocean variability estimated from regional TOPEX/POSEIDON altimeter measurements. *Journal of Physical Oceanography*, 27(8):1743–1769.

Stammer, D. and Cazenave, A. (2017). *Satellite Altimetry over Oceans and Land Surfaces*. CRC Press.

Stammer, D., Hinrichsen, H.-H., and Käse, R. H. (1991). Can meddies be detected by satellite altimetry? *Journal of Geophysical Research: Oceans*, 96(C4):7005–7014.

Stern, M. E. (1965). Interaction of a uniform wind stress with a geostrophic vortex. *Deep Sea Research and Oceanographic Abstracts*, 12(3):355 – 367.

Stommel, H. (1948). The westward intensification of wind-driven ocean currents. *Eos, Transactions American Geophysical Union*, 29(2):202–206.

Stramma, L. (1991). Geostrophic transport of the South Equatorial Current in the Atlantic. *Journal of Marine Research*, 49(2):281–294.

Stramma, L. and Peterson, R. G. (1989). Geostrophic transport in the Benguela Current region. *Journal of Physical Oceanography*, 19(10):1440–1448.

Stramma, L. and Peterson, R. G. (1990). The South Atlantic Current. *Journal of Physical Oceanography*, 20(6):846–859.

Swallow, J. (1969). A deep eddy off Cape St Vincent. *Deep-Sea Research*, page 285.

Swallow, J. C. (1955). A neutral-buoyancy float for measuring deep currents. *Deep Sea Research (1953)*, 3(1):74–81.

Talley, L. D. (2011). *Descriptive physical oceanography: an introduction*. Academic press.

Talley, L. D. (2013). Closure of the global overturning circulation through the Indian, Pacific, and Southern Oceans: Schematics and transports. *Oceanography*, 26(1):80–97.

Talley, L. D., Feely, R. A., Sloyan, B. M., Wanninkhof, R., Baringer, M. O., Bullister, J. L., Carlson, C. A., Doney, S. C., Fine, R. A., Firing, E., et al. (2016). Changes in ocean heat, carbon content, and ventilation: A review of the first decade of go-ship global repeat hydrography.

Tierny, J., Favelier, G., Levine, J. A., Gueunet, C., and Michaux, M. (2018). The Topology ToolKit. *IEEE transactions on visualization and computer graphics*, 24(1):832–842.

Trenberth, K. E. and Caron, J. M. (2001). Estimates of meridional atmosphere and ocean heat transports. *Journal of Climate*, 14(16):3433–3443.

Uda, M. (1938). Hydrographic fluctuation in the north-eastern sea-region adjacent to Japan of north Pacific ocean.(A result of the simultaneous oceanographical investigations in 1934-1937. *Bull. Imp. Fish. Exp.*, 9:1–66.

Vallis, G. K. (2006). *Atmospheric and oceanic fluid dynamics : fundamentals and large-scale circulation*. Cambridge University Press, Cambridge.

Van Aken, H., Van Veldhoven, A., Veth, C., De Ruijter, W., Van Leeuwen, P., Drijfhout, S., Whittle, C., and Rouault, M. (2003). Observations of a young Agulhas ring, Astrid, during MARE in March 2000. *Deep Sea Research Part II: Topical Studies in Oceanography*, 50(1):167–195.

van Ballegooyen, R. C., Gründlingh, M. L., and Lutjeharms, J. R. E. (1994). Eddy fluxes of heat and salt from the southwest Indian Ocean into the southeast Atlantic Ocean: A case study. *Journal of Geophysical Research: Oceans*, 99(C7):14053–14070.

van Sebille, E., Beal, L. M., and Johns, W. E. (2011). Advective time scales of Agulhas leakage to the North Atlantic in surface drifter observations and the 3D OFES model. *Journal of Physical Oceanography*, 41(5):1026–1034.

van Sebille, E. and van Leeuwen, P. J. (2007). Fast northward energy transfer in the Atlantic due to Agulhas rings. *Journal of physical oceanography*, 37(9):2305–2315.

van Sebille, E., Van Leeuwen, P. J., Biastoch, A., and de Ruijter, W. P. (2010). On the fast decay of Agulhas rings. *Journal of Geophysical Research: Oceans*, 115(C3).

Veneziani, M., Griffa, A., Reynolds, A. M., and Mariano, A. J. (2004). Oceanic Turbulence and Stochastic Models from Subsurface Lagrangian Data for the Northwest Atlantic Ocean. *Journal of Physical Oceanography*, 34:1884–1906.

Villar, E., Farrant, G. K., Follows, M., Garczarek, L., Speich, S., Audic, S., Bittner, L., Blanke, B., Brum, J. R., Brunet, C., et al. (2015). Environmental characteristics of Agulhas rings affect interocean plankton transport. *Science*, 348(6237):1261447.

Wang, Y., Beron-Vera, F., and Olascoaga, M. (2016). The life cycle of a coherent Lagrangian Agulhas ring. *Journal of Geophysical Research: Oceans*, 121(6):3944–3954.

Wang, Y., Olascoaga, M., and Beron-Vera, F. (2015). Coherent water transport across the South Atlantic. *Geophysical Research Letters*, 42(10):4072–4079.

Weijer, W., De Ruijter, W. P., and Dijkstra, H. A. (2001). Stability of the Atlantic overturning circulation: Competition between Bering Strait freshwater flux and Agulhas heat and salt sources. *Journal of Physical Oceanography*, 31(8):2385–2402.

Weijer, W., de Ruijter, W. P., Dijkstra, H. A., and Van Leeuwen, P. J. (1999). Impact of interbasin exchange on the Atlantic overturning circulation. *Journal of Physical Oceanography*, 29(9):2266–2284.

Weijer, W., De Ruijter, W. P., Sterl, A., and Drijfhout, S. S. (2002). Response of the Atlantic overturning circulation to South Atlantic sources of buoyancy. *Global and Planetary Change*, 34(3):293–311.

Weiss, J. (1991). The dynamics of enstrophy transfer in two-dimensional hydrodynamics. *Physica D: Nonlinear Phenomena*, 48(2-3):273–294.

Wijffels, S., Roemmich, D., Monselesan, D., Church, J., and Gilson, J. (2016). Ocean temperatures chronicle the ongoing warming of Earth. *Nature Climate Change*, 6(2):116.

Williams, R. (2001). Ocean Subduction. In Steele, J. H., editor, *Encyclopedia of Ocean Sciences*, pages 1982 – 1993. Academic Press, Oxford.

Williams, S., Petersen, M., Bremer, P.-T., Hecht, M., Pascucci, V., Ahrens, J., Hlawitschka, M., and Hamann, B. (2011). Adaptive extraction and quantification of geophysical vortices. *IEEE transactions on visualization and computer graphics*, 17(12):2088–2095.

Wunsch, C. (1999). Where do ocean eddy heat fluxes matter? *Journal of Geophysical Research: Oceans (1978–2012)*, 104(C6):13235–13249.

Wunsch, C. and Stammer, D. (1995). The global frequency-wavenumber spectrum of oceanic variability estimated from TOPEX/POSEIDON altimetric measurements. *Journal of Geophysical Research: Oceans*, 100(C12):24895–24910.

Wüst, G. (1935). Schichtung und Zirkulation des atlantischen Ozeans: Die Stratosphäre des Atlantisthen Ozeans, Wissenschaftliche Ergebnisse der Deutschen Atlantischen Expedition auf dem Forschungs-und Vermessungschiff METEOR 1925–1927, Band VI, Teil 1.

Wyrtki, K. (1967). The spectrum of ocean turbulence over distances between 40 and 1000 kilometers. *Deutsche Hydrografische Zeitschrift*, 20(4):176–186.

Xu, L., Li, P., Xie, S.-P., Liu, Q., Liu, C., and Gao, W. (2016). Observing mesoscale eddy effects on mode-water subduction and transport in the North Pacific. *Nature communications*, 7:10505.

Yang, G., Wang, F., Li, Y., and Lin, P. (2013). Mesoscale eddies in the northwestern subtropical Pacific Ocean: Statistical characteristics and three-dimensional structures. *Journal of Geophysical Research: Oceans*, 118(4):1906–1925.

Yasuda, I. and Flierl, G. R. (1997). Two-dimensional asymmetric vortex merger: merger dynamics and critical merger distance. *Dynamics of atmospheres and oceans*, 26(3):159–181.

Yi, J., Du, Y., He, Z., and Zhou, C. (2014). Enhancing the accuracy of automatic eddy detection and the capability of recognizing the multi-core structures from maps of sea level anomaly. *Ocean Science*, 10(1):39.

Zhang, Y., Liu, Z., Zhao, Y., Wang, W., Li, J., and Xu, J. (2014a). Mesoscale eddies transport deep-sea sediments. *Scientific reports*, 4:5937.

Zhang, Z., Tian, J., Qiu, B., Zhao, W., Chang, P., Wu, D., and Wan, X. (2016). Observed 3d structure, generation, and dissipation of oceanic mesoscale eddies in the south china sea. *Scientific reports*, 6:24349.

Zhang, Z., Wang, W., and Qiu, B. (2014b). Oceanic mass transport by mesoscale eddies. *Science*, page 1252418.

Zhang, Z., Zhang, Y., Wang, W., and Huang, R. X. (2013). Universal structure of mesoscale eddies in the ocean. *Geophysical Research Letters*, 40(14):3677–3681.

Zheng, S., Du, Y., Li, J., and Cheng, X. (2015). Eddy characteristics in the South Indian Ocean as inferred from surface drifters. *Ocean Science*, 11(3):361–371.

Liste des Figures

1.1 Évolution des anomalies de température historiques observées (a) et projetées par modélisation numérique (b) issus du 5^e rapport de GIEC [Pachauri et al. 2014]. Les couleurs du panneau a représentent différentes bases de données. Les deux couleurs dans le panneau b indiquent les résultats pour 2 scénarios d'émissions (RCP2.6 et RCP8.5) avec l'incertitude associée. 2

2.1 Schémas simplifiés 2D (panneau **a**) et 3D (panneau **b**) de la circulation globale de retournement. Les deux panneaux ont été reproduits depuis Talley [2013] d'aprés Talley [2011] à partir de Gordon [1986], Schmitz Jr [1995], Rahmstorf [2002] et Lumpkin and Pazos [2007]. . 4

2.2 Représentation graphique des trois hypothèses sur le moteur de la GOC traduit depuis Huang [2010] 6

2.3 Représentation des principaux processus agissant sur l'océan en fonction de leur extension spatio-temporelle inspirés de Huang [2010], Lampitt et al. [2010] et Dickey [2003]. Pour l'échelle de temps, des symboles ne faisant pas partie du système international de mesures ont été ajoutés: S pour semaine, M pour mois et A pour années. . . 7

2.4 Sélection d'images satellites du site internet "Earth Observatory" de la NASA [`http://earthobservatory.nasa.gov/`]. **a**) Image en fausse couleur du MODIS sur le satellite Aqua le 2 septembre 2017, **b**) Image du OLI sur le satellite Landsat 8 le 18 juillet 2018 et **c**) Image du MODIS sur le satellite Terra le 26 décembre 2011. 8

2.5 Types de tourbillons et anomalies de masses volumiques (ρ) en surface et dans le cœur légèrement modifié d'après Assassi et al. [2016]. . . 13

2.6 Principe de l'altimétrie par Cazenave and Massonnet [2004]. 14

2.7 Visualisation 3D centrée sur l'Atlantique Sud de la carte ADT en "delayed-time" du 1er janvier 2017. 16

2.8 Schémas de fonctionnement des instruments de mesure dérivants. **a**) Cycle d'un flotteur Argo traduit d'après une figure produite par le International Argo Project Office. **b**) Fonctionnement d'une bouée de surface traduit d'aprés une figure produite par le National Oceanic and Atmospheric Administration. 19

2.9 Visions statistiques de l'évolution de **a**) la taille (rayon) et de **b**) l'intensité (amplitude) normalisée des tourbillons en fonction de leur durée de vie normalisée en concaténant deux figures produites par Mason et al. [2014] et Pegliasco et al. [2015]. Ces deux auteurs ont utilisé des trajectoires obtenues à partir de suivis des tourbillons sur des cartes altimétriques afin d'obtenir ces statistiques. 21

2.10 Explication graphique des déplacements zonaux (panneau **a**) et méridiens (panneau **b**) des tourbillons d'échelle moyenne sous l'effet de gradient de voriticité planétaire. Ces schémas ont été adaptés d'après Cushman-Roisin et al. [1990], Cushman-Roisin and Beckers [2011] et Morrow et al. [2004] 22

2.11 Subduction d'un tourbillon anticyclonique sous un front tel que simulé par Herbette et al. [2004]. La vorticité potentielle (Q) est indiquée par les anomalies de hauteur potentielle correspondant aux anomalies de Q normalisées par Q. 25

2.12 Synthèse de l'impact des tourbillons océaniques de surface sur l'atmosphère traduit depuis Frenger et al. [2013]. Il est à noter que ce schéma représente des tourbillons dans l'hémisphère sud. 26

2.13 Représentation schématique du super-gyre de l'hémisphère Sud. Les couleurs indiquent la hauteur dynamique intégrée dans les 2000 premiers mètres de la base de données CARS [Ridgway and Dunn 2007]. Les flèches noires et les étiquettes indiquent des éléments importants de l'écoulement. Le super-gyre de l'hémisphère sud est marqué par des lignes pointillées grises. Figure traduite d'après Beal et al. [2011]. 28

2.14 Domaine d'étude et bathymétrie extraite de la base de données ETOPO2 [Smith and Sandwell 1997] 29

3.1 Study domain and a) bathymetry from the ETOPO2 data set [Smith and Sandwell 1997] and b) Mean Dynamic Topography (MDT, [Duacs/AVISO+ 2014]) with the main currents indicated. 39

3.2 Example of eddies detected near the Agulhas Current on 23 March 2000. Two cyclones and one anticyclone are shown in a) an ADT map and b) in terms of ADT amplitude along a section crossing the extrema of the eddies detected in (a). For each eddy, the ADT contours where the azimuthal speed is maximum (eddy core limit definition - dashed lines) and the outermost closed contour (eddy outer limit definition - dotted line) are shown. ADT isolines with 10 cm intervals and the geostrophic velocity vectors distributed by AVISO are superimposed in (a). 42

3.3 Schematic diagram of the eddy tracking step of the algorithm. a) Simplest situation where a single eddy is identified at the two different time intervals, t and $t + dt$. The area of the two eddy occurrences and their overlapping surface are shown, the latter in the form of a hatched surface. b) Splitting event. c) Merging event. Although the overlap threshold is applied in b) and c), these areas have not been represented to ensure readability of the figures. 43

3.4 Schematic of a simple network of trajectories up to order 2. This network is characterized by 4 formations, 4 disappearances, and 3 merging and splitting events. With each merging and splitting, the cost function is applied to follow the main trajectory by associating a segment with a higher order. 46

3.5 Number of eddies (on the ordinate) identified from surface drifting buoys by Lumpkin [2016] and used to validate the robustness of the eddies identified by the TOEddies algorithm shown as function of their radii (on the abscissa). The radii are sampled every 10 km. These numbers are computed separately for anticyclonic and cyclonic eddies. 48

3.6 Example of cross-detection of eddies for 12 December 2012 where an eddy identified from a surface drifter trajectory by LU16 (in black with a diamond symbol locating its center) and an anticyclone detected in the TOEddies Atlas (red contours for its outer limit and its maximum speed core) overlap. 49

3.7 Histograms (solid lines) and cumulative frequency (dashed lines) of the eddy R_{max} for TOEddies (red and blue lines) and META2017 (pink and light blue lines) computed over 2-km intervals. The vertical dotted line is the mean first baroclonic Rossby radius (L_R) of deformation in the area and the grey dashed area limits the 10 and 90 percentiles. The baroclonic Rossby radius of deformation is computed by applying the Chelton et al. [1998] method on the World Ocean Database [Boyer et al. 2013] averaged over seven years (i.e. 2005 to 2012). 52

3.8 Percentage of matching of LU16 eddies with TOEddies (solid lines) and META2017 (dashed lines) eddies as a function of LU16 eddy size. Values are expressed as a percentage of LU16 eddies collocated at 10 km intervals. We consider that eddies match if their polarity in LU16 and in the atlases based on altimetry is the same. When the polarities of the collocalised eddies differ, this is counted as a mismatch. Anticyclones are in red, cyclones are in blue. 53

3.9 Number of trajectories according to their order associated with Agulhas Rings. 54

3.10 a) Whole set of Agulhas Ring Eddy Network (AREN) trajectories (from order 0 to maximum order 27). The color of the trajectories is related to their order. The black color is for order 0, which we defined as the main trajectories for the Agulhas Rings. 7 sections [A-G] were used to derive the AR properties across the basins. b) percentage of time each 2°x2° grid cell is within an AREN trajectory. The gray shading in each figure represents water depths less than 3500 m in the ETOPO2 data set [Smith and Sandwell 1997]. 55

3.11 a) Median of Rossby number (Ro) and of the b) Equivalent radius of the characteristic contour (R_{Vmax}) of the Agulhas Ring Eddies Network. These properties are computed on a 2°x2° grid. The gray shading in each figure represents water depth shallower than 3500 m in the ETOPO2 data set [Smith and Sandwell 1997]. 57

3.12 a) Median of the propagation velocity of the Agulhas Ring Eddy Network (in m/s) and b) associated main propagation direction. These properties are calculated on a 2°x2° grid and the propagation direction is computed from the eddy positions one week apart. Schematic white arrows have been added in the bottom panel to highlight the main propagation direction. The gray shading in each figure represents water depth shallower than 3500 m in the ETOPO2 data set [Smith and Sandwell 1997]. 61

3.13 a) Mean surface geostrophic velocity estimated from AVISO satellite altimetry (in m/s) and b) associated main direction. These properties are computed on a 2°x2° grid. Schematic white arrows have been added in the bottom panel to highlight the main velocity direction. The gray shading in each figure represents water depth less than 3500 m in the ETOPO2 data set [Smith and Sandwell 1997]. 62

3.14 2°x2° gridded positions and number of first detections (a), last detections (b) , merging events (c) and splitting events (d) of the AREN4 (i.e. AREN with orders less than 4). Each dot size represents the number of events for each grid cell associated with more than 10 occurrences. The gray shading in each figure represents water depth shallower than 3500 m in the ETOPO2 data set [Smith and Sandwell 1997]. 63

3.15 2°x2° gridded positions and number of first detections (a), last detections (b) , merging events (c) and splitting events (d) of the AREN. Each dot size represents the number of events for each grid cell associated with more than 10 occurrences. The gray shading in each figure represents water depth shallower than 3500 m in the ETOPO2 data set [Smith and Sandwell 1997]. 64

3.16 Composite figure of the order-0 AREN starting the most to the east (a) and ending the most to the west (b). Snapshots on selected dates are given, with in blue the eddy centroid (cross symbol), the ADT contour associated with the maximum speed (dotted) and the outermost ADT (solid line) contours. The trajectory of panel b interacts with two order-1 trajectories whose paths are drawn in dashed lines. 66

4.1 The study domain presented in terms of a) the local bathymetry from the ETOPO2 data set [Smith and Sandwell 1997] and b) the percentage of time each 2°x2° grid cell is occupied by the core of an eddy occurrence taking part to the Agulhas Ring Eddy Network [Laxenaire et al. 2018]. Figure modified from Laxenaire et al. [2018]. 79

4.2 a) Geographical distribution of the segments (in colors) taking part to the network of trajectories for the Agulhas Ring sampled for the longest period by Argo profiling float. The positions of the Argo profiles sampling the whole set of eddies that composed this particular network are represented by the black crosses; b) A sketch displaying the various segments together with the eddy merging and splitting events and Argo profiles position as a function of time. The gray shading patches in (a) represents water depth shallower than 3500 m in the ETOPO2 data set [Smith and Sandwell 1997]. 85

4.3 Temporal evolution of a) the monthly averaged equivalent radius of the outer contour (R_{out}) and the eddy core contour where the azimuthal velocity is maximum (R_{Vmax}), b) the maximum of azimuthal velocity (V_{max}) and c) the absolute Rossby number of the core ($|Ro|$) as derived from the altimetry maps. The error bars correspond to the monthly STD of these parameters. 86

4.4 a) The outer contours and b) the characteristic contours (associated to the maximum of azimuthal speed) in the referential of the Agulhas Ring at times when an Argo float sample it. 87

4.5 a) Conservative Temperature, b) Conservative Temperature Anomaly, c) Absolute Salinity, d) Absolute Salinity Anomaly, e) Potential Density and f) Potential Density Anomaly for the closest Argo profiles to the Agulhas Rings center for every 10-day intervals as a function of time and depth. Black lines with markers in each right panel represent the distance of each profile from the eddy center (Dc) whose scale is presented in the y-axis on the right of panels b, d and f. The marker is a cross for profiles inside the characteristic contours otherwise it is indicated as a square. Selected isotherms, isohalines and isopycnals levels are added to the corresponding panels for both, the full fields and the anomalies. 89

4.6 a) Conservative Temperature, b) Absolute Salinity and c) σ_0 for the environment climatological profiles we used to compute the Agulhas Ring vertical property anomalies in Figure 4.5; d) Number of averaged Argo profiles used to produce the environment climatology. 90

4.7 Time evolution of the Brunt Väisälä frequency computed for the Argo float No. 5902281 profiles a) within the Agulhas Ring and b) for the environment climatology. Isopycnals levels separated by a 0.5 $kg.m^{-3}$ interval are added to the corresponding panels. 91

4.8 Sea Surface Temperature (blue) and associated anomalies (black) interpolated from the ODYSSEA SST dataset [Autret and Piolle 2011] at the position of the center of the AR. The anomalies are computed subtracting the mean SST computed in the region at less than 300 km from the eddy center to the SST at the center. All the data were smoothed by a moving average associated to a monthly window. 94

4.9 a) Argo vertical profiles of density anomaly. 4 lye close to the eddy center and show the two Mode Waters thermohaline extrema (plain lines) and 1 is located farther (dashed lines) and does not display these two Mode Waters related extrema. b) Depth of the two Mode Water cores as a function of Dc for all the profiles lying at less than 40 km from the eddy center. An outlier is identified if both extrema in a profile are at a distance from the black lines larger than the STD associated to the determination of each extremum. 95

4.10 Position of the Argo profiles in the moving frame of the Agulhas Ring. The center of the frame corresponds to the centroid of the characteristic eddy contour delimited by R_{Vmax} and computed from ADT maps. The filled circles indicate Argo profiles inside the characteristic eddy contour, the gray circles those inside outer eddy edge and the empty diamond those outside the Agulhas Ring and any other neighboring eddy and lying in a 160 km radius from the Agulhas Ring center. 96

4.11 Superposition of the observed (background color) and the reconstructed (black contours) Agulhas Ring of the a) Conservative Temperature, b) Absolute Salinity, c) σ_0, and d) root-mean-square error between the observed σ_0 anomalies and the reconstructed values computed at each depth. 98

4.12 Anomalies of a) Conservative Temperature, b) Absolute Salinity, c) σ_0, and d) Brunt Väisälä frequency squared (N^2) for the Reconstructed Agulhas Ring. Contours in d) are isopycnals of the Reconstructed Aulhas Ring. The grey patch near the surface in each panel corresponds to the region above the isopycnal surface 26.2 kg m^{-3} which marks the separation between the subtropical gyre upper warm waters and the eddy upper limit. 99

4.13 a) Velocity field of the Reconstructed Agulhas Ring computed from hydrographic data and b) evolution of the geostrophic currents derived from satellite altimetry maps as a function of the distance from the center. The black line in b) is the velocity derived from hydrographic data at -200 m (i.e. where this velocity is maximum). A dashed white line is added at this depth in panel a). The black line in panel a) corresponds to the separatrix where the velocity is equal to 5.7×10^{-2} m s^{-1} which is the median translation speed during the period November 2012 - November 2013. The two dashed lines correspond to this value $\pm$ a STD of 1.4×10^{-2} m s^{-1}. The grey patch in panel a corresponds to the region above the isopycnal surface 26.2 kg m^{-3} which marks the separation between the upper subtropical gyre waters and the upper limit of the eddy. 101

4.14 Anomalies of a) Heat Content and b) Salt Content as a function of the distance from the eddy center derived for both, the reconstructed Agulhas Ring and the Argo profiles sampling the eddy. These values are obtained by integrating vertically from the eddy separatrix up to 200 m equations 4.8 and 4.9. 103

4.15 Number of a) cores and b) type of internal structure of the Agulhas Rings described in the literature. Each article is associated to a unique marker type. The gray shading patches in a) represent water depth shallower than 3500 m in the ETOPO2 data set [Smith and Sandwell 1997]. 105

4.16 a) Position and b) hydrological properties in the Mode Water cores of the Agulhas Rings described in the literature. Each study discussing one or more of these eddies is associated to a specific marker and the color correspond to a particular type of eddy. Double Mode Water core eddies have two similar markers. The gray shaded patches in a) represent water depth shallower than 3500 m in the ETOPO2 data set [Smith and Sandwell 1997]. The background lines in b) represent isopycnals of potential density anomalies referenced to the surface pressure (σ_0). The blue and green shaded patches highlight the hydrological properties of, respectively, SASTMW2 and SASTMW3 as described by Sato and Polito [2014]. 107

5.1 a) Indian water Agulhas Ring Eddy Network (AREN) trajectories. The color of the trajectories is related to their order. The black color is for order 0, which we defined as Agulhas Rings "main trajectories". Seven sections (A–D) were used to derive the number of Indian water AREN trajectories crossing per year during the period 01/01/2000 – 31/12/2016. The gray shading in each figure represents water depths less than 3,500 m in the ETOPO2 data set [Smith and Sandwell 1997]. b) Schematic of the reconstructed Indian water AREN where the segments not considered in this study are indicated by a red cross. 122

5.2 Histogram showing the number of Argo profiles sampling Indian Water AREN according to a) the AREN order and b) the distance (Dc) of the profiles position from the eddy centers. Each bar is colored in dark gray when the Argo profiles lie within the eddy core or in light gray otherwise. 125

5.3 Type of anticyclonic eddies (surface and subsurface intensified) for a) Agulhas Rings and b) all other anticyclonic eddy identified in the region. Only Argo profiles sampling an anticyclone at a distance from the center lower than half of its instantaneous R_{Vmax} are considered. The Mean Dynamic Topography (MDT, [Duacs/AVISO+ 2014]) contours spaced by 10 cm are superposed to indicate the large-scale mean circulation in the area. The gray shading in each figure represents water depths less than 3,500 m in the ETOPO2 data set [Smith and Sandwell 1997]. 127

5.4 Heat Content Anomalies (HCA) for the profiles sampling an Agulhas Ring integrated between a) 1200 m to 200 m of depth and b) the contribution to HCA for the upper 200 m layer ($ContribHCA^0_{200}$) expressed as percentage of the total HCA following equation 5.2. c) HCA for anticyclonic eddies non identified as Agulhas Rings from the TOEddies Atlas. Negative values of HCA(r) are indicated in black in panels a and c. The gray shading in each figure represents water depths less than 3,500 m in the ETOPO2 data set [Smith and Sandwell 1997]. 130

5.5 (b to d) $HCA^{200}_{1200}(r)$ computed for all the Argo profiles sampling an Indian Water AREN as estimated in the four boxes presented in panel a. The color of each point in the two lower panels corresponds to the longitude of the sampling. 134

5.6 Three examples (panels a to c) of reconstructed $HCA(r)$ and their associated coefficient of determination (R^2) for eddies lying in close-by regions. The $HCA(r)$ values directly derived from observations are presented as grey circles while the Lagrangianly reconstructed $HCA(r)$ values are shown as black lines. The trajectories (in blue) and the position of the associated Argo profiles are presented in a map on the right top corner of each panel. The position of the Argo profiles are drawn in red if they sample the Agulhas Rings within their R_{Vmax} contours and black otherwise. 138

5.7 Reconstruction of HCA_{1200}^{200} using the whole set of Argo profiles sampling an Indian Water AREN (b to e) in the four geographical boxes presented in a). Each colored thick lines in b) to e) is associated with a different eddy-composite method of reconstruction whereas the dashed black lines represent the various Lagrangian reconstructions. 142

C.1 a) The order-0 Agulhas Ring Eddy Network trajectories. The trajectories color is related to their order. b) Percentage of time each 2°x2° grid cell lies within an Agulhas Ring Eddy Network. The gray shading in each figure represents water depths less than 3500 m in the ETOPO2 data set [Smith and Sandwell 1997]. 174

C.2 a) Orders 1 to 4 of Agulhas Ring Eddy Network trajectories. The trajectories color is related to their order. b) Percentage of time each 2°x2° grid cell lies within an Agulhas Ring Eddy Network. The gray shading in each figure represents water depths less than 3500 m in the ETOPO2 data set [Smith and Sandwell 1997]. 175

C.3 a) Orders 5 to 10 of Agulhas Ring Eddy Network trajectories. The trajectories color is related to their order. b) Percentage of time each 2°x2° grid cell lies within an Agulhas Ring Eddy Network. The gray shading in each figure represents water depths less than 3500 m in the ETOPO2 data set [Smith and Sandwell 1997]. 175

C.4 a) Orders 11 to 20 of Agulhas Ring Eddy Network trajectories. The trajectories color is related to their order. b) Percentage of time each 2°x2° grid cell lies within an Agulhas Ring Eddy Network. The gray shading in each figure represents water depths less than 3500 m in the ETOPO2 data set [Smith and Sandwell 1997]. 176

C.5 a) Orders 21 to 29 of Agulhas Ring Eddy Network trajectories. The trajectories color is related to their order. b) Percentage of time each 2°x2° grid cell lies within an Agulhas Ring Eddy Network. The gray shading in each figure represents water depths less than 3500 m in the ETOPO2 data set [Smith and Sandwell 1997]. 176

C.6 a) Trajectories non connected with the Agulhas Ring Eddy Network. Percentage of time each 2°x2° grid cell lies within an Agulhas Ring Eddy Network. The gray shading in each figure represents water depths less than 3500 m in the ETOPO2 data set [Smith and Sandwell 1997]. 177

C.7 Three order-0 Agulhas Ring Eddy Network trajectories with their properties specified at the crossing of the lines [C-F]. The gray shading in each figure represents water depths less than 3500 m in the ETOPO2 data set [Smith and Sandwell 1997]. 178

C.8 Density plot of the ratio of the mean AREN speed of propagation over the mean surface geostrophic geostrophic velocity derived from AVISO maps. This ratio is obtained by dividing the 2°x2° averaged propagation speed (see Figure 12a in the main article) by the temporal and spatial averaged of the AVISO surface geostrophic velocity calculated in the same grid-cel (see Figure 13a in the main article). 179

D.1 Trajectories and name of the profiling floats that sampled the AREN of interest. The profiles which are used in this study are marked by crosses. 182

D.2 Bathymetry below the fifth trajectory segment of the Agulhas Ring main trajectory studied in this work from the ETOPO2 data set [Smith and Sandwell 1997]. 182

D.3 Monthly averaged SST anomalies in the moving reference frame of the 5^{th} segment of the AREN interpolated from the ODYSSEA SST dataset [Autret and Piolle 2011]. These anomalies are computed subtracting the mean SST computed in each panels to the SST values at each point. 183

D.4 TS diagram of Argo profiles with a $Dc < 25$ km in red and those with a $150 < Dc < 200$ km in blue sampling the segment 5 between November 2012 and November 2013. 184

D.5 σ_0 anomalies derived from Argo observations (circles) and from the Reconstructed Agulhas Ring (solid black lines) at 6 different depths as function of the distance from the eddy center (Dc). The date for every observation is indicated by the color of the circles. 185

E.1 Potential density (σ_0) at a) the surface, b) 100 m and c) 200 m from the World Ocean Database [Boyer et al. 2013] averaged over seven years (i.e. 2005 to 2012). Isopycnals levels are drawn every 0.1 kg.m^{-3}. The gray shading in each figure represents water depths less than 3500 m in the ETOPO2 data set [Smith and Sandwell 1997]. . 194

E.2 Heat Content between 1200 and 200 m computed in the climatologic profiles associated to the Agulhas Ring (panel a) and those computed for all the Argo profiles extracted in this region (panel b) 195

E.3 Heat content Anomalies (panel a) and total Heat content (panel b), both between 1200 and 200 m, computed in the eddies reconstructed by the Agulhas Ring. The values obtained in the HCA are plotted at the position of the center derived from the altimetry. 196

Liste des Tableaux

3.1 Parameters of the six data sets tested against the independent LU16 eddy atlas derived from surface drifter buoys. Each row corresponds to a different dataset for which the version and the type of satellite altimetry maps used for the detection is specified. The suffix "_raw" is added when the 4-week threshold on lifetime eddy segments is not applied. The suffix "_rad" refers to the results of the LU16-TOEddies collocation performed using the eddy radius instead of the eddy area criterion. N/A (not applicable) is added when a parameter is not relevant for a dataset. 50

3.2 Detection and collocation matching statistics with LU16 eddies. "max" refers to the eddy contours associated with their maximum speed while "out" refers to their outer contours. The percentages indicate the proportions of eddies by polarity as defined in LU16. Anti and Cyclo mean, respectively, anticyclones and cyclones. N/A (not applicable) is added when a parameter is not relevant for a dataset. 51

3.3 Properties of the Agulhas Ring Eddy Network throughout the geographical domain. The values are computed at the lines [A-G] plotted in Figure 3.10a. For each variable, estimates of the median and standard deviation (STD) are provided. 59

3.4 Distribution of the orders of the Agulhas Ring Eddy Network expressed as percentage when they cross the lines [A-G] plotted in Figure 3.10a. 60

4.1 List of all the studies that described at least one Agulhas Ring in depth during dedicated oceanographic cruises. To be noted here that the list is limited to those Agulhas Rings that were sufficiently documented in the referenced studies. 104

4.2 Integrated properties of Agulhas Rings described in the literature. The reference for the bottom limit of integration are given in the last column. The integration are either achieved from an isotherm, for a fixed depth or by identifying the coherent part of the eddy assessed, by following Flierl [1981], as the volume of the eddy where eddy velocities are lower than the eddy drifting speed. The upper limit of integration is the surface for all eddies except for RecAR for which the integration is limited to σ_0=26.2 kg m^{-3}. 111

5.1 Eddy integrated HCA^{200}_{1200} obtained by applying different approaches (eddy-composite and Lagrangian) in each of the four geographical boxes presented in Figure 5.7a. 143

5.2 $HC(r = 0)$ computed from the $HCA(r = 0)$ for the reconstructed Indian Water AREN and the environment local average HC. Values are expressed as $11\,10^{11}$ J.m^{-2} 145

B.1 Eddy detection and collocation statistics with LU16 loopers for 4 data sets for the persistent threshold from 0 to 10 mm. The "max" annotation refers to the eddy contours associated with the maximum eddy azimuthal speed while the "out" annotation refers to the outer eddy contours. The percentages indicate the fractions of eddies by polarity as defined in LU16. Anti and Cyclo stand for respectively anticyclonic and cyclonic eddies. 167

B.2 Tracking skill statistics for 4 collocated data sets with LU16 eddy trajectories (traj) that lasted at least 1 week. The percentage of trajectories tracked indicates the number of LU16 trajectories that are only associated with trajectories of the same polarity. The percentage of the trajectory network explains the percentage of trajectories poorly tracked in META2017 and properly tracked through the reconstruction of the first order network in TOEddies. The columns "> 50%" and "> 90%" indicate the number of LU16 trajectories collocated with the eddies defined by the other atlases during, respectively, more than 50 and 90 % of the life of LU16 eddies. The "mean tracking time" column gives the average percentage of collocation time between the LU16 loopers and the eddies of the other atlases expressed in terms of LU16 eddy life. The trajectory errors column indicates the number of trajectories associated, for at least one day, with an unmatched polarity eddy. 172

D.1 Hydrological properties Potential Temperature (θ), Practical Salinity and σ_θ) of Mode Waters found in the South Atlantic as described in the literature. The standard deviations ($\pm$ STD) is provided when it is explicitly supplied in the articles. 187

D.2 Properties of the Agulhas Ring cores described in the literature. The precision of the variables is not fixed as it depends of each article. . 189

D.3 Properties of the Agulhas Ring cores described in the literature. The precision of the variables is not fixed as it depends of each article. . 190

D.4 Integrated properties of the Agulhas Rings describe in the literature expressed as percentage of the same variables obtained in the RecAR. We do not compare volume for a fixed depth as there is no meaning to do that. 192

université PARIS-SACLAY
ÉCOLE DOCTORALE
Sciences de l'environnement d'île-de-France (SEIF)

Titre : Étude du devenir des tourbillons des Aiguilles et de leur transport dans l'océan Atlantique Sud à partir d'observations satellitaires et in situ

Mots clés : Dynamique océanique à mésoéchelle, Caractéristiques tourbillonnaires, Transport de chaleur

Résumé : Les échanges de chaleur entre les océans Indiens et Atlantiques sont étroitement liés à la circulation globale et au climat. Ceux-ci sont principalement réalisés par les Anneaux des Aiguilles (AR pour "Agulhas Rings") qui sont étudiés dans cette thèse à l'aide de cartes quotidiennes d'altimétrie satellitaire et de profils hydrologiques de flotteurs Argo.
En développant et appliquant l'algorithme d'identification et de suivi des tourbillons TOEddies à 24 années de cartes de la topographie dynamique absolue, nous estimons les origines, les trajectoires et la durée de vie des AR. La principale nouveauté réside dans la détection de nombreux événements de fractionnement et de fusion des tourbillons. Cette innovation conduit à la définition d'un réseau de trajectoires au lieu d'une identification biunivoque entre un tourbillon et une trajectoire. Les résultats ainsi obtenus diffèrent considérablement des évaluations précédentes en connectant des tourbillons formés dans l'océan Indien en amont du courant des Aiguilles à d'autres dans le courant du Brésil.
La collocation des segments reconstruits des trajectoires des AR avec les profileurs Argo donne accès à leur structure thermohaline ce qui permet d'en estimer l'évolution au cours de leur propagation. En particulier, nous montrons la modification d'un AR passant d'une structure de surface à une de sub-surface dû à sa subduction lors de son entrée dans le gyre subtropical de l'Atlantique Sud. Cette transformation se traduit par la création de deux cœurs d'eau Modale qui concentrent la majeure partie du contenu de chaleur de cet AR.
Enfin, une estimation de la répartition géographique de plusieurs AR est obtenue à partir des tourbillons détectés dans le bassin du Cap et dans l'océan Atlantique Sud. Cette répartition géographique montre que, en général, les AR subductent lorsqu'ils quittent le bassin du Cap. De plus, pour chaque tourbillon suffisamment échantillonné par les flotteurs Argo, nous estimons son anomalie de contenu thermique calculée en fonction de son environnement. Ces anomalies s'avèrent être importantes tout au long de leur trajectoire bien que les AR perdent de la chaleur en se propageant. En combinant des méthodes eulériennes et lagrangiennes, nous estimons le transport de chaleur en sub-surface effectué par les AR lors de leur propagation dans l'Atlantique Sud.

Title : Assessments on the fate of the Agulhas Rings and their transport in the South Atlantic estimated by combining satellite altimetry and in situ observations

Keywords : Ocean mesoscale dynamics, Eddy characteristics, Heat Transport

Abstract : The Indo-Atlantic interocean heat exchanges are tightly linked to global ocean circulation and climate. They are principally achieved by the Agulhas Rings (AR) which are investigated in this thesis by means of 24 years of daily satellite-altimetry maps and Argo floats profiles.
By applying the TOEddies eddy identification and tracking algorithm, developped in this study, to daily maps of Absolute Dynamical Topography (ADT), we estimate Agulhas Rings origins, paths and lifetime. The main novelty lies in the detection of numerous eddy splitting and merging events that leads to the definition of a network of trajectories instead of a biunivocal identification between an eddy with a single trajectory. The results obtained by the network differ considerably with previous estimates connecting eddies formed in the Indian Ocean upstream of the Agulhas Current to eddies in the Brazil Current.
The collocation of the reconstructed segments of AR trajectories with Argo profiling floats gives access to their thermohaline structure which allows to estimate their in-route evolution. In particular, we show modification of an AR, transitioning from a surface to a subsurface intensified eddy while it subduct when entering the South Atlantic subtropical gyre. This transformation results in the creation of two Mode Water cores which concentrate most of the heat content of this AR. Finally, an estimate of AR geographical distribution was obtained from the numerous eddies detected in the Cape Basin and South Atlantic Ocean. It shows that AR generally subduct when they leave the Cape Basin. Moreover, for each eddy sufficiently sampled by Argo floats, we were able to estimate its heat content anomaly with respect of the environment. AR heat content anomalies result to be important all along their trajectories even if they release heat along their path. Combining both eulerian and lagrangian methods, we estimate the sub-surface heat transport achieved by their AR while they propagate in the South Atlantic.

Université Paris-Saclay
Espace Technologique / Immeuble Discovery
Route de l'Orme aux Merisiers RD 128 / 91190 Saint-Aubin, France